Conjugated Polymer-Recombinant *Escherichia coli* Biohybrid Systems for Hydrogen Production

Ying Yang

November 2023

Thesis submitted in accordance with the requirements of the University of Liverpool for the degree of Doctor of Philosophy

Conjugated Polymer-Recombinant *Escherichia coli* Biohybrid Systems for Hydrogen Production

Ying Yang

Biohybrid photosynthesis systems, which combine biological and non-biological materials, have attracted recent interest in solar-to-chemical energy conversion. However, the solar efficiencies of such systems remain low, despite advances in both artificial photosynthesis and synthetic biology.

Here, we show the potential of conjugated organic polymers as photosensitizers in biological hybrid systems by combining a series of polymer nanoparticles with recombinant *Escherichia coli* (*E. coli*) cells. Under simulated solar light irradiation, the biohybrids consisting of fluorene / dibenzo[*b,d*]thiophene sulfone copolymer (LP41) and recombinant *E. coli* (i.e., a LP41/*E. coli* biohybrid) show a sacrificial hydrogen evolution rate of 3.442 mmol g^{-1} h^{-1} that is 30 times higher than the polymer photocatalyst alone (0.105 mmol g^{-1} h^{-1}). No detectable hydrogen was generated from the *E. coli* cells alone, demonstrating the strong synergy between the polymer nanoparticles and bacterial cells. Photochemical activity trends were explained by differences in the physical interaction between synthetic materials and microorganisms, as well as redox energy level alignment. These results suggest that organic semiconductors may offer unique advantages, such as solution processability, low toxicity, and more tunable surface interactions with the biological components over more traditionally used inorganic materials.

Mechanism study was conducted to explore the possible both extracellular and intracellular charge transfer pathways. Fluorescence lifetime and transient absorption spectroscopy studies suggest, although do not prove, charge transfer between the conjugated polymer and the bacterial cells under irradiation.

Overall, this study adds to our fundamental understanding of this new type of organic biohybrid system. While these systems are far from practical, not least because of the use of a sacrificial hole scavenger, the results do suggest that organic semiconductors are equally viable for biohybrid photocatalyst manufacture and that they may offer certain advantages over inorganic materials, such as low toxicity, engineerable surface properties, and solution processability.

Acknowledgements

Undertaking this PhD has been a truly life-changing experience for me and it would not have been possible to do without the support and guidance that I received from many people.

Firstly, I would like to express my sincere gratitude to my supervisors Professor Andrew I. Cooper and Professor Lu-Ning Liu for the continuous support of my PhD study. Your guidance helped me in all the time of research and writing of this thesis and without your guidance and constant feedback this PhD would not have been achievable.

Many thanks also to my research coordinators Dr Reiner Sebastian Sprick and Dr Marc Little for your support and encouragement throughout the completion of my PhD. Thanks also go to the China Scholarship Council for a PhD studentship, the EPSRC and BBSRC for providing funding for this research.

I would also like to thank all those I have collaborated with on this work, especially Professor Martijn Zwijnenburg at University College London, Dr Adrian M. Gardner and Professor Alexander J. Cowan at the Stephenson Institute for Renewable Energy, Professor Roy Goodacre, Dr Nigel Gotts and Dr Adam Burke at Centre for Metabolomics Research. Your insights have helped shape this work and it would not have been possible without you.

I am also very grateful to Xiaofeng, Veronica, Rich, Liang, Tom, Chengxi, Rob, Bonnie, Haiyan, Qiuyao, Yu, and Yaqi who all helped me in numerous ways during various stages of my PhD. Thanks also go to all the other members of the Cooper group and Liu lab who have made this a lot more than a lab.

I also appreciate all the hiking, firework, tennis, and squash time that I had here, all of these made my study and life in the UK a wonderful time.

I would also like to say a heartfelt thank you to my former supervisor Aihua, and my friends Ally, Mengyang, Yawen, Shu, and Yani in China, without whom, I would not have had the courage to embark on this journey in the first place.

And finally, thank my family for believing in me and encouraging me throughout my PhD and my life in general.

List of Publications

Conjugated Polymer-Recombinant *Escherichia coli* Biohybrid Systems for Sacrificial Photobiocatalytic Hydrogen Production from Water.

ACS Nano, under review

Ying Yang, Martijn A. Zwijnenburg, Adrian M. Gardner, Sylwia Adamczyk, Yaqi Sun, Qiuyao Jiang, Alexander J. Cowan, Reiner Sebastian Sprick*, Lu-Ning Liu*, Andrew I. Cooper*

Making the connections: Physical and electric interactions in biohybrid photosynthetic systems.

Energy Environ. Sci. **2023**,*16*, 4305-4319

Ying Yang, Lu-Ning Liu, Haining Tian, Andrew I. Cooper*, Reiner Sebastian Sprick*

Table of Contents

Acknowledgements **II**

List of Publications **III**

Table of Contents **IV**

List of Abbreviations **IX**

List of Figures **XI**

List of Tables **VII**

Chapter 1 **1**

1.1 Renewable Energy Sources **2**

1.2 Solar Energy **4**

1.2.1 Solar Energy for Fuel Application 4

1.2.3 Artificial Photosynthesis 5

1.2.4 Semi-Artificial Photosynthesis 6

1.3 Hydrogen Technology **8**

1.3.1 Hydrogen Production from Fossil Fuels 9

1.3.2 Hydrogen Production from Renewable Sources 10

1.3.2.1 Biomass Process 10

1.3.2.2 Water Splitting 12

1.4 Photocatalytic Hydrogen Generation **14**

1.4.1 Basic Principles of Photocatalytic Hydrogen Generation 14

1.4.1.1 Main Process of Photocatalytic Hydrogen Generation 14

1.4.1.2 Evaluation of Photocatalytic Hydrogen Generation 16

1.4.2 Photocatalytic Hydrogen Generation Systems 17

1.4.2.1 Hydrogen Generation Systems Containing Sacrificial Reagents 17

1.4.2.2 Overall Water-Splitting System 18

1.4.3 Types of Solar-Driven Water-Splitting Devices 20

1.4.3.1 Photoelectrochemical (PEC) Water-Splitting Cells 20

1.4.3.2 Photovoltaic–Electrochemical (PV-EC) Systems 21

1.5 Semi-Artificial Photosynthesis **23**

1.5.1 Different Types of Semi-Artificial Systems 23

1.5.2 Material-Microorganism Complexes for Hybrid Photosynthesis 24
1.5.2.1 Chemical-Synthetic Inorganic Nanoparticles 24
1.5.2.2 Biosynthetic Inorganic NPs 25
1.5.2.3 Organic Photocatalysts 26
1.6 Experimental Techniques 31
1.6.1 Particle Analysis Using Dynamic Light Scattering 31
1.6.1.1 Size Analysis 31
1.6.1.2 Zeta-Potential Measurement 32
1.6.2 Time-Resolved Spectroscopy Techniques 35
1.6.2.1 Time-Correlated Single Photon Counting 35
1.6.2.2 Transient absorption spectroscopy 36
1.7 Project Aims 38
1.8 References 39
Chapter 2 56
2.1 Background 57
2.2 Incorporation of Cationic Property in Fluorene-Phenyl Polymer Photocatalysts 59
2.2.1 Synthesis 59
2.2.1.1 Monomer Synthesis 59
2.2.1.2 Polymer Synthesis 59
2.2.1.2 Polymer Nanoparticle Preparation 61
2.2.2 Characterization 61
2.2.3 Photocatalytic Hydrogen Evolution Performance 65
2.2.4 Summary 67
2.3 Cationic Group Ratio Variation in Solution-Processable Conjugated Polymer Photocatalysts 68
2.3.1 Synthesis 68
2.3.2 Characterization 68
2.3.3 Photocatalytic Hydrogen Evolution Performance 73
2.3.4 Summary 74
2.4 Backbone Variation in Cationic Solution-Processable Conjugated Polymer Photocatalysts 76

2.4.1 Synthesis 76
2.4.2 Characterization 76
2.4.3 Photocatalytic Hydrogen Evolution Performance 83
2.4.4 Summary 87
2.5 References 89
Chapter 3 94
3.1 Background 95
3.2 Conjugated Polymer-E. coli Biohybrid System Assembly 96
3.2.1 Expression of Heterologous [FeFe] Hydrogenase HydA in *E. coli* 96
3.2.2 Assembly Strategy I 97
3.2.1.1 Influence of Irradiation Period 102
3.2.1.2 Influence of Different Polymers 104
3.2.1.3 Influence of Sacrificial Electron Donors 105
3.2.1.4 Optimization of LP41/HydA BL21 Biohybrid System 107
3.2 Assembly Strategy II 110
3.3 Photobiocatalytic Hydrogen Evolution Performance 115
3.3.1 Different Conjugated Polymers 115
3.3.2 Different Reaction Medium 118
3.3.4 Different *E. coli* strain 121
3.3.5 Dye-Sensitized Biohybrid Systems 122
3.4 Summary 126
3.5 References 127
Chapter 4 131
4.1 Background 132
4.2 Spectroscopic Techniques 133
4.2.1 Fluorescence Intensity 133
4.2.2 Time-Correlated Single Photon Counting 137
4.2.3 Transient Absorption Spectroscopy 141
4.3 Metabolomics Analysis 144

4.3.1 Cell Loading Amount Determination 144
4.3.2 Sample Preparation 148
4.3.2.1 Quenching Procedure 148
4.3.2.2 Removal of Polymer Nanoparticles 149
4.3.2.3 Extraction Procedure 151
4.4 Summary 152
4.5 References 153
Chapter 5 155
5.1 Summary 156
5.2 Future Work 157
5.3 References 159
Chapter 6 161
6.1 Experimental Methods 162
6.1.1 Monomer Synthesis 162
6.1.2 Polymerization 162
6.1.2.1 General procedure for the synthesis of polymers via Suzuki-Miyaura-type polycondensation 162
6.1.2.2 General procedure for the synthesis of trimethylamine substituted polymers 164
6.1.3 Nanoparticle Fabrication 165
6.1.4 Characterization Methods 166
6.1.5 Photocatalysis Experiments 166
6.1.6 Computational Methods 167
6.2 Experimental Methods 168
6.2.1 Polymer Synthesis 168
6.2.2 Generation of Constructs 169
6.2.3 Western Blotting 169
6.2.4 Characterization Methods 169
6.2.4.1 Scanning electron microscope (SEM) characterization of *E. coli* incubated with polymer nanoparticles 169

6.2.4.2 Confocal fluorescence microscope characterization of E. coli incubated with polymer nanoparticles 170
6.2.5 Photobiocatalytic Hydrogen Production Measurement 170

6.3 Experimental Methods 171
6.3.1 Transient Absorption (TA) Measurements 171
6.3.2 Polymer/*E. Coli* Biohybrid Sample Preparation For GC-MS Measurement 171
6.3.2.1 Proposed polymer nanoparticle removal procedure 171
6.3.2.2 Proposed Sample Preparation Procedure for GCMS Analysis 172
6.3.2.3 GC-MS Instrument Method 174

6.4 References 175

6.5 Appendix 177
6.5.1 NMR spectra 177

List of Abbreviations

E. coli	*Escherichia coli*
(TD)-DFT	Time-dependent density functional theory
AA	Ascorbic acid
ATP	Adenosine triphosphate
AuNCs	Gold nanoclusters
CB	Conduction band
D	Translational diffusion coefficient
Đ	Dispersity index
EA	Electron affinity
EA	Electron affinity
E_g	Optical band gap
Fd	Ferredoxin
GPC	Gel permeation chromatography
HEP	Hydrogen evolution photocatalyst
HER	Hydrogen evolution rates
HOMO	Highest occupied molecular orbital
IP	Ionization potential;
IPTG	Isopropyl β-D-1-thiogalactopyranoside
IRF	Instrument response function
LHCs	Light-harvesting complexes
LUMO	Lowest unoccupied molecular orbital
M. thermoacetica	*Moorella thermoacetica*
M9	Minimal 9
M_n	Number-average molecular weight
M_w	Mass weighted molecular weight
MWCO	Molecular weight cut-off
NADPH	Nicotinamide adenine dinucleotide phosphate
NMWL	Nominal molecular weight limit
NPs	Nanoparticles
Nu^-	Nucleophile ion
OEP	Oxygen evolution photocatalyst
Ox	Oxidant
PBS	Phosphate Buffered Saline

PDI	Perylene diimide derivative
PDI	Polydispersity index
PEG	Poly (ethylene glycol)
PEM	Polymer electrolyte membrane
PESA	Photoelectron spectroscopy in air
PFP	Poly(fluorene-co-phenylene)
PFTP	Poly[2-methoxy-5-(2-ethylhexyloxy)-1,4-phenylenevinylene]
PL	photoluminescence
PPP	Poly(para-phenylene)
PSMA	Poly (styrene-co-maleic anhydride)
PXRD	Powder X-ray diffraction
QE	Quantum yield efficiency
RC	Reaction centre
Red	Reductant
S. oneidensis MR-1	*Shewanella oneidensis MR-1*
SCE	Saturated Calomel Electrode
SD	Standard deviation
SEDs	Sacrificial Electron Donors
SEM	Scanning electron microscopy
SHE	Standard Hydrogen Electrode
SN_2	Nucleophilic substitution reaction
T	Absolute temperature
TEA	Triethylamine
TGA	Thermogravimetric analysis
Tris-HCl	Tris(hydroxymethyl)aminomethane hydrochloride
TWh	Terawatt-hours
UV-vis	Ultraviolet-visible
VB	Valence band
ΔG	Gibbs function

List of Figures

Figure 1.1 Global primary energy consumption by source from 1800 to 2021. TWh: terawatt-hours. Figure adapted from Ref. [2].....2

Figure 1.2 Global primary energy consumption by source based on global energy for 2019. Figure adapted from Ref. [2]. 3

Figure 1.3 Major photosynthetic pigments in plants. The chemical structures of the chlorophyll and carotenoid pigments present in the thylakoid membrane. Figure adapted from Ref. [10]..4

Figure 1.4 Basic structure of a photosystem. Light energy is captured by the antenna pigments and transferred to the special pair of reaction centre chlorophylls which undergo a redox reaction leading to reduction of an acceptor molecule. The oxidized special pair is regenerated by an electron donor. Figure adapted from Ref. [10]. 5

Figure 1.5 Global hydrogen demand by sector in the Net Zero Scenario, 2019-2030. Figure adapted from Ref. [36]. 8

Figure 1.6 Hydrogen production methods from fossil fuels. Figure reproduced from Ref. [39]. 9

Figure 1.7 Hydrogen production methods from renewable sources. Figure reproduced from Ref. [39]. 10

Figure 1.8 Flow diagram of the direct bio-photolysis process. 11

Figure 1.9 Flow diagram of the dark fermentation process. 12

Figure 1.10 Flow diagram of the photo fermentation process. 12

Figure 1.11 Processes in photocatalytic water splitting. Figure adapted from Ref. [54]. 14

Figure 1.12 Fundamental principle of inorganic semiconductor-based photocatalytic water splitting for hydrogen generation. Figure adapted from Ref. [57]. 16

Figure 1.13 (a) One-step photoexcitation. (b) Two-step photoexcitation with an aqueous redox mediator. (c) Two-step photoexcitation with a solid-state electron mediator. CB, conduction band; Eg, semiconductor bandgap; HEP, hydrogen evolution photocatalyst; NHE, normal hydrogen electrode; OEP, oxygen evolution photocatalyst; Ox, oxidant; Red, reductant; VB, valence band. Figure adapted from Ref. [70]. 19

Figure 1.14 Unassisted PEC device for solar overall water splitting. (a) Schematic representation of PEC cell with Co_4O_4/pGO/$BiVO_4$/SnO_x photoanode (front) wired to the Pt/TiO_x/PIP/CuO_x photocathode (behind). (b) UV–vis spectra of $BiVO_4$ and PIP as light-harvesting semiconductors. (c) Schematic representation of integrated $BiVO_4$-based photoanode and PIP-based photocathode. PIP: organic polymer semiconductor PBDB-T:ITIC:$PC_{71}BM$. Figure adapted from Ref. [82]. 20

Figure 1.15 Schematic of two types of PV-EC devices/systems: (a) Traditional PV-EC. (b) Integrated PV-EC. Figure adapted from Ref. [79].....21

Figure 1.16 (a) [FeFe]-hydrogenase-catalysed H_2 production in a photoelectrochemical biofuel cell, figure adapted from Ref. [84]; (b) polymer dots as photoactive membrane vesicles for [FeFe]-hydrogenase self-assembly and solar-driven hydrogen evolution, figure adapted from Ref. [86]; (c) Cartoon representation of a hybrid (enzyme−TiO_2) nanoparticle system, figure adapted from Ref. [85].....23

Figure 1.17 Photocatalytic H_2 production by the combination of TiO_2, methyl viologen (MV), and the recombinant *E. coli* expressing [FeFe]-hydrogenase and relevant maturases, figure adapted from Ref. [26].....24

Figure 1.18 *M. thermoacetica*–CdS reaction schematics. Figure adapted from Ref. [96].....25

Figure 1.19 Overview of the different classes of polymeric photocatalysts. Figure adapted from Ref. [105].....27

Figure 1.20 Diagram of the PDI/PFP/*M. thermoacetica* photosynthesis hybrid system. Figure adapted from Ref. [31]......28

Figure 1.21 Intensity fluctuations and Brownian motion. Differences in diffusion coefficient or particle size results in different frequency fluctuations in light intensity. Image adapted from www.atascientific.com.au.....32

Figure 1.22 Schematic representation of zeta potential definition reproduced from Ref. [104]. 34

Figure 1.23 Schematic for TCSPC reproduced from Ref. [136]. 35

Figure 1.24 Basic principle of femtosecond transient absorption. Figure adapted from Ref. [140].....36

Figure 1.25 Three-state population model illustrating the formation of a transient non-emissive product in the singlet ground state from S_1. Figure adapted from Ref. [140].....37

Figure 2.1 Chemical structures of conjugated linear polymers in this chapter.....57

Figure 2.2 General reaction scheme of Suzuki coupling reaction. 59

Figure 2.3 General catalytic cycle for Suzuki coupling reaction.....60

Figure 2.4 Synthetic route to 2,7-dibromo-9,9-bis(8-bromo-n-octyl)-fluorene monomer (M1) and polymerisation of LP1 and LP11. 60

Figure 2.5 Synthetic route of polymer FP-Oct.....61

Figure 2.6 Chromatogram of polymer (a) FP-Oct and (b) LP1. 62

Figure 2.7 (a) Thermogravimetric analysis of LP11 under nitrogen at a heating rate of 10 °C min^{-1}. (b) PXRD patterns of powders of polymer LP11.....62

Figure 2.8 (a) Normalised UV-vis and (b) PL spectra of polymer FP-Oct and LP11 dissolved in chloroform. (c) UV-vis and (d) PL spectra of polymer nanoparticle FP-Oct and LP11 in aqueous solution.....63

Figure 2.9 Size distribution of nanoparticles of polymer FP-Oct and LP11 with 50 mg/L polymer concentration by (a) intensity and (b) number.....64

Figure 2.10 SEM images of polymer FP-Oct nanoparticle with 5 mg/L polymer concentration. 65

Figure 2.11 Synthetic route to polymerisation of LP5_χ. 68

Figure 2.12 Chromatogram of polymer (b) LP5_0.10, (c) LP5_0.25, and (d) LP5_0.50.....69

Figure 2.13 Thermogravimetric analysis of LP51_0.50, 0.25 and 0.10 under nitrogen at a heating rate of 10 °C min^{-1} with major mass changes of (b) LP51_0.50, (c) LP51_0.25, and (d) LP51_0.10.....70

Figure 2.14 PXRD patterns of powders of polymer LP51_0.10, 0.25, and 0.50.....70

Figure 2.15 (a) Normalised UV-vis and (b) PL spectra of polymer LP51_0.50, 0.25, and 0.10 in chloroform. (c) UV-vis and (d) PL spectra of polymer nanoparticle LP51_0.50, 0.25, and 0.10 in aqueous solution. 71

Figure 2.16 Size distribution of nanoparticles of polymer LP51_0.10, 0.25, and 0.50 with 50 mg/L polymer concentration by intensity (a) and number (b).....72

Figure 2.17 Hydrogen evolution rates of nanoparticles of polymer LP51_0.10/0.25/0.50 loaded with 3.0 wt.% platinum co-catalyst with 0.1 M ascorbic acid and TEA/methanol/water (1:1:1) over 3 hours irradiated with a solar simulator (AM1.5G, 1 sun). 0.225 mg polymer in each sample (4.5 mL polymer nanoparticle solution with 50 mg/L polymer concentration). 73

Figure 2.18 Synthetic routes of monomer M1, polymer LP1, LP2, LP3, and LP4, and chemical structures of polymer LP11, 21, 31, and 41. 76

Figure 2.19 Chromatogram of polymer (a) LP1, (b) LP2, (c) LP3, (d) LP4. 77

Figure 2.20 (a) Thermogravimetric analysis of LP11, LP21, LP31, and LP41 under nitrogen at a heating rate of 10 °C min^{-1}. (b) PXRD patterns of powders of polymer LP11, LP21, LP31, and LP41. 78

Figure 2.21 (a) Normalised UV-vis absorption and (b) fluorescence emission spectra of polymer LP1 (λ_{exc} 370 nm), LP2 (λ_{exc} 450 nm), LP3 (λ_{exc} 450 nm), and LP4 (λ_{exc} 400 nm) dissolved in chloroform. 78

Figure 2.22 Schematic representation of five energy structural factors in a D-A conjugated polymer-E_δ: bond length alternation energy factor, E_{res}: resonance energy factor, E_θ: rotational disorder energy factor, E_{sub}: substituent energy factor and E_{int}: intermolecular interaction energy factor. 79

Figure 2.23 Energy levels of D and A chemical units and their D–A conjugated polymer. ..79

Figure 2.24 PESA spectra of polymer thin films of LP1, LP2, LP3, and LP4. 81

Figure 2.25 (a) Normalised UV-vis and (b) fluorescence emission spectra of polymer nanoparticle LP11(λ_{exc} 370 nm), LP21 (λ_{exc} 450 nm), LP31 (λ_{exc} 450 nm), and LP41 (λ_{exc} 400 nm). 82

Figure 2.26 Size distribution of nanoparticle solution of polymer LP11, LP21, LP31, and LP41 by (a) intensity and (b) number. 83

Figure 2.27 SEM images of LP11, LP21, LP31, and LP41 polymer nanoparticles. 83

Figure 2.28 Hydrogen evolution rates of nanoparticles of polymer LP11, LP21, LP31, and LP41 loaded with 3.0 wt.% platinum co-catalyst in 0.1 M ascorbic acid, and TEA/methanol/water (1:1:1) over 3 hours irradiated with a solar simulator (AM 1.5G, 1 sun). 0.225 mg polymer in each sample (4.5 mL polymer nanoparticle solution with 50 mg/L polymer concentration). 84

Figure 2.29 Predicted charge carrier potentials (IP, EA) of the polymers considered calculated through density functional theory (DFT) for oligomer models in water. Dashed colored lines indicate the potentials for different solution reactions: orange, proton reduction in TEA system of pH 11.5; red, proton reduction in AA system of pH 4; blue, one-hole oxidation of TEA to TERA; cyan and green, two-hole (A/H_2A) and one-hole ($HA\cdot/H_2A$) oxidation of ascorbic acid (see details in **Table 2.9**). 85

Figure 2.30 Correlation between the hydrogen production activity in TEA/MeOH/Water system and (a) EA values (b) zeta-potential (c) IP value (d) optical gap of polymers. 86

Figure 2.31 Correlation between the hydrogen production activity in 0.1 M ascorbic acid system and (a) EA values (b) zeta-potential (c) IP value (d) optical gap of polymers. 87

Figure 3.1 Chemical structures of conjugated polymers LP1, LP2, LP3, LP4 and LP6 with imidazolium (LP10) and trimethylammonium (LP11, LP21, LP31, LP41, and LP61) functionalization. 95

Figure 3.2 Western Blotting of *E. coli* expressing the hyd vector confirms the presence of Fd-HydA. 97

Figure 3.3 Assembly strategy I: hydrogenase induction, biohybrid assembly, and hydrogen production. 98

Figure 3.4 Thermogravimetric analysis of LP61 and LP10 under nitrogen at a heating rate of 10 °C min^{-1}. 100

Figure 3.5 Size distribution of polymer nanoparticle LP61 with 50 mg/L polymer concentration by (a) intensity and (b) number. 100

Figure 3.6 Size distribution of polymer nanoparticle LP61 with 50 mg/L polymer concentration by (a) intensity and (b) number. 101

Figure 3.7 Normalised (a) absorption and (b) emission spectrum of polymer nanoparticle LP61. 101

Figure 3.8 Normalised (a) absorption and (b) emission spectrum of polymer nanoparticle LP10. 101

Figure 3.9 Hydrogen production performance of LP61/HydA BL21 biohybrid systems (irradiated and dark), *E. coli* (HydA BL21), and polymer (LP61) under 4-hour irradiation. Plots and error bars represent the averages and standard deviations of at least three assays. 102

Figure 3.10 Hydrogen production performance of LP61/HydA BL21 biohybrid system, *E. coli* (HydA BL21), and polymer (LP61) of 4 hours in dark and 4 hours under irradiation. Plots and error bars represent the averages and standard deviations of at least three assays. 103

Figure 3.11 Hydrogen production performance of LP10/HydA BL21 biohybrid system, *E. coli* (HydA BL21), and polymer (LP10) of 2 hours in dark and 6 hours under irradiation. Plots and error bars represent the averages and standard deviations of at least three assays. 104

Figure 3.12 Hydrogen production performance of biohybrid systems (under irradiation and in dark) containing different conjugated polymer nanoparticles (LP41, LP31, LP11, and LP10) with HydA BL21 cells with 1 mM cysteine as the sacrificial electron donor. The measurement was conducted after 2 hours in dark followed by 6 hours under irradiation. Plots and error bars represent the averages and standard deviations of at least three assays for samples containing *E. coli*. 105

Figure 3.13 Hydrogen production performance of LP41 biohybrid systems (under irradiation and in dark) and LP41 polymer alone with different ascorbic acid concentrations (0.1 M, 0.05 M, 0.01 M, and 1 mM) and 1 mM cysteine as the sacrificial electron donor. The measurement was conducted after 2 hours in dark followed by 6 hours under irradiation. Plots and error bars represent the averages and standard deviations of at least three assays for samples containing *E. coli*. 106

Figure 3.14 Hydrogen production performance of LP21 biohybrid systems (under irradiation and in dark) and LP21 polymer alone with different ascorbic acid concentrations (0.1 M, 0.01 M, and 1 mM) and 1 mM cysteine as the sacrificial electron donor. The measurement was conducted after 2 hours in dark followed by 6 hours under irradiation. Plots and error bars represent the averages and standard deviations of at least three assays for samples containing *E. coli*. 107

Figure 3.15 Hydrogen production performance of LP41 biohybrid systems (under irradiation and in dark) and LP41 polymer alone with different LP41 polymer concentrations (100, 50, 25 mg/L). The measurement was conducted after 2 hours in dark followed by 6 hours under irradiation with 1 mM cysteine as sacrificial electron donor. Plots and error bars represent the averages and standard deviations of at least three assays for samples containing *E. coli*. 108

Figure 3.16 Hydrogen production performance of LP41 biohybrid systems (under irradiation and in dark) and LP41 polymer alone with 6-hour and 13-hour irradiation respectively. The measurement was conducted with 1 mM ascorbic acid as sacrificial electron donor. Plots and

error bars represent the averages and standard deviations of at least three assays for samples containing *E. coli.* 108

Figure 3.17 Hydrogen production performance of LP41/HydA BL21 biohybrid systems. The measurement was conducted after 2 hours in dark followed by 6 hours under irradiation with 1 mM ascorbic acid as sacrificial electron donor. Plots and error bars represent the averages and standard deviations of at least three assays for samples containing *E. coli.*.....109

Figure 3.18 Assembly strategy II: hydrogenase induction, biohybrid assembly, and hydrogen production. 110

Figure 3.19 Confocal images of HydA *E. coli* (100 µL concentrates in 10 mM Tris-HCl) incubated with LP41 nanoparticles (1.0 mL, 5 mg L^{-1}) for 5 mins (λ_{exc} = 488 nm) imaged on 10 mM tris(hydroxymethyl)aminomethane hydrochloride (Tris-HCl)/agar, 1 ×phosphate-buffered saline (PBS)/agar, and 1 ×M9 minimal media (M9)/agar plates.....112

Figure 3.20 SEM images of HydA *E. coli* (200 µL concentrates in 10 mM Tris-HCl) incubated with LP10, LP11, LP21, LP31, and LP41 nanoparticles (2.0 mL, 10 mg L^{-1}).....113

Figure 3.21 Confocal images of HydA *E. coli* (100 µL concentrates in 10 mM Tris-HCl) incubated with LP10, LP11, LP21, L31, and LP41 nanoparticles (1.0 mL, 5 mg L^{-1}) for 5 mins (λexc = 488 nm). 114

Figure 3.22 Hydrogen production performance of five biohybrid systems with different conjugated polymer nanoparticles (50 mg L^{-1}, LP10, LP11, LP21, LP31, and LP41) alongside polymer and *E. coli* control groups. All of the hydrogen production reactions were conducted in 10 mM tris(hydroxymethyl)aminomethane chloride buffer (pH 7, Tris-HCl) supplemented with 1 mM ascorbic acid as the hole sacrificial agent under irradiation of an AM 1.5G solar simulator for 3 h. Biohybrid reactions consist of 4.3 mL polymer nanoparticle solution, 200 µL *E. coli* concentrates, 0.5 mL 100 mM Tris-HCl, and 50 µL 0.1 M ascorbic acid. 115

Figure 3.23 Correlation between the biohybrids' photobiocatalytic activity and the polymer fundamental gap **(a)** / EA value **(b)** / IP value **(c)**/zeta-potential **(d)**.....116

Figure 3.24 Predicted charge carrier potentials (IP, EA) of the polymers considered calculated through (TD-)DFT for oligomer models in water. Dashed colored lines indicate the potentials for different solution reactions: red, proton reduction; cyan and green, two-hole (A/H_2A) and one-hole ($HA\cdot/H_2A$) oxidation of ascorbic acid. All solution potentials shown are for pH 6.5,

the experimentally measured pH of a 10 mM tris(hydroxymethyl)aminomethane chloride buffer (pH 7, Tris-HCl) supplemented with 1 mM ascorbic acid. 117

Figure 3.25 (a) The H_2 formation rate by the biohybrid (10 mg L^{-1} LP41/HydA BL21), the polymer (10 mg L^{-1} LP41), and *E. coli* (HydA BL21). (b) The H_2 formation rate by the biohybrid (LP41/HydA BL21) and the polymer (LP41) with 50 and 10 mg L^{-1} polymer concentration, respectively. 118

Figure 3.26 Hydrogen production performance of LP41 coupled with WT *E. coli* in 10 mM Tris-HCl with 1 mM ascorbic acid under irradiation with the comparison of the biohybrid system in dark and the one without ascorbic acid. 119

Figure 3.27 Hydrogen production performance of LP41 coupled with WT *E. coli* in 100 mM Tris-HCl/150 mM NaCl/0.4 wt. % glucose medium with and without irradiation. 120

Figure 3.28 Hydrogen production performance of LP41 coupled with WT *E. coli* in 100 mM Tris-HCl/150 mM NaCl/0.4 wt. % glucose medium with 1 mM ascorbic acid as sacrificial electron donor with and without irradiation. 120

Figure 3.29 Influence of ascorbic acid (AA) concentration on hydrogen production performance. 121

Figure 3.30 Hydrogen production performance of LP41 coupled with the wide type (WT) BL21 and HydA BL21 without [FeFe] hydrogenase expression was selected as control groups alongside LP41. Evolved hydrogen was normalized to same cell concentration (optical density, OD_{600} = 1.0) for different *E. coli* strains. All of the hydrogen production reactions were conducted in 10 mM tris(hydroxymethyl)aminomethane chloride buffer (pH 7, Tris-HCl) supplemented with 1 mM ascorbic acid as the hole sacrificial agent under irradiation of an AM 1.5G solar simulator for 3 h. Biohybrid reactions consist of 4.3 mL polymer nanoparticle solution, 200 µL *E. coli* concentrates, 0.5 mL 100 mM Tris-HCl, and 50 µL 0.1 M ascorbic acid. Plots and error bars represent the averages and standard deviations of at least two assays. 122

Figure 3.31 Chemical structures of dyes. 123

Figure 3.32 Hydrogen production performance of photocatalytic active organic molecules/WT *E. coli* biohybrid systems (D12: 1,3,5-Tribenzoylbenzene, D13: 9H-Thioxanthen-9-one, D14: 4,4'-Biphenyldicarboxaldehyde, D15: Azobenzene). 125

Figure 4.1 Emission (a) and excitation (b) spectrum of LP41/*E. coli* biohybrid systems with different ascorbic acid concentrations; Emission (c) and excitation (d) spectrum of LP41/*E. coli* biohybrid systems with different *E. coli* amount; Emission (e) and excitation (f) spectrum of LP41 sample with different ascorbic acid concentrations. Excitation wavelength is 400 nm, and emission wavelength was 470 nm for all measurements. 134

Figure 4.2 Linear relationship between I_0/I and $C_{quencher}/C_{quencher,0}$ of LP41/*E. coli* biohybrid systems with different amounts of *E. coli* concentrates. $C_{quencher}/C_{quencher,0}$: the relative equivalence of quenchers. 136

Figure 4.3 Decay curves of LP41/*E. coli* biohybrid systems with different *E. coli* amounts (a) and different ascorbic acid concentrations (b); and LP41 with different ascorbic acid concentrations with instrument response function (IRF). 138

Figure 4.4 Quenching by intersystem crossing. 140

Figure 4.5 Schematic for stepwise electron exchange. 141

Figure 4.6 Photoinduced electron transfer. 141

Figure 4.7 TA spectra normalized at the global maximum (ΔA) for 10 mg/L LP41 polymer nanoparticle in Tris-HCl aqueous solution (solid line) and 10 mg/L LP41 polymer nanoparticle in Tris-HCl aqueous solution with 1 mM ascorbic acid (dashed line) at key pump-probe delays as indicated. 142

Figure 4.8 TA spectra normalized at the global maximum (ΔA) for 10 mg/L LP41 polymer nanoparticle in Tris-HCl aqueous solution (solid line) and 10 mg/L LP41 polymer nanoparticle/25 µL *E. coli* in Tris-HCl aqueous solution (dashed line) at key pump-probe delays as indicated. 143

Figure 4.9 UV-vis spectra of samples conducted for TA measurements, 10 mg/L LP41 polymer nanoparticle in Tris-HCl aqueous solution (with/without ascorbic acid, with/without 25 µL *E. coli*). 143

Figure 4.10 Linear relationship between *E. coli* amounts and OD_{600} values with 0, 5, 10, 25, and 50 mg/L LP41 polymer concentrations in LP41/*E. coli* biohybrid samples. Each point represents the mean value of three replicates. Statistics analysis was conducted for three replicates and it shows that there is no significant difference at the 0.05 level. 146

Figure 4.11 Linear relationship between polymer concentrations and OD_{600} values with 50, 100, 150, and 200 µL *E. coli* separately in LP41/*E. coli* biohybrid samples. Each point

represents the mean value of three replicates. Statistics analysis was conducted for three replicates and it shows that there is no significant difference at the 0.05 level. 147

Figure 4.12 Initial quenching and pelletization process. 148

Figure 4.13 Emission spectrum of untreated LP41 polymer nanoparticle solution, supernatant solutions after initial quenching step (sample 0-1, 0-2, and 0-3) and following centrifugation (sample 1-1, 1-2, and 1-3), supernatant solutions after filtration by using 3000 NMWL (sample 1-4, 1-5, and 1-6) and 30,000 NMWL (sample 1-7 and 1-8)..... 149

Figure 4.14 Removal of polymer nanoparticles from supernatant samples. 150

Figure 4.15 Extraction process of supernatant and pellet samples. 151

Figure 5.1 Structures of polymers. 158

Figure 6.1 NMR spectra of 2,7-Dibromo-9,9-bis(8-bromo-n-octyl)-fluorene in $CDCl_3$..... 177

Figure 6.2 NMR spectra of polymer LP1, LP2, LP3, and LP4 in $CDCl_3$. 177

Figure 6.3 NMR spectra of polymer LP5_0.50, 0.25, .010 in $CDCl_3$..... 178

Figure 6.4 NMR spectrum of polymer LP6 in $CDCl_3$. 178

Figure 6.5 NMR spectra of polymer LP11, LP21, LP31, and LP41 in DMSO. 178

Figure 6.6 NMR spectra of polymer LP10 and LP61 in DMSO. 178

Figure 6.7 NMR spectra of LP41 in DMSO from two batches. 178

List of Tables

Table 1.1 Summary of selected cell/photosensitiser-based biohybrid systems for semi-artificial photosynthesis.....7

Table 1.2 Reports on material-microorganism biohybrid systems for hydrogen production .30

Table 2.1 GPC data for all chloroform-soluble polymer fractions. 61

Table 2.2 Particle average size and zeta-potential (polymer conc. 50 mg L^{-1}) by dynamic light scattering. 64

Table 2.3 Dispersion in water, optical properties as well as HERs of nanoparticles of polymer FP-Oct and LP11.....66

Table 2.4 Predicted charge carrier (IP, EA) potentials of polymers considered calculated through (TD-)B3LYP for oligomer models in water (ε_r 80.1) and PESA (ε_r 2). LP1 data for polymer in water taken from previous work. Ref. [19] 66

Table 2.5 Predicted potentials for the different solution half-reactions at pH 0. Ascorbic acid* (HA*) and dehydroascorbic acid (A) are the one-hole and two-hole oxidation products of ascorbic acid, respectively, ...67

Table 2.6 Synthesis of LP5_χ.....68

Table 2.7 GPC data for all chloroform-soluble polymer fractions. 69

Table 2.8 Particle average size and zeta-potential (polymer conc. 50 mg L^{-1}) by dynamic light scattering. 72

Table 2.9 Potentials for the different solution half-reactions. Ascorbic acid* and dehydroascorbic acid are the one-hole and two-hole oxidation products of ascorbic acid, respectively. 74

Table 2.10 GPC data for all chloroform-soluble polymer fractions. 77

Table 2.11 Photoelectron spectroscopy in air data for polymer thin films. 80

Table 2.12 Predicted charge carrier (IP, EA) and excitons (IP*, EA*) potentials of polymers considered calculated through (TD-)B3LYP for oligomer models in water (ε_r 80.1) and PESA (ε_r 2). LP1 and LP4 data for polymer in water taken from previous work. Ref. [19].....81

Table 2.13 Photophysical properties of nanoparticle solution of polymer LP11, LP21, LP31, and LP41. 82

Table 2.14 Particle average size and zeta-potential (polymer conc. 50 mg L^{-1}) by dynamic light scattering. 82

Table 3.1 Components of Lysogeny broth (LB) medium. 98

Table 3.2 Components of 1×M9 minimal media, per litre 98

Table 3.3 Components in a sample vial under assembly strategy I. 99

Table 3.4 GPC data for all chloroform-soluble polymer fractions. 99

Table 3.5 Components of PBS (Phosphate Buffered Saline) (1×, pH 7.4) per litre. 110

Table 3.6 Predicted potentials for the different solution half-reactions at pH 0 were taken from previous work, potentials at pH 6.5 were estimated based on equation: $E = E^0 – 0.05916 \times pH$, E^0: potential at pH 0. Ascorbic acid* and dehydroascorbic acid are the one-hole and two-hole oxidation products of ascorbic acid, respectively. 117

Table 3.7 Hydrogen production performance of water-soluble dye/*E. coli* biohybrid systems 10 mM tris(hydroxymethyl)aminomethane chloride buffer (pH 7, Tris-HCl) supplemented with 1 mM ascorbic acid as the hole sacrificial agent under irradiation of an AM 1.5G solar simulator for 3 h. Plots and error bars represent the averages and standard deviations of at least two assays. 124

Table 4.1 Measurement groups for fluorescence spectroscopy. 133

Table 4.2 Stern-Volmer analysis of three sets of samples: LP41 with different amounts of *E. coli*, LP41/*E. coli* with different AA concentrations, and LP41 with different AA concentrations. I_0 / I: the inverse of normalized emission intensity at 470 nm; $C_{quencher}/C_{quencher,0:}$ the relative equivalence of quenchers. 136

Table 4.3 Estimated fluorescence lifetimes for biohybrid systems with different *E. coli* amounts and different ascorbic acid concentrations; and LP41 nanoparticle solution with different ascorbic acid concentrations. 139

Table 4.4 Measured OD_{600} values for all the sample groups. Three replicates were conducted for samples containing *E. coli*. 145

Table 6.1 GCMS instrument method 174

Chapter 1 :

Introduction

1.1 Renewable Energy Sources

Substantial economic development and population growth around the globe is the reason for augmented energy demand.[1] The energy system has transformed dramatically since the Industrial Revolution. We see this transformation of the global energy supply in **Figure 1.1**. Global energy consumption was over 170,000 terawatt-hours (TWh) in 2021 and has increased nearly every year for more than half a century.[2] 84.3% of the energy we use comes from fossil fuels. In 2019, oil was the biggest energy source (33.1%), followed by coal (27%) and natural gas (24.3%), as displayed in **Figure 1.2**. The key drawback of consuming these traditional resources (fossil fuels) is CO_2 emissions and increased global warming.[3]

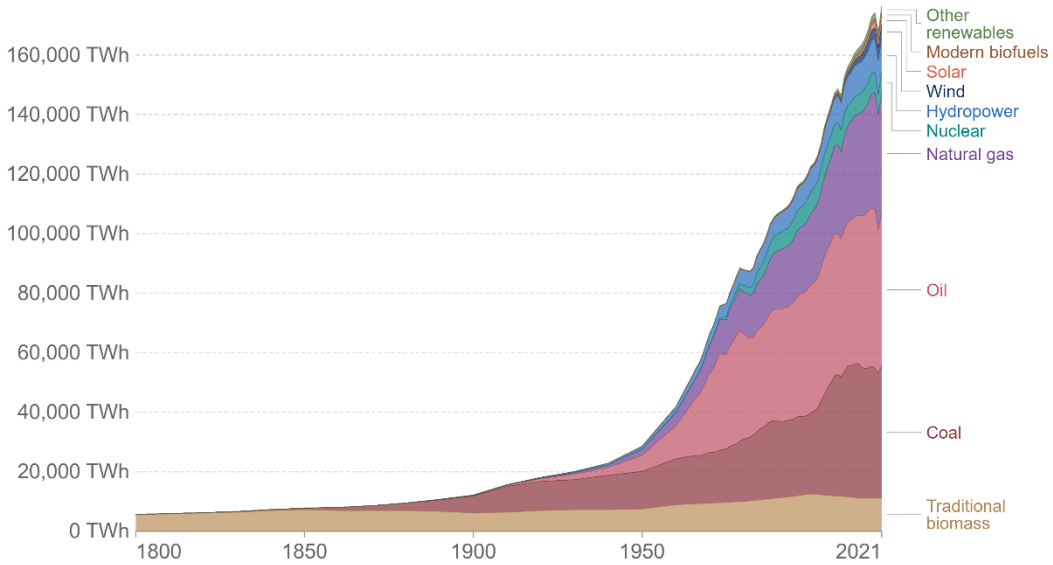

Figure 1.1 Global primary energy consumption by source from 1800 to 2021. TWh: terawatt-hours. Figure adapted from Ref. [2].

Renewable energy is a collective term used to capture several different energy sources. 'Renewables' typically include energy sourced from hydropower, solar, wind, geothermal, biomass, wave, and tidal energy.[1] The increasing greenhouse gas emissions, environmental problems, and global temperature rise are the main reasons for the global transition from conventional to renewable energy resources. Renewable energy resources are among the most promising applicants to replace fossil fuels.[4] In 2019, almost 15.7% of global primary energy came from low-carbon sources with 11.4% from renewables and 4.3% from nuclear (**Figure 1.2**). Low-carbon sources are the sum of nuclear energy and renewables, including hydropower, wind, solar, bioenergy, geothermal, wave, and tidal.[2] Hydropower and nuclear account for most

of our low-carbon energy (10.7%), and wind produces just 2.2% and solar produces 1.1% – but both sources are growing quickly.

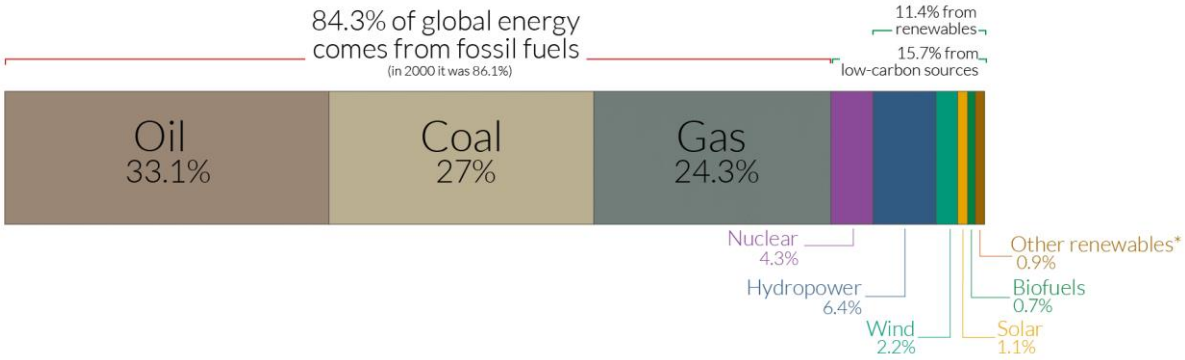

Figure 1.2 Global primary energy consumption by source based on global energy for 2019. Figure adapted from Ref. [2].

Among this, solar energy is often referred to as a 'modern renewable' – a couple of decades ago, it made only a tiny contribution to the global energy supply. Increasing global energy demands force us to seek environmentally sustainable alternatives to fossil fuels. In recent years, solar energy has become one renewable energy source that could address this need over the next century.[5]

1.2 Solar Energy

1.2.1 Solar Energy for Fuel Application

The use of solar energy requires solar capture/conversion and storage; chemical fuels are one sustainable solution to energy storage.[6] A wide range of potential fuels can potentially be generated, including hydrocarbons, nitrogen-based fuels, and hydrogen.[7] Beyond the direct use of fuels, new solar-derived chemical building blocks can also play an important role in the chemical industry, which is still heavily dependent on non-renewable feedstocks.[8]

1.2.2 Natural Photosynthesis

Over billions of years of evolution, photosynthetic organisms have developed the photosynthetic machinery to capture sunlight and convert it into organic molecules (*i.e.*, biomass) to store solar energy in the form of chemical bonds.[9]

Photosynthesis begins with the absorption of light by pigment molecules located in the thylakoid membrane, such as chlorophyll. These pigments all have in common within their chemical structures an alternating series of carbon single and double bonds, which form a conjugated π-electron system (**Figure 1.3**).[10]

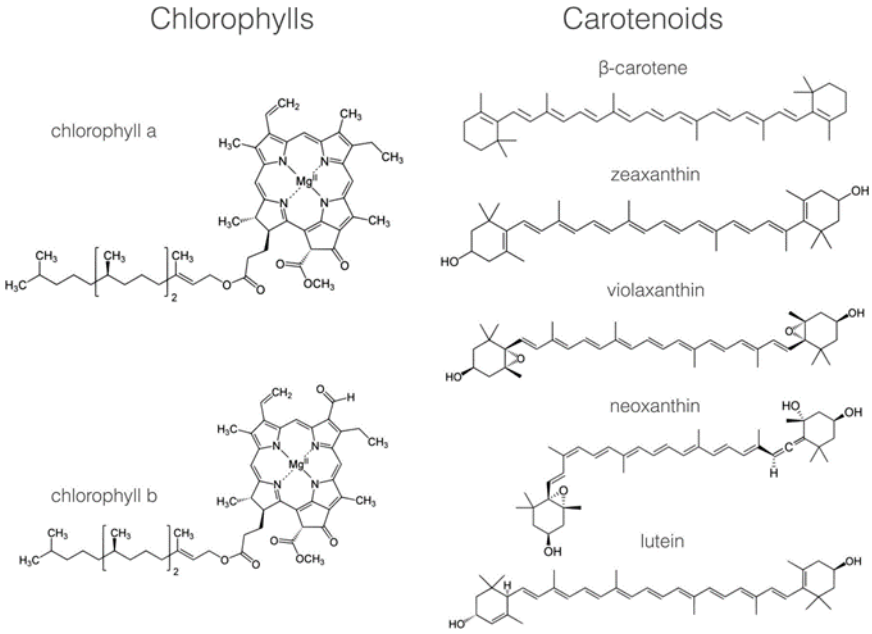

Figure 1.3 Major photosynthetic pigments in plants. The chemical structures of the chlorophyll and carotenoid pigments present in the thylakoid membrane. Figure adapted from Ref. [10].

In photosynthetic systems, chlorophylls and carotenoids are found attached to membrane-embedded proteins known as light-harvesting complexes (LHCs). Absorbed energy can be transferred among them by excitation energy transfer. A photosystem consists of numerous LHCs that form an antenna of hundreds of pigment molecules. The antenna pigments collect excitation energy and transfer it towards a 'special pair' of chlorophyll molecules in the reaction centre (RC) (**Figure 1.4**). The special pair of chlorophyll can undergo charge separation by returning to the ground state through the transfer of the electrons in the excited state to another species in an electron transport chain. High-energy electrons are then transferred through a series of membrane carriers, coupled to the synthesis of adenosine triphosphate (ATP) and nicotinamide adenine dinucleotide phosphate (NADPH).

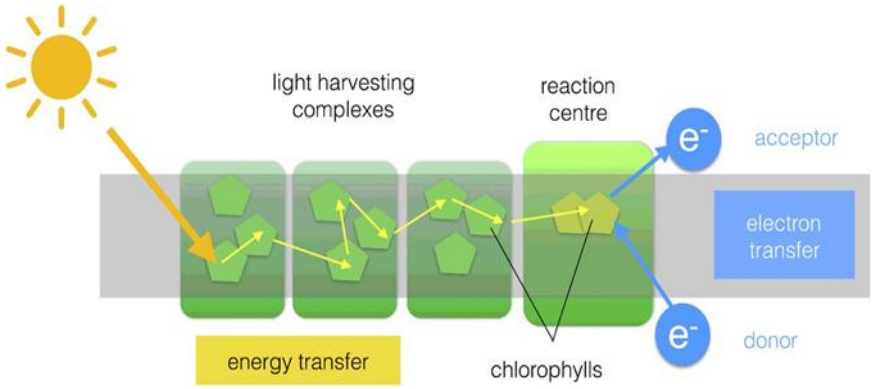

Figure 1.4 Basic structure of a photosystem. Light energy is captured by the antenna pigments and transferred to the special pair of reaction centre chlorophylls which undergo a redox reaction leading to reduction of an acceptor molecule. The oxidized special pair is regenerated by an electron donor. Figure adapted from Ref. [10].

However, natural photosynthesis is relatively inefficient, a maximum photosynthetic efficiency of about 4.5% has been calculated by Thorndike.[11] Normally crops produce yields of biomass at efficiencies less than 1%.[12]

1.2.3 Artificial Photosynthesis

Artificial photosynthesis aims to use photogenerated charge carriers for chemical reactions, such as hydrogen production from water or to produce other organic molecules, such as methanol via CO_2 reduction.[13] However, the solar-to-hydrogen efficiencies of artificial photocatalysts are much lower than those of photosynthetic organisms,[12] even though solar light absorption can be more efficient in artificial semiconductors. This has prompted researchers to explore artificial photosynthetic systems that are inspired by natural photosynthetic machinery, intending to combine the advantages of biological systems with carefully designed semiconductors.

Artificial photosynthesis mimics biological systems by using solar energy to drive a thermodynamically uphill reaction to generate fuels.[13] It has been a long-standing challenge to develop practical artificial photosynthetic systems, and many different approaches have been used, such as photoelectrochemical systems,[14] photovoltaic cells,[15] and photocatalyst materials.[16,17]

Compared with natural biological systems, these artificial photosynthetic systems can capture sunlight and drive fuel production more efficiently, mainly because of the highly efficient light-absorbing materials that are available. However, there are numerous advantages of biological systems over artificial photosynthesis, including the ability to generate active multi-complex macromolecules continually and selectively and to facilitate electron transfer, as well as sustainable repair and physiological regulation.[21] Hence, to enhance solar-fuel conversion efficiencies, different strategies have been employed to interface synthetic and biological components.

1.2.4 Semi-Artificial Photosynthesis

This relatively new approach, often termed semi-artificial photosynthesis or biological-chemical hybrid photosynthesis, leverages the light-absorbing ability of photovoltaics, photoelectrodes, and photocatalyst materials as well as the integration and dynamic regulation of metabolic pathways in biological systems.[18]

The general process is that an irradiated solar energy capture material transfers photoexcited electrons to biocatalysts, including enzymes and microbes, to produce H_2 or other products. Progress has been made in this field since the early 1980s when scientists began to combine inorganic semiconductors with microorganisms to increase hydrogen production,[19] However, semi-artificial photosynthesis has only been studied more extensively since the beginning of this century. A range of systems that capture sunlight can be coupled with biological systems such as photovoltaics,[20] photoelectrodes,[21] and photocatalysts,[22] thus allowing the construction of diverse hybrid photosynthetic systems. Most studies report either hydrogen or acetate as their product (**Table 1.1**). The crucial goal of biohybrid photosynthetic systems is to transform essentially inexhaustible atmospheric CO_2, N_2, or even wastewater into high-value chemicals with high yield and selectivity,[21,23] and longer term, with high catalyst stability.

Table 1.1 Summary of selected cell/photosensitiser-based biohybrid systems for semi-artificial photosynthesis

Material	Microorganism	Product and activity	Ref.
CdS	*M. thermoacetica*	Acetate, 0.48 mM day^{-1}, QE: 2.14 ± 0.16%	[24]
CdS, TiO_2-MnPc	*M. thermoacetica*	Acetate, 1.2 mM day^{-1}	[25]
TiO_2	Engineered *E. coli*	H_2, 0.72 µmol min^{-1} (mg wet cell)$^{-1}$	[26]
Water-soluble dyes, inorganic complexes	*S. oneidensis*	Activity for several processes: H_2 production, fumarate and pyruvate reduction, CO_2 reduction	[27]
CdS	*E. coli*	H_2, > 1.8 mmol over 3 hours	[28]
CdS	Engineered *E. coli*	H_2, 13.4 µmol after 6 hours, 81.8 µmol after 24 hours (10^8 cells)	[29]
AuNCs	*M. thermoacetica*	H_2, After 24 hours overall QE: 2.86 ± 0.38%	[30]
PFP/PDI	*M. thermoacetica*	Acetic acid, 0.63 mM accumulated over a 3-day experiment, QE: 1.6%	[31]
CdS	*S. oneidensis MR-1*	H_2, 362.44 ± 119.69 µmol mg^{-1} produced over a total of 72 hours	[32]
$CdS/CsgA_{A7}$	Engineered *E. coli*	Formic acid, 0.84 mM within 8 hours, QE: 0.13%	[33]
PFTP- PSMA D-A CPNs@ threonine deaminase	Engineered *E. coli*	2-Oxobutyrate, 6.0 ± 0.15 mM cumulative over 72 hours	[34]
La/Rh co-doped $SrTiO_3$, Mo-doped $BiVO_4$	*Sporomusa ovata*	Acetate, Solar-to-fuel conversion efficiency of 0.7% at ambient conditions (298 K, 1 atm)	[35]

NPs: nanoparticles, *M. thermoacetica*: *Moorella thermoacetica*, MnPc: Mn (II) phthalocyanine, water-soluble dyes: proflavine, Eosin Y, fluorescein, inorganic complexes: $Ru(bpy)_3^{2+}$ (bpy = 2,2′-bipyridine) and $[Ru(bpy)_2(4,4'\text{-}(PO_3H_2)_2bpy)]^{2+}$ (RuP), *S. oneidensis MR-1: Shewanella oneidensis MR-1*, *E. coli*: *Escherichia coli*, AuNCs: gold nanoclusters, QE: quantum yield efficiency. PFP: poly(fluorene-*co*-phenylene), PDI: perylene diimide derivative, D-A CPNs@Enzyme: enzyme-modified donor-acceptor conjugated polymer nanoparticles, PFTP: poly[2-methoxy-5-(2-ethylhexyloxy)-1,4-phenylenevinylene] (MEH-PPV) as electron donor and poly(fluorene-*alt*-thienopyrazine), PSMA: poly (styrene-co-maleic anhydride); n.d. = not determined

1.3 Hydrogen Technology

The increase in the contribution of renewable energy sources to global energy support, would not be feasible without using energy storage systems.[36] The major challenge for a storage device is to maintain the energy stored as long as needed and, when required, to be able to supply it as soon as possible.[37] For this purpose, several studies in their effort to provide a clean and reliable alternative to traditional fossil fuels, which enjoy this particular feature, were led to hydrogen technology.

Hydrogen is free of carbon and releases no greenhouse gases or harmful substances when used. Hydrogen also has a gravimetric heating value (141.9 MJ kg^{-1}) which is much higher than that of traditional fuels, such as petrol (47.5 MJ kg^{-1}) and natural gas (55.5 MJ kg^{-1}).[43] Hydrogen and its derivatives, therefore, should play an important role in the decarbonisation of those sectors where emissions are hard to abate, and alternative solutions are either unavailable or difficult to implement, such as heavy industry, shipping, aviation and heavy-duty transport.[38]

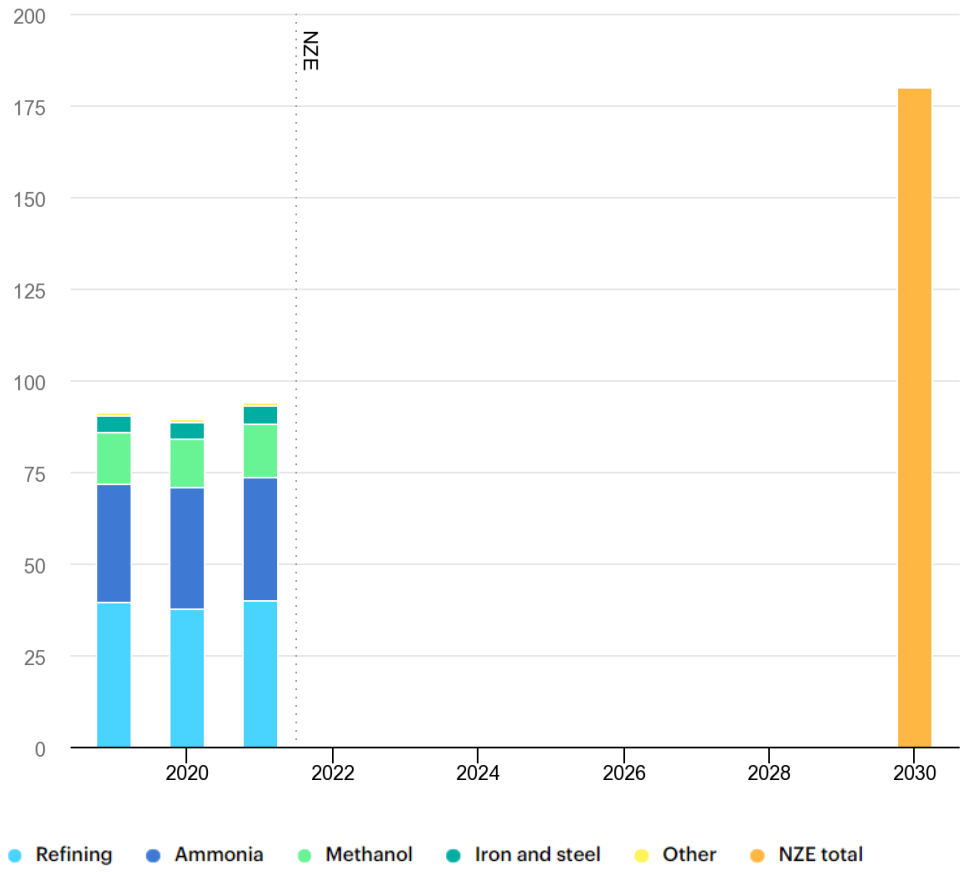

Figure 1.5 Global hydrogen demand by sector in the Net Zero Scenario, 2019-2030. Figure adapted from Ref. [36].

In **Figure 1.5**, global hydrogen demand reached 94 Mt in 2021, a 5% increase in demand in 2020, driven mainly by the recovery of chemical and refining activity.[38] Hydrogen demand remains concentrated in traditional applications in the refining and chemical sectors, with very limited penetration in new applications. By 2030 hydrogen demand will reach around 180 Mt, with nearly half of that demand coming from new applications, particularly in heavy industry, power generation and the production of hydrogen-based fuels.

A wide variety of processes are available for H_2 production, which according to the raw materials used, could be divided into two major categories, namely, conventional and renewable technologies.

1.3.1 Hydrogen Production from Fossil Fuels

The first category processes fossil fuels and includes the methods of hydrocarbon reforming and pyrolysis. In the hydrocarbon reforming process, the participating chemical techniques are steam reforming, partial oxidation and autothermal steam reforming.[39]

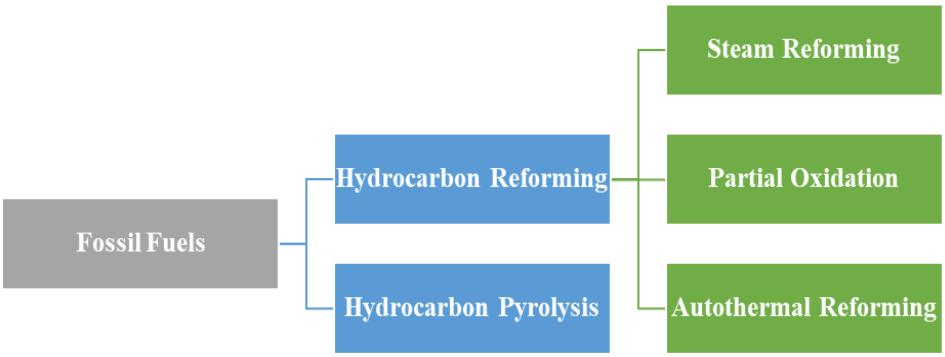

Figure 1.6 Hydrogen production methods from fossil fuels. Figure reproduced from Ref. [39].

Hydrocarbon reforming is a process by which the hydrocarbon fuel is converted into hydrogen through reforming techniques.[42] It produces relatively pure hydrogen with high efficiency but is a slow endothermic reaction.[44] In addition to the hydrocarbon, the other reactant for the reforming process can be either steam and then the endothermic reaction, known as steam reforming, or oxygen and the exothermic reaction is known as partial oxidation, as shown in **Figure 1.6**. When these two reactions are combined, it is termed the autothermal reaction.[45] Hydrocarbon pyrolysis is a process in which the only source of hydrogen is the hydrocarbon itself, which undergoes thermal decomposition through the following general reaction:

$$C_nH_m \rightarrow nC + \frac{1}{2}mH_2 \qquad \textbf{1.1}$$

1.3.2 Hydrogen Production from Renewable Sources

Although hydrocarbons are currently the main feedstock used for H_2 production, the share of renewable technologies will become unavoidable and increase shortly as fossil fuels are declining and the Greenhouse effect is attracting greater attention.[40] There are many processes for H_2 production from renewable resources and biomass-based technologies and water splitting are included here in **Figure 1.7**.

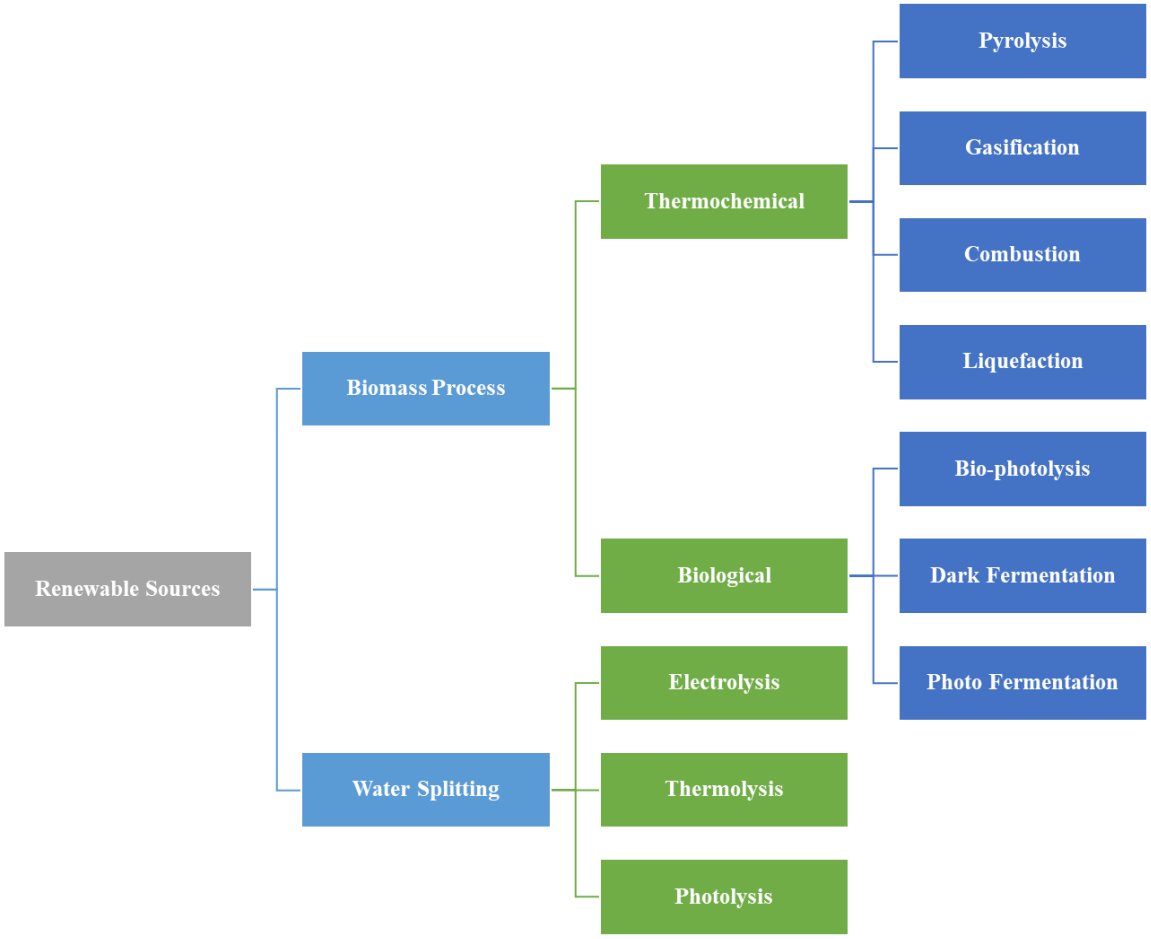

Figure 1.7 Hydrogen production methods from renewable sources. Figure reproduced from Ref. [39].

1.3.2.1 Biomass Process

Biomass is a renewable source of primary energy derived from plant and animal material.[41] It stems from plants and is organic matter in which the energy of sunlight is stored in chemical bonds via photosynthesis.[42] Thermochemical and biological methods are the two modes for H_2 production from biomass (**Figure 1.7**).

Thermochemical technology mainly involves pyrolysis, gasification, combustion, and liquefaction. Biomass pyrolysis is the thermochemical process of generating liquid oils, solid charcoal and gaseous compounds by heating the biomass at a temperature of 650-800 K at 0.1-0.5 MPa.[41] Biomass gasification is the thermochemical conversion of biomass into a gaseous fuel (syngas) in a gasification medium such as air, oxygen and/or steam.[37] Biomass combustion and liquefaction are two less preferable methods as they offer low H_2 production with emitting polluting by-products and require high operation conditions of 5-20 MPa in the absence of air.[43]

Biological methods mainly involve direct (**Figure 1.8**) and indirect bio-photolysis, dark and photo fermentation.[37] Bio-photolysis is a process using the same principles found in plants and algal photosynthesis but adapting them for H_2 generation. Green algae and blue-green algae can split water molecules into hydrogen ions and oxygen via direct and indirect bio-photolysis separately. In direct photolysis, green algae split water molecules into hydrogen ions and oxygen via photosynthesis.[37] The hydrogen ion was then converted into hydrogen gas by hydrogenase. It may be represented by the following general reaction:

$$2H_2O \xrightarrow{h\nu} 2H_2 + O_2 \qquad \textbf{1.2}$$

The sunlight represents in photochemical reactions denoted as 'hv', is proportional to its frequency (v) by a constant factor (h) known as Plank's Constant.

In indirect bio-photolysis, the general reaction for H_2 formation from water by cyanobacteria

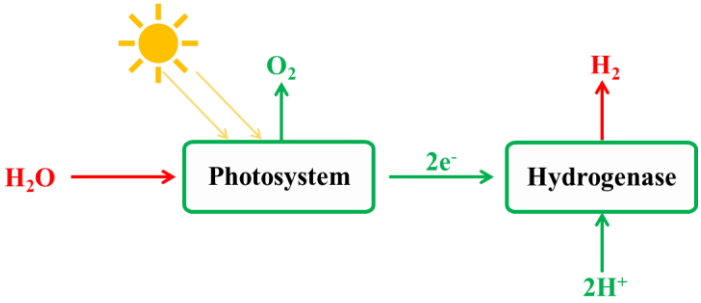

Figure 1.8 Flow diagram of the direct bio-photolysis process.

or blue-green algae can be represented by the following reactions:

$$12H_2O + 6CO_2 \xrightarrow{h\nu} C_6H_{12}O_6 + 6O_2 \qquad \textbf{1.3}$$

$$C_6H_{12}O_6 + 12H_2O \xrightarrow{h\nu} 12H_2 + 6CO_2 \qquad \textbf{1.4}$$

Fermentations are biochemical processes that take place with or without oxygen and perform microbial transformations of organic feed materials producing alcohols, acetone and H_2 in minimal amounts as well as CO_2. Dark fermentation (**Figure 1.9**) primarily uses anaerobic bacteria on carbohydrate-rich substrates under anoxic and dark conditions.[37] With glucose as the model substrates and acetic acid as the main end-product, the general reaction can be seen as follows[44]:

$$C_6H_{12}O_6 + 2H_2O \rightarrow 2CH_3COOH + 4H_2 + 2CO_2 \qquad \textbf{1.5}$$

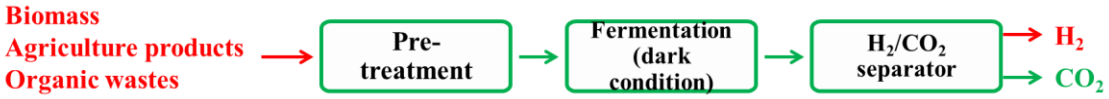

Figure 1.9 Flow diagram of the dark fermentation process.

Photo-fermentation (**Figure 1.10**) is a process conducted in deficient nitrogen conditions using solar energy and organic acids. Some photosynthetic bacteria due to the presence of nitrogenase can convert the organic acids (acetic, lactic and butyric) into hydrogen and carbon dioxide according to the following reaction with acetic acid as the reactant [45]:

$$CH_3COOH + 2H_2O + \text{light energy} \rightarrow 4H_2 + 2CO_2 \qquad \textbf{1.6}$$

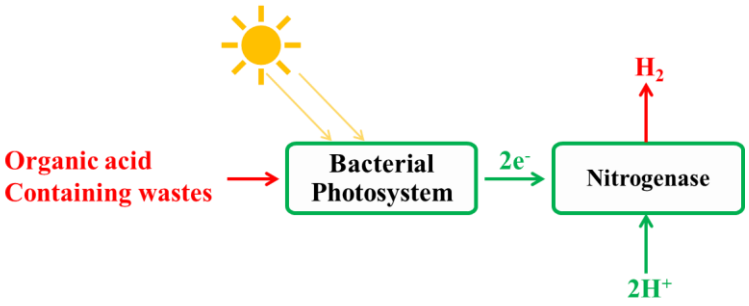

Figure 1.10 Flow diagram of the photo fermentation process.

1.3.2.2 Water Splitting

Water can be used for H_2 production through water-splitting processes such as electrolysis, thermolysis, and photo-electrolysis.[46] Water electrolysis uses electricity to split water into oxygen and hydrogen components. Although extremely pure hydrogen could be simply produced from water by electrolysis, the high electricity consumption by electrolysers prevents the production cost from competing with other large-scale technologies contributing with a share of about 5% to the total generation.[37]

Thermolysis or thermochemical water splitting is the process by which water is heated to a high temperature until decomposed to hydrogen and oxygen. The decomposition of water is not affected until the temperature is very high, generally over 2500 °C, for the Gibbs function (ΔG) to become zero and the separation of hydrogen from the equilibrium mixture to become feasible.[38]

Photolysis, in general, is affected when the energy of visible light is absorbed with the help of photocatalysts and is then utilised to decompose water into H_2 and O_2.[38] In photo-electrolysis, the sunlight is absorbed through semiconducting materials and the process of water splitting is similar to electrolysis. The mechanism of photocatalytic water splitting and the different materials studied as photocatalysts are discussed in the following sections.

1.4 Photocatalytic Hydrogen Generation

The seminal work of Honda and Fujishima in 1972 on photoelectrochemical water splitting using TiO_2 electrodes built the foundations of solar photocatalysis research.[47] There is extensive research in this direction in the following decades using inorganic heterogeneous photocatalysts, primarily metal oxides and chalcogenides.[48,49] However, difficulties in tuning and adapting inorganic photocatalysts led to the development of molecular homogeneous systems, such as copper molecular catalysts,[50] but at the expense of stability and efficiency.[51] Organic polymeric photocatalysts tend to combine the merits of homogeneous and heterogeneous photocatalysis, thus, constituting a promising new class of photocatalysts with wide molecular-level design space, owing to their molecular backbone.[52]

1.4.1 Basic Principles of Photocatalytic Hydrogen Generation

1.4.1.1 Main Process of Photocatalytic Hydrogen Generation

Photocatalysis can be deconvoluted into four independent steps as depicted in **Figure 1.11**: light absorption leading to exciton formation; charge-carrier (electrons and holes) separation; charge-carrier transport to the surface catalytic centre; and the surface reaction often with the assistance of co-catalysts.[53,54] All of these processes affect the final hydrogen generation efficiency.

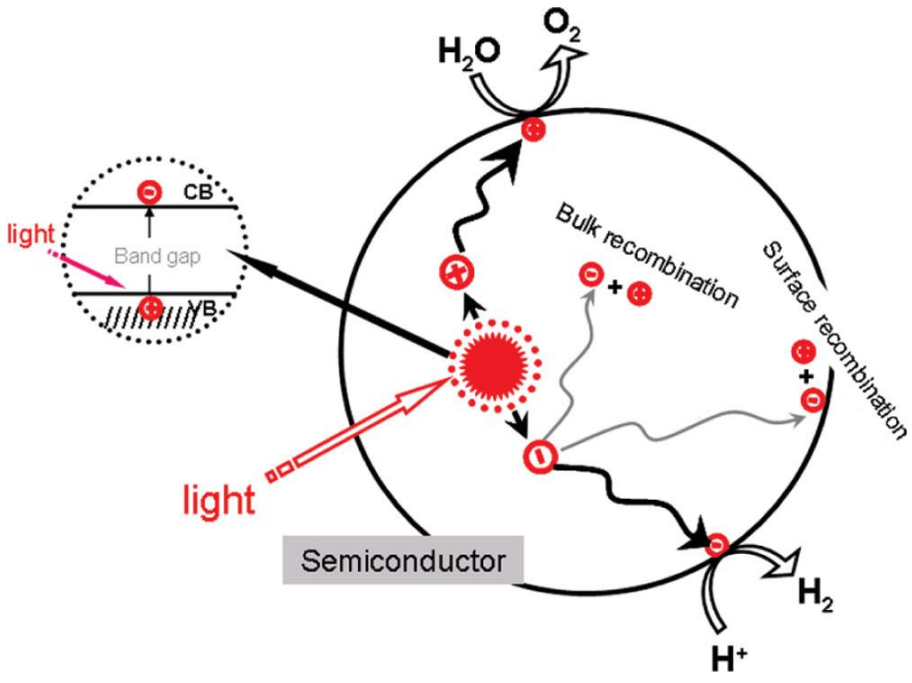

Figure 1.11 Processes in photocatalytic water splitting. Figure adapted from Ref. [54].

When a photocatalyst absorbs light of energy larger than its optical gap (also commonly referred to as the absorption onset), electrons get excited from the valence band (VB) of inorganic semiconductors/highest occupied molecular orbital (HOMO) of organic semiconductors, to the conduction band (CB) of inorganic semiconductors/the lowest unoccupied molecular orbital (LUMO) of organic semiconductors. The amount of light that can be absorbed depends on the band-gap energy, the type of the band gap, and the absorbance of the materials.

Light absorption leads to the generation of electron-hole pairs, which subsequently relax into bound excitons.[55] After excitons are created, charge recombination and separation/migration are competitive. The separation of excited electrons and holes sometimes may need to overcome an energy barrier, which is the binding energy of the excited electron-hole pairs, excitons. Thus, the exciton binding energy and the exciton diffusion length are crucial parameters that are affected by particle size and morphology.[52] For inorganic semiconductors, their experimental exciton binding energy is in the order of only tens of meV which is negligible, and it is assumed that excitons spontaneously dissociate.[56] However, the exciton binding energy of organic semiconductors is not necessarily the same case. For example, for poly(para-phenylene) (PPP), the vertical exciton binding energy is predicted to be $\approx$ 1200 meV in the middle of a polymer matrix and $\approx$ 170 meV on or near the interface with water.[56] These free charge carriers can drive redox reactions but also re-form excitons. Charge recombination reduces the excited charges by emitting light (radiative recombination) or generating phonons (non-radiative recombination), and the latter occurs when excess energy is converted into heat by phonon emission.[57] Both free charge carriers and excitons can also become trapped on a part of the semiconductor.[58] The excited electrons and holes separate and migrate within the limits of their diffusion length towards the surface and the catalytic centre.[52] The surface catalytic reaction is a chemical process that depends on the performance of the co-catalysts. The absolute band positions of the photocatalyst determine the thermodynamic driving force for the surface catalytic reaction.[59] Here, in the photocatalytic water-splitting reaction, they act as reducing agents and oxidizing agents to produce H_2 and O_2, respectively as depicted in **Figure 1.12**. Water splitting into H_2 and O_2 is an uphill reaction and it needs the standard Gibbs free energy change ΔG^0 of 237 kJ/mol or 1.23 eV, as shown in **Reaction 1.7**.[48]

$$H_2O \rightarrow \frac{1}{2}O_2 + H_2 \qquad \textbf{\textit{1.7}}$$

Therefore, the band gap energy of the photocatalyst should be > 1.23 eV. Both the reduction and oxidation potentials of water should lie within the band gap of the photocatalyst. The bottom level of the conduction band has to be more negative than the reduction potential of H^+/H_2, whereas the top level of the valence band has to be more positive than the oxidation

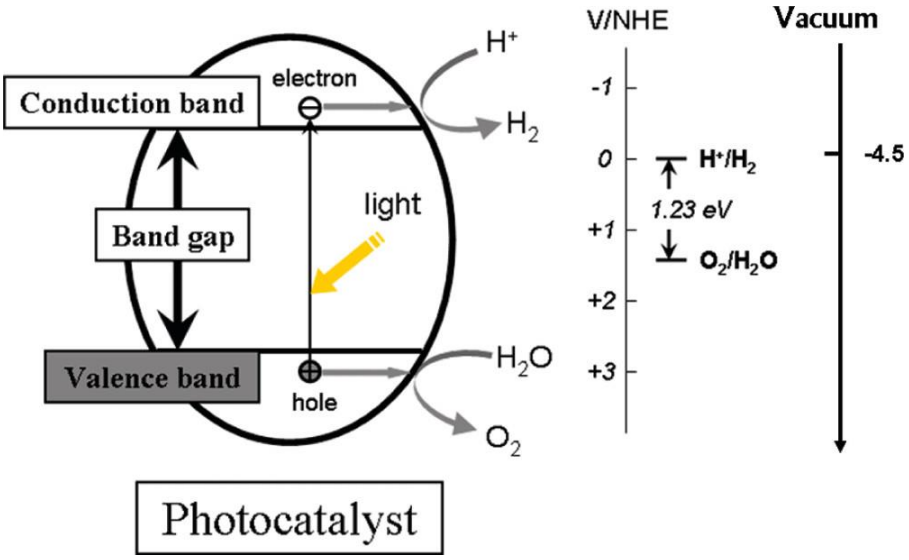

Figure 1.12 Fundamental principle of inorganic semiconductor-based photocatalytic water splitting for hydrogen generation. Figure adapted from Ref. [57].

1.4.1.2 Evaluation of Photocatalytic Hydrogen Generation

Two indicators should be considered in evaluating the photocatalytic hydrogen generation efficiency. One is photocatalytic activity, and the other one is photocatalytic stability.[57]

The photocatalytic activity can be measured directly on the amount of hydrogen generated or indirectly on the electrons transferred from semiconductors to water within a certain time under light irradiation. Different photocatalytic setup configurations and light sources, such as the Xe lamp and Hg lamp, may give different rates of hydrogen evolution even when the same photocatalyst is used. This makes it difficult to compare the results across different research groups and measurement systems.

For the indirect method, the overall quantum yield and apparent quantum yield are defined by **Equations 1.8** and **1.9**, respectively.[60] The apparent quantum yield is estimated to be smaller than the overall quantum yield because the number of absorbed photons is usually smaller than that of incident light.

$$Overall\ quantum\ yield\ (\%) = \frac{Number\ of\ reacted\ electrons}{Number\ of\ absorbed\ photons} \times 100\% \qquad \textbf{1.8}$$

1.9

$$(Apparent)\ Quantum\ yield\ (QY, \%) = \frac{Number\ of\ reacted\ electrons}{Number\ of\ incident\ photons} \times 100\%$$

$$= \frac{2 \times Number\ of\ evolved\ H_2\ molecules}{Number\ of\ incident\ photons} \times 100\%\ (\text{for } H_2 \text{ evolution})$$

$$= \frac{4 \times Number\ of\ evolved\ O_2\ molecules}{Number\ of\ incident\ photons} \times 100\%\ (\text{for } O_2 \text{ evolution})$$

Besides a high photocatalytic activity or quantum yield, a good photocatalyst should also have good stability for H_2 and/or O_2 production.[57] A long-time experiment or a repeated experiment is always necessary to test photocatalytic stability.

1.4.2 Photocatalytic Hydrogen Generation Systems

1.4.2.1 Hydrogen Generation Systems Containing Sacrificial Reagents

Photocatalytic hydrogen production from water is a low-efficiency process, which is primarily due to a high recombination rate of photoinduced electrons and holes. Electron donors are usually required to act as sacrificial reagents to consume holes and prevent the recombination of electrons and holes. When the system is constructed in the presence of an electron donor, the photogenerated holes irreversibly oxidise the reducing electron donors instead of H_2O.

Organic compounds, such as alcohols (methanol, ethanol, isopropanol, etc.),[61,62] organic acids (formic acid, acetic acid, etc.),[63,64] and aldehydes (formaldehyde, acetaldehyde, etc.)[65,66] have all been used as electron donors for photocatalytic hydrogen generation. The choice of sacrificial reagent can significantly affect performance. It was found that low oxidation potentials and high relative permittivity are desirable properties for sacrificial electron donors.[67] The interaction between sacrificial reagents and photocatalysts surface determines the final availability of electron donors. It can be seen from the Gouy-Chapman theory:[68]

$$\sigma_S = \frac{2\varepsilon_0 \varepsilon R T}{F} \sinh^{-1}\left(\frac{F\psi_0}{2RT}\right) \qquad \textbf{1.10}$$

with the increase of dielectric constant or permittivity of the solvent, the final availability of electron donors increases and the trapping of holes achieves more efficiently. σ_s is the surface charge density, ε is the dielectric constant of the solvent or mixed solvent system, ε_0 is the permittivity of free space, R is the gas constant, T is the temperature, F is Faraday constant and ψ_0 is the potential at the solid surface.

Tertiary amines like triethylamine (TEA) and triethanolamine (TEOA) are commonly used because of the irreversibility of their degradation pathways, especially for polymetric photocatalysts.[69]

1.4.2.2 Overall Water-Splitting System

In photochemical overall water splitting (OWS) both water oxidation and reduction reactions take place on the same semiconducting photocatalysts (**Figure 1.13a**) - or composites of photocatalysts (**Figure 1.13b** and **c**). The photogenerated charge carriers (h^+ and e^-) should diffuse rapidly within their lifetimes to respective active sites on the surface of the semiconductor usually decorated with co-catalysts for high efficiency.

The performance of photocatalytic water-splitting cells is most commonly quantified by the solar-to-hydrogen (STH) conversion efficiency (η_{STH}), thus all water-splitting systems can be reliably compared.[70,71] It is determined under standard solar irradiation generated with the Air Mass 1.5 global (AM 1.5 G) filter or one sun (100 mW cm^{-12}) with no applied bias.[72] The Air Mass quantifies the reduction in the power of light as it is passes through the atmosphere and is absorbed by air and dust. The standard spectrum at the Earth's surface is called AM 1.5G, (the G stands for global and includes both direct and diffuse radiation). The STH efficiency is defined as the amount of chemical (H_2) energy produced against the incident solar energy.[73]

1.11

$$\eta_{\mathrm{STH}}\,(\%) = \frac{Chemical\ energy\ produced}{Solar\ energy\ input}$$

$$= \frac{Rate\ of\ H_2\ production\ \times\ \Delta G}{Total\ incident\ solar\ power\ \times Electrode\ area}$$

$$= \frac{(\mathrm{mmol}\ H_2\ per\ s) \times (237000\ \mathrm{J\ mol^{-1}})}{P_{\mathrm{Total}}\ (\mathrm{mW\ cm^{-2}}) \times Area\ (\mathrm{cm^2})}$$

ΔG is the Gibbs free energy of hydrogen molecules (at 25 °C ΔG = 237 kJ mol^{-1}). P_{Total} is the standard solar irradiation generated with AM 1.5 g filter.

Recently, C_3N_4 has received much attention as a metal-free conjugated photocatalyst for stable visible light water splitting.[74] With carbon dots (CDots) as a co-catalyst, a CDots–C_3N_4 nanocomposite photocatalyst showed quite a high η_{STH} of 2.0% with a robust stability of 4800 h and generated H_2 at a remarkable rate of 8.4 mmol h^{-1}.[74]

A single photocatalyst for achieving OWS is extremely difficult to find, thus an ingenious strategy is to employ two photocatalysts to increase their overall OWS efficiency; this technique is inspired by natural photosynthesis and is termed Z-scheme water splitting.[75] The photoexcited electrons and holes remain in the oxygen evolution photocatalyst (OEP) and the hydrogen evolution photocatalyst (HEP), respectively, and their recombination via an aqueous redox mediator ($IO3^-/I^-$)[76] or a solid-state electron mediator (Au metal)[77] completes the photocatalytic cycle. In addition, an electron-mediator-free Z-scheme photocatalytic water-splitting was also reported by making an efficient $BiVO_4$–Ru/Rh:$SrTiO_3$ composite.[78]

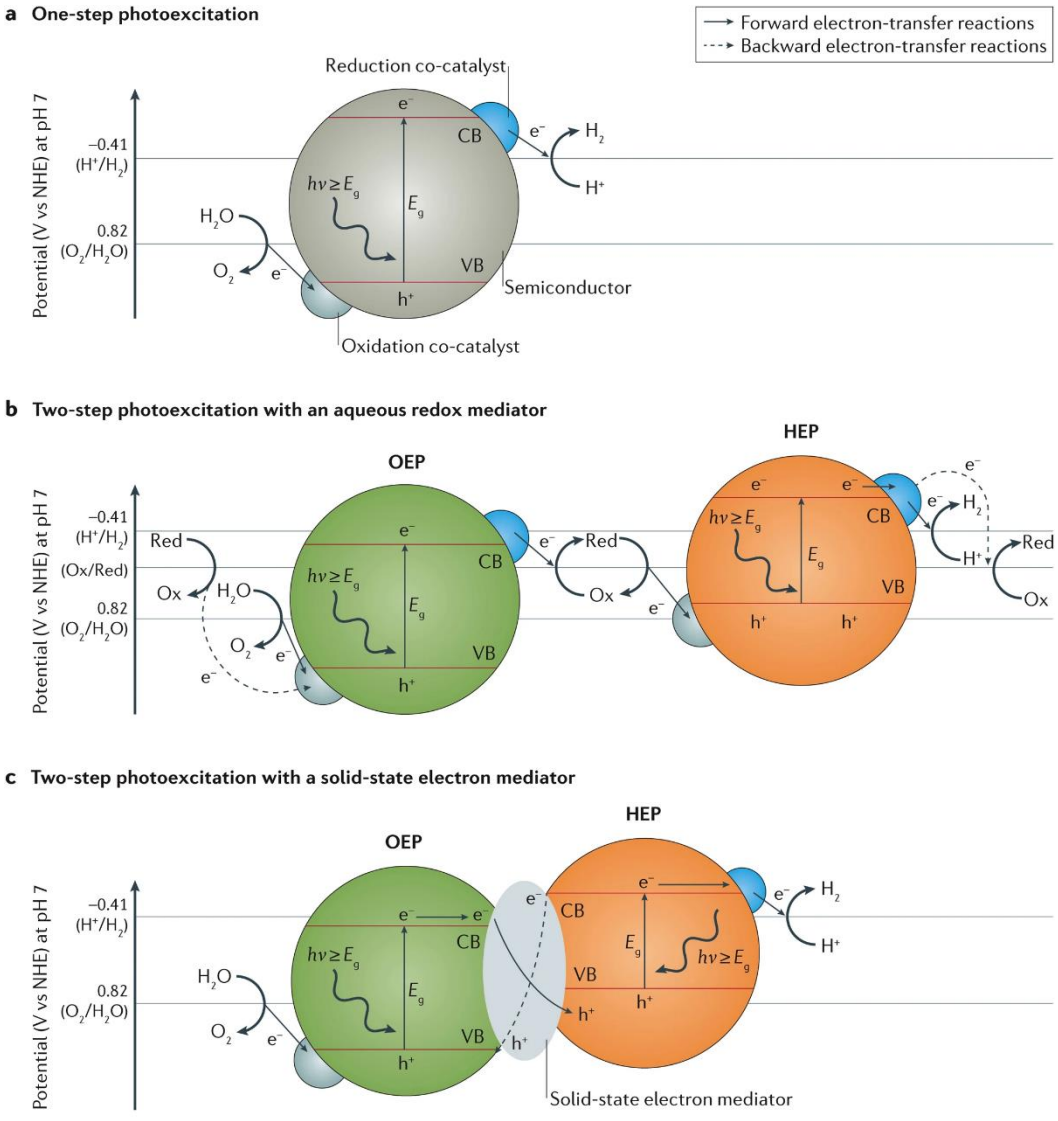

Figure 1.13 (a) One-step photoexcitation. (b) Two-step photoexcitation with an aqueous redox mediator. (c) Two-step photoexcitation with a solid-state electron mediator. CB, conduction band; Eg, semiconductor bandgap; HEP, hydrogen evolution photocatalyst; NHE, normal hydrogen electrode; OEP, oxygen evolution photocatalyst; Ox, oxidant; Red, reductant; VB, valence band. Figure adapted from Ref. [70].

The photocatalysis (PC) system needs the smallest complexity for achieving OWS, but there are still many requirements for the light absorber of a proper band gap, band edge potentials, and stability in an aqueous medium.[79] In addition, it is difficult to control the charge carriers since there is no applied bias.[75]

1.4.3 Types of Solar-Driven Water-Splitting Devices

Apart from particulate photocatalytic (PC) systems, photoelectrochemical (PEC) water-splitting cells, and photovoltaic–electrochemical (PV-EC) systems are also water-splitting systems for sustainable solar H_2 production.

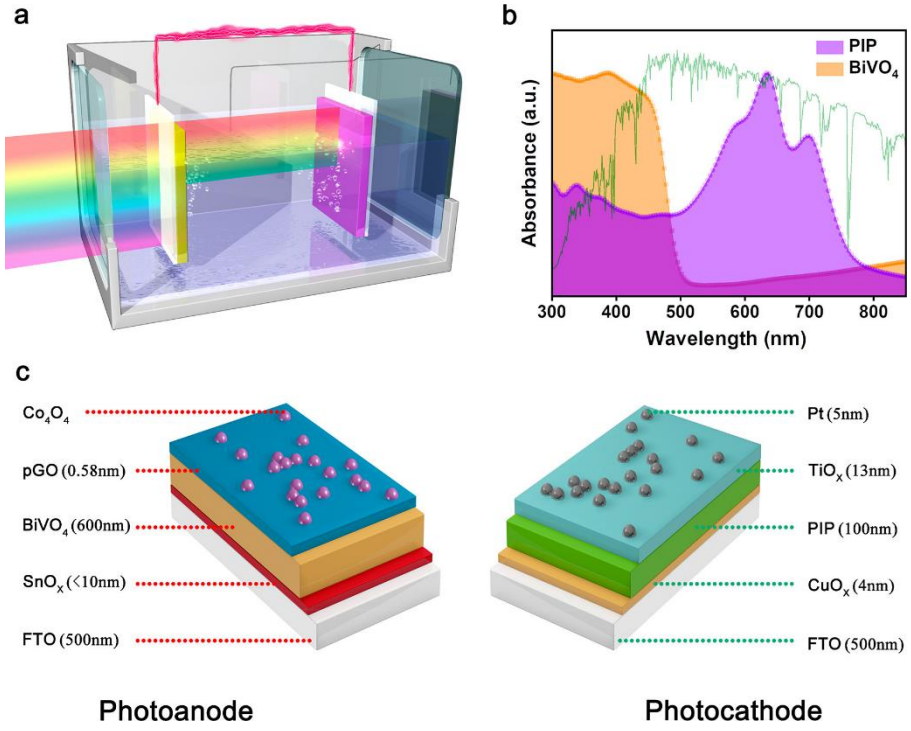

Figure 1.14 Unassisted PEC device for solar overall water splitting. (a) Schematic representation of PEC cell with Co_4O_4/pGO/$BiVO_4$/SnO_x photoanode (front) wired to the Pt/TiO_x/PIP/CuO_x photocathode (behind). (b) UV–vis spectra of $BiVO_4$ and PIP as light-harvesting semiconductors. (c) Schematic representation of integrated $BiVO_4$-based photoanode and PIP-based photocathode. PIP: organic polymer semiconductor PBDB-T:ITIC:$PC_{71}BM$. Figure adapted from Ref. [82].

1.4.3.1 Photoelectrochemical (PEC) Water-Splitting Cells

A PEC cell requires two electrodes (an anode for the oxidation reaction and a cathode for the reduction reaction). At least one of the electrodes is a semiconductor (n-type for photoanode

and p-type for photocathode) designed to absorb the sunlight and split water directly at the surface (**Figure 1.14b**).[80]

In 1972, the first unassisted photoanode–photocathode PEC cell was demonstrated with a p-GaP/n-TiO_2 tandem combination.[47] Despite that it showed only a 0.25% STH efficiency with the unstable cell, this result inspired the idea of water decomposition without bias. Recently, an unassisted PEC water-splitting by coupling a Co_4O_4/pGO/$BiVO_4$/SnO_x photoanode and a Pt/TiO_x/PIP/CuO_x photocathode exhibited the highest STH efficiency of 4.3% for dual-photoelectrode PEC devices to date.[81]

1.4.3.2 Photovoltaic–Electrochemical (PV-EC) Systems

Compared to the PEC devices, where a light absorber is immersed in the electrolyte, the PV-EC devices employ a separate function of light absorption and electrolysis. Specifically, two well-established technologies, PV and EC, are combined. Solar energy is transformed into electrical power by PV devices and then transported to the electrolysers through the wires for water splitting.[82] The PV modules and electrolysers are connected in series through wires, referred to as "traditional PV-EC" (**Figure 1.15a**). The other integrated configuration is called "integrated PV-EC," the distance between the PV modules and the electrolysers is shortened by coating the conducting layers and electrocatalyst layers contacting the electrolyte (**Figure 1.15b**).[80]

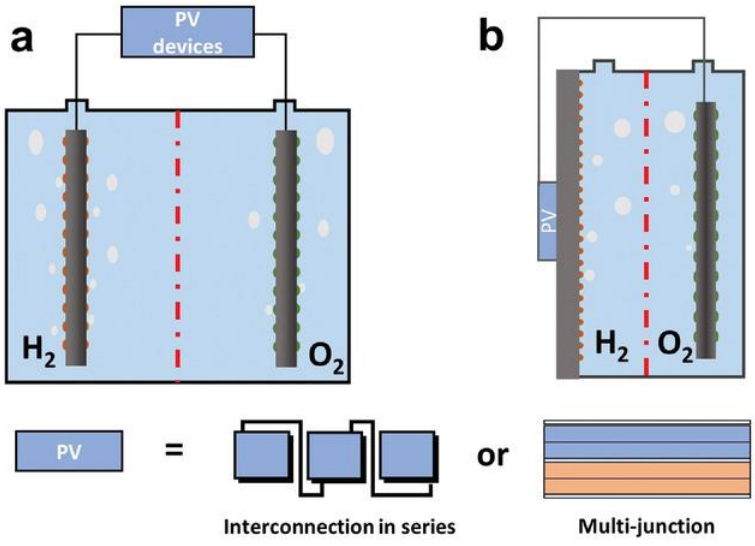

Figure 1.15 Schematic of two types of PV-EC devices/systems: (a) Traditional PV-EC. (b) Integrated PV-EC. Figure adapted from Ref. [79].

The major advantage of PV-EC in comparison to PC and PEC is that PV and water electrolysis are already well-established technologies and a high η_{STH} of >10% is easily achievable.[83] Recently, Jia *et al.*[84] achieved the highest ever η_{STH} (>30%) with a PV-EC system of InGaP/GaAs/GaInNAsSb triple-junction solar cells connected to 2 polymer electrolyte membrane (PEM) electrolysers in series with Pt–Ir as the cathode–anode coated on a Nafion membrane under 42 sun.

The PV-grade materials exhibit high efficiencies, but their higher complexity means higher cost. Thus, efficiency is one of the many considerations to make in the selection of solar hydrogen production technology.

1.5 Semi-Artificial Photosynthesis

1.5.1 Different Types of Semi-Artificial Systems

Two classes of semi-artificial systems are common: enzyme hybrids and cell hybrids; each has limitations and strengths.[18] Examples of enzyme hybrids include direct immobilization of enzymes onto electrodes (**Figure 1.16a**), *e.g.*, [FeFe]-hydrogenase adsorbed onto a carbon electrode in a dye-sensitized photoelectrochemical cell,[85] and nanoparticulate semiconductors ([NiFeSe] hydrogenase adsorbed to particulates such as dye-sensitized TiO_2[86], [FeFe]-hydrogenase adsorbed polymer nanoparticles[87]) (**Figure 1.16 b, c**). While their poor scalability and inherent instability render enzyme hybrids impractical for commercial applications,[88] these studies have advanced the fundamental understanding of these systems and aid in understanding the potential of future applications in cell hybrids.

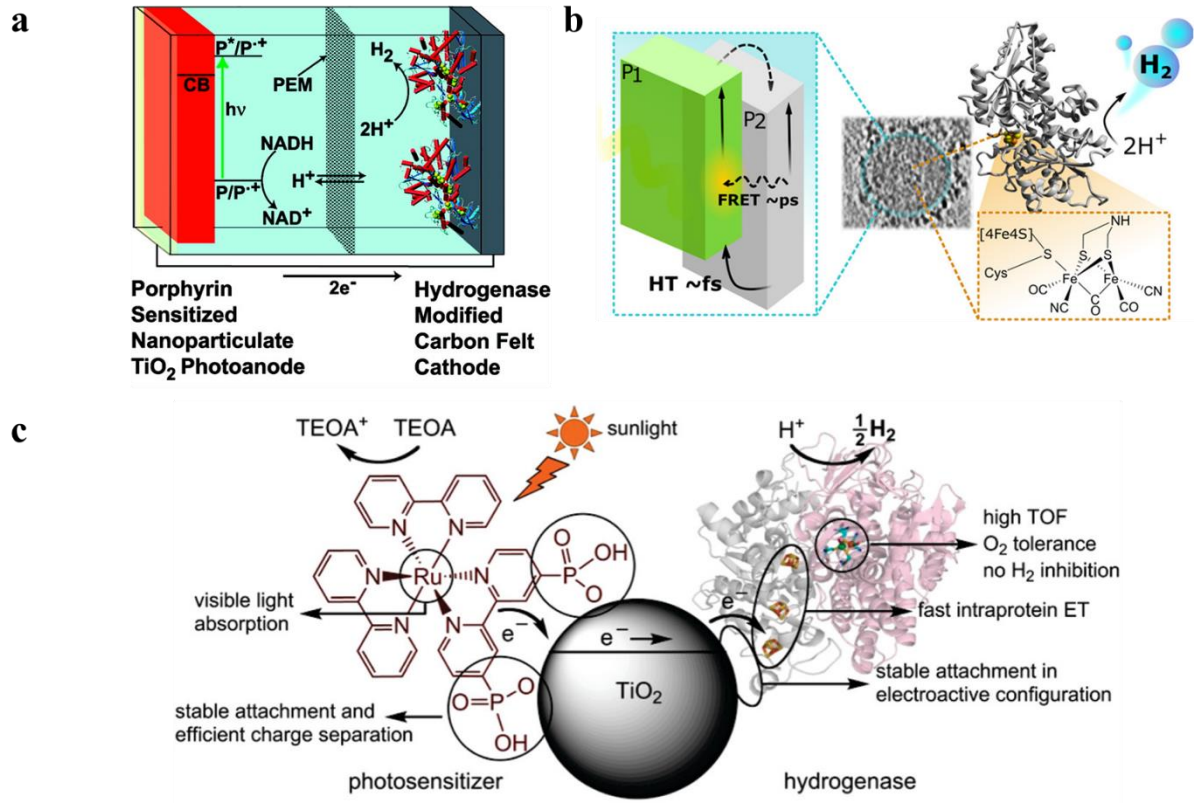

Figure 1.16 (a) [FeFe]-hydrogenase-catalysed H_2 production in a photoelectrochemical biofuel cell, figure adapted from Ref. [84]; (b) polymer dots as photoactive membrane vesicles for [FeFe]-hydrogenase self-assembly and solar-driven hydrogen evolution, figure adapted from Ref. [86]; (c) Cartoon representation of a hybrid (enzyme−TiO_2) nanoparticle system, figure adapted from Ref. [85].

Bacterial cells have been used as biocatalysts to overcome the limitations of enzymes in the field of semi-artificial photosynthesis. The interactions between microorganisms and electrodes have been reviewed, such as microbial electrosynthesis reactors[89] in conjunction with or without solid-state photovoltaic, microbial fuel cells [90], and photobio-electrochemical cells.[91,92] Compared with the material-based biohybrids, these electrode-based systems have been more widely studied and understood in terms of their configuration and application.

1.5.2 Material-Microorganism Complexes for Hybrid Photosynthesis

1.5.2.1 Chemical-Synthetic Inorganic Nanoparticles

Several studies have reported hydrogen production for systems consisting of TiO_2 and cells of a gram-positive bacillus *Clostridium acetobutylicum*,[19] cobalt phosphate, and genetically engineered *Saccharomyces cerevisiae*,[93] or by using bismuth oxide or dye-sensitized TiO_2 and the purple photosynthetic bacterium *Rhodopseudomonas capsulatus*.[94] (**Table 1.2**) Upon irradiation, photoinduced electrons generated in the inorganic semiconductor NPs were transferred to microbes to produce hydrogen via redox couples. Recently, recombinant *Escherichia coli* cells expressing both hydrogenase and maturase genes have been reported to enable photocatalytic hydrogen production with TiO_2 NPs acting as the semiconductors (**Figure 1.17**).[26]

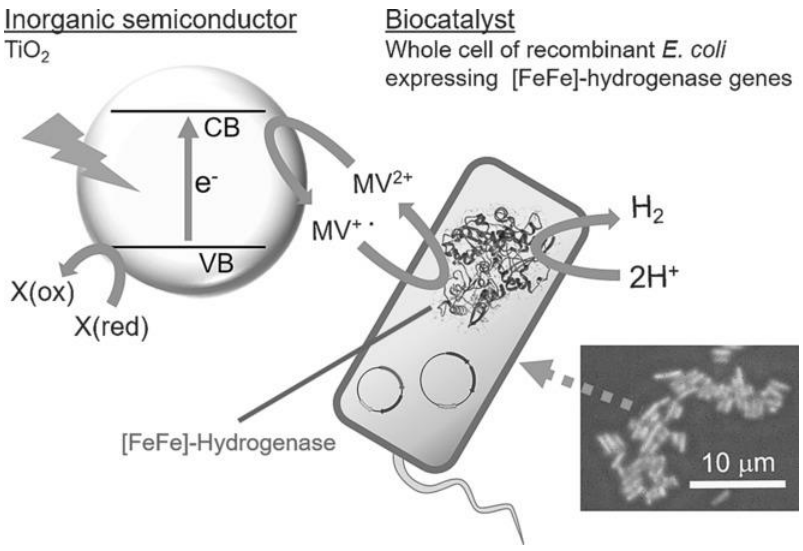

Figure 1.17 Photocatalytic H_2 production by the combination of TiO_2, methyl viologen (MV), and the recombinant *E. coli* expressing [FeFe]-hydrogenase and relevant maturases, figure adapted from Ref. [26].

Compared with purely artificial photocatalysts and enzyme-material-based systems, there has been a significant breakthrough in using whole-bacterial cells as biocatalysts. One of the greatest advantages is that the cells that serve as biocatalysts can be easily harvested from a liquid culture without the need for manipulations such as cell disruption and protein purification.[26] Beyond this, the self-replicating nature of microorganisms grants cell hybrids potentially high scalability.[95] Despite these benefits, a host of challenges must be overcome before the application in commercial solar energy conversion. We struggled to find a clear description of the nature of the interactions between the chemical synthetic inorganic semiconductors and microbes in any studies on biohybrid photosynthesis.

1.5.2.2 Biosynthetic Inorganic NPs

In addition to the chemical-synthetic methods for the synthesis of inorganic semiconductors, the use of biological organisms in this area is rapidly gaining importance, especially for CdS nanoparticles.[96] Among them prokaryotic bacteria have been most extensively studied for the synthesis of inorganic materials. Recently, the bio-precipitation of CdS NPs on the surface of the acetogenic, thermophilic bacterium *Moorella thermoacetica* (*M. thermoacetica*) successfully constructed an inorganic-cell hybrid system to produce acetic acid from carbon dioxide.[97]

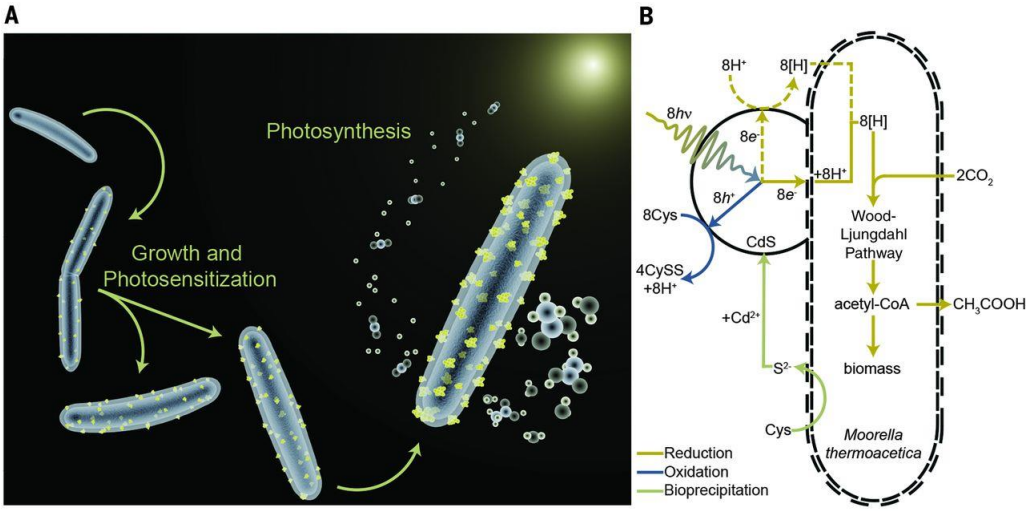

Figure 1.18 *M. thermoacetica*–CdS reaction schematics. Figure adapted from Ref. [96].

E. coli has also been used to drive the production of hydrogen with precipitated CdS on the cell surface.[28] *E. coli* produces cysteine from sulfides as part of its detoxification strategy through the expression of cysteine desulfhydrase, an aminotransferase that converts cysteine into pyruvate, ammonia, and hydrogen sulfide.[98] This has been used by engineered *E. coli* to

overexpress cysteine desulfhydrase to facilitate sulfide production and cadmium precipitation.[98] Also, the gene encoding serine acetyltransferase was overexpressed for the production of cysteine.[99] In addition, *E. coli* mutants were constructed to express a lead-specific binding protein PbrR on the cell surface, permitting selective adsorption of both lead and cadmium ions and the formation of PbS and CdS NPs on the cell membrane.[29,100] These genetically engineered *E. coli* strains showed the impressive capability of facilitating the bio-precipitation of CdS and thus improving the hydrogen production of CdS-*E. coli* hybrids.

1.5.2.3 Organic Photocatalysts

Most of the research in this area is mainly focused on inorganic materials no matter it is chemical synthetic (TiO_2) or biosynthetic (CdS) as discussed above and shown in **Table 1.2**. However, considering the interactions between materials and microorganisms, polymers are ideal for bacteria adsorption due to their hydrophobic surface that reduces hydration and maximises adhesion.[101] In addition, organic semiconductors are carbon based which allows the materials to be designed to be closer in terms of physio-chemical properties compared to inorganic materials.[102] The cell surface of most prokaryotic organisms is associated with complex glycosylated macromolecules, secondary cell wall polymers, and capsular polysaccharide[103] which share similar nature with organic polymers. Furthermore, the extracellular matrix (ECM) made by bacterial cells to form biofilms is a mixture of high-molecular weight polymers.[104] This plays an important role in biohybrid systems as the surface of organic semiconductors is in the direct contact with biological systems, thus, it must be biocompatible with the surface.[105]

Adhesion can be further increased through the modification of the polymers with positively charged functional groups, such as quaternary ammonium groups. As the surface of bacteria is negatively charged it allows for increased electrostatic interactions. Surface roughness can be related to the increased surface area which in turn increases bacteria adhesion,[106] but patterning of surfaces and submicrometric roughness has been shown to suppress the adhesion of bacteria.[107] Following primary adhesion to the surface mediated by nonspecific interactions such as hydrophobic and electrostatic interaction[108] irreversible adhesion takes place forming non-equilibrium hybrids.[109]

The development and advances in 'soft photocatalysis', using organic polymeric photocatalysts (**Figure 1.19**),[110] such as carbon nitrides, π-conjugated polymers, covalent triazine frameworks (CTFs) and covalent organic frameworks (COFs), is

another driving force for the application of polymeric photocatalysts in semi-artificial photosynthesis field.[52]

Carbon nitride is composed of alternating carbon and nitrogen atoms in the form of triazine or heptazine units, connected by imide bridges.[52] They are powerful photocatalysts primarily owing to their oxidative and reductive power, high chemical stability and straightforward synthesis from inexpensive precursors.[111] However, the high-temperature synthesis of carbon nitrides and the resulting inertness of their backbones limit the possibilities of functional-group engineering.

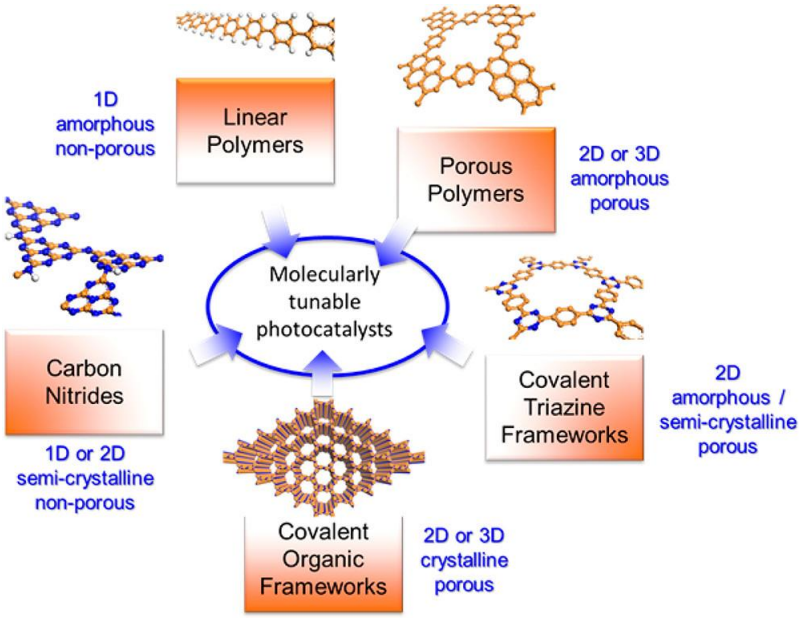

Figure 1.19 Overview of the different classes of polymeric photocatalysts. Figure adapted from Ref. [105].

π-Conjugated polymer catalysts were first reported for solar-fuel photocatalysis using linear poly(phenylene)-type polymers for photocatalytic hydrogen evolution reaction (HER).[112] Opto-electronic properties of conjugated polymers can also be tuned through synthetic methods. This can be used to obtain materials with strong and broad absorption in the visible region of the solar spectrum, also tuning the band positions, charge separation, and charge migration efficiency.[16] Furthermore, there are many widely available conjugated organic monomers, enabling the synthesis of a broad range of conjugated polymers by well-established methods.

CTFs bridge carbon nitrides and π-conjugated polymers, with the robust triazine motif from carbon nitrides forming an extended conjugated framework, as is the case in conjugated polymers.[113] Unlike carbon nitrides, CTFs possess inherent microporosity

and/or mesoporosity. However, high-temperature synthesis further causes functional-group intolerance, which considerably limits the choice of monomers.

COFs are 2D or 3D polymers that are made by linking molecules through reversible reactions using thermodynamically controlled dynamic covalent chemistry.[114] COFs are important photocatalysts because of the essentially unlimited chemical tunability of the parameters determining photocatalytic activity, like light harvesting, charge separation and charge transport.[115,116] In addition, the COF backbone is crystalline, rigid and conjugated, which can improve light harvesting and charge transport, also by reducing unproductive quenching events at structural defects.[117]

As discussed above, polymers have some benefits and can also be further tuned to bind to bacteria surfaces. This has been exploited to maximise selective and non-selective interactions. Positively charged polymers can bind with the negatively charged outer membrane of bacteria through electrostatically non-selective interactions. Specific biomolecular recognition units have also been utilized to obtain selective binding towards certain microbes, such as aptamers,[118] anti-*E. coli* antibody,[119] boronic acid derivatives,[120] and mannose.[121] The ability to copolymerize or functionalize polymers with the above recognition elements gives rise to specificity. Other strategies include the grafting of polymers to surfaces,[122] cell encapsulation,[123] surface-initiated polymerisations,[124] polymerisations inside cells, and templating of polymers on cell surfaces to maximise interaction.

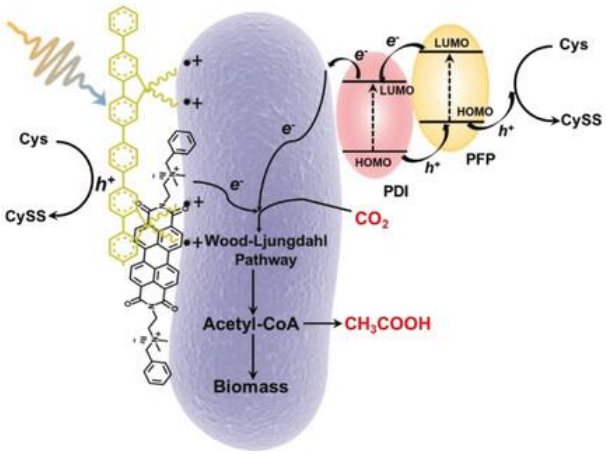

Figure 1.20 Diagram of the PDI/PFP/*M. thermoacetica* photosynthesis hybrid system. Figure adapted from Ref. [31]..

Based on this, organic hybrid systems have been explored to combine the advantages of organic materials with biological systems recently. The photosensitizers consisting of perylene diimide (PDI) derivative and poly(fluorene-*co*-phenylene) (PFP) were coated onto the surface of *M. thermoacetica* to create a biohybrid system for solar-to-chemical conversion (**Figure 1.20**).[31] It was found that PDI/PFP interacted with the bacteria by electrostatic interactions and the cationic side chains of organic semiconductors could intercalate into the cell membrane by hydrophobic interactions.[31]

Table 1.2 Reports on material-microorganism biohybrid systems for hydrogen production

Material	Microorganism	Reaction solution	Energy source	Light Source	Activity	Ref.
Bacterially precipitated CdS	*S. oneidensis MR-1*	50 mM HEPES, 50 mM NaCl, 20 mM sodium lactate	Sodium lactate, light	300 W Xe lamp with a 420 nm cut-off filter	362.44 ± 119.69 μmol mg^{-1} hydrogen produced over 72 hours	32
Cu_2O/Reduced graphene oxide	*S. oneidensis MR-1*	100 mM Tris-HCl, 150 mM NaCl, 5% (v/v) glycerol and 100 mM ascorbic acid	Glycerol, light	300 W Xe lamp with a 420 nm cut-off filter	322.0 μmol/g_{Cu2O} within 4 h	125
Water-soluble dyes, inorganic complexes	*S. oneidensis*	50 mM HEPES, 50 mM NaCl, pH 7	Light	KL5125 cold light	725 ± 97 nmol of hydrogen over 30 min with sodium dithionite and MV	27
Bacterially precipitated CdS	*E. coli* K-12	SBC medium with 1 mM cysteine, 20 mM glucose	Glucose, light	300 W Xe lamp with bandpass filters	> 1.8 mmol hydrogen over 3 hours	28
Bacterially precipitated CdS	Engineered *E. coli* BL21	100 mM Tris-HCl (pH 7), 150 mM NaCl, 5% glycerol, 100 mM ascorbic acid, 5 mM MV	Glycerol, light	350 W Xe lamp	13.4 μmol at 6 h, 81.8 μmol at 24 h by 10^8 cells	29
Bacterially precipitated CdS	Engineered *E. coli* BL21	100 mM BisTris-HCl (pH 5), 5 mM MV	Light	Monochromatic LED light	AQY: 0.11, 0.10, and 0.04% at 385, 420, and 470 nm	126
Bacterially Precipitated $AgInS_2/In_2S_3$	*E. coli* MG1655	SBC medium with 1 mM cysteine, 20 mM glucose	Glucose, light	300 W Xe lamp	2.2 mmol-hydrogen/mmol-glucose at 2000 W m^{-2}	127
Biogenic $CdSe_xS_{1-x}$ nanoparticles	*E. coli*	3 mL LB medium (pH 7, with 100 mM Tris-HCl buffer), 8 g/L glucose	LB, glucose, light	300 W Xe lamp with a 420 nm cut-off filter	2.9- fold higher hydrogen production rate than the pure *E. coli*	128
Anatase TiO_2 powder	Engineered *E. coli*	100 mM Tris-HCl (pH 7), 150 mM NaCl, 5 mM methyl viologen, 5% glycerol, 100 mM ascorbic acid	Glycerol, light	Xe lamp	0.72 μmol min^{-1} (mg wet cell)$^{-1}$ hydrogen	26
TiO_2 (P-25)	Engineered *E. coli* BL21	100 mM Tris-HCl (pH 7), 5 mM methyl viologen	Light	300 W Xe lamp with bandpass filters	AQY_{300}: 26.4%, AQY_{350}: 31.2%	129
TiO_2	*E. coli* K-12	100 mM Tris-HCl (pH 7), 150 mM NaCl, 5 mM methyl viologen, 6 mM glucose, 100 mM ascorbic acid	Glucose, light	Xe lamp	a 2-fold increase in the hydrogen production compared to that without TiO_2	130
Iodine-doped hydrothermally carbonized carbon	*E. coli*-K12 (MG1655)	Simplified BC medium, 20 mm glucose, 1 mM cysteine	Glucose, light	Xe lamp	quantum efficiency of 9.11%	131

S. oneidensis: *Shewanella oneidensis*, HEPES: 4-(2-hydroxyethyl)-1-piperazineethanesulfonicacid, AQY: apparent quantum yield, MV: Methyl viologen, LB: Lysogeny broth, AQY_{300}: apparent quantum yield at 300 nm.

1.6 Experimental Techniques

1.6.1 Particle Analysis Using Dynamic Light Scattering

1.6.1.1 Size Analysis

Dynamic Light Scattering (DLS) is a non-invasive technique for measuring the size and size distribution of molecules and particles that have been dispersed or dissolved in a liquid, typically in the submicron region. It measures Brownian motion and relates this to the size of the particles. Brownian motion is the random motion of particles which results from their collision with solvent molecules such as water. The rate of Brownian motion is quantified as the translational diffusion coefficient D and is inversely related to hydrodynamic diameter d_H according to the Stokes-Einstein equation,[132]

$$d_H = \frac{kT}{3\pi\eta D} \qquad 1.12$$

Where:

d_H = hydrodynamic diameter

D = translational diffusion coefficient

k = Boltzmann's constant

T = absolute temperature

η = viscosity

In DLS measurement, when a laser is passed through a suspension, the Brownian motion of particles or molecules causes the laser light to be scattered at different intensities. The rate at which these intensity fluctuations occur will depend on the size of the particles.[133] Figure **1.21** illustrates typical intensity fluctuations arising from a dispersion of large particles and a dispersion of small particles. The small particles cause the intensity to fluctuate more quickly than for larger particles.

The oscillating intensity signal is then converted into size information using a correlation function in which the time analysis is carried out with a correlator which constructs the time

autocorrection function of the scattered intensity.[134] The correlation function contains the diffusion coefficient information by fitting it with a suitable algorithm.

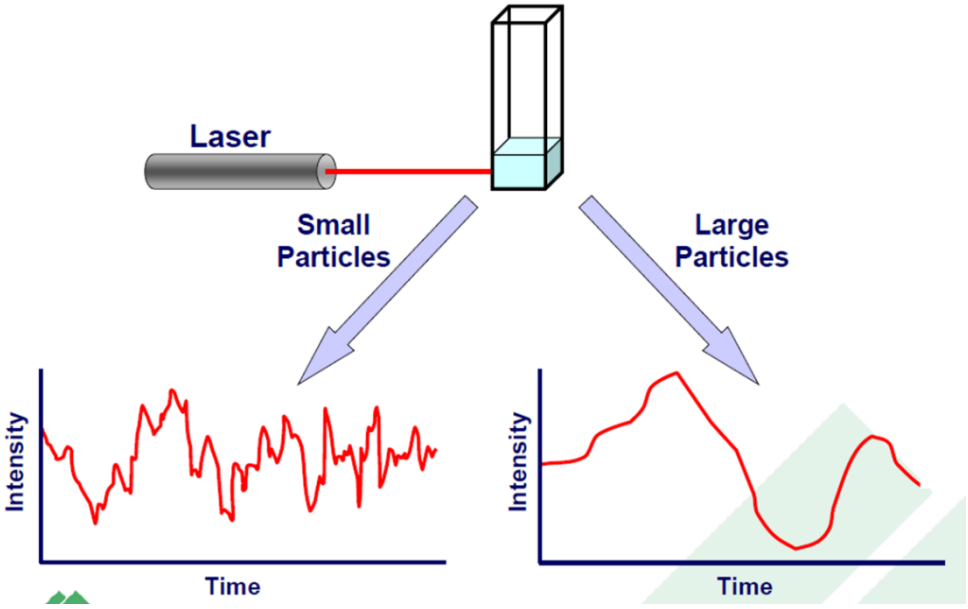

Figure 1.21 Intensity fluctuations and Brownian motion. Differences in diffusion coefficient or particle size results in different frequency fluctuations in light intensity. Image adapted from www.atascientific.com.au.

1.6.1.2 Zeta-Potential Measurement

When charged nanoparticles (NPs) are dispersed in a liquid, a layer of ions of opposite charge is strongly bound to their surface, forming a charged thin layer, known as the "Stern layer" (see **Figure 1.22**). The Stern layer induces the formation of a second diffuse outer layer, composed of loosely associated ions called the "diffusive ion layer". These two layers are collectively called "the electrical double layer". When the NPs move in the liquid phase (due to gravity, kinetic energy, and/or under an applied electrical field),[135] there exists a boundary between the ions in the diffuse layer that move with the particle and ions that remain with the bulk dispersant. The zeta potential is the electrostatic potential at this "slipping plane" boundary (**Figure 1.22**).[136]

During a zeta potential measurement, an electrical field is applied across the sample, inducing the movement of charged particles. The ratio between the NP velocity (U) and the externally applied field (E), known as electrophoretic mobility (μ_e), is then measured and converted to the zeta potential (ζ) using the Henry equation:[137,138]

$$\mu_e = \frac{U}{E} = \frac{2 \cdot \epsilon \cdot \zeta \cdot f(\kappa \cdot \alpha)}{3 \cdot \eta} \qquad \textbf{1.13}$$

Where

ε = solvent dielectric constant

η = solvent viscosity

$f(\kappa \cdot \alpha)$: Henry function, the ratio of the particle size (α) to the Debye length (1/κ). Debye length represents the thickness of the electrical double layer that depends on the ionic strength of the medium and on the temperature of the sample. In an electrolyte or a colloidal suspension, the Debye length for a monovalent electrolyte is usually denoted with symbol κ^{-1}

$$\kappa^{-1} = \sqrt{\frac{\varepsilon_r \varepsilon_0 k_B T}{2e^2 I}} \qquad \textbf{1.14}$$

Where

I = the ionic strength of the electrolyte

ε_0 = the permittivity of free space

ε_r = dielectric constant

k_B = the Boltzmann constant

T = the absolute temperature

e = the elementary charge

Henry function $f(\kappa \cdot \alpha)$ is used to describe the electrophoretic mobility of spherical colloids.[139] For NPs in a polar media (e.g. NaCl > 10 mM), $f(\kappa \cdot \alpha)$ is approximate to its maximum value, 1.5, which is known as the Smoluchowski approximation;[133] for non-polar media $f(\kappa \cdot \alpha)$ can be approximated to its minimum value, 1 (Hukel Approximation).[140] In most water-based media relevant to biological applications, the value 1.5 is the most appropriate.

During a zeta potential measurement, the electrophoretic mobility is quantified by measuring the small frequency shift of the light of a coherent laser source (laser) scattered by the charged NPs that are moving in an external electric field. The shift in frequency is measured by a Doppler interferometer.[138]

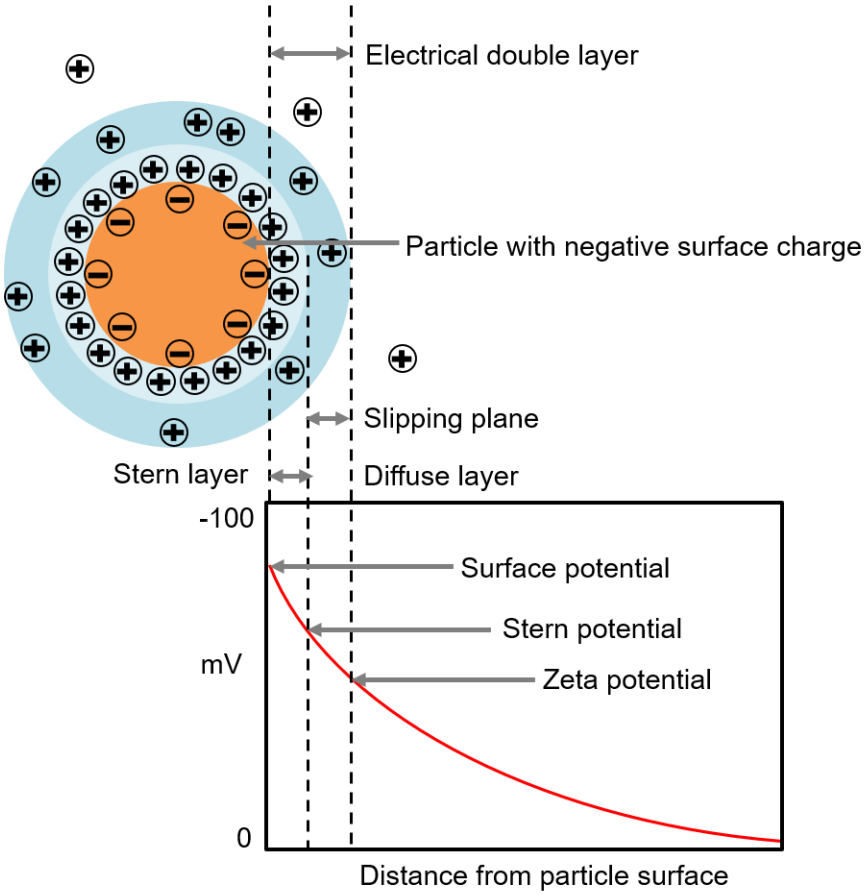

Figure 1.22 Schematic representation of zeta potential definition reproduced from Ref. [104].

1.6.2 Time-Resolved Spectroscopy Techniques

1.6.2.1 Time-Correlated Single Photon Counting

Time-correlated single photon counting (TCSCP) is a method for determining fluorescence lifetimes (τ). This method relies on the probability of detecting a photon at time t after the excitation pulse is proportional to the fluorescence intensity $I(t)$ at that time.[141]

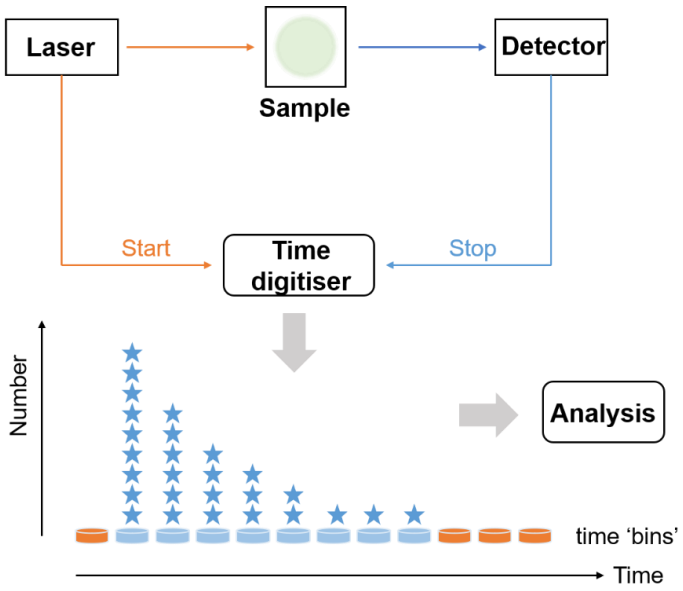

Figure 1.23 Schematic for TCSPC reproduced from Ref. [136].

It makes use of a pulsed excitation source (typically laser or LED), as shown schematically in **Figure. 1.23**. Production of a light pulse 'starts' the timing electronics. These are 'stopped' by a signal from the detector, triggered when a fluorescence photon hits the detector. The difference in time between these two signals is then outputted to a histogram, consisting of time bins, with fixed time width (Δt).[142] Timing electronics in the form of a time-to-digital converter or time-to-amplitude converter are used to record these events in succession, until sufficient statistics are collected to reconstruct the decay.

The signal is then fit to a multiexponential function to model the lifetime decay to obtain fluorescence lifetimes. χ^2 is a goodness-of-fit parameter, and ideal χ^2 value typically is 1.2 or less. After fitting, the average fluorescence lifetime (τ_{avg}) can be calculated according to equation 1 with coefficient α_i of each component representing a contribution to overall decay.[143]

$$\tau_{\text{avg}} = \sum \alpha_i \tau_i \qquad \textbf{1.15}$$

1.6.2.2 Transient absorption spectroscopy

Transient absorption spectroscopy (TA) is a pump-probe technique used to investigate the excited state of molecules or materials on the ultrafast (fs to ns) and slow (µs to s) timescales.[144] Two light pulses are required: a femtosecond narrow-bandwidth pump pulse to excite the sample and a delayed broad-bandwidth probe pulse to measure the changes in sample transmittance (**Figure 1.24**).[145] In ultrafast TA measurements, the probe beam passes through an adjustable delay line and is focused onto a supercontinuum medium (such as CaF_2 or sapphire), resulting in the generation of broadband radiation, which is spatially overlapped with the pump beam at the sample. After transmission through the sample, the broadband probe is dispersed by a spectrograph and detected by an array detector.[144]

The time resolution of such experiments depends mainly on the duration of the pump and probe pulses, that is, the pump-probe correlation function. However, due to the limited length of the delay line, most ultrafast TA systems have a limit on the achievable delay of <10 ns.[144]

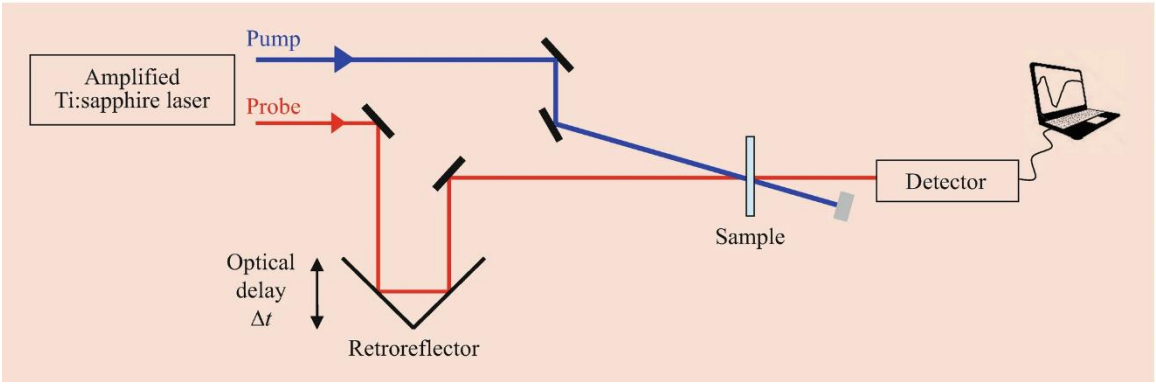

Figure 1.24 Basic principle of femtosecond transient absorption. Figure adapted from Ref. [140].

The high-intensity pump laser excites a significant percentage of the molecules in the sample to a higher energy level, altering the population difference and reducing the absorption coefficient of the transition.[146] Next, a low-intensity probe laser is passed through the sample to measure the absorption. Based on the difference between the probe laser absorption with and without the pump for different pump-probe delays Δt at a given wavelength λ, the measured signals are usually expressed as the differential absorbance of the sample with and without the pump, A_p and A_{np}, respectively:[147]

$$\Delta A\,(\lambda, \Delta t) = A_p(\lambda, \Delta t) - A_{np}(\lambda, \Delta t) = -\log\left(\frac{I_{probe\,p}(\lambda,\Delta t)}{I_{probe\,np}(\lambda,\Delta t)}\right) \qquad \textbf{1.16}$$

with $I_{probe\ p}$ and $I_{probe\ np}$ the probe intensity transmitted by the sample with and without the pump, respectively. Measurements for different pump-probe delays and different wavelengths allow us to reconstruct the sequence of events leading to the formation of intermediates or the photoreaction products.[148] A three-dimensional spectrum (ΔO.D. vs λ vs t) is then constructed by repeating the measurement at a range of pump-probe time delays.

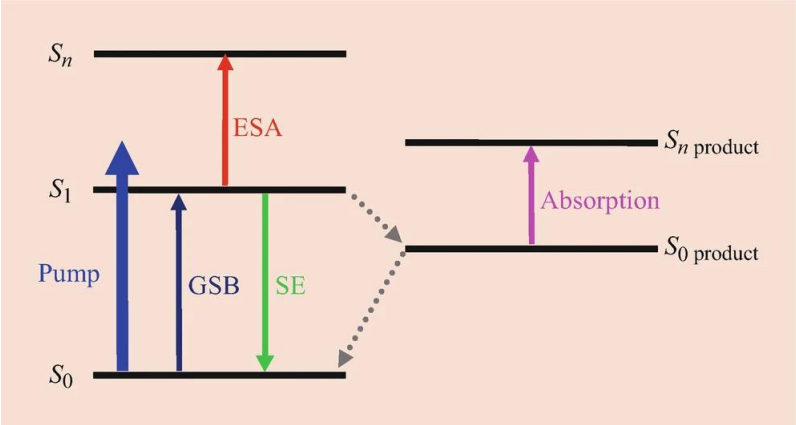

Figure 1.25 Three-state population model illustrating the formation of a transient non-emissive product in the singlet ground state from S_1. Figure adapted from Ref. [140].

Spectrum features commonly observed in a TA spectrum (**Figure 1.25**) include (i) ground-state bleach (GSB) resulting from the depopulation of the ground state by the pump laser and expected to have similar profiles to the steady-state UV-Vis absorbance spectrum; (ii) simulated emission (SE) which are resulted from excited species radiatively relaxing to their ground electronic state; (iii) excited-state absorptions (ESAs)/photochemical product absorptions[149] which are formed when excited species are subsequently excited to higher level electronic states through the absorption of the probe light.[150]

In time-resolved spectroscopic experiments, to extract valuable information, one method is a kinetic trace, to take one wavelength and look at its evolution in time; or a Δ*A* spectrum, to plot the signal at different wavelengths for a given point. Analysis of how these spectroscopic features grow in or decay over time can then be used to establish the timescales of key species formation, and their lifetimes, to unravel their kinetics.

1.7 Project Aims

The core aim of this thesis is to assemble conjugated polymer - *E. coli* biohybrid systems for the evolution of hydrogen from water. As previously discussed, organic photocatalysts, such as conjugated polymers, are much less explored in biohybrid systems, despite their advantages such as the synthetically tunable optoelectronic properties and surface properties that are derived from a wide range of accessible monomers.

This project will explore the potential of organic semiconductors focusing on nanoparticles of processable linear polymers (Chapter 2) as light absorbers in semi-artificial photosynthesis systems. Recombinant *E. coli* expressing [FeFe]-hydrogenase will be coupled with these nanoparticles to fabricate cell hybrids (Chapter 3) and their performance will be evaluated in terms of sacrificial photobiocatalytic hydrogen generation from water.

Firstly, the optical properties of the organic photocatalyst will be tuned by using different building blocks in the polymer backbone, such as phenylene, thiophene, dithiophene, and dibenzo[*b,d*]thiophene sulfone, which allows the system to absorb visible light. The polarity of the polymer side-chains will be tuned by incorporating imidazolium or quaterinized ammonium groups, which will improve the surface interaction between the polymer and the *E. coli* cells. Furthermore, the processability of conjugated polymers by incorporation of solubilising side chains into linear polymers will open up opportunities for the processing of polymers into nanoparticles and films,[151] which will improve photocatalytic performance[152,153] and enhance interactions further.

Secondly, two biohybrid system assembly strategies will be studied in Chapter 3, and different parameters, such as irradiation time, sacrificial electron donors, reaction medium, polymer backbones, *E. coli* strains, and dye-sensitization will be explored to optimize the conjugated polymer-*E. coli* biohybrid systems.

Lastly, a further aim of this project is to investigate the possible charge transfer mechanism in order to give our understanding of the extracellular/intracellular electron transfer pathways of this new type of organic biohybrid system. In Chapter 4, spectroscopic techniques, such as transient absorption spectroscopy alongside metabolic analysis will be applied to explore the underlying mechanism.

1.8 References

(1) Ishaq, H.; Dincer, I.; Crawford, C. A Review on Hydrogen Production and Utilization: Challenges and Opportunities. *Int. J. Hydrogen Energy* **2022**, *47* (62), 26238–26264. https://doi.org/10.1016/j.ijhydene.2021.11.149.

(2) Smil, V. *Energy Transitions: Global and National Perspectives*; ABC-CLIO, LLC, 2017.

(3) Zhang, X.; Dincer, I. *Energy Solutions to Combat Global Warming*; Springer, 2017.

(4) Ishaq, H.; Dincer, I. The Role of Hydrogen in Global Transition to 100% Renewable Energy BT - Accelerating the Transition to a 100% Renewable Energy Era; Uyar, T. S., Ed.; Springer International Publishing: Cham, 2020; pp 275–307. https://doi.org/10.1007/978-3-030-40738-4_13.

(5) Lewis, N. S.; Nocera, D. G. Powering the Planet: Chemical Challenges in Solar Energy Utilization. *Proc. Natl. Acad. Sci.* **2006**, *103* (43), 15729 LP – 15735. https://doi.org/10.1073/pnas.0603395103.

(6) Wang, Q.; Pornrungroj, C.; Linley, S.; Reisner, E. Strategies to Improve Light Utilization in Solar Fuel Synthesis. *Nat. Energy* **2022**, *7* (1), 13–24. https://doi.org/10.1038/s41560-021-00919-1.

(7) Cook, T. R.; Dogutan, D. K.; Reece, S. Y.; Surendranath, Y.; Teets, T. S.; Nocera, D. G. Solar Energy Supply and Storage for the Legacy and Nonlegacy Worlds. *Chem. Rev.* **2010**, *110* (11), 6474–6502. https://doi.org/10.1021/cr100246c.

(8) Detz, R. J.; Reek, J. N. H.; van der Zwaan, B. C. C. The Future of Solar Fuels: When Could They Become Competitive? *Energy Environ. Sci.* **2018**, *11* (7), 1653–1669. https://doi.org/10.1039/C8EE00111A.

(9) Chen, L. X. From Photosynthesis to Photocatalysis: Dual Catalytic Oxidation/Reduction in One System. *Proc. Natl. Acad. Sci. U. S. A.* **2020**, *117* (16), 8672–8673. https://doi.org/10.1073/pnas.2003512117.

(10) Johnson, M. P. Photosynthesis. *Essays Biochem.* **2016**, *60* (3), 255–273. https://doi.org/10.1042/EBC20160016.

(11) Thorndike, E. H. *Energy and Environment: A Primer for Scientists and Engineers*;

Addison-Wesley Publishing Company, 1976.

(12) Barber, J. Photosynthetic Energy Conversion: Natural and Artificial. *Chem. Soc. Rev.* **2009**, *38* (1), 185–196. https://doi.org/10.1039/b802262n.

(13) Bard, A. J.; Fox, M. A. Artificial Photosynthesis: Solar Splitting of Water to Hydrogen and Oxygen. *Acc. Chem. Res.* **1995**, *28* (3), 141–145. https://doi.org/10.1021/ar00051a007.

(14) Jiang, C.; Moniz, S. J. A.; Wang, A.; Zhang, T.; Tang, J. Photoelectrochemical Devices for Solar Water Splitting-Materials and Challenges. *Chem. Soc. Rev.* **2017**, *46* (15), 4645–4660. https://doi.org/10.1039/c6cs00306k.

(15) Lewis, N. S. Research Opportunities to Advance Solar Energy Utilization. *Science (80-.).* **2016**, *351* (6271), aad1920. https://doi.org/10.1126/science.aad1920.

(16) Sachs, M.; Sprick, R. S.; Pearce, D.; Hillman, S. A. J.; Monti, A.; Guilbert, A. A. Y.; Brownbill, N. J.; Dimitrov, S.; Shi, X.; Blanc, F.; Zwijnenburg, M. A.; Nelson, J.; Durrant, J. R.; Cooper, A. I. Understanding Structure-Activity Relationships in Linear Polymer Photocatalysts for Hydrogen Evolution. *Nat. Commun.* **2018**, *9* (1), 1–11. https://doi.org/10.1038/s41467-018-07420-6.

(17) Nishiyama, H.; Yamada, T.; Nakabayashi, M.; Maehara, Y.; Yamaguchi, M.; Kuromiya, Y.; Nagatsuma, Y.; Tokudome, H.; Akiyama, S.; Watanabe, T.; Narushima, R.; Okunaka, S.; Shibata, N.; Takata, T.; Hisatomi, T.; Domen, K. Photocatalytic Solar Hydrogen Production from Water on a 100-M2 Scale. *Nature* **2021**, *598* (7880), 304–307. https://doi.org/10.1038/s41586-021-03907-3.

(18) Kornienko, N.; Zhang, J. Z.; Sakimoto, K. K.; Yang, P.; Reisner, E. Interfacing Nature's Catalytic Machinery with Synthetic Materials for Semi-Artificial Photosynthesis. *Nat. Nanotechnol.* **2018**, *13* (10), 890–899. https://doi.org/10.1038/s41565-018-0251-7.

(19) Krasnovsky, A. A.; Nikandrov, V. V. The Photobiocatalytic System: Inorganic Semiconductors Coupled to Bacterial Cells. *FEBS Lett.* **1987**, *219* (1), 93–96. https://doi.org/10.1016/0014-5793(87)81197-3.

(20) Tschörtner, J.; Lai, B.; Krömer, J. O. Biophotovoltaics: Green Power Generation from Sunlight and Water. *Front. Microbiol.* **2019**, *10* (APR). https://doi.org/10.3389/fmicb.2019.00866.

(21) Fang, X.; Kalathil, S.; Reisner, E. Semi-Biological Approaches to Solar-to-Chemical Conversion. *Chem. Soc. Rev.* **2020**, *49* (14), 4926–4952. https://doi.org/10.1039/C9CS00496C.

(22) Cestellos-Blanco, S.; Zhang, H.; Yang, P. Solar-Driven Carbon Dioxide Fixation Using Photosynthetic Semiconductor Bio-Hybrids. *Faraday Discuss.* **2019**, *215*, 54–65. https://doi.org/10.1039/C8FD00187A.

(23) Cestellos-Blanco, S.; Zhang, H.; Kim, J. M.; Shen, Y. xiao; Yang, P. Photosynthetic Semiconductor Biohybrids for Solar-Driven Biocatalysis. *Nat. Catal.* **2020**, *3* (3), 245–255. https://doi.org/10.1038/s41929-020-0428-y.

(24) Sakimoto, K. K.; Wong, A. B.; Yang, P. Self-Photosensitization of Nonphotosynthetic Bacteria for Solar-to-Chemical Production. *Science (80-.).* **2016**, *351* (6268), 74–77. https://doi.org/10.1126/science.aad3317.

(25) Sakimoto, K. K.; Zhang, S. J.; Yang, P. Cysteine-Cystine Photoregeneration for Oxygenic Photosynthesis of Acetic Acid from CO2 by a Tandem Inorganic-Biological Hybrid System. *Nano Lett.* **2016**, *16* (9), 5883–5887. https://doi.org/10.1021/acs.nanolett.6b02740.

(26) Honda, Y.; Hagiwara, H.; Ida, S.; Ishihara, T. Application to Photocatalytic H2Production of a Whole-Cell Reaction by Recombinant Escherichia Coli Cells Expressing [FeFe]-Hydrogenase and Maturases Genes. *Angew. Chemie - Int. Ed.* **2016**, *55* (28), 8045–8048. https://doi.org/10.1002/anie.201600177.

(27) Rowe, S. F.; Le Gall, G.; Ainsworth, E. V.; Davies, J. A.; Lockwood, C. W. J.; Shi, L.; Elliston, A.; Roberts, I. N.; Waldron, K. W.; Richardson, D. J.; Clarke, T. A.; Jeuken, L. J. C.; Reisner, E.; Butt, J. N. Light-Driven H2 Evolution and C=C or C=O Bond Hydrogenation by Shewanella Oneidensis: A Versatile Strategy for Photocatalysis by Nonphotosynthetic Microorganisms. *ACS Catal.* **2017**, *7* (11), 7558–7566. https://doi.org/10.1021/acscatal.7b02736.

(28) Wang, B.; Zeng, C.; Chu, K. H.; Wu, D.; Yip, H. Y.; Ye, L.; Wong, P. K. Enhanced Biological Hydrogen Production from Escherichia Coli with Surface Precipitated Cadmium Sulfide Nanoparticles. *Adv. Energy Mater.* **2017**, *7* (20), 1–10. https://doi.org/10.1002/aenm.201700611.

(29) Wei, W.; Sun, P.; Li, Z.; Song, K.; Su, W.; Wang, B.; Liu, Y.; Zhao, J. A Surface-Display Biohybrid Approach to Light-Driven Hydrogen Production in Air. *Sci. Adv.* **2018**, *4* (2), eaap9253. https://doi.org/10.1126/sciadv.aap9253.

(30) Zhang, H.; Liu, H.; Tian, Z.; Lu, D.; Yu, Y.; Cestellos-Blanco, S.; Sakimoto, K. K.; Yang, P. Bacteria Photosensitized by Intracellular Gold Nanoclusters for Solar Fuel Production. *Nat. Nanotechnol.* **2018**, *13* (10), 900–905. https://doi.org/10.1038/s41565-018-0267-z.

(31) Gai, P.; Yu, W.; Zhao, H.; Qi, R.; Li, F.; Liu, L.; Lv, F.; Wang, S. Solar-Powered Organic Semiconductor–Bacteria Biohybrids for CO 2 Reduction into Acetic Acid. *Angew. Chemie Int. Ed.* **2020**, *59* (18), 7224–7229. https://doi.org/10.1002/anie.202001047.

(32) Han, H.-X.; Tian, L.-J.; Liu, D.-F.; Yu, H.-Q.; Sheng, G.-P.; Xiong, Y. Reversing Electron Transfer Chain for Light-Driven Hydrogen Production in Biotic–Abiotic Hybrid Systems. *J. Am. Chem. Soc.* **2022**. https://doi.org/10.1021/jacs.2c00934.

(33) Wang, X.; Zhang, J.; Li, K.; An, B.; Wang, Y.; Zhong, C. Photocatalyst-Mineralized Biofilms as Living Bio-Abiotic Interfaces for Single Enzyme to Whole-Cell Photocatalytic Applications. *Sci. Adv.* **2022**, *8* (18), 1–12. https://doi.org/10.1126/sciadv.abm7665.

(34) Yu, W.; Bai, H.; Zeng, Y.; Zhao, H.; Xia, S.; Huang, Y.; Lv, F.; Wang, S. Solar-Driven Producing of Value-Added Chemicals with Organic Semiconductor-Bacteria Biohybrid System. *Research* **2022**, *2022*, 1–13. https://doi.org/10.34133/2022/9834093.

(35) Wang, Q.; Kalathil, S.; Pornrungroj, C.; Sahm, C. D.; Reisner, E. Bacteria–Photocatalyst Sheet for Sustainable Carbon Dioxide Utilization. *Nat. Catal.* **2022**, *5* (7), 633–641. https://doi.org/10.1038/s41929-022-00817-z.

(36) Hall, P. J.; Bain, E. J. Energy-Storage Technologies and Electricity Generation. *Energy Policy* **2008**, *36* (12), 4352–4355. https://doi.org/https://doi.org/10.1016/j.enpol.2008.09.037.

(37) Nikolaidis, P.; Poullikkas, A. A Comparative Overview of Hydrogen Production Processes. *Renew. Sustain. Energy Rev.* **2017**, *67*, 597–611. https://doi.org/10.1016/j.rser.2016.09.044.

(38) Kibsgaard, J.; Chorkendorff, I. Considerations for the Scaling-up of Water Splitting Catalysts. *Nat. Energy* **2019**, *4* (6), 430–433.

(39) Kothari, R.; Buddhi, D.; Sawhney, R. L. Comparison of Environmental and Economic Aspects of Various Hydrogen Production Methods. *Renew. Sustain. Energy Rev.* **2008**, *12* (2), 553–563. https://doi.org/https://doi.org/10.1016/j.rser.2006.07.012.

(40) Staffell, I.; Scamman, D.; Velazquez Abad, A.; Balcombe, P.; Dodds, P. E.; Ekins, P.; Shah, N.; Ward, K. R. The Role of Hydrogen and Fuel Cells in the Global Energy System. *Energy Environ. Sci.* **2019**, *12* (2), 463–491. https://doi.org/10.1039/c8ee01157e.

(41) Demirbaş, A. Biomass Resource Facilities and Biomass Conversion Processing for Fuels and Chemicals. *Energy Convers. Manag.* **2001**, *42* (11), 1357–1378. https://doi.org/https://doi.org/10.1016/S0196-8904(00)00137-0.

(42) McKendry, P. Energy Production from Biomass (Part 1): Overview of Biomass. *Bioresour. Technol.* **2002**, *83* (1), 37–46. https://doi.org/https://doi.org/10.1016/S0960-8524(01)00118-3.

(43) Ni, M.; Leung, D. Y. C.; Leung, M. K. H.; Sumathy, K. An Overview of Hydrogen Production from Biomass. *Fuel Process. Technol.* **2006**, *87* (5), 461–472. https://doi.org/https://doi.org/10.1016/j.fuproc.2005.11.003.

(44) Balat, H.; Kırtay, E. Hydrogen from Biomass – Present Scenario and Future Prospects. *Int. J. Hydrogen Energy* **2010**, *35* (14), 7416–7426. https://doi.org/https://doi.org/10.1016/j.ijhydene.2010.04.137.

(45) Das, D.; Veziroglu, T. N. Advances in Biological Hydrogen Production Processes. *Int. J. Hydrogen Energy* **2008**, *33* (21), 6046–6057. https://doi.org/https://doi.org/10.1016/j.ijhydene.2008.07.098.

(46) Steinfeld, A. Solar Thermochemical Production of Hydrogen—a Review. *Sol. Energy* **2005**, *78* (5), 603–615. https://doi.org/https://doi.org/10.1016/j.solener.2003.12.012.

(47) FUJISHIMA, A.; HONDA, K. Electrochemical Photolysis of Water at a Semiconductor Electrode. *Nature* **1972**, *238* (5358), 37–38. https://doi.org/10.1038/238037a0.

(48) Xing, J.; Fang, W. Q.; Zhao, H. J.; Yang, H. G. Inorganic Photocatalysts for Overall Water Splitting. *Chem. Asian J.* **2012**, *7* (4), 642–657.

https://doi.org/10.1002/asia.201100772.

(49) Osterloh, F. E. Inorganic Nanostructures for Photoelectrochemical and Photocatalytic Water Splitting. *Chem. Soc. Rev.* **2013**, *42* (6), 2294–2320. https://doi.org/10.1039/C2CS35266D.

(50) Liu, S.; Lei, Y.-J.; Xin, Z.-J.; Lu, Y.-B.; Wang, H.-Y. Water Splitting Based on Homogeneous Copper Molecular Catalysts. *J. Photochem. Photobiol. A Chem.* **2018**, *355*, 141–151. https://doi.org/https://doi.org/10.1016/j.jphotochem.2017.09.060.

(51) Du, P.; Eisenberg, R. Catalysts Made of Earth-Abundant Elements (Co, Ni, Fe) for Water Splitting: Recent Progress and Future Challenges. *Energy Environ. Sci.* **2012**, *5* (3), 6012–6021. https://doi.org/10.1039/C2EE03250C.

(52) Banerjee, T.; Podjaski, F.; Kröger, J.; Biswal, B. P.; Lotsch, B. V. Polymer Photocatalysts for Solar-to-Chemical Energy Conversion. *Nature Reviews Materials*. 2020. https://doi.org/10.1038/s41578-020-00254-z.

(53) Takanabe, K. Photocatalytic Water Splitting: Quantitative Approaches toward Photocatalyst by Design. *ACS Catal.* **2017**, *7* (11), 8006–8022.

(54) Linsebigler, A. L.; Lu, G.; Yates, J. T. J. Photocatalysis on TiO2 Surfaces: Principles, Mechanisms, and Selected Results. *Chem. Rev.* **1995**, *95* (3), 735–758. https://doi.org/10.1021/cr00035a013.

(55) Wang, Q.; Domen, K. Particulate Photocatalysts for Light-Driven Water Splitting: Mechanisms, Challenges, and Design Strategies. *Chem. Rev.* **2020**, *120* (2), 919–985. https://doi.org/10.1021/acs.chemrev.9b00201.

(56) Guiglion, P.; Butchosa, C.; Zwijnenburg, M. A. Polymer Photocatalysts for Water Splitting: Insights from Computational Modeling. *Macromol. Chem. Phys.* **2016**, *217* (3), 344–353. https://doi.org/10.1002/macp.201500432.

(57) Chen, X.; Shen, S.; Guo, L.; Mao, S. S. Semiconductor-Based Photocatalytic Hydrogen Generation. *Chem. Rev.* **2010**, *110* (11), 6503–6570. https://doi.org/10.1021/cr1001645.

(58) Lin, L.; Hisatomi, T.; Chen, S.; Takata, T.; Domen, K. Visible-Light-Driven Photocatalytic Water Splitting: Recent Progress and Challenges. *Trends Chem.* **2020**, *2* (9), 813–824. https://doi.org/10.1016/j.trechm.2020.06.006.

(59) Habisreutinger, S. N.; Schmidt-Mende, L.; Stolarczyk, J. K. Photocatalytic Reduction of CO2 on TiO2 and Other Semiconductors. *Angew. Chemie Int. Ed.* **2013**, *52* (29), 7372–7408. https://doi.org/https://doi.org/10.1002/anie.201207199.

(60) Serpone, N. Relative Photonic Efficiencies and Quantum Yields in Heterogeneous Photocatalysis. *J. Photochem. Photobiol. A Chem.* **1997**, *104* (1), 1–12. https://doi.org/https://doi.org/10.1016/S1010-6030(96)04538-8.

(61) Zhang, S.; Chu, C.; Huang, M.; Wu, B.; Zhong, L.; Sun, Y. Enhanced Carrier Spatial Separation and Interfacial Transfer for Photocatalytic Cyanation of Olefins. *ACS Sustain. Chem. Eng.* **2022**, *10* (2), 831–837. https://doi.org/10.1021/acssuschemeng.1c06288.

(62) Ahouei, M. A.; Syed, T. H.; Bishop, V.; Halacoglu, S.; Wang, H.; Wei, W. Ti3C2Tx MXene Framework Materials: Preparation, Properties and Applications in Energy and Environment. *Catal. Today* **2023**, *409*, 162–172. https://doi.org/https://doi.org/10.1016/j.cattod.2022.11.001.

(63) He, J.; Hu, L.; Shao, C.; Jiang, S.; Sun, C.; Song, S. Photocatalytic H2O Overall Splitting into H2 Bubbles by Single Atomic Sulfur Vacancy CdS with Spin Polarization Electric Field. *ACS Nano* **2021**, *15* (11), 18006–18013. https://doi.org/10.1021/acsnano.1c06524.

(64) Shang, Y.; Fan, H.; Chen, Y.; Dong, W.; Wang, W. Synergism between Nitrogen Vacancies and a Unique Electrons Transfer Pathway of Ag Modified S-Scheme g-C3N4/CdS Heterojunction for Efficient H2 Evolution. *J. Alloys Compd.* **2023**, *933*, 167620. https://doi.org/https://doi.org/10.1016/j.jallcom.2022.167620.

(65) Khan, H.; Mehtab, A.; Ahmed, J.; Lofland, S. E.; Ramanujachary, K. V; Ahmad, T. Harvesting Green Hydrogen by Self-Propelling Built-in Electric Field Photo/Electro-Catalytic Performance of DyCrO3 Nanoparticles Developed by Reverse Microemulsion Route. *ChemNanoMat* **2023**, *n/a* (n/a), e202300091. https://doi.org/https://doi.org/10.1002/cnma.202300091.

(66) Li, L.; Zhang, R.; Lin, Y.; Wang, D.; Xie, T. Plasmon-Enhanced Bulk Charge Separation via Morphological and Interfacial Engineering in Au@carbon Dots@CdS Hybrid. *Chem. Eng. J.* **2023**, *453*, 139970. https://doi.org/https://doi.org/10.1016/j.cej.2022.139970.

(67) Wang, M.; Shen, S.; Li, L.; Tang, Z.; Yang, J. Effects of Sacrificial Reagents on Photocatalytic Hydrogen Evolution over Different Photocatalysts. *J. Mater. Sci.* **2017**,

52 (9), 5155–5164. https://doi.org/10.1007/s10853-017-0752-z.

(68) Hesleitner, P.; Kallay, N.; Matijevic, E. Adsorption at Solid/Liquid Interfaces. 6. The Effect of Methanol and Ethanol on the Ionic Equilibria at the Hematite/Water Interface. *Langmuir* **1991**, *7* (1), 178–184.

(69) Pellegrin, Y.; Odobel, F. Sacrificial Electron Donor Reagents for Solar Fuel Production. *Comptes Rendus Chim.* **2017**, *20* (3), 283–295. https://doi.org/https://doi.org/10.1016/j.crci.2015.11.026.

(70) Walter, M. G.; Warren, E. L.; McKone, J. R.; Boettcher, S. W.; Mi, Q.; Santori, E. A.; Lewis, N. S. Solar Water Splitting Cells. *Chem. Rev.* **2010**, *110* (11), 6446–6473. https://doi.org/10.1021/cr1002326.

(71) Döscher, H.; Geisz, J. F.; Deutsch, T. G.; Turner, J. A. Sunlight Absorption in Water – Efficiency and Design Implications for Photoelectrochemical Devices. *Energy Environ. Sci.* **2014**, *7* (9), 2951–2956. https://doi.org/10.1039/C4EE01753F.

(72) Dotan, H.; Mathews, N.; Hisatomi, T.; Grätzel, M.; Rothschild, A. On the Solar to Hydrogen Conversion Efficiency of Photoelectrodes for Water Splitting. *J. Phys. Chem. Lett.* **2014**, *5* (19), 3330–3334. https://doi.org/10.1021/jz501716g.

(73) GRIMES, C.; VARGHESE, O.; RANJAN, S. *Light, Water, Hydrogen: The Solar Generation of Hydrogen by Water Photoelectrolysis*; Fuel Cells and Hydrogen Energy; Springer US, 2007.

(74) Liu, J.; Liu, Y.; Liu, N.; Han, Y.; Zhang, X.; Huang, H.; Lifshitz, Y.; Lee, S. T.; Zhong, J.; Kang, Z. Metal-Free Efficient Photocatalyst for Stable Visible Water Splitting via a Two-Electron Pathway. *Science (80-.).* **2015**, *347* (6225), 970–974. https://doi.org/10.1126/science.aaa3145.

(75) Chen, S.; Takata, T.; Domen, K. Particulate Photocatalysts for Overall Water Splitting. *Nat. Rev. Mater.* **2017**, *2* (10), 17050. https://doi.org/10.1038/natrevmats.2017.50.

(76) Chen, S.; Qi, Y.; Hisatomi, T.; Ding, Q.; Asai, T.; Li, Z.; Ma, S. S. K.; Zhang, F.; Domen, K.; Li, C. Efficient Visible-Light-Driven Z-Scheme Overall Water Splitting Using a MgTa2O(6-x)N(y)/TaON Heterostructure Photocatalyst for H2 Evolution. *Angew. Chem. Int. Ed. Engl.* **2015**, *54* (29), 8498–8501. https://doi.org/10.1002/anie.201502686.

(77) Wang, Q.; Hisatomi, T.; Jia, Q.; Tokudome, H.; Zhong, M.; Wang, C.; Pan, Z.; Takata,

T.; Nakabayashi, M.; Shibata, N.; Li, Y.; Sharp, I. D.; Kudo, A.; Yamada, T.; Domen, K. Scalable Water Splitting on Particulate Photocatalyst Sheets with a Solar-to-Hydrogen Energy Conversion Efficiency Exceeding 1. *Nature materials*. England June 2016, pp 611–615. https://doi.org/10.1038/nmat4589.

(78) Jia, Q.; Iwase, A.; Kudo, A. BiVO4–Ru/SrTiO3:Rh Composite Z-Scheme Photocatalyst for Solar Water Splitting. *Chem. Sci.* **2014**, *5* (4), 1513–1519. https://doi.org/10.1039/C3SC52810C.

(79) Kim, J. H.; Hansora, D.; Sharma, P.; Jang, J. W.; Lee, J. S. Toward Practical Solar Hydrogen Production-an Artificial Photosynthetic Leaf-to-Farm Challenge. *Chem. Soc. Rev.* **2019**, *48* (7), 1908–1971. https://doi.org/10.1039/c8cs00699g.

(80) Li, Z.; Fang, S.; Sun, H.; Chung, R. J.; Fang, X.; He, J. H. Solar Hydrogen. *Adv. Energy Mater.* **2023**, *2203019*, 1–26. https://doi.org/10.1002/aenm.202203019.

(81) Ye, S.; Shi, W.; Liu, Y.; Li, D.; Yin, H.; Chi, H.; Luo, Y.; Ta, N.; Fan, F.; Wang, X.; Li, C. Unassisted Photoelectrochemical Cell with Multimediator Modulation for Solar Water Splitting Exceeding 4% Solar-to-Hydrogen Efficiency. *J. Am. Chem. Soc.* **2021**, *143* (32), 12499–12508. https://doi.org/10.1021/jacs.1c00802.

(82) Licht, S.; Wang, B.; Mukerji, S.; Soga, T.; Umeno, M.; Tributsch, H. Over 18% Solar Energy Conversion to Generation of Hydrogen Fuel; Theory and Experiment for Efficient Solar Water Splitting. *Int. J. Hydrogen Energy* **2001**, *26* (7), 653–659. https://doi.org/https://doi.org/10.1016/S0360-3199(00)00133-6.

(83) Sapountzi, F. M.; Gracia, J. M.; Weststrate, C. J. (Kees-J.; Fredriksson, H. O. A.; Niemantsverdriet, J. W. (Hans). Electrocatalysts for the Generation of Hydrogen, Oxygen and Synthesis Gas. *Prog. Energy Combust. Sci.* **2017**, *58*, 1–35. https://doi.org/https://doi.org/10.1016/j.pecs.2016.09.001.

(84) Jia, J.; Seitz, L. C.; Benck, J. D.; Huo, Y.; Chen, Y.; Ng, J. W. D.; Bilir, T.; Harris, J. S.; Jaramillo, T. F. Solar Water Splitting by Photovoltaic-Electrolysis with a Solar-to-Hydrogen Efficiency over 30. *Nat. Commun.* **2016**, *7*, 13237. https://doi.org/10.1038/ncomms13237.

(85) Hambourger, M.; Gervaldo, M.; Svedruzic, D.; King, P. W.; Gust, D.; Ghirardi, M.; Moore, A. L.; Moore, T. A. [FeFe]-Hydrogenase-Catalyzed H2 Production in a

Photoelectrochemical Biofuel Cell. *J. Am. Chem. Soc.* **2008**, *130* (6), 2015–2022. https://doi.org/10.1021/ja077691k.

(86) Reisner, E.; Powell, D. J.; Cavazza, C.; Fontecilla-Camps, J. C.; Armstrong, F. A. Visible Light-Driven H2 Production by Hydrogenases Attached to Dye-Sensitized TiO2 Nanoparticles. *J. Am. Chem. Soc.* **2009**, *131* (51), 18457–18466. https://doi.org/10.1021/ja907923r.

(87) Pavliuk, M. V.; Lorenzi, M.; Morado, D. R.; Gedda, L.; Wrede, S.; Mejias, S. H.; Liu, A.; Senger, M.; Glover, S.; Edwards, K.; Berggren, G.; Tian, H. Polymer Dots as Photoactive Membrane Vesicles for [FeFe]-Hydrogenase Self-Assembly and Solar-Driven Hydrogen Evolution. *J. Am. Chem. Soc.* **2022**, *144* (30), 13600–13611. https://doi.org/10.1021/jacs.2c03882.

(88) Freguia, S.; Virdis, B.; Harnisch, F.; Keller, J. Bioelectrochemical Systems: Microbial versus Enzymatic Catalysis. *Electrochim. Acta* **2012**, *82*, 165–174. https://doi.org/https://doi.org/10.1016/j.electacta.2012.03.014.

(89) Rabaey, K.; Rozendal, R. A. Microbial Electrosynthesis - Revisiting the Electrical Route for Microbial Production. *Nat. Rev. Microbiol.* **2010**, *8* (10), 706–716. https://doi.org/10.1038/nrmicro2422.

(90) Lovley, D. R. Bug Juice: Harvesting Electricity with Microorganisms. *Nat. Rev. Microbiol.* **2006**, *4* (7), 497–508. https://doi.org/10.1038/nrmicro1442.

(91) Nichols, E. M.; Gallagher, J. J.; Liu, C.; Su, Y.; Resasco, J.; Yu, Y.; Sun, Y.; Yang, P.; Chang, M. C. Y.; Chang, C. J. Hybrid Bioinorganic Approach to Solar-Tochemical Conversion. *Proc. Natl. Acad. Sci. U. S. A.* **2015**, *112* (37), 11461–11466. https://doi.org/10.1073/pnas.1508075112.

(92) Bachmeier, A. S. J. L. Selective Visible-Light-Driven CO 2 Reduction on a p-Type Dye-Sensitised NiO Photocathode. In *Metalloenzymes as Inspirational Electrocatalysts for Artificial Photosynthesis*; Springer, 2017; pp 179–191.

(93) Guo, J.; Suástegui, M.; Sakimoto, K. K.; Moody, V. M.; Xiao, G.; Nocera, D. G.; Joshi, N. S. Light-Driven Fine Chemical Production in Yeast Biohybrids. *Science (80-.).* **2018**, *362* (6416), 813 LP – 816. https://doi.org/10.1126/science.aat9777.

(94) Gurunathan, K. Photobiocatalytic Production of Hydrogen Using Sensitized TiO 2–MV

2+ System Coupled Rhodopseudomonas Capsulata. *J. Mol. Catal. A-chemical - J MOL CATAL A-CHEM* **2000**, *156*, 59–67. https://doi.org/10.1016/S1381-1169(99)00417-3.

(95) Zhang, T.; Tremblay, P. L. Hybrid Photosynthesis-Powering Biocatalysts with Solar Energy Captured by Inorganic Devices. *Biotechnol. Biofuels* **2017**, *10* (1), 1–13. https://doi.org/10.1186/s13068-017-0943-5.

(96) Marusak, K. E.; Feng, Y.; Eben, C. F.; Payne, S. T.; Cao, Y.; You, L.; Zauscher, S. Cadmium Sulphide Quantum Dots with Tunable Electronic Properties by Bacterial Precipitation. *RSC Adv.* **2016**, *6* (80), 76158–76166. https://doi.org/10.1039/c6ra13835g.

(97) Sakimoto, K. K.; Wong, A. B.; Yang, P. Self-Photosensitization of Nonphotosynthetic Bacteria for Solar-to-Chemical Production. *Science (80-.).* **2016**, *351* (6268), 74–77. https://doi.org/10.1126/science.aad3317.

(98) Cunningham, D. P.; Lundie, L. L. Precipitation of Cadmium by Clostridium Thermoaceticum. *Appl. Environ. Microbiol.* **1993**, *59* (1), 7 LP – 14.

(99) Wang, C. L.; Clark, D. S.; Keasling, J. D. Metabolic Engineering of an Aerobic Sulfate Reduction Pathway and Its Application to Precipitation of Cadmium on the Cell Surface. *Biotechnol. Bioeng.* **2001**, *75* (3), 285–291. https://doi.org/10.1002/bit.10030.

(100) Wei, W.; Liu, X.; Sun, P.; Wang, X.; Zhu, H.; Hong, M.; Mao, Z.-W.; Zhao, J. Simple Whole-Cell Biodetection and Bioremediation of Heavy Metals Based on an Engineered Lead-Specific Operon. *Environ. Sci. Technol.* **2014**, *48* (6), 3363–3371. https://doi.org/10.1021/es4046567.

(101) Di Ciccio, P.; Vergara, A.; Festino, A. R.; Paludi, D.; Zanardi, E.; Ghidini, S.; Ianieri, A. Biofilm Formation by Staphylococcus Aureus on Food Contact Surfaces: Relationship with Temperature and Cell Surface Hydrophobicity. *Food Control* **2015**, *50*, 930–936. https://doi.org/https://doi.org/10.1016/j.foodcont.2014.10.048.

(102) Laurencin, C.; Deng, M. *Natural and Synthetic Biomedical Polymers*; Newnes, 2014.

(103) Schäffer, C.; Messner, P. Glycobiology of Surface Layer Proteins. *Biochimie* **2001**, *83* (7), 591–599. https://doi.org/https://doi.org/10.1016/S0300-9084(01)01299-8.

(104) Kular, J. K.; Basu, S.; Sharma, R. I. The Extracellular Matrix: Structure, Composition, Age-Related Differences, Tools for Analysis and Applications for Tissue Engineering. *J. Tissue Eng.* **2014**, *5*, 2041731414557112. https://doi.org/10.1177/2041731414557112.

(105) Ma, R.; Tang, T. Current Strategies to Improve the Bioactivity of PEEK. *Int. J. Mol. Sci.* **2014**, *15* (4), 5426–5445.

(106) Achinas, S.; Charalampogiannis, N.; Euverink, G. J. A Brief Recap of Microbial Adhesion and Biofilms. *Applied Sciences* . 2019. https://doi.org/10.3390/app9142801.

(107) Encinas, N.; Yang, C.-Y.; Geyer, F.; Kaltbeitzel, A.; Baumli, P.; Reinholz, J.; Mailänder, V.; Butt, H.-J.; Vollmer, D. Submicrometer-Sized Roughness Suppresses Bacteria Adhesion. *ACS Appl. Mater. Interfaces* **2020**, *12* (19), 21192–21200. https://doi.org/10.1021/acsami.9b22621.

(108) Carpentier, B.; Cerf, O. Biofilms and Their Consequences, with Particular Reference to Hygiene in the Food Industry. *J. Appl. Bacteriol.* **1993**, *75* (6), 499–511. https://doi.org/https://doi.org/10.1111/j.1365-2672.1993.tb01587.x.

(109) Dunne, W. M. Bacterial Adhesion: Seen Any Good Biofilms Lately? *Clin. Microbiol. Rev.* **2002**, *15* (2), 155–166. https://doi.org/10.1128/CMR.15.2.155-166.2002.

(110) Vyas, V. S.; Lau, V. W.; Lotsch, B. V. Soft Photocatalysis: Organic Polymers for Solar Fuel Production. *Chem. Mater.* **2016**, *28* (15), 5191–5204. https://doi.org/10.1021/acs.chemmater.6b01894.

(111) Kessler, F. K.; Zheng, Y.; Schwarz, D.; Merschjann, C.; Schnick, W.; Wang, X.; Bojdys, M. J. Functional Carbon Nitride Materials — Design Strategies for Electrochemical Devices. *Nat. Rev. Mater.* **2017**, *2* (6), 17030. https://doi.org/10.1038/natrevmats.2017.30.

(112) Yanagida, S.; Kabumoto, A.; Mizumoto, K.; Pac, C.; Yoshino, K. Poly(p-Phenylene)-Catalysed Photoreduction of Water to Hydrogen. *J. Chem. Soc. Chem. Commun.* **1985**, No. 8, 474–475. https://doi.org/10.1039/C39850000474.

(113) Liu, M.; Guo, L.; Jin, S.; Tan, B. Covalent Triazine Frameworks: Synthesis and Applications. *J. Mater. Chem. A* **2019**, *7* (10), 5153–5172.

(114) Rowan, S. J.; Cantrill, S. J.; Cousins, G. R. L.; Sanders, J. K. M.; Stoddart, J. F. Dynamic Covalent Chemistry. *Angew. Chemie Int. Ed.* **2002**, *41* (6), 898–952.

(115) Banerjee, T.; Gottschling, K.; Savasci, G.; Ochsenfeld, C.; Lotsch, B. V. H2 Evolution with Covalent Organic Framework Photocatalysts. *ACS Energy Lett.* **2018**, *3* (2), 400–409.

(116) Pachfule, P.; Acharjya, A.; Roeser, J.; Langenhahn, T.; Schwarze, M.; Schomäcker, R.; Thomas, A.; Schmidt, J. Diacetylene Functionalized Covalent Organic Framework (COF) for Photocatalytic Hydrogen Generation. *J. Am. Chem. Soc.* **2018**, *140* (4), 1423–1427.

(117) He, T.; Geng, K.; Jiang, D. Engineering Covalent Organic Frameworks for Light-Driven Hydrogen Production from Water. *ACS Mater. Lett.* **2019**, *1* (2), 203–208.

(118) Sheikhzadeh, E.; Chamsaz, M.; Turner, A. P. F.; Jager, E. W. H.; Beni, V. Label-Free Impedimetric Biosensor for Salmonella Typhimurium Detection Based on Poly [Pyrrole-Co-3-Carboxyl-Pyrrole] Copolymer Supported Aptamer. *Biosens. Bioelectron.* **2016**, *80*, 194–200. https://doi.org/https://doi.org/10.1016/j.bios.2016.01.057.

(119) Li, C.; Zhang, L.; Ding, L.; Ren, H.; Cui, H. Effect of Conductive Polymers Coated Anode on the Performance of Microbial Fuel Cells (MFCs) and Its Biodiversity Analysis. *Biosens. Bioelectron.* **2011**, *26* (10), 4169–4176. https://doi.org/https://doi.org/10.1016/j.bios.2011.04.018.

(120) Wannapob, R.; Kanatharana, P.; Limbut, W.; Numnuam, A.; Asawatreratanakul, P.; Thammakhet, C.; Thavarungkul, P. Affinity Sensor Using 3-Aminophenylboronic Acid for Bacteria Detection. *Biosens. Bioelectron.* **2010**, *26* (2), 357–364. https://doi.org/https://doi.org/10.1016/j.bios.2010.08.005.

(121) Elgiddawy, N.; Ren, S.; Yassar, A.; Louis-Joseph, A.; Sauriat-Dorizon, H.; El Rouby, W. M. A.; El-Gendy, A. O.; Farghali, A. A.; Korri-Youssoufi, H. Dispersible Conjugated Polymer Nanoparticles as Biointerface Materials for Label-Free Bacteria Detection. *ACS Appl. Mater. Interfaces* **2020**, *12* (36), 39979–39990. https://doi.org/10.1021/acsami.0c08305.

(122) Wilson, J. T.; Cui, W.; Kozlovskaya, V.; Kharlampieva, E.; Pan, D.; Qu, Z.; Krishnamurthy, V. R.; Mets, J.; Kumar, V.; Wen, J.; Song, Y.; Tsukruk, V. V; Chaikof, E. L. Cell Surface Engineering with Polyelectrolyte Multilayer Thin Films. *J. Am. Chem. Soc.* **2011**, *133* (18), 7054–7064. https://doi.org/10.1021/ja110926s.

(123) Barlow, J.; Gozzi, K.; Kelley, C. P.; Geilich, B. M.; Webster, T. J.; Chai, Y.; Sridhar, S.; van de Ven, A. L. High Throughput Microencapsulation of Bacillus Subtilis in Semi-Permeable Biodegradable Polymersomes for Selenium Remediation. *Appl. Microbiol. Biotechnol.* **2017**, *101* (1), 455–464. https://doi.org/10.1007/s00253-016-7896-7.

(124) Niu, J.; Lunn, D. J.; Pusuluri, A.; Yoo, J. I.; O'Malley, M. A.; Mitragotri, S.; Soh, H. T.; Hawker, C. J. Engineering Live Cell Surfaces with Functional Polymers via Cytocompatible Controlled Radical Polymerization. *Nat. Chem.* **2017**, *9* (6), 537–545. https://doi.org/10.1038/nchem.2713.

(125) Shen, H.; Wang, Y. Z.; Liu, G.; Li, L.; Xia, R.; Luo, B.; Wang, J.; Suo, D.; Shi, W.; Yong, Y. C. A Whole-Cell Inorganic-Biohybrid System Integrated by Reduced Graphene Oxide for Boosting Solar Hydrogen Production. *ACS Catal.* **2020**, *10* (22), 13290–13295. https://doi.org/10.1021/acscatal.0c03594.

(126) Honda, Y.; Shinohara, Y.; Watanabe, M.; Ishihara, T.; Fujii, H. Photo-Biohydrogen Production by Photosensitization with Biologically Precipitated Cadmium Sulfide in Hydrogen-Forming Recombinant Escherichia Coli. *ChemBioChem* **2020**, *21* (23), 3389–3397. https://doi.org/10.1002/cbic.202000383.

(127) Jiang, Z.; Wang, B.; Yu, J. C.; Wang, J.; An, T.; Zhao, H.; Li, H.; Yuan, S.; Wong, P. K. AglnS2/In2S3 Heterostructure Sensitization of Escherichia Coli for Sustainable Hydrogen Production. *Nano Energy* **2018**, *46* (January), 234–240. https://doi.org/10.1016/j.nanoen.2018.02.001.

(128) Cui, S.; Tian, L. J.; Li, J.; Wang, X. M.; Liu, H. Q.; Fu, X. Z.; He, R. L.; Lam, P. K. S.; Huang, T. Y.; Li, W. W. Light-Assisted Fermentative Hydrogen Production in an Intimately-Coupled Inorganic-Bio Hybrid with Self-Assembled Nanoparticles. *Chem. Eng. J.* **2022**, *428* (May 2021). https://doi.org/10.1016/j.cej.2021.131254.

(129) Honda, Y.; Watanabe, M.; Hagiwara, H.; Ida, S.; Ishihara, T. Inorganic/Whole-Cell Biohybrid Photocatalyst for Highly Efficient Hydrogen Production from Water. *Appl. Catal. B Environ.* **2017**, *210*, 400–406. https://doi.org/10.1016/j.apcatb.2017.04.015.

(130) Ramprakash, B.; Incharoensakdi, A. Light-Driven Biological Hydrogen Production by Escherichia Coli Mediated by TiO2 Nanoparticles. *Int. J. Hydrogen Energy* **2020**, *45* (11), 6254–6261. https://doi.org/10.1016/j.ijhydene.2020.01.011.

(131) Xiao, K.; Tsang, T. H.; Sun, D.; Liang, J.; Zhao, H.; Jiang, Z.; Wang, B.; Yu, J. C.; Wong, P. K. Interfacing Iodine-Doped Hydrothermally Carbonized Carbon with Escherichia Coli through an "Add-on" Mode for Enhanced Light-Driven Hydrogen Production. *Adv. Energy Mater.* **2021**, *11* (21), 1–13. https://doi.org/10.1002/aenm.202100291.

(132) Sharma, S.; Shukla, P.; Misra, A.; Mishra, P. R. Chapter 8 - Interfacial and Colloidal Properties of Emulsified Systems: Pharmaceutical and Biological Perspective; Ohshima, H., Makino, K. B. T.-C. and I. S. in P. R. and D., Eds.; Elsevier: Amsterdam, 2014; pp 149–172. https://doi.org/https://doi.org/10.1016/B978-0-444-62614-1.00008-9.

(133) von Smoluchowski, M. Contribution à La Théorie de l'endosmose Électrique et de Quelques Phénomènes Corrélatifs. *Bull. Akad. Sci. Cracovie.* **1903**, *8*, 182–200.

(134) Winter, W. T. Measurement of Suspended Particles by Quasi-Elastic Light Scattering, Barton E. Dahneke, Ed., Wiley, New York, 1983, 570 Pp. Price:$39.95. *J. Polym. Sci. Polym. Lett. Ed.* **1983**, *21* (12), 1020. https://doi.org/https://doi.org/10.1002/pol.1983.130211210.

(135) Lunardi, C. N.; Gomes, A. J.; Rocha, F. S.; De Tommaso, J.; Patience, G. S. Experimental Methods in Chemical Engineering: Zeta Potential. *Can. J. Chem. Eng.* **2021**, *99* (3), 627–639. https://doi.org/10.1002/cjce.23914.

(136) Gittings, M. R.; Saville, D. A. The Determination of Hydrodynamic Size and Zeta Potential from Electrophoretic Mobility and Light Scattering Measurements. *Colloids Surfaces A Physicochem. Eng. Asp.* **1998**, *141* (1), 111–117.

(137) Leroy, P.; Tournassat, C.; Bizi, M. Influence of Surface Conductivity on the Apparent Zeta Potential of TiO2 Nanoparticles. *J. Colloid Interface Sci.* **2011**, *356* (2), 442–453. https://doi.org/10.1016/j.jcis.2011.01.016.

(138) Delgado, A.; González-Caballero, F.; Salcedo, J. On the Zeta Potential of Spherical Polystyrene Particles from Electrophoresis Theories. *Acta Polym.* **1986**, *37* (6), 361–364. https://doi.org/https://doi.org/10.1002/actp.1986.010370608.

(139) Henry, D. C.; Lapworth, A. The Cataphoresis of Suspended Particles. Part I.—The Equation of Cataphoresis. *Proc. R. Soc. London. Ser. A, Contain. Pap. a Math. Phys. Character* **1997**, *133* (821), 106–129. https://doi.org/10.1098/rspa.1931.0133.

(140) Ohshima, H. Electrophoretic Mobility of a Cylindrical Colloidal Particle in a Salt-Free Medium. *J. Colloid Interface Sci.* **2002**, *255* (1), 202–207. https://doi.org/https://doi.org/10.1006/jcis.2002.8650.

(141) Time-Domain Lifetime Measurements BT - Principles of Fluorescence Spectroscopy; Lakowicz, J. R., Ed.; Springer US: Boston, MA, 2006; pp 97–155.

https://doi.org/10.1007/978-0-387-46312-4_4.

(142) Phillips, D.; Drake, R. C.; O'Connor, D. V; Christensen, R. L. Time Correlated Single-Photon Counting (Tcspc) Using Laser Excitation. *Instrum. Sci. Technol.* **1985**, *14* (3–4), 267–292. https://doi.org/10.1080/10739148508543581.

(143) Sillen, A.; Engelborghs, Y. The Correct Use of "Average" Fluorescence Parameters. *Photochem. Photobiol.* **1998**, *67* (5), 475–486.

(144) Li, C.; Cowan, A. J.; Gardner, A. M. Transient Absorption Spectroscopic Studies of Linear Polymeric Photocatalysts for Solar Fuel Generation. *Chem. Phys. Rev.* **2022**, *3* (3), 031304. https://doi.org/10.1063/5.0098274.

(145) Ha-Thi, M.-H.; Burdzinski, G.; Pino, T.; Changenet, P. Transient Absorption Spectroscopy in Inorganic Systems BT - Springer Handbook of Inorganic Photochemistry; Bahnemann, D., Patrocinio, A. O. T., Eds.; Springer International Publishing: Cham, 2022; pp 107–130. https://doi.org/10.1007/978-3-030-63713-2_5.

(146) Saleh, B. E. A.; Teich, M. C. *Fundamentals of Photonics*; john Wiley & sons, 2019.

(147) Berera, R.; van Grondelle, R.; Kennis, J. T. M. Ultrafast Transient Absorption Spectroscopy: Principles and Application to Photosynthetic Systems. *Photosynth. Res.* **2009**, *101* (2), 105–118. https://doi.org/10.1007/s11120-009-9454-y.

(148) Abbruzzetti, S.; Bruno, S.; Faggiano, S.; Grandi, E.; Mozzarelli, A.; Viappiani, C. Time-Resolved Methods in Biophysics. 2. Monitoring Haem Proteins at Work with Nanosecond Laser Flash Photolysis. *Photochem. Photobiol. Sci.* **2006**, *5*, 1109–1120.

(149) Forster, M.; Cheung, D. W. F.; Gardner, A. M.; Cowan, A. J. Potential and Pitfalls: On the Use of Transient Absorption Spectroscopy for in Situ and Operando Studies of Photoelectrodes. *J. Chem. Phys.* **2020**, *153* (15), 150901.

(150) Xu, J.-Y.; Tong, X.; Yu, P.; Wenya, G. E.; McGrath, T.; Fong, M. J.; Wu, J.; Wang, Z. M. Ultrafast Dynamics of Charge Transfer and Photochemical Reactions in Solar Energy Conversion. *Adv. Sci.* **2018**, *5* (12), 1800221. https://doi.org/https://doi.org/10.1002/advs.201800221.

(151) Woods, D. J.; Sprick, R. S.; Smith, C. L.; Cowan, A. J.; Cooper, A. I. A Solution-Processable Polymer Photocatalyst for Hydrogen Evolution from Water. *Adv. Energy Mater.* **2017**, *7* (22), 1–6. https://doi.org/10.1002/aenm.201700479.

(152) Aitchison, C. M.; Sprick, R. S. Conjugated Nanomaterials for Solar Fuel Production. *Nanoscale* **2021**, *13*, 634–646. https://doi.org/10.1039/D0NR07533G.

(153) Holá, K.; Pavliuk, M. V; Németh, B.; Huang, P.; Zdražil, L.; Land, H.; Berggren, G.; Tian, H. Carbon Dots and [FeFe] Hydrogenase Biohybrid Assemblies for Efficient Light-Driven Hydrogen Evolution. *ACS Catal.* **2020**, *10* (17), 9943–9952. https://doi.org/10.1021/acscatal.0c02474.

Chapter 2 :

Cationic Conjugated Polymer Photocatalysts

All polymers and nanoparticles of polymers in this chapter were prepared by the thesis author. Gel permeation chromatography (GPC) was performed by Dr Steven Robinson, Photoelectron spectroscopy in air (PESA) measurements were carried out by Sylwia Adamczyk. Time-dependent density functional theory ((TD)-DFT) calculations were performed by Dr Martijn Zwijnenburg.

2.1 Background

In this chapter, firstly two series of polymers with fluorene-phenylene (LP1) and fluorene (LP5) backbones were synthesized. For the fluorene series, the cationic group density (χ) was altered by the introduction of a third diluent monomer (2,7-dibromo-9,9-bis(8-octyl)-fluorene (M1') and 9,9-dioctyl-9*H*-fluorene-2,7-diboronic acid bis(pinacol) ester (M2') to obtain polymer LP5_χ (χ = 0.10, 0.25, 0.50) as shown in **Figure 2.1**. Furthermore, building on experience with conjugated polymers that act as photocatalysts for sacrificial hydrogen production from water in conjunction with palladium, a series of co-polymers of bis(8-bromo-n-octyl)-fluorene with thiophene (LP2), 2,2'-bithiophene (LP3), and dibenzo[*b*,*d*]thiophene sulfone (LP4) were prepared.

All the polymers were synthesized by Pd (0)-catalysed Suzuki–Miyaura-type coupling reactions and the products were purified by Soxhlet extraction, followed by reprecipitation from chloroform in methanol. Polymers produced through Suzuki coupling showed relatively good reproducibility which can be told from their NMR spectra and UV-absorption spectra, but the amount of residual of Pd might not be the same from different batches. Therefore, it is important to keep using the same batch of polymers for good comparison. The polymers were then self-assembled into polymer nanoparticles in water by reprecipitation methods.[1,2] Photocatalytic experiments of these conjugated polymer nanoparticles for hydrogen evolution were then explored.

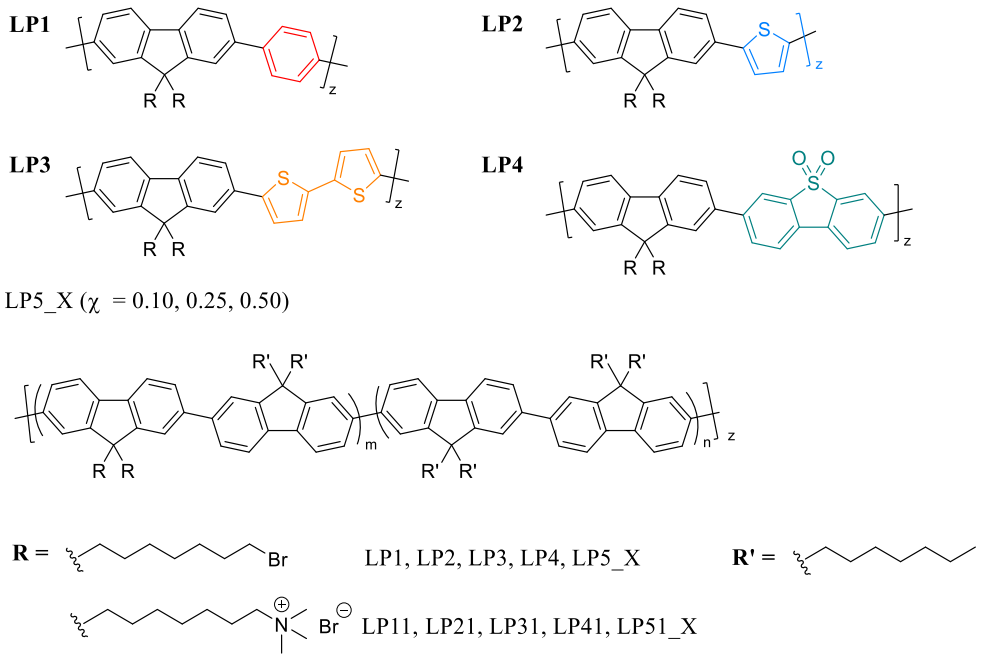

Figure 2.1 Chemical structures of conjugated linear polymers in this chapter.

2.2 Incorporation of Cationic Property in Fluorene-Phenyl Polymer Photocatalysts

2.2.1 Synthesis

2.2.1.1 Monomer Synthesis

The monomer 2,7-dibromo-9,9-bis(8-bromo-n-octyl)-fluorene (M1) was synthesized following a previously reported procedure by a nucleophilic substitution reaction (S_N2).[3] The deprotonation of dibromofluorene by NaOH formed the nucleophile ion (Nu^-), and the nucleophile ion attacked the δ^+ carbon in the electrophile and firmly attached to the carbon, and the bromine was expelled as a Br^- ion. The Br^- ion combined with Na^+ ion in the reaction mixture to form NaBr. The electronegative atom or the leaving group of electrophiles could be oxygen, nitrogen, sulfur, or a halogen, and their pK_b values can be used to evaluate the approximate leaving group ability.

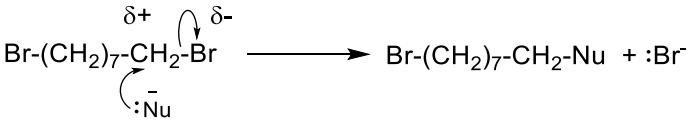

2.1

2.2.1.2 Polymer Synthesis

Polymer LP1 was synthesized via Suzuki-Miyaura polycondensation using a literature-reported procedure.[4] Suzuki-Miyaura coupling (or Suzuki coupling) is a metal catalysed reaction between an aryl, alkene (vinyl), or alkyne organoborane (boronic acid or boronic ester) and halide or triflate under basic conditions, as described in **Figure 2.2**.[5]

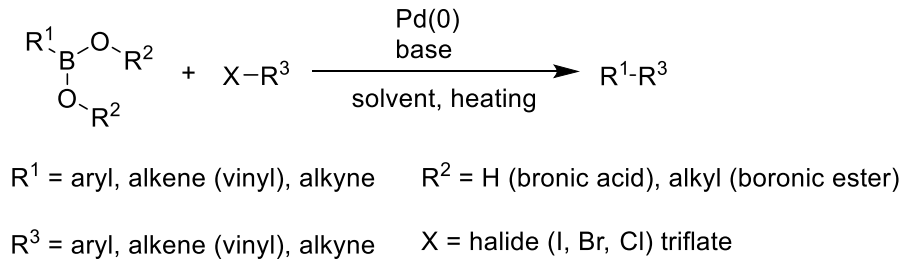

Figure 2.2 General reaction scheme of Suzuki coupling reaction.

The general catalytic cycle for Suzuki cross-coupling involves three fundamental steps: oxidative addition, transmetalation, and reductive elimination as shown in **Figure 2.3**.[6] The oxidative addition of aryl halides to Pd (0) complex gives intermediate 1 (Pd(II) species). Under basic condition, an organoborane compound reacts with intermediate 1 in transmetalation to

give intermediate 2. And this is followed by reductive elimination to give the product and regenerate the original Pd (0) species. Phosphine ligands, such as PPh_3, are the most popular Pd ligands in both the laboratory and industry.

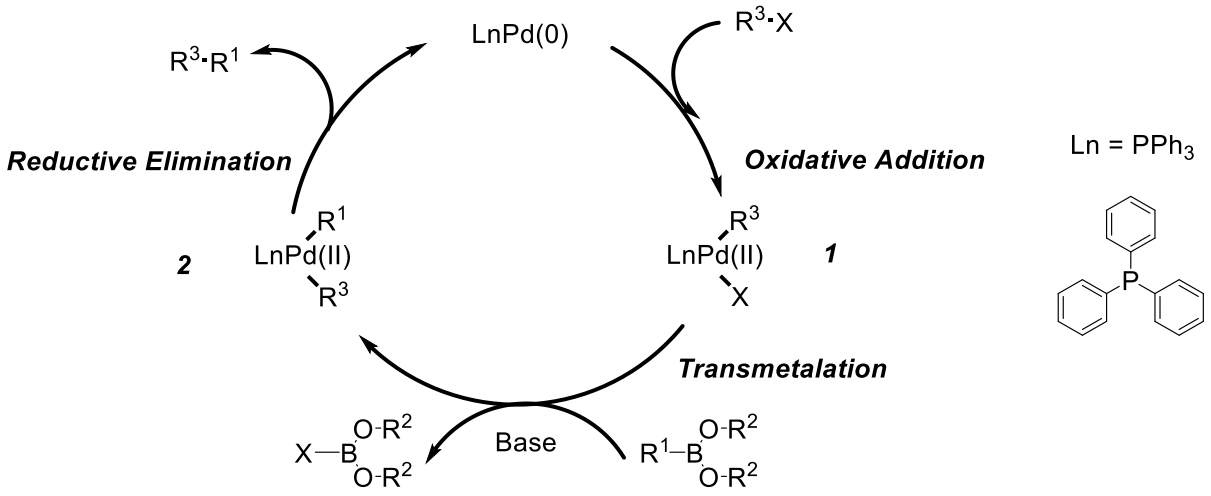

Figure 2.3 General catalytic cycle for Suzuki coupling reaction.

The oxidative addition of 2,7-dibromo-9,9-bis(8-bromo-n-octyl)-fluorene (M1) to Pd(0) complex [$Pd(PPh_3)_4$] was the initial step to give intermediate 1, a Pd(II) species. Under the participation of Na_2CO_3, 1,4-benzene boronic acid bis(pinacol) ester reacted with intermediate 1 in trans-metalation to afford intermediate 2. This was followed by reductive elimination to give the polymer LP1 and regenerated the original Pd (0) species. Polymer LP1 was then modified through polymer-analogous reactions on the alkyl-bromo functional groups giving a trimethylammonium-substituted polymer LP11.

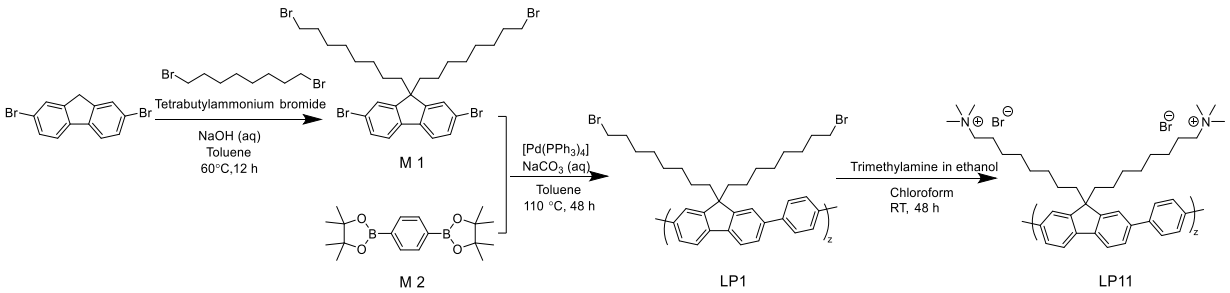

Figure 2.4 Synthetic route to 2,7-dibromo-9,9-bis(8-bromo-n-octyl)-fluorene monomer (M1) and polymerisation of LP1 and LP11.

Polymer FP-Oct was a reported polymer[4] and synthesized as shown in **Figure 2.5**.

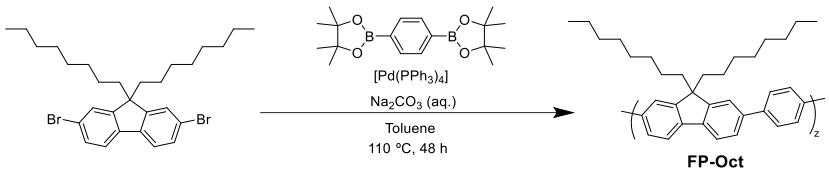

Figure 2.5 Synthetic route of polymer FP-Oct.

2.2.1.2 Polymer Nanoparticle Preparation

The polymers were then self-assembled into polymer nanoparticles in water through nanoprecipitation (or direct injection) method.[1] The process generally involves three steps: (i) the dissolution of polymer in a good solvent (THF in this work); (ii) the addition of a poor solvent (normally water); (iii) the removal of the good solvent by evaporation under sonication or stirring.[7] When the polymer-solvent solution is injected into an aqueous solution, the polymer becomes insoluble due to the increase of interfacial tension between the polymer and surrounding water molecules.[8] This triggers the self-assembly of polymer particles. Particle size can be controlled by changing the preparation conditions including the solution concentration and the mixing ratio between the good and poor solvents. Furthermore, hydrodynamic shear (during sonication or stirring), polymer chain conformation in the good solvent, and polymer precipitation rate will all affect the resulting colloidal morphologies.[9]

2.2.2 Characterization

The materials were subsequently characterized via ^{1}H NMR, microanalysis, thermogravimetric analysis (TGA), gel permeation chromatography (GPC), ultraviolet-visible (UV-Vis), and photoluminescence spectroscopy.

GPC results in **Table 2.1** and **Figure 2.6** showed their number-average molecular weight (M_n) of 26,400 for FP-Oct and 15,400 for LP1 with dispersity index (Đ) of 2.0 and 1.9 respectively.

Table 2.1 GPC data for all chloroform-soluble polymer fractions.

Polymer	M_n[a] / g mol^{-1}	M_w[a] / g mol^{-1}	Đ[b]
FP-Oct	26,400	52,700	2.0
LP1	15,400	30,600	1.9

a. Obtained from gel permeation chromatography in chloroform (FP-Oct) and THF (LP1) calibrated against polystyrene standards; M_n: the number-weighted molecular weight, M_w: the mass-weighted molecular weight; b. Dispersity, Đ = M_w/M_n.

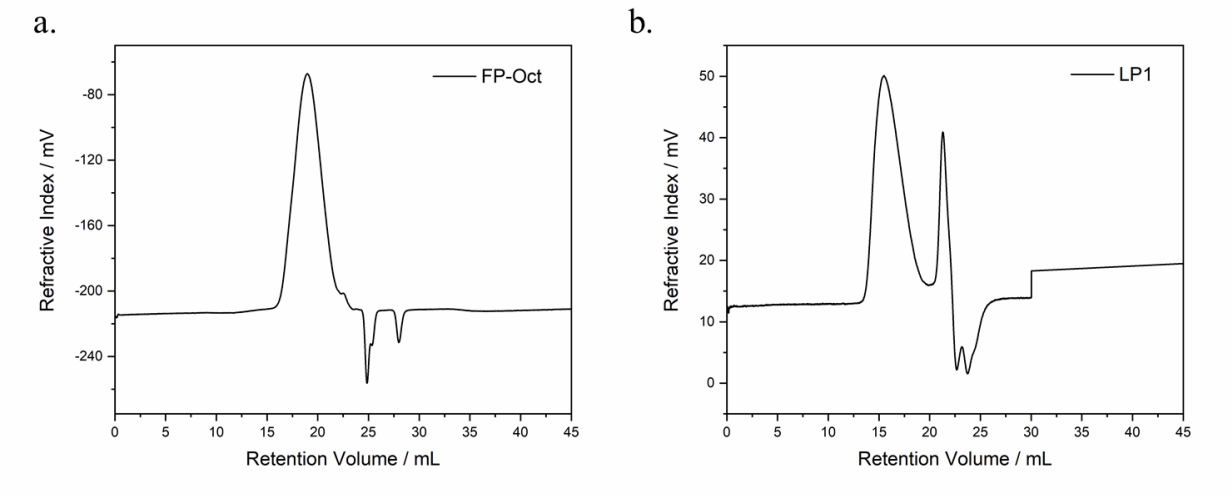

Figure 2.6 Chromatogram of polymer (a) FP-Oct and (b) LP1.

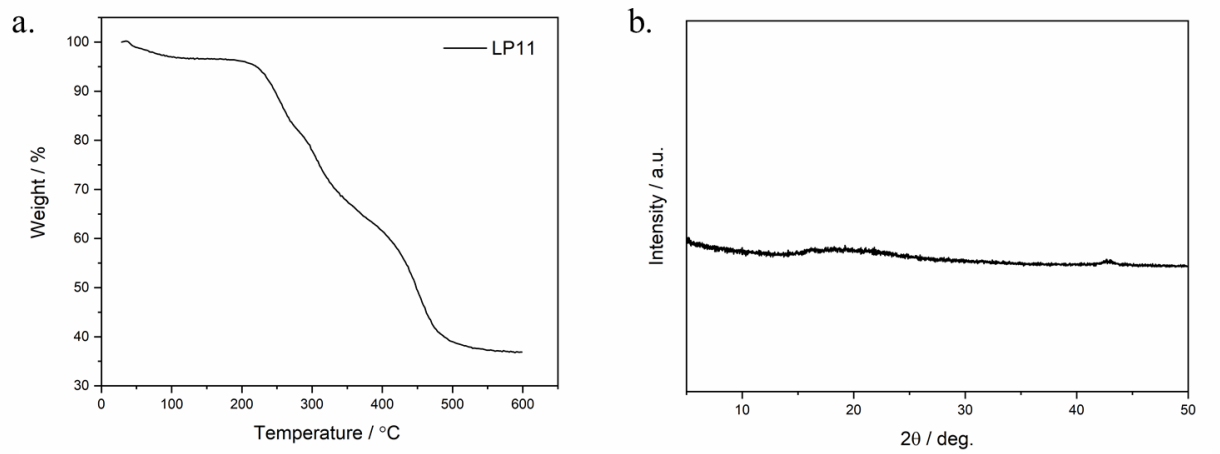

Figure 2.7 (a) Thermogravimetric analysis of LP11 under nitrogen at a heating rate of 10 °C min^{-1}. (b) PXRD patterns of powders of polymer LP11.

TGA showing the thermal decomposition of LP11 in **Figure 2.7a.** The polymer begins decomposition at around 203 °C (with a small amount of H_2O loss at lower temperatures), leaving a ~35% residual at 600 °C. The first mass loss corresponds to the loss of methyl bromide,[10,11] and the second (onset decomposition temperature at around 300 °C) is due to side chain cleavage, which is typically observed in polyfluorenes with solubilising side-chains.[12,13] Polymer FP-Oct was reported to exhibit thermal stability up to temperature over 300 °C under air, when decomposition starts to occur.[4] The thermal stability of these polymers confirms they are suitable for application in the mild temperatures required for photocatalytic hydrogen evolution.

In addition, the powder X-ray diffraction (PXRD) pattern of LP11 appears to be no crystalline in **Figure 2.7b**.

The photophysical properties of these two polymers were studied by UV-vis absorption and photoluminescence (PL) spectroscopy as shown in **Figure 2.8**. The absorption band of polymer FP-Oct is centred at 380 nm (λ_{max}), ascribing to π–π* transition of the polymer backbone.[14] However, when substituted by trimethylamine, the λ_{max} of polymer LP11 blueshifts to 355 nm, which might correspond to a conformation change.[15] It was reported that an increased torsional angle between adjacent rings would result in a hypochromic (blue) shift in the π–π* transition.[16] It is possible that, for polymer LP11 in chloroform, the mutual repulsion of positive charges housed on alternate rings leads to the lowest energy conformation where the torsional angle is increased.[16] In addition, polymer FP-Oct and LP11 exhibit similar emission spectra in **Figure 2.8b**.

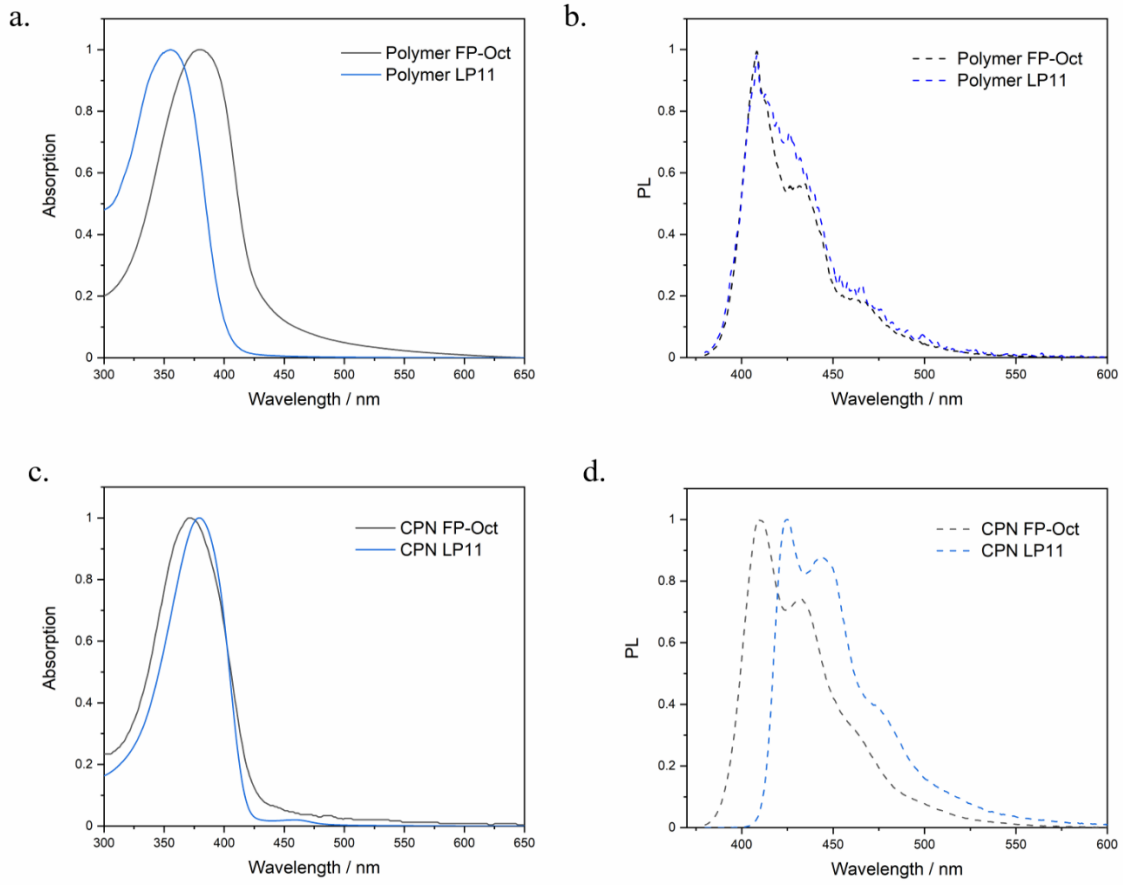

Figure 2.8 (a) Normalised UV-vis and (b) PL spectra of polymer FP-Oct and LP11 dissolved in chloroform. (c) UV-vis and (d) PL spectra of polymer nanoparticle FP-Oct and LP11 in aqueous solution.

Another feature was observed in a comparison of the absorption spectra of FP-Oct in chloroform and the nanoparticles (CPN FP-Oct) in an aqueous solution. As indicated in **Figure 2.8c**, the absorption spectrum of the nanoparticle FP-Oct blueshifted (λ_{max} 370 nm) as

compared to that of polymer FP-Oct in chloroform (λ_{max} 380 nm). The blueshifted absorption peak is attributed to a reduction of the conjugation length caused by kinks and bends of the polymer backbones as the polymer is constrained into a small volume and is believed to adopt a collapsed conformation.[2,17] However, the λ_{max} of the LP11 nanoparticle redshifted from 355 nm to 370 nm which might be due to the dominant solvatochromism effect on the λ_{max} of the π–π^* transition. It is caused by attractive polarisation forces between the solvent (water) and the solute (LP11), which lower the energy level of both the excited and unexcited states. This effect is greater for the excited state, and so the energy difference between the excited and unexcited states is slightly reduced resulting in a redshift.[18] This effect could also be found in the emission spectra in **Figure 2.8d** where nanoparticle LP11 showed a redshift compared with polymer LP11 in chloroform.

Table 2.2 Particle average size and zeta-potential (polymer conc. 50 mg L^{-1}) by dynamic light scattering.

Polymer	Average size / nm	PDI[a]	Zeta-potential / mV
FP-Oct	597	0.562	n/a
LP11	151	0.334	34.5 ± 5.76 mV

a. PDI: polydispersity index. n/a: not applicable.

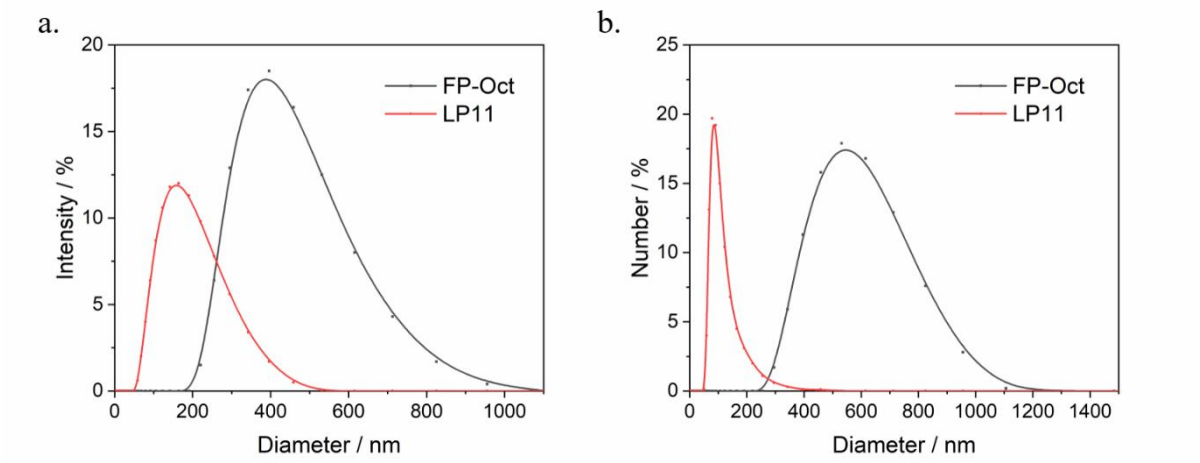

Figure 2.9 Size distribution of nanoparticles of polymer FP-Oct and LP11 with 50 mg/L polymer concentration by (a) intensity and (b) number.

Dynamic light scattering measurements showed that nanoparticles of cationic polymer LP11 have a much smaller average size (151 nm) compared with non-charged one FP-Oct (597 nm) as described in **Table 2.2,** which might be partly attributed to the better dispersibility of LP11 in water.[11] For the reprecipitation method, the nanoparticle size is adjustable primarily via the concentration of the organic polymer solution. The mechanism of the colloidal stabilization of the nanoparticles especially for non-charged polymers remains unclear in this particular case, as no surfactant was added and the polymer contains no significantly hydrophilic moieties. By using very dilute polymer concentration (5 mg/L), smaller polymer FP-Oct particle could also be obtained as shown in **Figure 2.10**. In addition, the charge accumulated at the particle-dispersing medium interface may contribute to stabilization towards particle aggregation and coalescence. Therefore, the quaternary ammonium functional group which gives the nanoparticle cationic property with a zeta-potential of 34 mV could inhibit nanoparticle aggregation through electrostatic repulsion between each particle.[19] In addition, as the polymer chains are suggested to possess a collapsed conformation in these particles, using this method, it is possible to tune the size of nanoparticles by using polymers with appropriate molecular weights. For example, nanoparticles were produced with a 5-10 nm diameter containing a single polymer chain.[19]

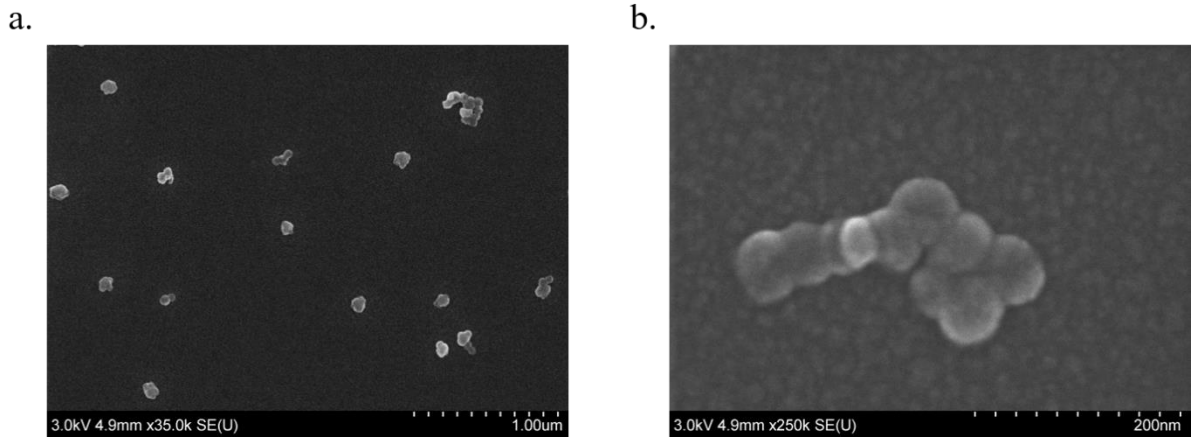

Figure 2.10 SEM images of polymer FP-Oct nanoparticle with 5 mg/L polymer concentration.

2.2.3 Photocatalytic Hydrogen Evolution Performance

Photocatalytic hydrogen evolution experiments were performed using ascorbic acid (0.2 M) as a sacrificial electron donor under irradiation of a solar simulator. The hydrogen evolution rates (HERs) of 0.017 and 0.298 μmol h^{-1} were observed for nanoparticles of FP-Oct and LP11 respectively, as shown in **Table 2.3**. In comparison, FP-Oct showed a relatively lower HER, which can mainly be ascribed to its large particle size. A study on fluorene-type co-polymers

has shown that particle size was a dominant factor of importance for their activity, with materials that consist of large particles being less active.[20] The reason for an activity-size effect in polymer photocatalysts is the fact that exciton diffusion lengths are typically shorter (10 s of nm) than the length scales over which light can penetrate organic semiconductors (100 s of nm).[21] In bulk materials (typically μm scale) or particles of semiconductors with a broad size distribution, excitons generated within the materials are further away from the interface than their exciton diffusion length. These excitons relax to the ground state before reaching the particle surface and therefore cannot contribute to catalysis.[22]

Table 2.3 Dispersion in water, optical properties as well as HERs of nanoparticles of polymer FP-Oct and LP11.

	Dispersion in water	**λ_{onset}[a] / nm**	**Optical gap[b] / eV**	**HER[c] / μmol h^{-1}**
FP-Oct	Poor	417	2.98	0.017 ± 0.01
LP11	Good	422	2.93	0.298 ± 0.03

a. Absorption onset wavelength of polymer nanoparticles; b. The optical gap (E_g^{opt}) was calculated from the absorption onset of polymer nanoparticles ($E_g^{opt} = hc \approx 1240/\lambda_{onset}$, *h*: Planck's constant, c: the speed of light); c. HERs with 0.2 M ascorbic acid as a sacrificial electron donor. Samples were illuminated for 2 h using a solar simulator (AM1.5G, 1 sun). 0.25 mg polymer in each sample (5.0 mL polymer nanoparticle solution with 50 mg/L polymer concentration).

Polymer FP-Oct and LP1 have the same backbone structure and nanoparticles of these two polymers share similar absorption profiles, resulting in similar optical gaps (2.98 and 2.93 eV respectively, **Table 2.3**) and the same predicted charge carrier (IP, ionization potential; EA, electron affinity) potentials in **Table 2.4**. Therefore, the driving force for both the proton reduction and sacrificial electron donor oxidation is supposed to be the same for polymer FP-Oct and LP11. The oxidation potential of ascorbic acid as the sacrificial donor was listed in **Table 2.5**. H_2A designates plain ascorbic acid, and HA^- is the predominant form within the usual pH window for a photocatalysis system (between 5 and 9). HA^- is first oxidized to HA*, which is a much stronger acid[23] than HA^-, and then HA* quickly dissociates into A^{*-} and H^+.[24] A^{*-} then disproportionates into dehydroascorbic acid (A) and ascorbate (A^{2-}).[25]

Table 2.4 Predicted charge carrier (IP, EA) potentials of polymers considered calculated through (TD-)B3LYP for oligomer models in water (ε_r 80.1) and PESA (ε_r 2). LP1 data for polymer in water taken from previous work. Ref. [19]

	Water condition IP vs. SHE / V	**Water condition EA vs. SHE / V**	**PESA condition IP vs. SHE / V**
FP-Oct/LP1	0.73	-2.38	1.19

Table 2.5 Predicted potentials for the different solution half-reactions at pH 0. Ascorbic acid* (HA*) and dehydroascorbic acid (A) are the one-hole and two-hole oxidation products of ascorbic acid, respectively,

Solution half-reaction	Potential (V vs. SHE) pH 0
H+ (aq) + e- -> 1/2 H_2 (g)	0
Ascorbic acid* (aq) + H^+ (aq) + e- -> Ascorbic acid (aq)	0.755[a]
Dehydroascorbic acid + 2 H^+ (aq) + 2e- -> Ascorbic acid (aq)	0.524[a]

a. Values published vs. SCE (Saturated Calomel Electrode)[26], obtained vs. SHE (Standard Hydrogen Electrode) by adding 0.244 V.

2.2.4 Summary

A hydrogen evolution rate of 0.298 μmol/h^{-1} was achieved under a solar simulator for 0.25 mg polymer LP11, which was a dramatic increase (>15 times) in comparison with polymer FP-Oct (0.017 μmol/h^{-1}) with the same backbone structure. It shows that particle size is a dominant factor here, with materials that consist of large particles being less active. The nanoparticles of cationic conjugated polymer could inhibit particle aggregation through electrostatic repulsion, which gives a much narrower size distribution.

2.3 Cationic Group Ratio Variation in Solution-Processable Conjugated Polymer Photocatalysts

2.3.1 Synthesis

Firstly, to explore the potential of cationic conjugated polymers as photocatalysts, another series of polymers with fluorene backbones was synthesized. Secondly, within this series, an *n*-octyl-trimethylamine side-chain was utilized (**Figure 2.11**) and the cationic group density was altered by the introduction of a third diluent monomer (2,7-dibromo-9,9-bis(8-octyl)-fluorene (M1') and 9,9-dioctyl-9*H*-fluorene-2,7-diboronic acid bis(pinacol) ester (M2') as shown in **Table 2.6**. All the polymers were synthesized by Pd (0)-catalyzed Suzuki–Miyaura-type coupling reactions and the products were purified by Soxhlet extraction, followed by reprecipitation from chloroform in methanol. The polymers were then self-assembled into polymer nanoparticles in water by reprecipitation methods.[1,2]

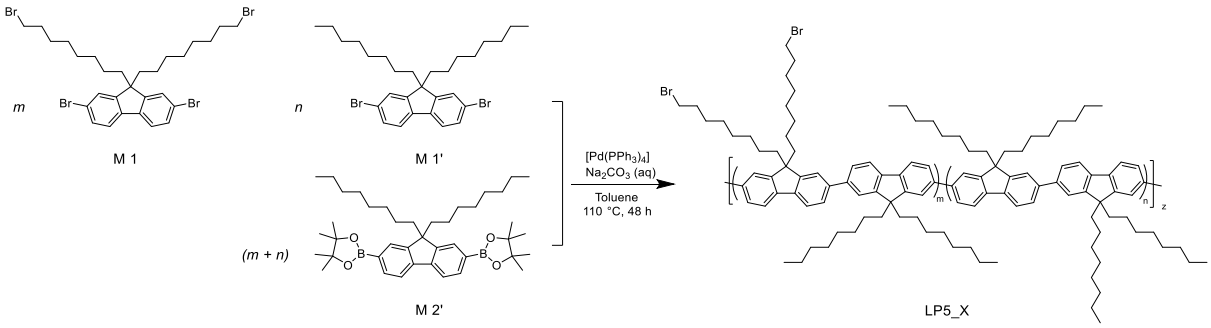

Figure 2.11 Synthetic route to polymerisation of LP5_χ.

Table 2.6 Synthesis of LP5_χ.

	LP5_0.10	LP5_0.25	LP5_0.50
M1 / mmol	0.32	0.8	1.6
M1' / mmol	1.28	0.8	0
M2' / mmol	1.6	1.6	1.6
χ^a	0.10	0.25	0.50
χ^b	0.075	0.22	0.50

a. molar ratio of dibromo groups to aromatic rings, $\chi = m/2(m+n)$. b. the actual molar ratio of dibromo groups to aromatic rings calculated by NMR.

2.3.2 Characterization

The polymers were subsequently characterized via ^{1}H NMR, microanalysis, TGA, GPC, and UV-Vis spectroscopy.

GPC showed that the polymers had number weighted molecular weights between 11,400 to 70,000 g mol^{-1} (**Table 2.7**).

Table 2.7 GPC data for all chloroform-soluble polymer fractions.

Polymer	M_n[a] / g mol^{-1}	M_w[a] / g mol^{-1}	Đ[b]
LP5_0.10	11,400	18,400	1.6
LP5_0.25	70,000	177,000	2.5
LP5_0.50	18,300	26,000	1.4

a. Obtained from gel permeation chromatography in THF calibrated against polystyrene standards; M_n: the number-weighted molecular weight, M_w: the mass-weighted molecular weight; b. Dispersity, Đ = M_w/M_n.

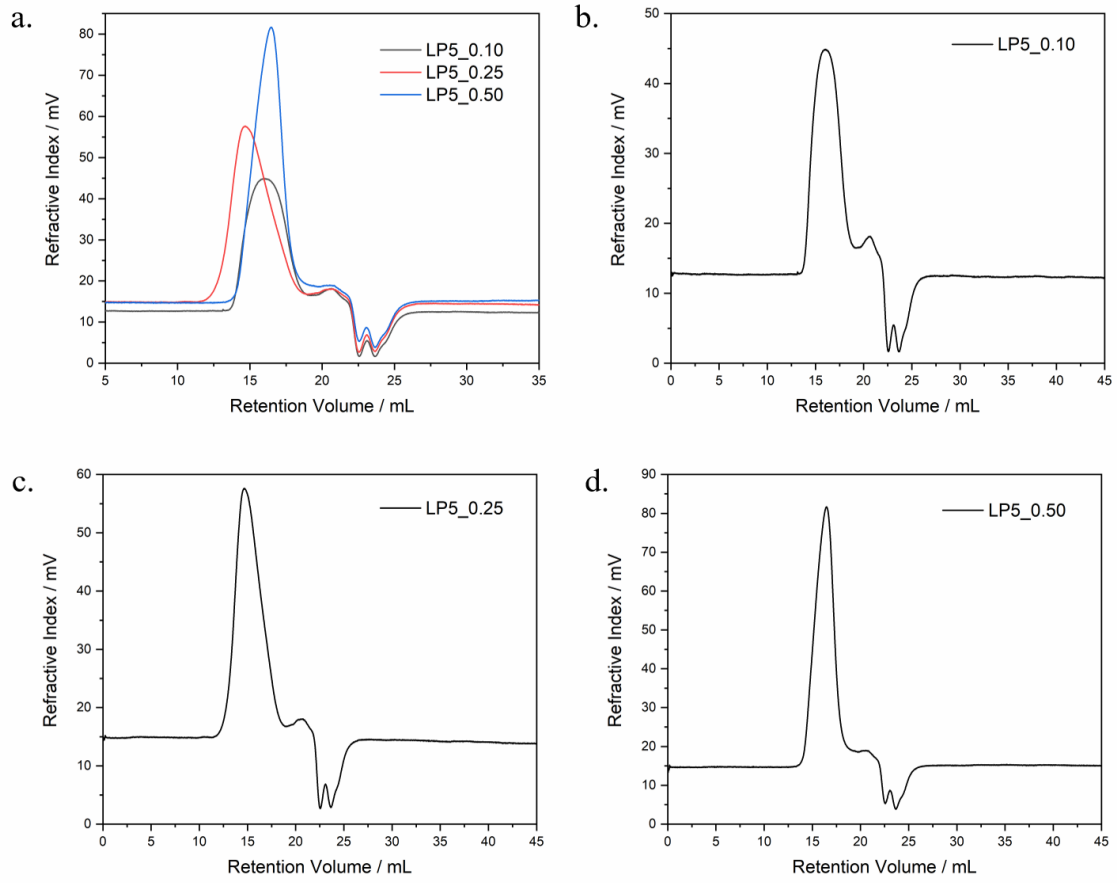

Figure 2.12 Chromatogram of polymer (b) LP5_0.10, (c) LP5_0.25, and (d) LP5_0.50.

The TGA thermogram for all three polymers has two major mass losses as shown in **Figure 2.13**. As the first major decomposition was aligned to loss of methyl bromide,[11,16] the first mass loss percentage of each polymer is consistent with their cationic group ratios with ~20% for LP51_0.50 (onset decomposition temperature ~174°C), ~10% for LP51_0.25 (onset decomposition temperature ~204°C), and ~6% for LP51_0.10 (onset decomposition temperature ~208°C). The second mass change was supposed to be due to cleavage of side

chains[11,16] with onset decomposition temperatures of ~300 °C for LP51_50, ~210 °C for LP51_0.25, and ~260 °C for LP51_0.10

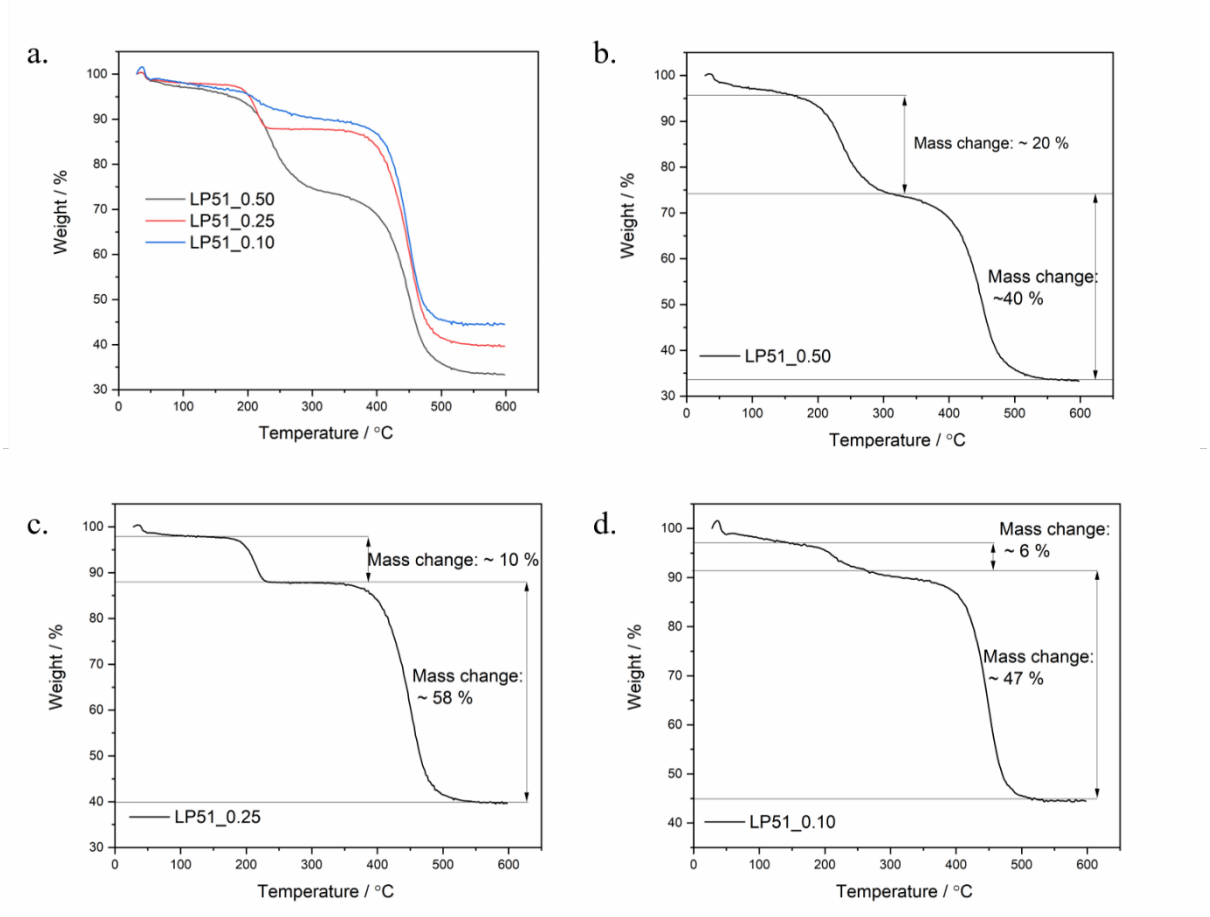

Figure 2.13 Thermogravimetric analysis of LP51_0.50, 0.25 and 0.10 under nitrogen at a heating rate of 10 °C min^{-1} with major mass changes of (b) LP51_0.50, (c) LP51_0.25, and (d) LP51_0.10.

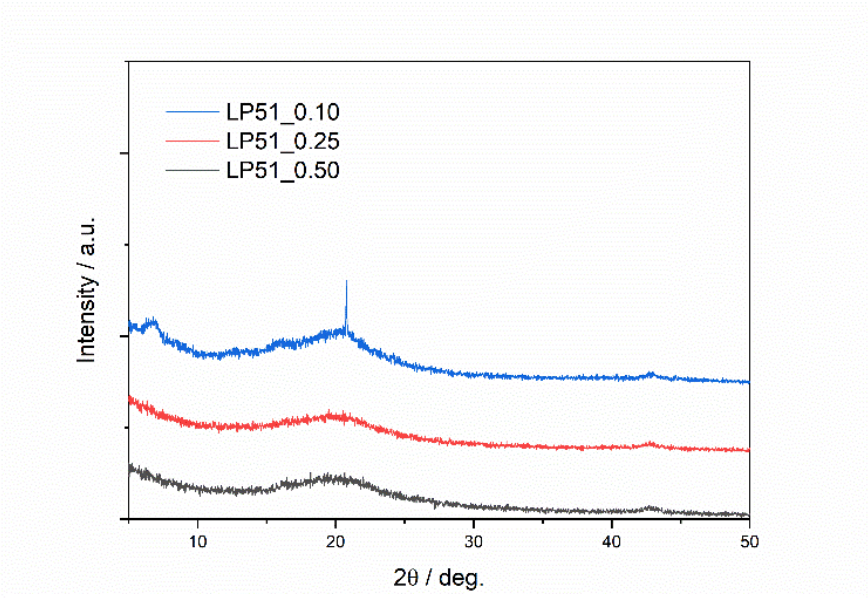

Figure 2.14 PXRD patterns of powders of polymer LP51_0.10, 0.25, and 0.50.

The PXRD patterns of LP51 series in **Figure 2.14** all appear to be non-crystalline.

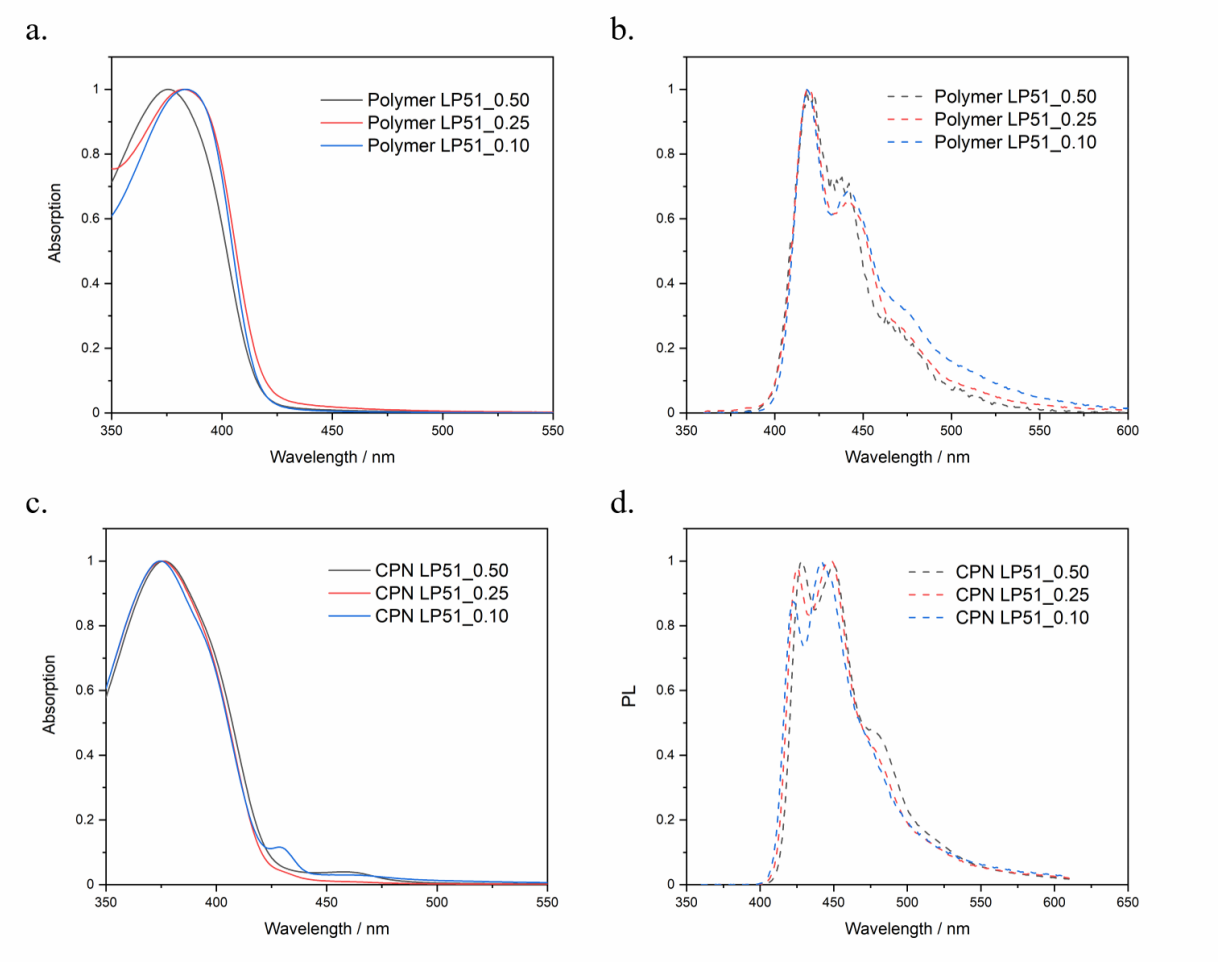

Figure 2.15 (a) Normalised UV-vis and (b) PL spectra of polymer LP51_0.50, 0.25, and 0.10 in chloroform. (c) UV-vis and (d) PL spectra of polymer nanoparticle LP51_0.50, 0.25, and 0.10 in aqueous solution.

All materials absorb visible light with LP51_0.50 showing the most blueshifted absorption onset followed by LP51_0.25 and LP51_0.10 (**Figure 2.15a**) resulting from the conformation changes by introducing different ratios of cationic end-groups in the side chain as in LP11.[16] In addition, absorption spectra of nanoparticles blueshifted compared to that of polymers in chloroform solution as expected due to the decreased polymer conjugation length after fabrication into nanoparticles (**Figure 2.15 c**).[17] Besides, there is a shoulder at $\lambda = 430$ nm for nanoparticle of LP51_0.10, which is indicative of the partial formation of β-phase and that was found in other polyfluorene nanoparticles as well.[17,27] β-phase is a phase with extended chain conformation,[28] and it appears to be populated by a single compact structural isomer.[29] Recent studies have demonstrated that there are 3 distinguishable classes of conformational isomers with different chain torsional angles for poly(9,9-dioctylfluorene).[30] These classes have been termed the α-phase, the β-phase and the γ-phase. The nanoparticle preparation method involves

the rapid addition of a dilute solution of hydrophobic conjugated polymer dissolved in a water-miscible organic solvent (THF) to water. The addition of organic solvent to the aqueous suspension could result in the formation of β-phase, presumably by solvent-induced swelling, which facilitates the formation of the thermodynamically favoured β-phase.[31] Polyfluorenes with poly(ethylene glycol) (PEG) side-chains have been shown to reduce the formation of a β-phase in comparison to alkylated polymers as a result of improving compatibility with water,[32] and it might also explain why it was not observed in nanoparticles of LP51_0.25 and 0.50 that with higher cationic end-group ratios. All polymers and polymer nanoparticles also exhibit similar emission profiles and display minimal variations across both series (polymer in chloroform and nanoparticle in aqueous solution) as shown in **Figure 2.15b, d.**

Dynamic light scattering measurements showed the average size and size distribution of polymer nanoparticles with varied cationic density in **Table 2.8** and **Figure 2.16**. LP51_0.25 was found to have the broadest size distribution (PDI 0.28) which might be attributed to its higher molecular weight compared with the other two polymers. Zeta-potentials were determined to be between +35-40 mV for all the quaternary ammonium functionalized polymer nanoparticles (**Table 2.8**) with relatively large deviations, especially for LP51_0.10.

Table 2.8 Particle average size and zeta-potential (polymer conc. 50 mg L^{-1}) by dynamic light scattering.

Polymer	Average size / nm	PDI[a]	Zeta-potential / mV
LP5_0.10	106.7	0.198	35.0 ± 9.37
LP5_0.25	100.5	0.282	40.3 ± 5.82
LP5_0.50	100.9	0.132	36.6 ± 3.01

a. PDI: polydispersity index

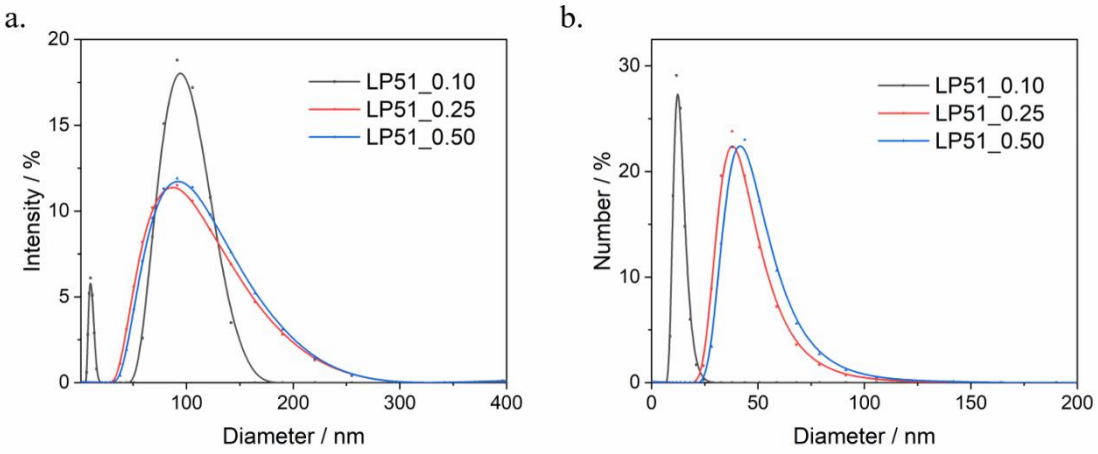

Figure 2.16 Size distribution of nanoparticles of polymer LP51_0.10, 0.25, and 0.50 with 50 mg/L polymer concentration by intensity (a) and number (b).

2.3.3 Photocatalytic Hydrogen Evolution Performance

Photocatalytic hydrogen evolution experiments were performed using ascorbic acid (0.1 M) and TEA/methanol/water (1:1:1) as sacrificial electron donors with 3.0 wt% H_2PtCl_6 as a cocatalyst under irradiation of a solar simulator. The HERs of 0.072, 0.052, and 0.064 μmol h^{-1} were observed for nanoparticles of LP51_0.10, 0.25 and 0.50 respectively with 0.1 M ascorbic acid (AA) as a sacrificial electron donor, as shown in **Figure 2.17**.

However, nanoparticles of these three conjugated polymers obtained much higher photocatalytic activity (>10 times) in the TEA system. In TEA system, the HER is 1.571 μmol h^{-1} for LP51_0.10, 0.576 μmol h^{-1} for LP51_0.25, and 0.884 μmol h^{-1} for LP51_0.50.

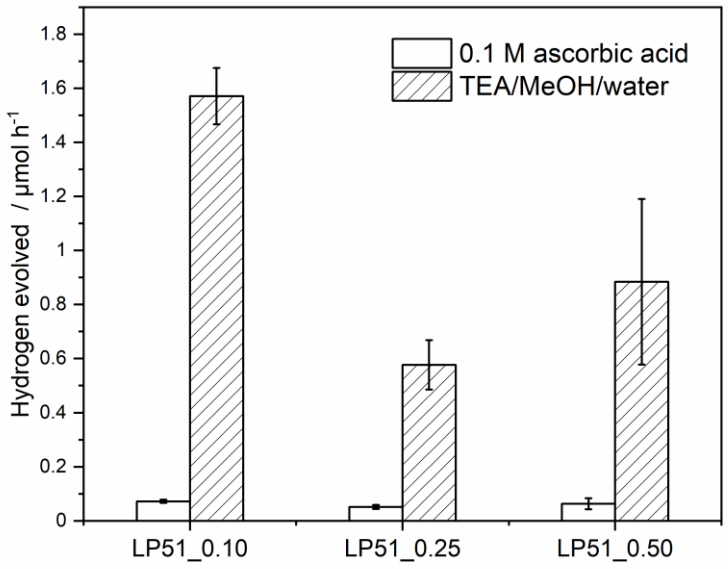

Figure 2.17 Hydrogen evolution rates of nanoparticles of polymer LP51_0.10/0.25/0.50 loaded with 3.0 wt.% platinum co-catalyst with 0.1 M ascorbic acid and TEA/methanol/water (1:1:1) over 3 hours irradiated with a solar simulator (AM1.5G, 1 sun). 0.225 mg polymer in each sample (4.5 mL polymer nanoparticle solution with 50 mg/L polymer concentration).

The pH values of AA and TEA systems were around 4 and 11.5, respectively. By the Nernst equation, the proton reduction potential of AA and TEA systems are -0.236 V and -0.679 V versus SHE, respectively (**Table 2.9**). Besides, the one-hole oxidation potential of AA and TEA are 0.518 V and 0.690 V versus SHE, respectively. The difference in the proton reduction potentials at different pH values and sacrificial electron donor oxidation potentials might lead to the different driving forces for the enhancement of charge transfer. In addition, polymer LP51 with different cationic group ratios shares the same absorption onset (420 nm) and thus

has the same relatively large optical gap of 2.95 eV. It has been reported that AA is a suitable sacrificial donor for narrow optical gap photocatalysts and the TEA is a suitable sacrificial donor for wide optical gap photocatalysts owing to the existence of the optimal thermodynamic driving force.[33]

Table 2.9 Potentials for the different solution half-reactions. Ascorbic acid* and dehydroascorbic acid are the one-hole and two-hole oxidation products of ascorbic acid, respectively.

Solution half-reaction	Potential (V vs. SHE)		
	pH 0	**pH 4.0**	**pH 11.5**
H^+ (aq) + e- -> 1/2 H_2 (g)	0	-0.236	-0.679
Ascorbic acid* (aq) + H^+ (aq) + e^- -> Ascorbic acid (aq)	0.755[a]	0.518	n/a
Dehydroascorbic acid + 2 H^+ (aq) + 2e^- -> Ascorbic acid (aq)	0.524[a]	0.286	n/a
TERA + H^+ + e^- -> TEA	n/a	n/a	0.690[26]

a. Values published vs. SCE (Saturated Calomel Electrode), Ref. [26], obtained vs. SHE (Standard Hydrogen Electrode) by adding 0.244 V. Potentials at pH 4.0 and 11.5 were estimated based on the Nernst equation: $E = E^0 - 0.05916 \times pH$, E^0: potential at pH 0. TEAR is the deprotonated TEA radical $N(Et)_2CHCH_3$. The potential for the overall oxidation of TEA to diethylamine (DEA) and acetaldehyde (AcO) is not shown because it lies at a similar value to the H^+/H_2 potential; the potential for the oxidation of TEAR to DEA and AcO is not shown since it is more negative than −3 V, Ref. [19]. n/a, not applicable.

When comparing their HERs in TEA system, nanoparticles of LP51_0.10 showed the highest photocatalytic hydrogen evolution among these three polymers. As these polymers share the same backbone structure, the thermodynamic driving forces for proton reduction and sacrificial electron donor oxidation are supposed to be the same. However, there is a shoulder at $\lambda = 430$ nm for nanoparticle of LP51_0.10 in **Figure 2.15c**, which is indicative of the partial formation of β-phase and that was found in other polyfluorene nanoparticles as well.[17,27] This more ordered β-phase may be beneficial for hydrogen evolution as the formation of planarized ladder-type structures has been shown to enhance photocatalytic performance.[34] The fluorene oligomers have been reported with decreasing optical gaps and more negative predicted ionization potentials relative to their unfused equivalent phenylene, both of which could contribute to their higher photocatalytic hydrogen production performance.[35]

2.3.4 Summary

The cationic group density was altered by the introduction of a third diluent monomer to obtain polymer LP51_0.10, 0.25, 0.50 in this chapter, and the cationic group density was confirmed by NMR and TGA data. Polymer and nanoparticles of polymers showed almost the same UV-vis absorption and fluorescence emission spectra except for the partial formation of β-phase in the nanoparticle of LP51_0.10. The photocatalytic hydrogen evolution rate in the TEA system

was over 10-fold higher than that of the ascorbic acid system, which could be attributed to the existence of the optimal thermodynamic driving force in TEA system.

2.4 Backbone Variation in Cationic Solution-Processable Conjugated Polymer Photocatalysts

2.4.1 Synthesis

Building on experience with conjugated polymer photocatalysts for sacrificial hydrogen production from water in conjunction with palladium,[36,4] a series of co-polymers were prepared. Using Suzuki-Miyaura polycondensation reaction (**Figure 2.18**), co-polymers of bis(8-bromo-*n*-octyl)-fluorene with phenylene (LP1), thiophene (LP2), 2,2'-bithiophene (LP3), and dibenzo[*b*,*d*]thiophene sulfone (LP4) were synthesized and purified via Soxhlet extraction with methanol, acetone, and ethyl acetate. The polymers were then modified through polymer-analogous reactions on the alkyl-bromo functional groups giving trimethylammonium-substituted polymers (LP11, LP21, LP31, and LP41).

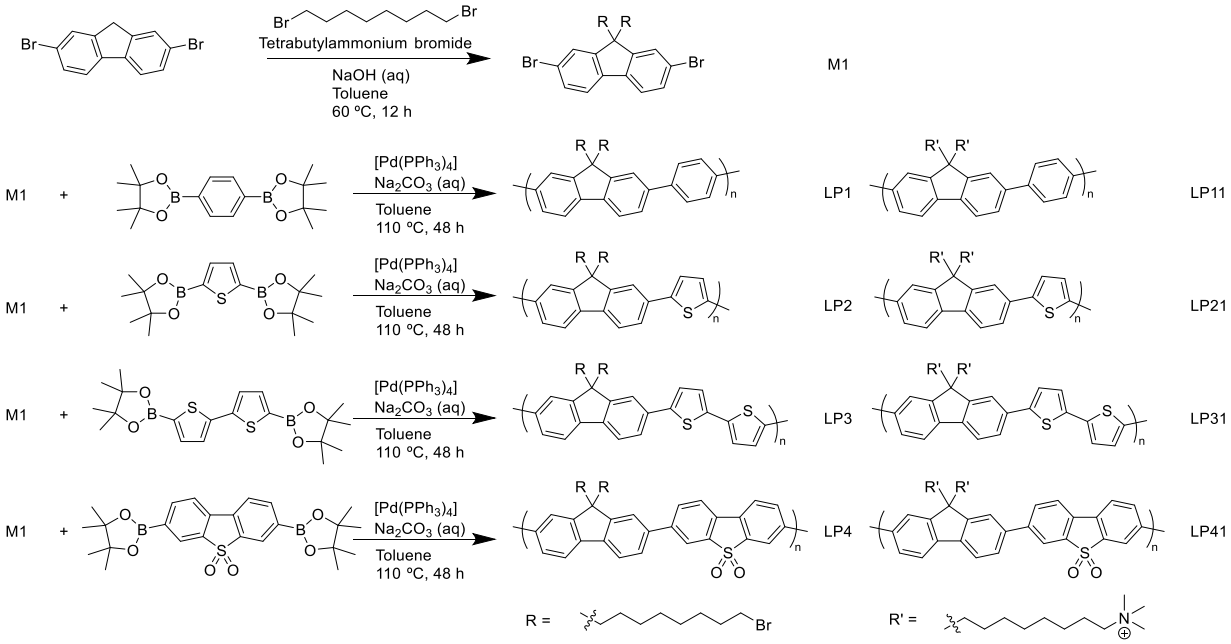

Figure 2.18 Synthetic routes of monomer M1, polymer LP1, LP2, LP3, and LP4, and chemical structures of polymer LP11, 21, 31, and 41.

2.4.2 Characterization

The materials were subsequently characterized via ^{1}H NMR, microanalysis, TGA, GPC, UV-Vis absorption and fluorescence spectroscopy. GPC showed that the polymers have number-weighted molecular weights between 13,900 to 125,900 g mol^{-1} (**Table 2.10, Figure 2.19**).

Table 2.10 GPC data for all chloroform-soluble polymer fractions.

Polymer	M_n[a] / g mol^{-1}	M_w[a] / g mol^{-1}	Đ[b]
LP1	14,000	24,700	1.8
LP2	25,500	48,900	1.9
LP3	125,900	219,800	1.7
LP4	33,500	87,900	2.6

a. Obtained from gel permeation chromatography in THF calibrated against polystyrene standards; M_n: the number-weighted molecular weight, M_w: the mass-weighted molecular weight; b. Dispersity, Đ = M_w/M_n.

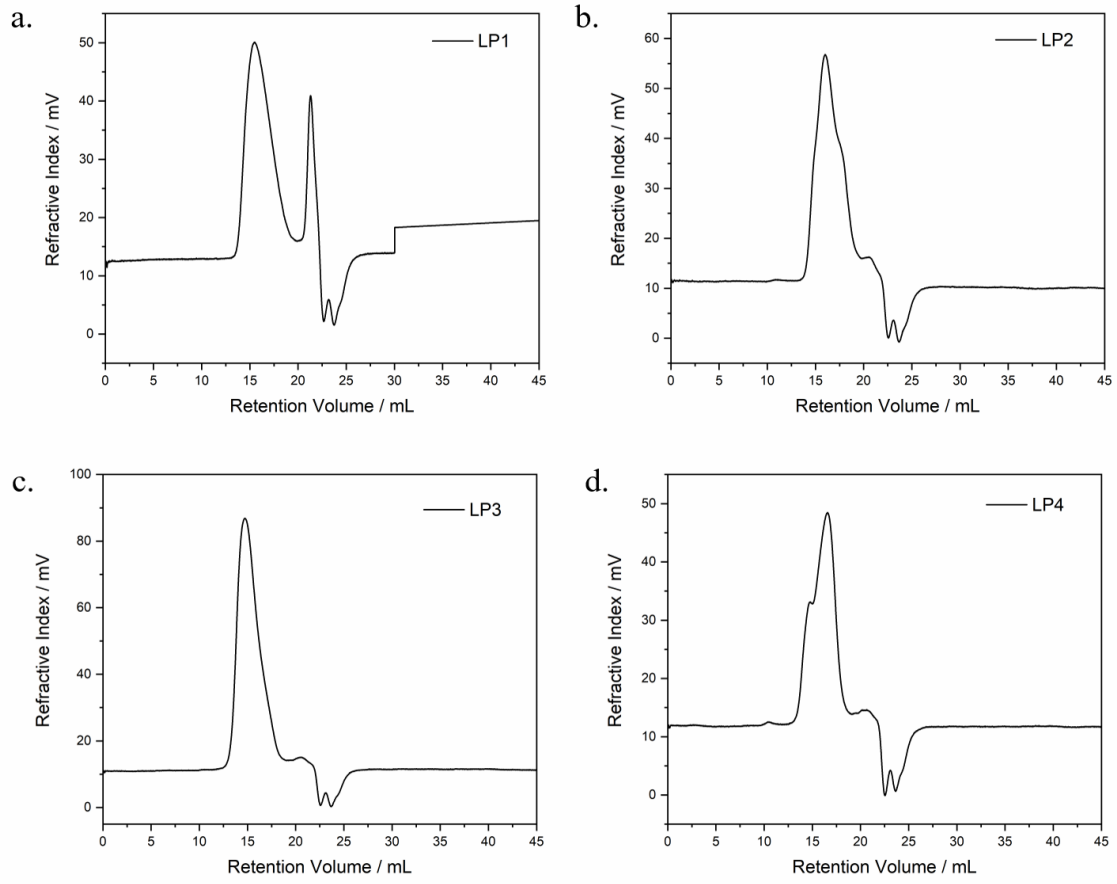

Figure 2.19 Chromatogram of polymer (a) LP1, (b) LP2, (c) LP3, (d) LP4.

TGA showed (**Figure 2.20a**) the onset thermal decomposition temperatures of these polymers to be similar to ~200 °C in nitrogen (with a small amount of H_2O loss at lower temperatures). The first mass loss corresponds to the loss of methyl bromide,[16,11] and the second (onset decomposition temperature at around 300 °C) is due to side chain cleavage.[37,38] The PXRD patterns of LP11, LP21, LP31, and LP41 all appeared to be non-crystalline in **Figure 2.20b**.

The optoelectronic properties of polymers were studied by UV-vis and PL spectroscopy. All polymers exhibited visible light absorption (> 400 nm), with the incorporation of thiophene units (LP2, and LP3) or dibenzo[*b*,*d*]thiophene sulfone (LP4) in place of phenylene (LP1)

leading to significant redshifts of the absorption onset (**Figure 2.21a**). The absorption spectra of LP2 and LP3 showed an extended range up to 500 and 525 nm, respectively, which might be a result of the polymer chains with a greater variation degree in both chain and conjugation lengths. And the redshift of the absorption onsets of polymer LP2 and LP3 correspond to a reduction in the optical gap[39] as the absorption onset is directly related to the optical gap[40]:

$$E_g^{opt} = hc \approx 1240/\lambda_{onset} \qquad \textbf{2.2}$$

h: Planck's constant; c: the speed of light.

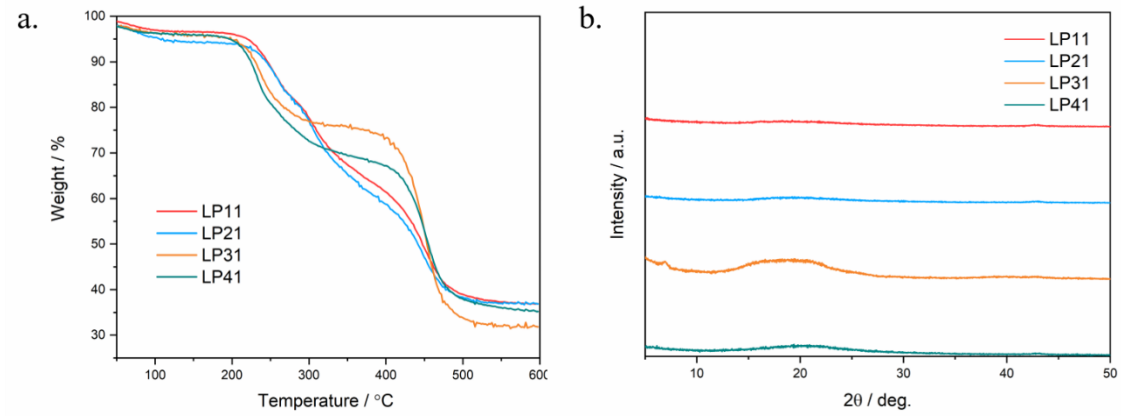

Figure 2.20 (a) Thermogravimetric analysis of LP11, LP21, LP31, and LP41 under nitrogen at a heating rate of 10 °C min^{-1}. (b) PXRD patterns of powders of polymer LP11, LP21, LP31, and LP41.

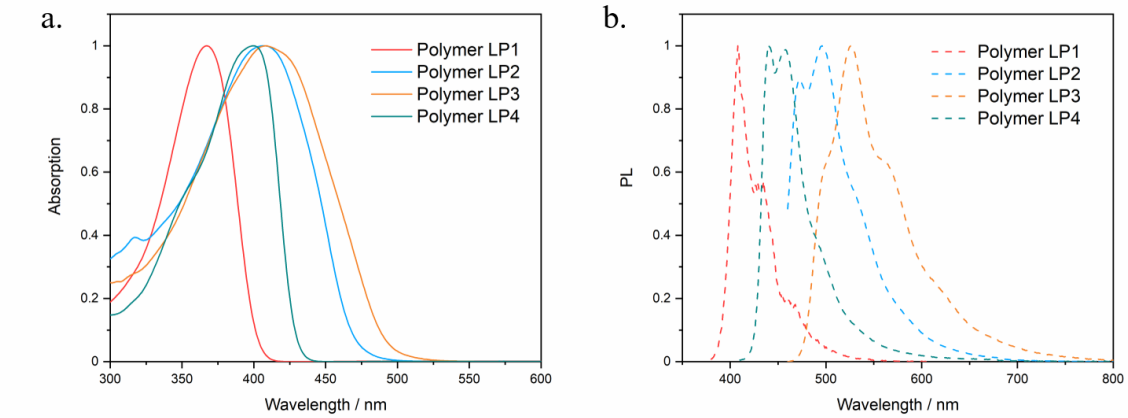

Figure 2.21 (a) Normalised UV-vis absorption and (b) fluorescence emission spectra of polymer LP1 (λ_{exc} 370 nm), LP2 (λ_{exc} 450 nm), LP3 (λ_{exc} 450 nm), and LP4 (λ_{exc} 400 nm) dissolved in chloroform.

An effective way to tune the band gap of the polymer is to give it a molecular structure in which an electron-rich donor (D) unit is conjugated with an electron-withdrawing acceptor (A) unit; this D-A conjugated structure induces intramolecular charge transfer between the D and A units.[41] Based on the molecular perturbation theory, the highest occupied molecular orbital (HOMO) of the D and A units will interact to produce two hybrid HOMOs for the D-A conjugated polymer; similarly, two hybrid lowest unoccupied molecular orbital (LUMO) will arise for the D-A conjugated polymer from the LUMOs of the D and A units as shown in **Figure 2.22**.[42] The redistribution of electrons from their original orbitals to the newly hybridized orbitals results in a higher lying hybrid HOMO and a lower lying hybrid LUMO, relative to that of the individual D and A units.

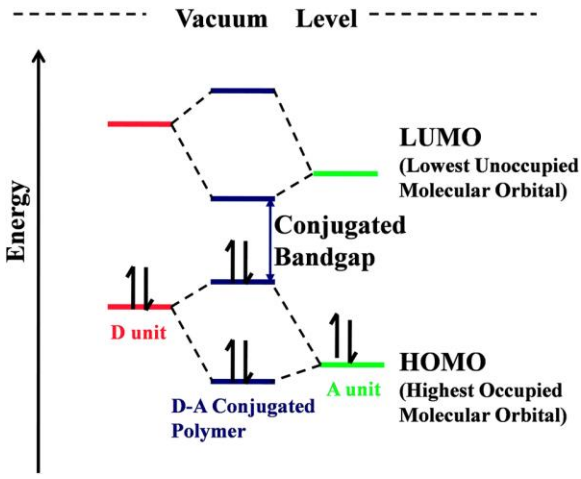

Figure 2.23 Energy levels of D and A chemical units and their D–A conjugated polymer.

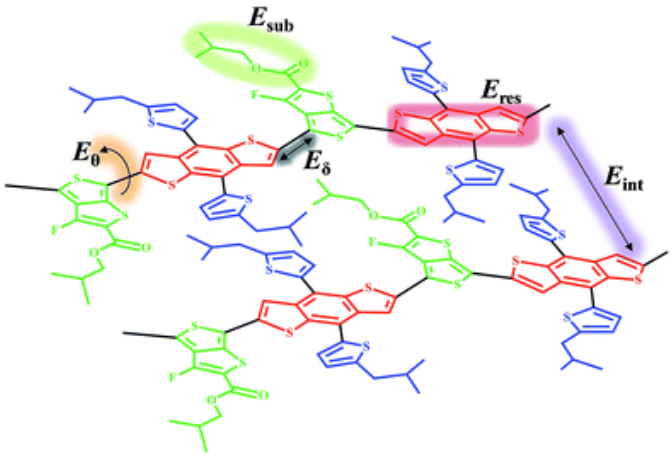

Figure 2.22 Schematic representation of five energy structural factors in a D-A conjugated polymer-E_{δ}: bond length alternation energy factor, E_{res}: resonance energy factor, E_{θ}: rotational disorder energy factor, E_{sub}: substituent energy factor and E_{int}: intermolecular interaction energy factor.

A deep understanding of the dependence of the band gap on the molecular structure is essential. The molecular design of π-conjugated systems consisting of electron donor moieties alternating with electron acceptors has been explored to redshift the absorption.[43,44] In addition, the planarization of part of the conjugated backbone, e.g. by using fused π-conjugated building blocks, has also resulted in reduced band gaps.[45] The effective conjugated band gaps are largely determined by the energies of five structural factors (see equation below) as shown in **Figure 2.23**.[46]

$$E_g = E_\delta + E_{res} + E_\theta + E_{sub} + E_{int} \qquad \textbf{2.3}$$

E_δ: bond length alternation energy factor,[47] the energy difference between the average lengths of the nominally single and double bonds along the linear π-conjugated backbone.

E_{res}: resonance energy factor, the energy required to switch from the aromatic form to the quinoid form through delocalization of moving π-electrons along the conjugated chain.

E_θ: energy factor for the rotational disorder around inter-angular single bonds.

E_{sub}: energy factor is related to modulating the HOMO and LUMO energy levels with electron-donating or -withdrawing substituents.

E_{int}: intermolecular interactions of multiple individual polymer chains.

Table 2.11 Photoelectron spectroscopy in air data for polymer thin films.

Material	UV Intensity / nW	Work function[a] / eV	PESA-inferred ionization potentials vs. SHE[b] / V
LP1	20	5.77	+ 1.33
LP2	20	5.53	+ 1.09
LP3	20	5.51	+ 1.07
LP4	100	5.89	+ 1.45

a. Work functions determined using a Riken Keiki PESA spectrometer (Model AC-2) with a power number of 0.33. Samples were prepared on ITO glass substrates; b. Obtained using the formula: IP = work function - 4.44 eV.

The ionisation potentials (IPs) of thin films of LP1-LP4 were measured using PESA, see **Table 2.11** and **Figure 2.24**. The IPs as measured by PESA, as well as values predicted using density functional theory (DFT) for oligomer models of the polymers embedded in a dielectric continuum typical of organic solids (ε_r 2.0), the results of which agree well with their PESA counterparts in line with previous work (**Table 2.12**),[48,4] show that LP2 and LP3 have very similar IP values, that LP1 has a deeper, more positive IP value, and that LP4 has the deepest, most positive, IP value. Similar DFT calculations but then for oligomer models in water (ε_r

80.1), modelling the IP of the polymers when in contact with water, a regime more difficult to probe experimentally, taken in the case of LP1 and LP4 from previous work,[20] show the same trend.

Table 2.12 Predicted charge carrier (IP, EA) and excitons (IP*, EA*) potentials of polymers considered calculated through (TD-)B3LYP for oligomer models in water (ε_r 80.1) and PESA (ε_r 2). LP1 and LP4 data for polymer in water taken from previous work. Ref. [19]

	Water condition IP vs. SHE / V	Water condition EA vs. SHE / V	PESA condition IP vs. SHE / V	Water condition EA* vs. SHE / V	Water condition IP* vs. SHE / V
LP1	0.73	-2.38	1.19	n/a	n/a
LP2	0.46	-2.14	1.00	n/a	n/a
LP3	0.44	-2.11	0.89	n/a	n/a
LP4	1.00	-1.92	1.55	0.92	-1.73

n/a: not applicable.

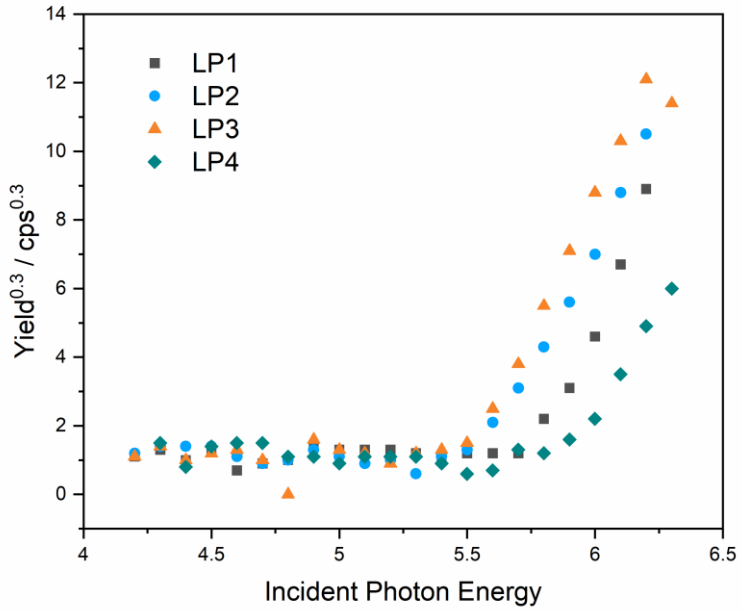

Figure 2.24 PESA spectra of polymer thin films of LP1, LP2, LP3, and LP4.

The polymers were then used to make nanoparticles through a reprecipitation method. The UV-vis spectra of nanoparticles LP11 and LP41 exhibit similar profiles with polymer samples (LP1 and LP4), while nanoparticles of LP31 and LP41 both have redshifted absorption onset in **Figure 2.25a**. All polymer nanoparticles also exhibit similar emission profiles (λ_{exc} = 370 nm for LP11, and 400 nm for LP21, LP31, and LP41).

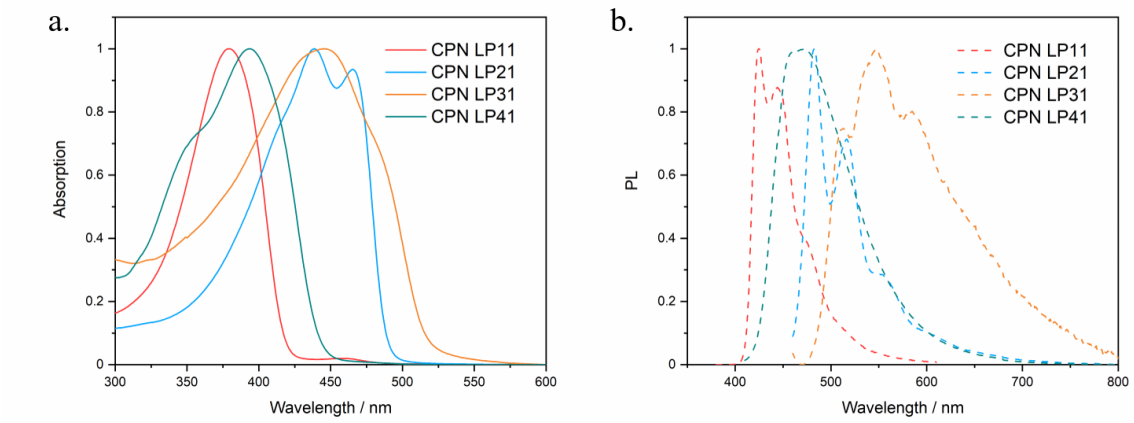

Figure 2.25 (a) Normalised UV-vis and (b) fluorescence emission spectra of polymer nanoparticle LP11(λ_{exc} 370 nm), LP21 (λ_{exc} 450 nm), LP31 (λ_{exc} 450 nm), and LP41 (λ_{exc} 400 nm).

Table 2.13 Photophysical properties of nanoparticle solution of polymer LP11, LP21, LP31, and LP41.

	λ_{onset}[a] / nm	Optical gap[b] / eV
LP11	417	2.97
LP21	488	2.55
LP31	518	2.39
LP41	441	2.81

a. Absorption onset wavelength of polymer nanoparticles; b. The optical gap (E_g^{opt}) was calculated from the absorption onset of polymer nanoparticles (($E_g^{opt} = hc \approx 1240/\lambda_{onset}$, h: Planck's constant, c: the speed of light).

Table 2.14 Particle average size and zeta-potential (polymer conc. 50 mg L^{-1}) by dynamic light scattering.

Polymer	Average size / nm	PDI[a]	Zeta-potential / mV
LP11	161	0.293	34.5 ± 5.8 mV
LP21	151	0.334	39.1 ± 5.6 mV
LP31	258	0.404	28.8 ± 1.0 mV
LP41	95	0.364	56.1 ± 5.0 mV

a. PDI: polydispersity index.

Dynamic light scattering measurements showed that nanoparticles of varied sizes in a 95-258 nm range with relatively high polydispersity were obtained, which is typical for conjugated polymer nanoparticles (**Figure 2.26**). LP41 was found to have the smallest particles size (95 nm). Zeta-potentials were determined to be between +28-56 mV for the quaternary ammonium functionalized polymer nanoparticles (**Table 2.14**) with LP41 having the highest zeta-potential value (56.1 ± 5.0 mV) within these five polymer nanoparticles.

Although the particle preparation process was under the same conditions (polymer concentration and mixing ratio between THF and water), the polymer chain

conformation in THF and their interaction with THF might be different due to their different molecular weights (**Table 2.10**) and backbone structures. These might explain a variable morphology with varying degrees of aggregation in the solid-state in scanning electron microscopy (SEM) images (**Figure 2.27**).

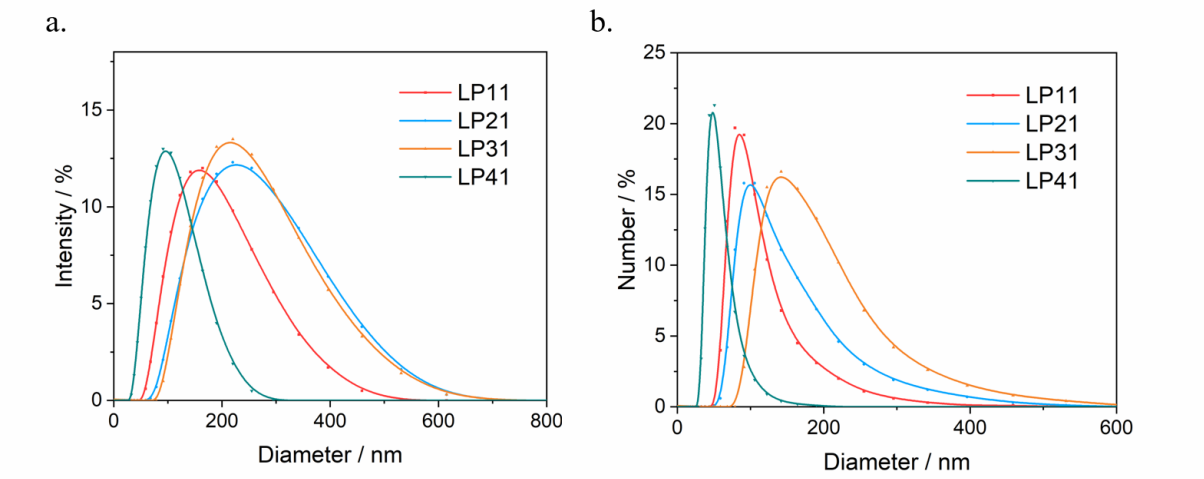

Figure 2.26 Size distribution of nanoparticle solution of polymer LP11, LP21, LP31, and LP41 by (a) intensity and (b) number.

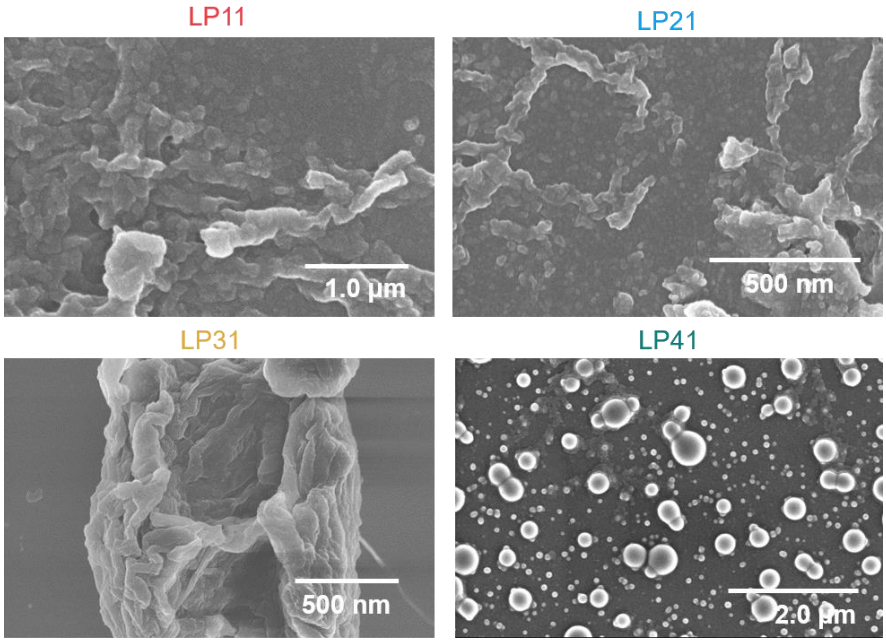

Figure 2.27 SEM images of LP11, LP21, LP31, and LP41 polymer nanoparticles.

2.4.3 Photocatalytic Hydrogen Evolution Performance

The performance of the nanoparticles of polymers for photocatalytic hydrogen production was evaluated under AM1.5G solar simulator irradiation for three hours with 0.1 M ascorbic acid

and TEA /methanol/water (1:1:1) acting as the sacrificial hole-scavengers, respectively (**Figure 2.28**).

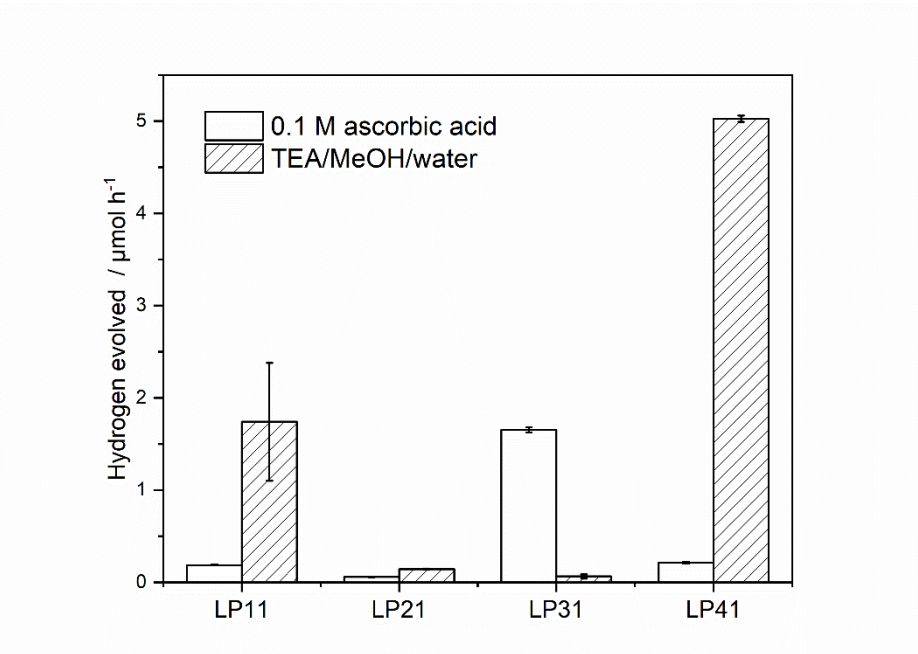

Figure 2.28 Hydrogen evolution rates of nanoparticles of polymer LP11, LP21, LP31, and LP41 loaded with 3.0 wt.% platinum co-catalyst in 0.1 M ascorbic acid, and TEA/methanol/water (1:1:1) over 3 hours irradiated with a solar simulator (AM 1.5G, 1 sun). 0.225 mg polymer in each sample (4.5 mL polymer nanoparticle solution with 50 mg/L polymer concentration).

All polymers were estimated to have a very negative electron affinity (EA) in **Figure 2.29**, as a result the polymers should have ample driving force for proton reduction in both systems. However, polymer LP2 and LP3 were predicted to have limited driving force for TEA oxidation, which might explain their limited hydrogen evolution activity in TEA system with only 0.142 μmol h^{-1} for LP21 and 0.0645 μmol h^{-1} for LP31.

The predicted IP values of all polymers were positive enough for ascorbic acid oxidation, and one interesting finding is that nanoparticles of LP31 showed the highest hydrogen evolution activity (1.654 μmol h^{-1}) with 0.1 M ascorbic acid as a sacrificial electron donor. This might suggest that the rate of ascorbic acid oxidation and hence the driving force for ascorbic acid oxidation is not the only factor that controls the hydrogen evolution rate of the LP31 polymer. It might also be due to the hole scavenger abilities of AA being better than TEA in this system, which was also reported previously for photocatalysts with narrow and similar optical gap (E_g 2.05-2.30 V).[33] Through the steady-state photoluminescence properties and time-resolved fluorescence decay spectra, they showed that the photoluminescence quenching of polymer with a narrow optical gap in the AA system was extremely stronger than that in the TEA system,

suggesting that the recombination of photogenerated electron-hole pair in the AA system was significantly suppressed by comparison with the TEA system.[33] Contrary to narrow optical gap polymer photocatalysts, wide bandgap polymer photocatalysts had opposite results. LP11 (E_g 2.97 V) and LP41 (E_g 2.81 V) showed better hydrogen evolution performance with 1.740 μmol h^{-1} and 5.026 μmol h^{-1} in the TEA system compared with 0.187 μmol h^{-1} and 0.214 μmol h^{-1} in AA system.

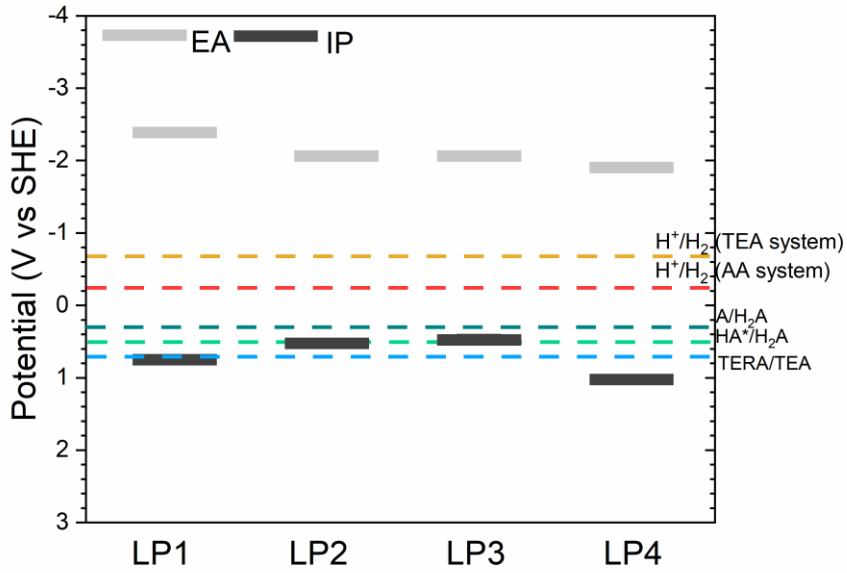

Figure 2.29 Predicted charge carrier potentials (IP, EA) of the polymers considered calculated through density functional theory (DFT) for oligomer models in water. Dashed colored lines indicate the potentials for different solution reactions: orange, proton reduction in TEA system of pH 11.5; red, proton reduction in AA system of pH 4; blue, one-hole oxidation of TEA to TERA; cyan and green, two-hole (A/H_2A) and one-hole ($HA\cdot/H_2A$) oxidation of ascorbic acid (see details in **Table 2.9**).

The observed hydrogen evolution rates show a clear correlation with the predicted IP values in the TEA system, see **Figure 2.30c**. This is in line with the photocatalytic results above that show that the oxidation of the sacrificial electron donor is required for hydrogen evolution and the fact that all polymers are predicted to have a sufficiently negative EA and thus a significant driving force for proton reduction and the predicted IP of LP1 and LP4, is positive enough to drive TEA oxidation. However, different from the TEA system, no clear correlation was found in the ascorbic acid system as shown in **Figure 2.31**.

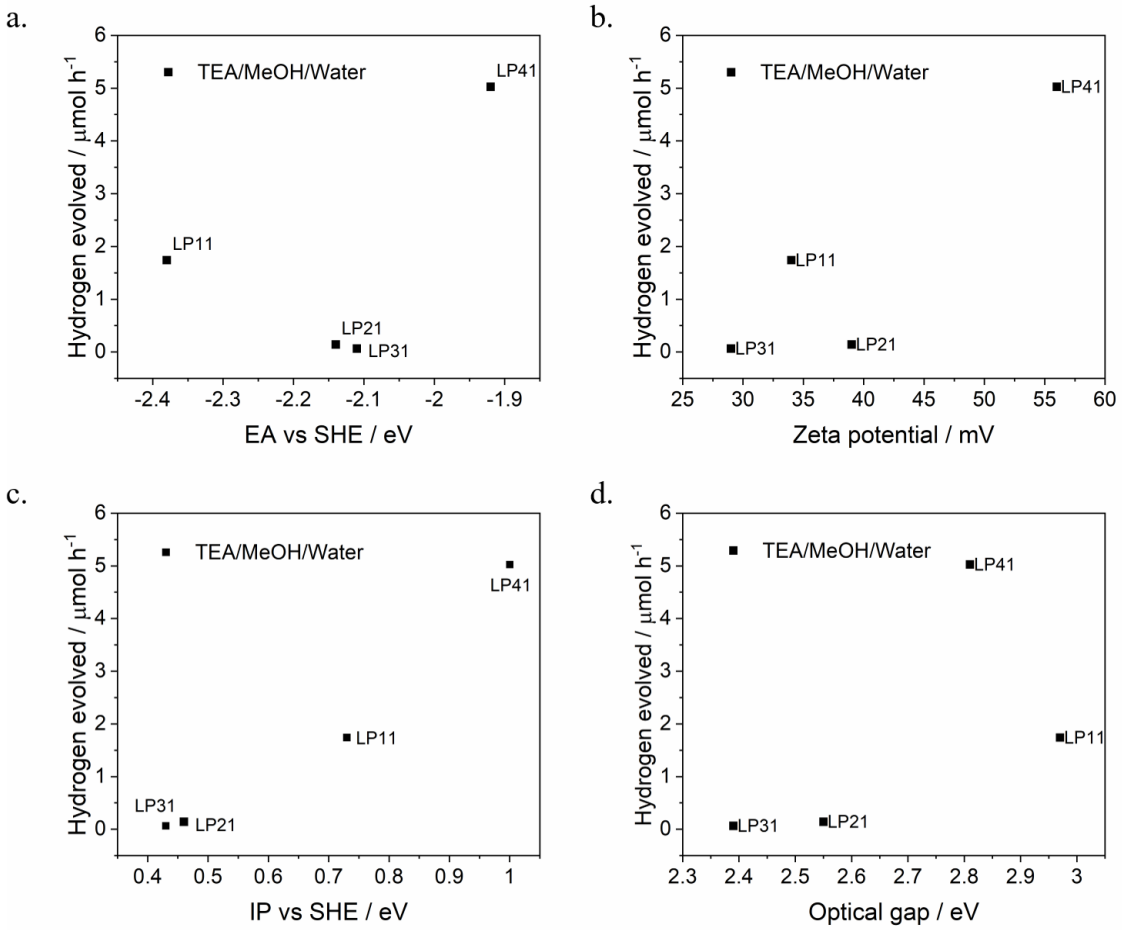

Figure 2.30 Correlation between the hydrogen production activity in TEA/MeOH/Water system and (a) EA values (b) zeta-potential (c) IP value (d) optical gap of polymers.

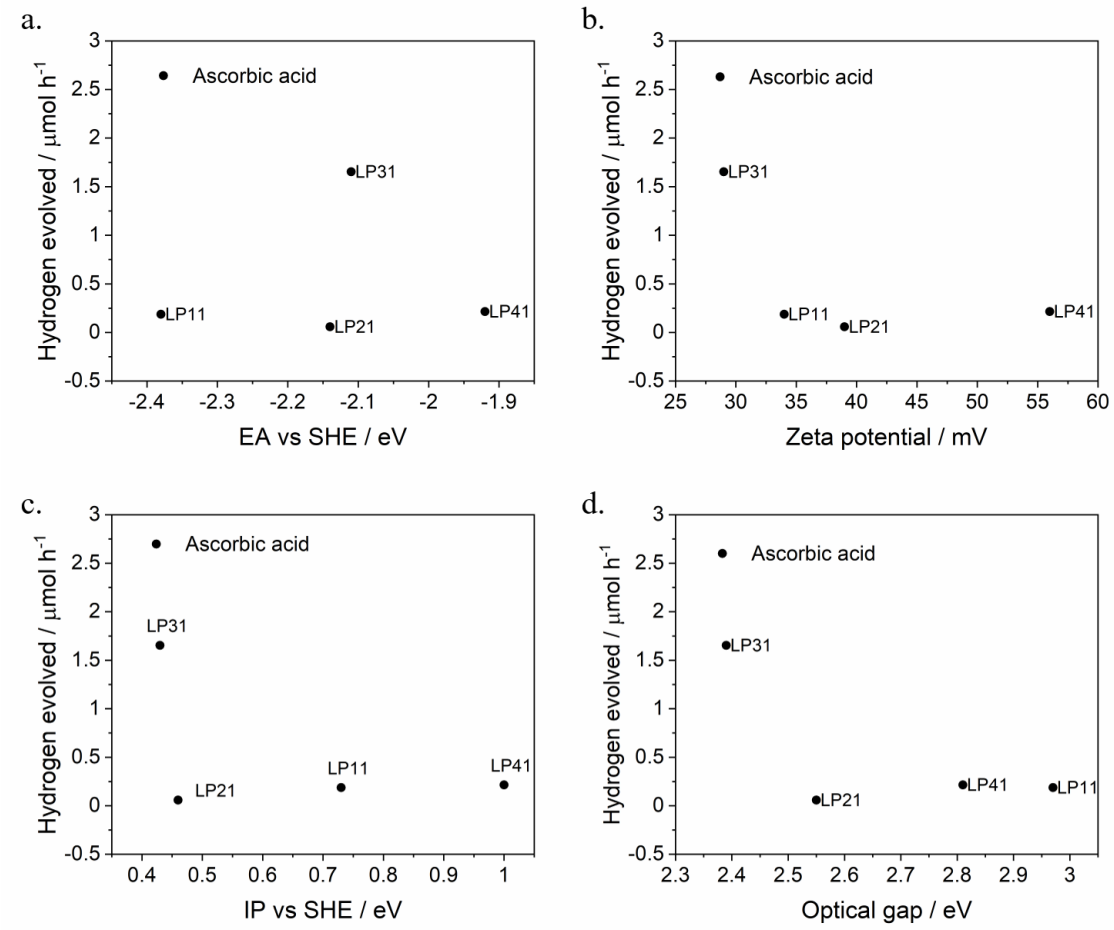

Figure 2.31 Correlation between the hydrogen production activity in 0.1 M ascorbic acid system and (a) EA values (b) zeta-potential (c) IP value (d) optical gap of polymers.

2.4.4 Summary

In this chapter, a series of co-polymers of bis(8-bromo-*n*-octyl)-fluorene with phenylene (LP1), thiophene (LP2), 2,2'-bithiophene (LP3), and dibenzo[*b*,*d*]thiophene sulfone (LP4) were synthesized. The polymers were then modified through polymer-analogous reactions on the alkyl-bromo functional groups giving trimethylammonium-substituted polymers (LP11, LP21, LP31, and LP41). Backbone variation alters the optical gap of polymers as the HOMO/LUMO character of the individual monomer pairs makes up the HOMO/LUMO of the conjugated polymer. It was reflected on their UV-vis absorption spectra with polymer LP2 and LP3 showing significant redshift of the absorption onset compared with LP1 and LP4.

The photocatalytic hydrogen evolution rate of nanoparticles of these 4 polymers was evaluated in ascorbic acid and TEA systems, respectively. For polymer LP11 and LP41, there were over

10-times (1.740 μmol h^{-1}) and 25-times (5.026 μmol h^{-1}) higher photocatalytic activities observed in the TEA system than that of the ascorbic acid system while for polymer LP31 it showed the opposite trend. Although a full understanding of the underlying photocatalytic mechanism remains unclear, it might suggest that the rate of sacrificial electron donor oxidation and hence the driving force for ascorbic acid/TEA oxidation is not the only factor that controls the hydrogen evolution rates of these four conjugated polymers. It might also be due to the different hole scavenger abilities for different polymers in this case.

2.5 References

(1) Wu, C.; Bull, B.; Szymanski, C.; Christensen, K.; McNeill, J. Multicolor Conjugated Polymer Dots for Biological Fluorescence Imaging. *ACS Nano* **2008**, *2* (11), 2415–2423. https://doi.org/10.1021/nn800590n.

(2) Wu, C.; Szymanski, C.; McNeill, J. Preparation and Encapsulation of Highly Fluorescent Conjugated Polymer Nanoparticles. *Langmuir* **2006**, *22* (7), 2956–2960. https://doi.org/10.1021/la060188l.

(3) Kim, K.; Suh, M.; Choi, J.; Lee, D.; Kim, Y.; Cheong, S. H.; Kim, D.; Jeon, D. Y. Conjugated Polyelectrolyte Hybridized ZnO Nanoparticles as a Cathode Interfacial Layer for Efficient Polymer Light-Emitting Diodes. *Adv. Funct. Mater.* **2015**, *25* (48), 7450–7456. https://doi.org/10.1002/adfm.201502360.

(4) Woods, D. J.; Hillman, S. A. J.; Pearce, D.; Wilbraham, L.; Flagg, L. Q.; Duffy, W.; McCulloch, I.; Durrant, J. R.; Guilbert, A. A. Y.; Zwijnenburg, M. A.; Sprick, R. S.; Nelson, J.; Cooper, A. I. Side-Chain Tuning in Conjugated Polymer Photocatalysts for Improved Hydrogen Production from Water. *Energy Environ. Sci.* **2020**, *13* (6), 1843–1855. https://doi.org/10.1039/d0ee01213k.

(5) Chemler, S. R.; Trauner, D.; Danishefsky, S. J. The B-Alkyl Suzuki-Miyaura Cross-Coupling Reaction: Development, Mechanistic Study, and Applications in Natural Product Synthesis A List of Abbreviations Can Be Found at the End of the Article. *Angew. Chem. Int. Ed. Engl.* **2001**, *40* (24), 4544–4568. https://doi.org/10.1002/1521-3773(20011217)40:24<4544::aid-anie4544>3.0.co;2-n.

(6) Miyaura, N.; Suzuki, A. Palladium-Catalyzed Cross-Coupling Reactions of Organoboron Compounds. *Chem. Rev.* **1995**, *95* (7), 2457–2483.

(7) Wong, C. K.; Lai, R. Y.; Stenzel, M. H. Dynamic Metastable Polymersomes Enable Continuous Flow Manufacturing. *Nat. Commun.* **2023**, *14* (1), 6237. https://doi.org/10.1038/s41467-023-41883-6.

(8) Lefley, J.; Waldron, C.; Becer, C. R. Macromolecular Design and Preparation of Polymersomes. *Polym. Chem.* **2020**, *11* (45), 7124–7136. https://doi.org/10.1039/D0PY01247E.

(9) Bang, R. S.; Roh, S.; Williams, A. H.; Stoyanov, S. D.; Velev, O. D. Fluid Flow

Templating of Polymeric Soft Matter with Diverse Morphologies. *Adv. Mater.* **2023**, *35* (16), 2211438. https://doi.org/https://doi.org/10.1002/adma.202211438.

(10) Balanda, P. B.; Ramey, M. B.; Reynolds, J. R. Water-Soluble and Blue Luminescent Cationic Polyelectrolytes Based on Poly(p-Phenylene). *Macromolecules* **1999**, *32* (12), 3970–3978. https://doi.org/10.1021/ma982017w.

(11) Dai, C.; Panahandeh-Fard, M.; Gong, X.; Xue, C.; Liu, B. Water-Dispersed Conjugated Polyelectrolyte for Visible-Light Hydrogen Production. *Sol. RRL* **2019**, *3* (3), 1–6. https://doi.org/10.1002/solr.201800255.

(12) Meng, B.; Song, H.; Chen, X.; Xie, Z.; Liu, J.; Wang, L. Replacing Alkyl with Oligo(Ethylene Glycol) as Side Chains of Conjugated Polymers for Close π–π Stacking. *Macromolecules* **2015**, *48* (13), 4357–4363. https://doi.org/10.1021/acs.macromol.5b00702.

(13) Blondin, P.; Bouchard, J.; Beaupré, S.; Belletête, M.; Durocher, G.; Leclerc, M. Molecular Design and Characterization of Chromic Polyfluorene Derivatives. *Macromolecules* **2000**, *33* (16), 5874–5879. https://doi.org/10.1021/ma000020l.

(14) Qin, R.; Li, W.; Li, C.; Du, C.; Veit, C.; Schleiermacher, H.-F.; Andersson, M.; Bo, Z.; Liu, Z.; Inganäs, O.; Wuerfel, U.; Zhang, F. A Planar Copolymer for High Efficiency Polymer Solar Cells. *J. Am. Chem. Soc.* **2009**, *131* (41), 14612–14613. https://doi.org/10.1021/ja9057986.

(15) Schweizer, K. S. Configurational Dependence of the Optical Properties of Π-conjugated Polymers. I. Strong Disorder Limit. *J. Chem. Phys.* **1986**, *85* (7), 4181–4193. https://doi.org/10.1063/1.450891.

(16) Balanda, P. B.; Ramey, M. B.; Reynolds, J. R. Water-Soluble and Blue Luminescent Cationic Polyelectrolytes Based on Poly(p-Phenylene). *Macromolecules* **1999**, *32* (12), 3970–3978. https://doi.org/10.1021/ma982017w.

(17) Wu, C.; McNeill, J. Swelling-Controlled Polymer Phase and Fluorescence Properties of Polyfluorene Nanoparticles. *Langmuir* **2008**, *24* (11), 5855–5861. https://doi.org/10.1021/la8000762.

(18) Avcı, D.; Tamer, Ö.; Atalay, Y. Solvatochromic Effect on UV–Vis Absorption and Fluorescence Emission Spectra, Second- and Third-Order Nonlinear Optical Properties

of Dicyanovinyl-Substituted Thienylpyrroles: DFT and TDDFT Study. *J. Mol. Liq.* **2016**, *220*, 495–503. https://doi.org/https://doi.org/10.1016/j.molliq.2016.05.023.

(19) Tuncel, D.; Demir, H. V. Conjugated Polymer Nanoparticles. *Nanoscale* **2010**, *2* (4), 484–494. https://doi.org/10.1039/b9nr00374f.

(20) Bai, Y.; Woods, D. J.; Wilbraham, L.; Aitchison, C. M.; Zwijnenburg, M. A.; Sprick, R. S.; Cooper, A. I. Hydrogen Evolution from Water Using Heteroatom Substituted Fluorene Conjugated Co-Polymers. *J. Mater. Chem. A* **2020**, *8* (17), 8700–8705. https://doi.org/10.1039/D0TA02599B.

(21) Najafov, H.; Lee, B.; Zhou, Q.; Feldman, L. C.; Podzorov, V. Observation of Long-Range Exciton Diffusion in Highly Ordered Organic Semiconductors. *Nat. Mater.* **2010**, *9* (11), 938–943. https://doi.org/10.1038/nmat2872.

(22) Aitchison, C. M.; Sprick, R. S. Conjugated Nanomaterials for Solar Fuel Production. *Nanoscale*. 2021. https://doi.org/10.1039/d0nr07533g.

(23) Laroff, G. P.; Fessenden, R. W.; Schuler, R. H. Electron Spin Resonance Spectra of Radical Intermediates in the Oxidation of Ascorbic Acid and Related Substances. *J. Am. Chem. Soc.* **1972**, *94* (26), 9062–9073. https://doi.org/10.1021/ja00781a013.

(24) Craw, M. T.; Depew, M. C.; Wan, J. K. S. An Unusual CIDEP Observation in the Photochemical Reactions of Benzophenone and Ascorbyl Palmitate: The Elusive Neutral Ascorbate Radical. *J. Am. Chem. Soc.* **1985**, *107* (4), 1084–1085. https://doi.org/10.1021/ja00290a069.

(25) Raula, M.; Rashid, M. H.; Paira, T. K.; Dinda, E.; Mandal, T. K. Ascorbate-Assisted Growth of Hierarchical ZnO Nanostructures: Sphere, Spindle, and Flower and Their Catalytic Properties. *Langmuir* **2010**, *26* (11), 8769–8782. https://doi.org/10.1021/la904507q.

(26) Pellegrin, Y.; Odobel, F. Les Donneurs d'électron Sacrificiels Pour La Production de Combustible Solaire. *Comptes Rendus Chim.* **2017**, *20* (3), 283–295. https://doi.org/10.1016/j.crci.2015.11.026.

(27) Tsoi, W. C.; Charas, A.; Cadby, A. J.; Khalil, G.; Adawi, A. M.; Iraqi, A.; Hunt, B.; Morgado, J.; Lidzey, D. G. Observation of the β-Phase in Two Short-Chain Oligofluorenes. *Adv. Funct. Mater.* **2008**, *18* (4), 600–606.

https://doi.org/10.1002/adfm.200700530.

(28) M Ariu; D G Lidzey; M Sims; A J Cadby; P A Lane; D D C Bradley. The Effect of Morphology on the Temperature-Dependent Photoluminescence Quantum Efficiency of the Conjugated Polymer Poly(9, 9-Dioctylfluorene). *J. Phys. Condens. Matter* **2002**, *14* (42), 9975. https://doi.org/10.1088/0953-8984/14/42/310.

(29) Behrendt, J. M.; Wang, Y.; Willcock, H.; Wall, L.; McCairn, M. C.; O'Reilly, R. K.; Turner, M. L. Fluorescent Nanoparticles from PEGylated Polyfluorenes. *Polym. Chem.* **2013**, *4* (5), 1333–1336. https://doi.org/10.1039/C3PY21068E.

(30) Lin, W. C.; Jayakumar, J.; Chang, C. L.; Ting, L. Y.; Elsayed, M. H.; Abdellah, M.; Zheng, K.; Elewa, A. M.; Lin, Y. T.; Liu, J. J.; Wang, W. S.; Lu, C. Y.; Chou, H. H. Effect of Energy Bandgap and Sacrificial Agents of Cyclopentadithiophene-Based Polymers for Enhanced Photocatalytic Hydrogen Evolution. *Appl. Catal. B Environ.* **2021**, *298* (June), 120577. https://doi.org/10.1016/j.apcatb.2021.120577.

(31) Vogel, A.; Forster, M.; Wilbraham, L.; Smith, C. L.; Cowan, A. J.; Zwijnenburg, M. A.; Sprick, R. S.; Cooper, A. I. Photocatalytically Active Ladder Polymers. *Faraday Discuss.* **2019**, *215* (0), 84–97. https://doi.org/10.1039/C8FD00197A.

(32) Woods, D. J.; Sprick, R. S.; Smith, C. L.; Cowan, A. J.; Cooper, A. I. A Solution-Processable Polymer Photocatalyst for Hydrogen Evolution from Water. *Adv. Energy Mater.* **2017**, *7* (22), 1–6. https://doi.org/10.1002/aenm.201700479.

(33) Meng, B.; Song, H.; Chen, X.; Xie, Z.; Liu, J.; Wang, L. Replacing Alkyl with Oligo(Ethylene Glycol) as Side Chains of Conjugated Polymers for Close π–π Stacking. *Macromolecules* **2015**, *48* (13), 4357–4363. https://doi.org/10.1021/acs.macromol.5b00702.

(34) Blondin, P.; Bouchard, J.; Beaupré, S.; Belletête, M.; Durocher, G.; Leclerc, M. Molecular Design and Characterization of Chromic Polyfluorene Derivatives. *Macromolecules* **2000**, *33* (16), 5874–5879. https://doi.org/10.1021/ma000020l.

(35) Costa, C.; Farinhas, J.; Avó, J.; Morgado, J.; Galvão, A. M.; Charas, A. Structural Dependence of the Optical Properties of Narrow Band Gap Thiophene–Thiadiazoloquinoxaline Derivatives and Their Application in Organic Photovoltaic Cells. *New J. Chem.* **2019**, *43* (13), 5202–5213. https://doi.org/10.1039/C8NJ06012F.

(36) De Jongh, L. J. *Physics and Chemistry of Metal Cluster Compounds: Model Systems for Small Metal Particles*; Springer Science & Business Media, 2013; Vol. 18.

(37) Su, Y.-W.; Lan, S.-C.; Wei, K.-H. Organic Photovoltaics. *Mater. Today* **2012**, *15* (12), 554–562. https://doi.org/https://doi.org/10.1016/S1369-7021(13)70013-0.

(38) Su, Y.-W.; Lin, Y.-C.; Wei, K.-H. Evolving Molecular Architectures of Donor–Acceptor Conjugated Polymers for Photovoltaic Applications: From One-Dimensional to Branched to Two-Dimensional Structures. *J. Mater. Chem. A* **2017**, *5* (46), 24051–24075. https://doi.org/10.1039/C7TA07228G.

(39) Han, C.; Dong, P.; Tang, H.; Zheng, P.; Zhang, C.; Wang, F.; Huang, F.; Jiang, J.-X. Realizing High Hydrogen Evolution Activity under Visible Light Using Narrow Band Gap Organic Photocatalysts. *Chem. Sci.* **2021**, *12* (5), 1796–1802. https://doi.org/10.1039/D0SC05866A.

(40) Bundgaard, E.; Krebs, F. C. Low-Band-Gap Conjugated Polymers Based on Thiophene, Benzothiadiazole, and Benzobis(Thiadiazole). *Macromolecules* **2006**, *39* (8), 2823–2831. https://doi.org/10.1021/ma052683e.

(41) Costa, C.; Farinhas, J.; Avó, J.; Morgado, J.; Galvão, A. M.; Charas, A. Structural Dependence of the Optical Properties of Narrow Band Gap Thiophene–Thiadiazoloquinoxaline Derivatives and Their Application in Organic Photovoltaic Cells. *New J. Chem.* **2019**, *43* (13), 5202–5213. https://doi.org/10.1039/C8NJ06012F.

(42) Roncali, J. Synthetic Principles for Bandgap Control in Linear π-Conjugated Systems. *Chem. Rev.* **1997**, *97* (1), 173–206. https://doi.org/10.1021/cr950257t.

(43) Gieseking, R. L.; Risko, C.; Brédas, J.-L. Distinguishing the Effects of Bond-Length Alternation versus Bond-Order Alternation on the Nonlinear Optical Properties of π-Conjugated Chromophores. *J. Phys. Chem. Lett.* **2015**, *6* (12), 2158–2162. https://doi.org/10.1021/acs.jpclett.5b00812.

(44) Guiglion, P.; Monti, A.; Zwijnenburg, M. A. Validating a Density Functional Theory Approach for Predicting the Redox Potentials Associated with Charge Carriers and Excitons in Polymeric Photocatalysts. *J. Phys. Chem. C* **2017**, *121* (3), 1498–1506. https://doi.org/10.1021/acs.jpcc.6b11133.

Chapter 3 :

Conjugated Polymer-*Escherichia coli* Biohybrid Systems for Hydrogen Production

Chapter Contributions: The thesis author prepared all polymers and polymer nanoparticles in this chapter. Confocal microscopy measurements were performed by Dr Yaqi Sun. The thesis author and Dr Keith Arnold carried out the SEM for polymer-E. coli biohybrid systems and polymer nanoparticles.

3.1 Background

In this chapter, nanoparticles of conjugated linear polymers were assembled with *Escherichia coli* (*E. coli*) cells to develop photobiocatalytic systems for hydrogen formation. Building on our experience with conjugated polymer photocatalysts for sacrificial hydrogen production from water in conjunction with palladium in Chapter 2, a series of co-polymers with potential as visible light photocatalysts in **Figure 3.1** were synthesised.

The use of synthetic biology allowed us to access genetically engineered *E. coli* that can express [FeFe] hydrogenase in addition to their endogenous [NiFe] hydrogenase[1] while the use of conjugated polymers enabled us to tune the properties of the hybrids via synthesis. This modification significantly increases the proton reduction activity of the biohybrid system. The resulting biohybrid materials exhibited functional synergy between the two components and enhanced biohydrogen production.

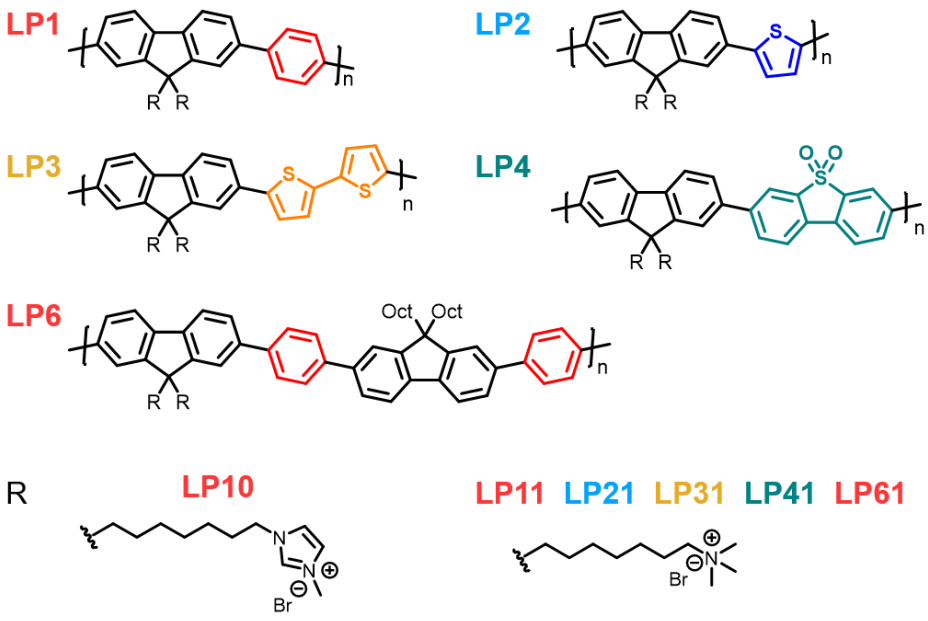

Figure 3.1 Chemical structures of conjugated polymers LP1, LP2, LP3, LP4 and LP6 with imidazolium (LP10) and trimethylammonium (LP11, LP21, LP31, LP41, and LP61) functionalization.

3.2 Conjugated Polymer-*E. coli* Biohybrid System Assembly

3.2.1 Expression of Heterologous [FeFe] Hydrogenase HydA in *E. coli*

Various microbial systems have been engineered for producing native and heterologous [FeFe] hydrogenases, such as *Clostridium pasteurianum*,[2] *E. coli*,[3] green algae,[4] and *Shewanella oneidensis*.[5] *E. coli* has several advantages that make it desirable for hydrogenase production. Firstly, it does not contain a native [FeFe] hydrogenase that needs to be knocked out to simplify analytical measurement; Secondly, it is capable of anaerobic respiration and heterologous expression techniques are well-established; Lastly, active hydrogenase production using *E. coli* has been demonstrated.[6]

The [FeFe] hydrogenase from the green alga *Chlamydomonas reinhardtii*, HydA, is one of the simplest [FeFe] hydrogenases and represents the 'minimal unit' for biological H_2 production.[7] A *hyd* plasmid was generated to express the following proteins: (1) algal HydA that was fused with algal ferredoxin (Fd); Fd serves as the native electron donor of algal HydA, and the Fd-HydA fusion increased the rate of H_2 production.[8] (2) The maturase enzymes HydE, HydF, and HydG, are crucial for the formation and activation of HydA.[9] This plasmid was transformed into *E. coli*.

The expression of mature, functional [FeFe] hydrogenase HdyA in *E. coli* BL21 (DE3), as well as Fd, was conducted by using a procedure based on previously reported work.[10] *E. coli* BL21 cells containing the *hyd* vector were firstly grown aerobically in Lysogeny broth (LB) medium containing 0.2 mM ferric ammonium citrate and 50 μg mL^{-1} spectinomycin at 37 ℃ until OD_{600} reached 0.7-0.8. Cells were then transferred to falcon tubes sealed with rubber turn-over closures and degassed with nitrogen for 15 mins before the addition of 0.5 mM Isopropyl β-D-1-thiogalactopyranoside (IPTG), 0.2 mM L-cysteine, and 2.5 mM sodium fumarate for anaerobic treatment. Cells were then grown at 25 °C for 16 hours.

Expression of hyd plasmid was induced by the addition of IPTG by removing a repressor from the lac operon. The [FeFe] hydrogenase active site cofactor, termed the H-cluster, is a complex iron-sulfur cluster that is stabilized by carbon monoxide and cyanide ligands as well as a dithiol bridging molecule.[11] Ferric ammonium citrate and cysteine were added as the source of iron and sulfur separately for the formation of iron-sulfur clusters in HydA and its maturases.

Spectinomycin, an antibiotic, was added to cell culture to select the transformed cells. The expression of [FeFe] hydrogenase was then confirmed by Western Blotting in **Figure 3.2**.

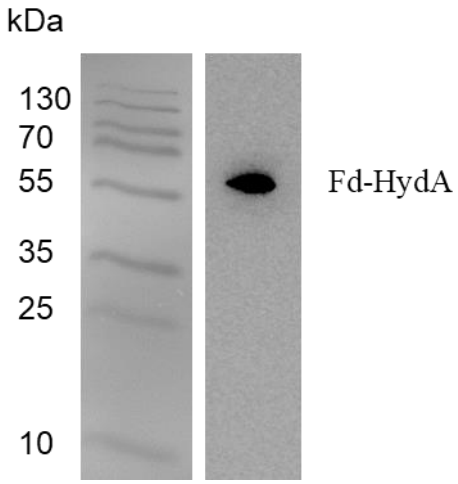

Figure 3.2 Western Blotting of *E. coli* expressing the hyd vector confirms the presence of Fd-HydA.

3.2.2 Assembly Strategy I

The reduced nature of the H-cluster and accessory iron-sulfur clusters makes them susceptible to damage by O_2 oxidation.[6] As both hydrogenase expression and hydrogen production measurement need to be conducted in anaerobic conditions, assembly strategy I (**Figure 3.3**) was to conduct the [FeFe] hydrogenase expression in *E. coli* in the same sample vial with the assembly of nanoparticles of conjugated polymers with *E. coli* cells. In addition, assembly strategy I is a relatively simple strategy by adding all components (*E. coli* pellet, chemicals for hydrogenase induction/expression, polymer nanoparticle, sacrificial electron donors) in a sample vial which is also potentially suitable for automatic photocatalysis measurement workflow.

After a quick proliferation of *E. coli* cells in Lysogeny broth (LB) medium, cell pellets were harvested by centrifuge (5 min, 4, 000 g) and washed with Minimal 9 (M9) medium three times. LB medium is a nutritionally rich medium primarily used for the growth of bacteria[12] but not a suitable reaction medium for the hydrogen performance measurement as it is not a 'defined culture medium' since the components in the medium are unknown as shown in **Table 3.1**. The M9 medium in **Table 3.2** is chemically defined and was therefore used as a reaction medium.

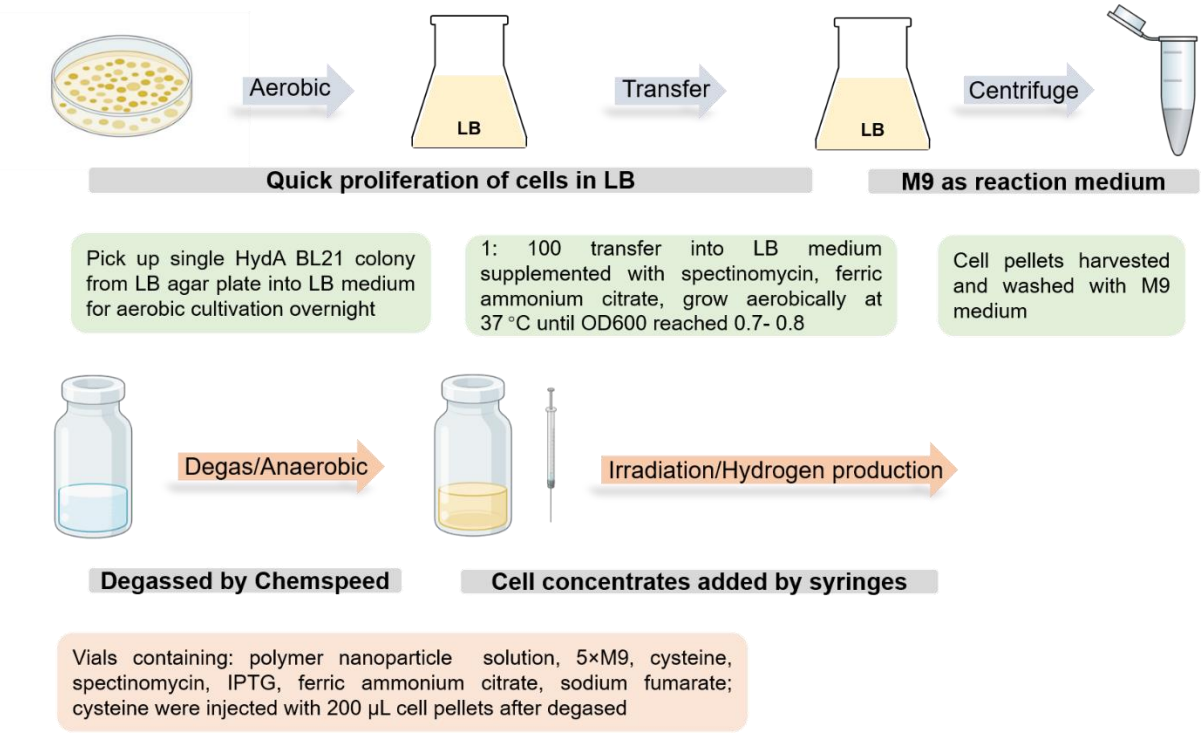

Figure 3.3 Assembly strategy I: hydrogenase induction, biohybrid assembly, and hydrogen production.

Table 3.1 Components of Lysogeny broth (LB) medium.

Component	Component	Concentration
Tryptone	Peptides and amino acids	10 g / 1L H_2O
Yeast extracts	Amino acids, vitamins, nucleotides and carbohydrates	5 g / 1L H_2O
Sodium chloride	n.a.	10 g / 1L H_2O

n.a. not applicable

Table 3.2 Components of 1×M9 minimal media, per litre

Component	Amount	Concentration
$Na_2HPO_4.2H_2O$	8.5 g	0.047 M
KH_2PO_4	3.0 g	0.022 M
NH_4Cl	1.0 g	0.019 M
NaCl	0.5 g	0.008 M
100 mM $CaCl_2$	1.0 mL	0.1 mM
1 M $MgSO_4$	1.0 mL	1.0 mM

Adjust to pH 7.0 using 4 M NaOH.

All components in a sample vial are listed in **Table 3.3**. All the components except *E. coli* pellets were added into vials and vials were capped by Chemspeed after 3-hour nitrogen purging. Cell pellets (100-200 µL) were then injected into vials by syringes.

As [FeFe]-hydrogenase expression was conducted with the presence of polymers, sacrificial electron donors, and irradiation by a solar simulator, all these parameters might influence the

hydrogenase expression or/and the overall hydrogen formation performance of the biohybrid systems. Therefore, different parameters such as irradiation time, polymers, sacrificial electron donors, and polymer concentration were studied separately as shown below.

Table 3.3 Components in a sample vial under assembly strategy I.

Components		Function
Name	Vol./Conc.	
Polymer nanoparticle	4.5 mL, 50 mg L^{-1}	/
M9	0.5 mL, 5 ×	Cell culture medium
Spectinomycin	50 μg mL^{-1}	Antibiotics
IPTG	0.5 mM	Induce protein expression where the gene is under the control of the lac operator
Ferric ammonium citrate	0.2 mM	Source of Fe for [FeFe] hydrogenase
Sodium fumarate	2.5 mM	Final electron acceptor
Cysteine	1.2 mM	Source of S for [FeFe] hydrogenase and sacrificial electron donor
Cell pellets	100-200 μL	/

Apart from ascorbic acid and TEA introduced in Chapter 2 as sacrificial electron donors in photocatalytic measurements, cysteine is a very relevant monoelectronic sacrificial donor because of its low oxidation potential and the irreversibility of the oxidation process.[13]

$$RSH \underset{-H^+}{\longrightarrow} RS^*, 2RS^* \rightarrow RSSR$$

3.1

The formation of the radical Cys^* (RS^*) occurred first, followed by dimerization to form the disulfide bridged dimers (RSSR).[14]

LP61 as shown in **Figure 3.1**, with the same backbone structure with LP10, is a positively-charged polymer and was chosen for the assembly with *E. coli*. Polymer LP61 and LP10 were characterized via ^1H NMR, microanalysis, thermogravimetric analysis (TGA), gel permeation chromatography (GPC), ultraviolet-visible (UV-Vis), and photoluminescence spectroscopy. GPC results in **Table 3.4** showed a number-average molecular weight (M_n) of 69,000 for with dispersity index (Đ) of 2.1.

Table 3.4 GPC data for all chloroform-soluble polymer fractions.

Polymer	M_n[a] / g mol^{-1}	M_w[a] / g mol^{-1}	Đ[b]
LP6	69,000	144,600	2.1

a. Obtained from gel permeation chromatography in **THF** calibrated against polystyrene standards; M_n: the number weighted molecular weight, M_w: the mass weighted molecular weight; b. Dispersity, $Đ = M_w/M_n$

TGA shows the thermal decomposition of LP61 in **Figure 3.4a.** The polymer begins decomposition at around 200 °C (with a small amount of H_2O loss at lower temperatures), leaving a ~40% residual at 500 °C. The first mass loss corresponds to the loss of methyl

bromide,[15,16] and the second (onset decomposition temperature at around 300 °C) is due to side chain cleavage. Nanoparticles of polymer LP61 and LP10 have an average particle size around 500 nm and 150 nm, respectively (**Figure 3.5**, **3.6**). The photophysical properties of these two polymers were studied by UV-vis absorption and photoluminescence (PL) spectroscopy as shown in **Figure 3.7** and **Figure 3.8.** The absorption band of nanoparticle of polymer LP61

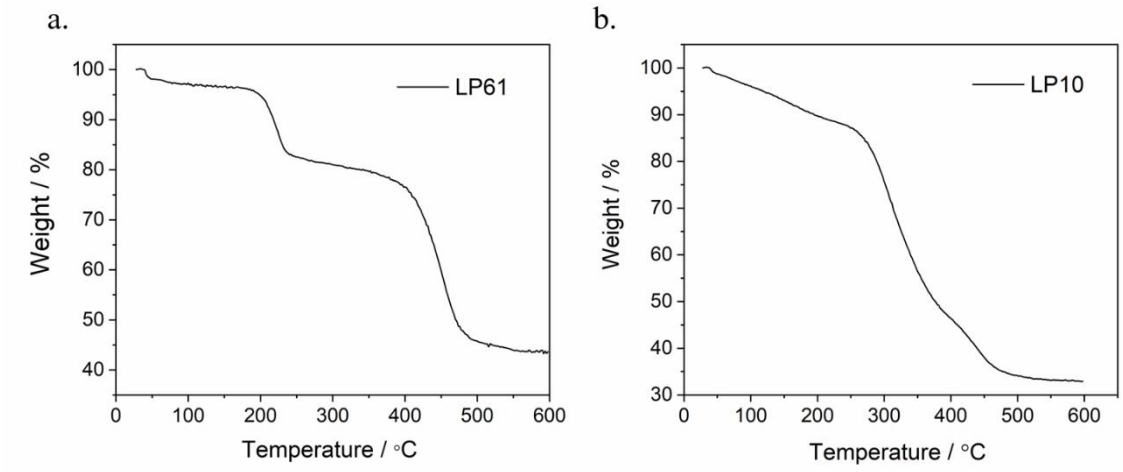

Figure 3.4 Thermogravimetric analysis of LP61 and LP10 under nitrogen at a heating rate of 10 °C min^{-1}.

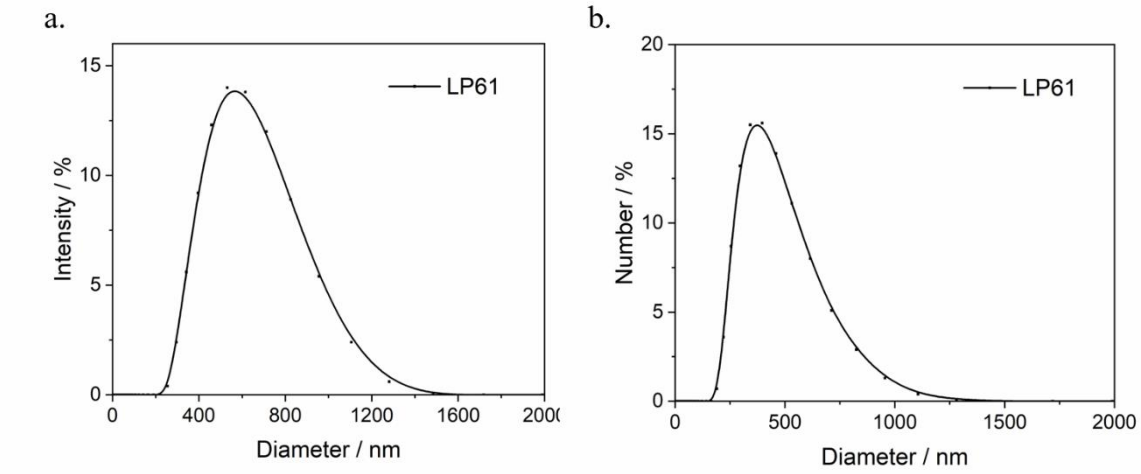

Figure 3.5 Size distribution of polymer nanoparticle LP61 with 50 mg/L polymer concentration by (a) intensity and (b) number.

and LP10 is centred at 375 nm; both polymers are emissive with a Stokes shift around 40 nm.

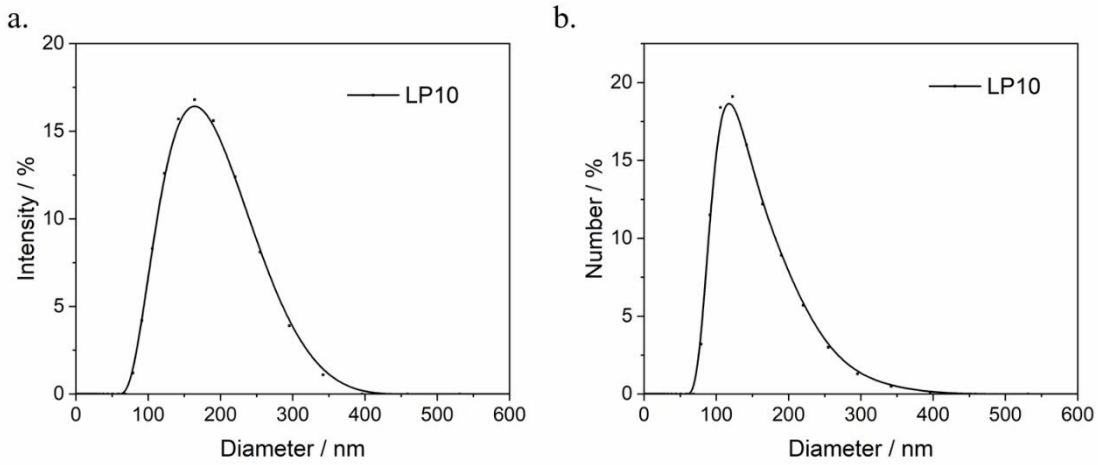

Figure 3.6 Size distribution of polymer nanoparticle LP61 with 50 mg/L polymer concentration by (a) intensity and (b) number.

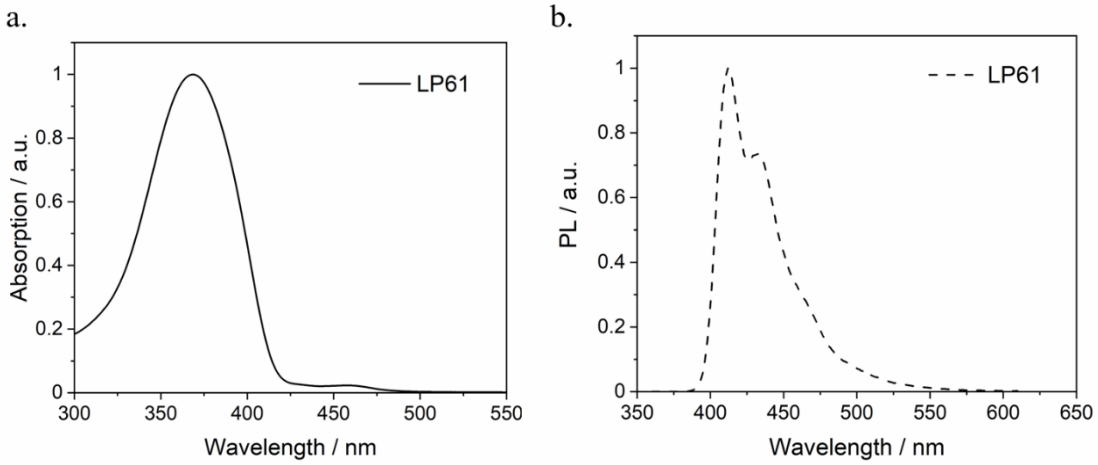

Figure 3.7 Normalised (a) absorption and (b) emission spectrum of polymer nanoparticle LP61.

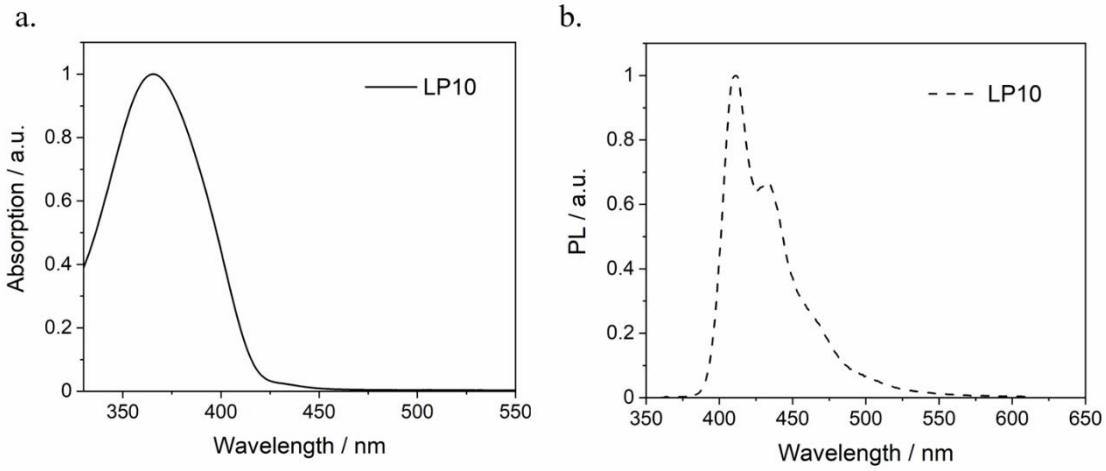

Figure 3.8 Normalised (a) absorption and (b) emission spectrum of polymer nanoparticle LP10.

3.2.1.1 Influence of Irradiation Period

The 5-h irradiation period was first studied. In **Figure 3.9**, there was around 0.30 μmol hydrogen produced from LP61/HydA BL21 biohybrid system after 5-h irradiation by a solar simulator while there was only 0.03 μmol produced from LP61 polymer alone and 0.07 μmol from HydA *E. coli* alone.

Interestingly, the performance of the dark control of the biohybrid system showed a similar but a bit lower trend as the *E. coli* alone under irradiation, which might indicate that either the irradiation itself or the presence of polymer would also influence the [FeFe] hydrogenase induction or hydrogen production performance of *E. coli*.

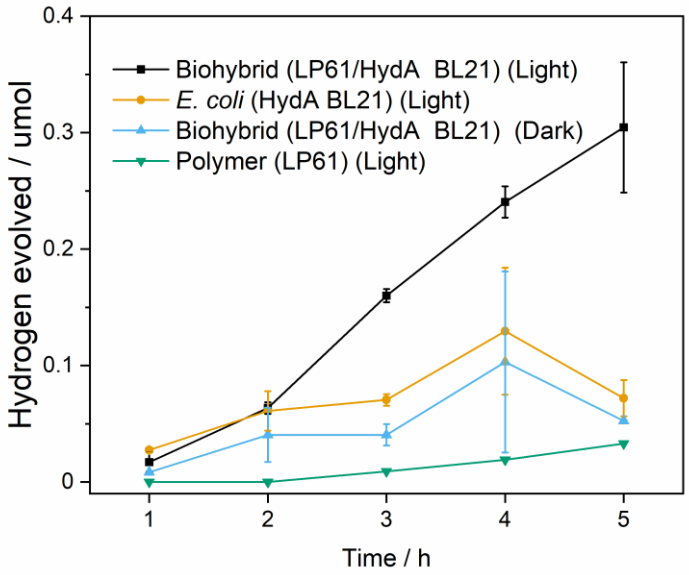

Figure 3.9 Hydrogen production performance of LP61/HydA BL21 biohybrid systems (irradiated and dark), *E. coli* (HydA BL21), and polymer (LP61) under 4-hour irradiation. Plots and error bars represent the averages and standard deviations of at least three assays.

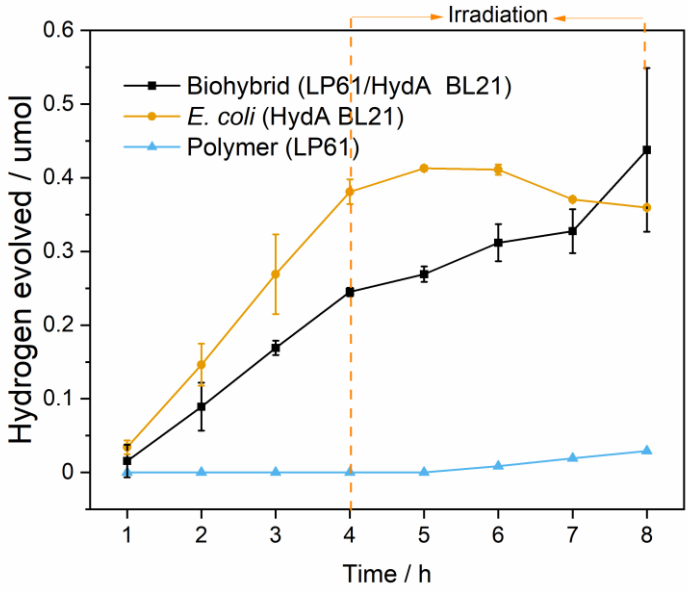

Figure 3.10 Hydrogen production performance of LP61/HydA BL21 biohybrid system, *E. coli* (HydA BL21), and polymer (LP61) of 4 hours in dark and 4 hours under irradiation. Plots and error bars represent the averages and standard deviations of at least three assays.

Therefore, we first measured the hydrogen production performance of LP61/HydA BL21 biohybrid system, HydA BL21, and LP61 polymer after 5 hours in dark in **Figure 3.10**, there was no detectable hydrogen produced from the polymer sample, and 0.24 µmol hydrogen was formed from biohybrid sample while there was 0.38 µmol produced from the *E. coli* alone with a higher production rate. It might indicate that the presence of polymer has a negative influence on the hydrogen production performance of HydA BL21 *E. coli*. After 4-hour irradiation, the accumulated amount of hydrogen produced by the biohybrid system was increased to 0.44 µmol while for *E. coli* alone it had no obvious increase. There might be multiple reasons behind the ceased or step-down hydrogen formation of *E. coli* alone like the irradiation might have a native influence on [FeFe] hydrogenase expression. As there are supposed to be two pathways here for HydA BL21 *E. coli* to produce hydrogen, one is through the constructed [FeFe] hydrogenase,[10] and the other is through the glucose fermentation pathway,[17] and there is no clear evidence to show that which might be the dominant one.

We further shortened the dark period time to 2 hours and extended the irradiation time to 6 hours as shown in **Figure 3.11**. After 2 hours in dark and 6 hours under irradiation, the hydrogen production performance of the LP10/HydA BL21 biohybrid system ended up with 0.60 µmol for biohybrid and 0.36 µmol for *E. coli* alone. Therefore, the hydrogen production

performance of the biohybrid systems was further studied and optimized based on this dark/irradiation setting (2 hours in dark followed by 6 hours under irradiation).

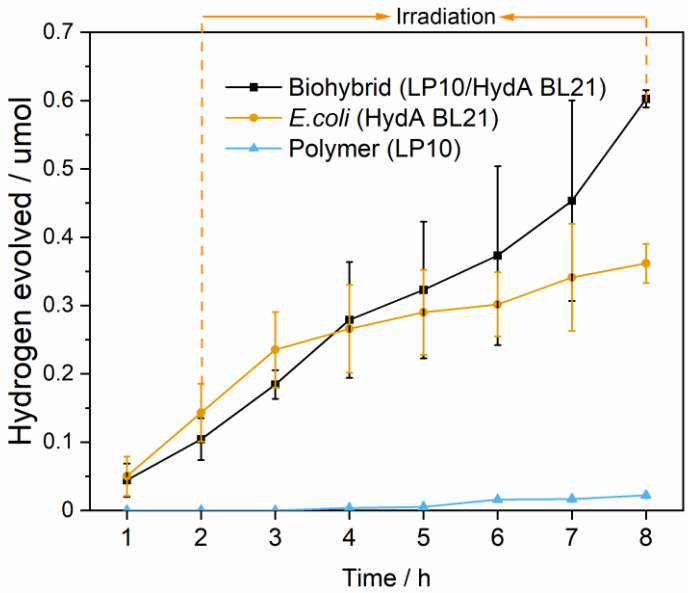

Figure 3.11 Hydrogen production performance of LP10/HydA BL21 biohybrid system, *E. coli* (HydA BL21), and polymer (LP10) of 2 hours in dark and 6 hours under irradiation. Plots and error bars represent the averages and standard deviations of at least three assays.

3.2.1.2 Influence of Different Polymers

Nanoparticles of different conjugated polymers (LP10, LP11, LP31, LP41) were assembled with HydA BL21 cells in **Figure 3.12**. We first explored the influence of residual Pd on the activity of *E. coli* in dark. The performance of these conjugated polymers with different amounts of residual Pd (269 ppm/LP41, 93 ppm/LP31, 1710 ppm/LP11, 1600 ppm/LP10) coupled with *E. coli* cells was in the range of 0.73 – 0.89 μmol in dark, which shows no clear correlation of the amount of residual Pd in different polymers. For the biohybrid systems under irradiation, LP31/HydA BL21 has the highest performance with 1.82 μmol followed by LP41/HydA BL21 and LP11/HydA BL21 with 1.53 μmol, and LP10/HydA BL21 with 1.43 μmol. Among all these four biohybrid systems, the hydrogen production performance of LP31/HydA BL21 under irradiation was increased by 2.5 times compared with its dark control (from 0.74 to 1.82 μmol), which is the largest increase; the LP11 biohybrid system shows 2 times increase (from 0.73 to 1.53 μmol) followed by the LP41 biohybrid with 1.9 times increase (from 0.80 to 1.53 μmol), and LP10 biohybrid with 1.6 times increase (from 0.89 to 1.44 μmol).

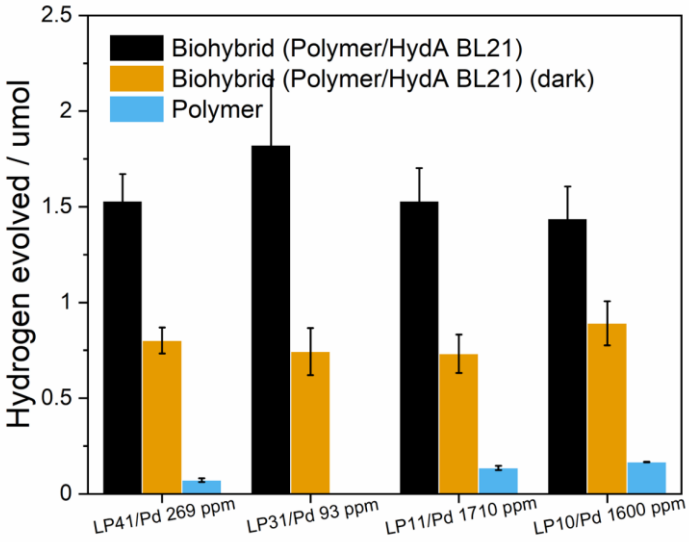

Figure 3.12 Hydrogen production performance of biohybrid systems (under irradiation and in dark) containing different conjugated polymer nanoparticles (LP41, LP31, LP11, and LP10) with HydA BL21 cells with 1 mM cysteine as the sacrificial electron donor. The measurement was conducted after 2 hours in dark followed by 6 hours under irradiation. Plots and error bars represent the averages and standard deviations of at least three assays for samples containing *E. coli*.

3.2.1.3 Influence of Sacrificial Electron Donors

Different ascorbic acid concentrations (0.1 M, 0.05 M, 0.01 M, and 1 mM) were studied in LP41 biohybrid systems in **Figure 3.13**, and it turns out that 1 mM was optimal for the hydrogen production performance which shows 2.7 times increase from 0.89 to 2.43 μmol under irradiation compared with its dark control. When the concentration of ascorbic acid was too high reaching 0.1 M, the reaction medium would be too acidic with a pH of 2.6 (the experimentally measured pH of a 0.1 M ascorbic acid solution), which is not suitable for the growth of *E. coli*. *E. coli* can survive without growth for several hours at pH 2.0,[18] and the acid limit for growth of *E. coli* is pH 4.0 in rich medium, or pH 4.5 in minimal medium.[19] However, for LP21 biohybrid systems, it shows a different trend in **Figure 3.14.**

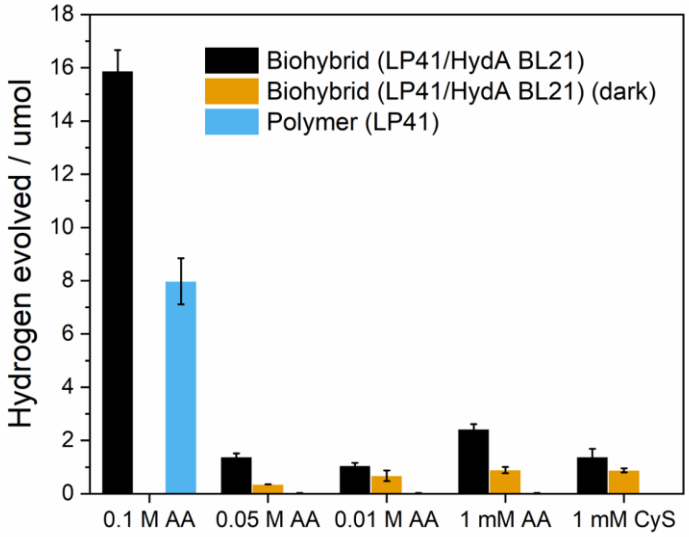

Figure 3.13 Hydrogen production performance of LP41 biohybrid systems (under irradiation and in dark) and LP41 polymer alone with different ascorbic acid concentrations (0.1 M, 0.05 M, 0.01 M, and 1 mM) and 1 mM cysteine as the sacrificial electron donor. Hydrogen amounts were normalised to 1 mg polymer amount. The measurement was conducted after 2 hours in dark followed by 6 hours under irradiation. Plots and error bars represent the averages and standard deviations of at least three assays for samples containing *E. coli*.

Among different ascorbic acid concentrations, 0.01 M ascorbic acid was the optimal one with 2.6 times increase from 0.65 to 1.67 μmol but the polymer alone also contributed 0.37 μmol. When 1 mM cysteine was used, the LP21 biohybrid produced 0.82 μmol in the dark and 1.78 μmol under irradiation, and the polymer alone produced 0.14 μmol hydrogen. Different preferences of sacrificial electron donors for biohybrid systems composed of conjugated polymers with different backbone structures might indicate different interactions between SED and polymers, such as their different driving forces for SED oxidation.

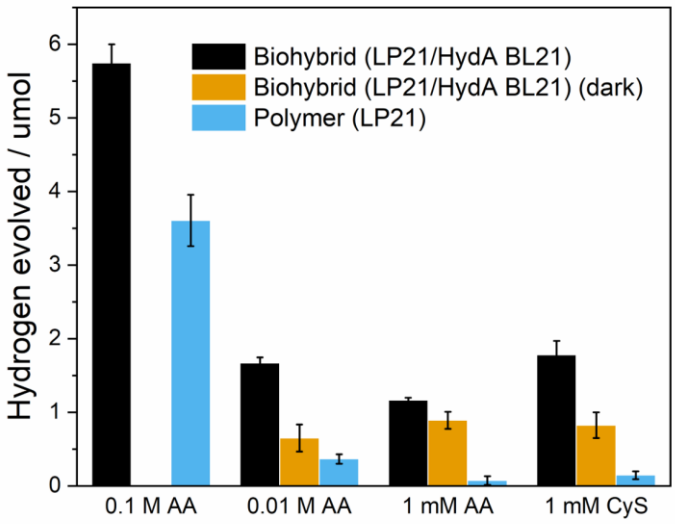

Figure 3.14 Hydrogen production performance of LP21 biohybrid systems (under irradiation and in dark) and LP21 polymer alone with different ascorbic acid concentrations (0.1 M, 0.01 M, and 1 mM) and 1 mM cysteine as the sacrificial electron donor. Hydrogen amounts were normalised to 1 mg polymer amount. The measurement was conducted after 2 hours in dark followed by 6 hours under irradiation. Plots and error bars represent the averages and standard deviations of at least three assays for samples containing *E. coli*.

3.2.1.4 Optimization of LP41/HydA BL21 Biohybrid System

The LP41/HydA BL21 biohybrid system was further optimized by using 100, 50, and 25 mg/L LP41 polymer concentrations respectively in **Figure 3.15**.

By using a higher polymer concentration (100 mg/L, 0.66 mg polymer), the hydrogen production performance of the biohybrid system both under irradiation (1.53 μmol) and in dark (0.80 μmol) was almost similar to the one with 50 mg/L polymer concentration with 0.33 mg polymer (1.44 μmol under irradiation, 0.75 μmol in dark). It might be due to the increased polymer concentration contributing little to the interactions between conjugated polymer nanoparticles and *E. coli* cells. However, when decreasing the polymer concentration to 25 mg/L, the biohybrid system produced slightly less hydrogen (1.22 μmol) under irradiation while more in the dark (0.92 μmol). It is consistent with previous data in **Figure 3.9** which showed that the presence of polymers might have a negative influence on the hydrogen production performance of HydA BL21 cells. For polymer samples with different polymer concentrations, all produced around 0.07 μmol hydrogen without any significant difference.

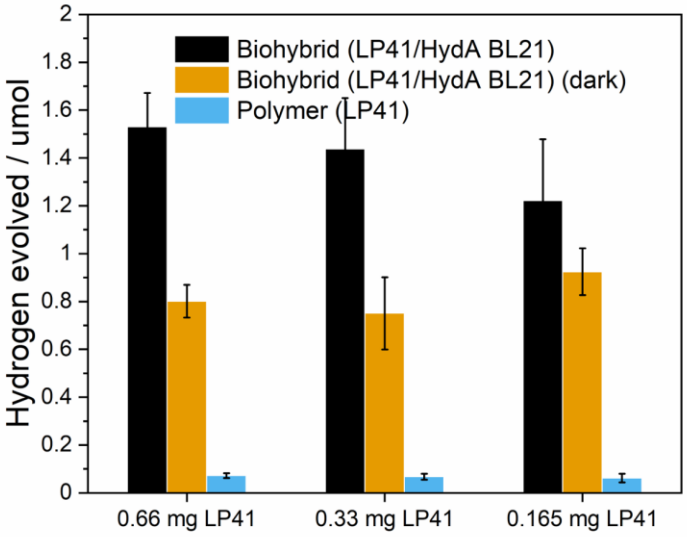

Figure 3.15 Hydrogen production performance of LP41 biohybrid systems (under irradiation and in dark) and LP41 polymer alone with different LP41 polymer concentrations (100, 50, 25 mg/L). The measurement was conducted after 2 hours in dark followed by 6 hours under irradiation with 1 mM cysteine as sacrificial electron donor. Plots and error bars represent the averages and standard deviations of at least three assays for samples containing *E. coli*.

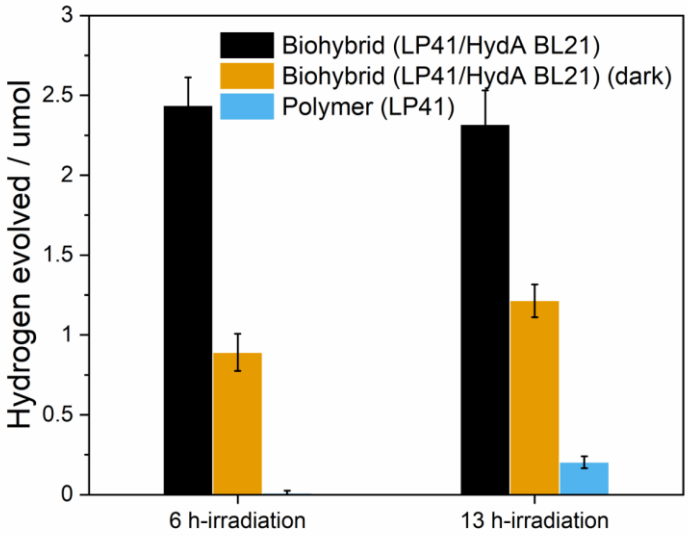

Figure 3.16 Hydrogen production performance of LP41 biohybrid systems (under irradiation and in dark) and LP41 polymer alone with 6-hour and 13-hour irradiation respectively. The measurement was conducted with 1 mM ascorbic acid as sacrificial electron donor. Plots and error bars represent the averages and standard deviations of at least three assays for samples containing *E. coli*.

In addition, in **Figure 3.16**, when the irradiation time was extended from 6 hours to 13 hours, the hydrogen evolution activity of biohybrid in dark and polymer alone were increased from 0.89 to 1.21 μmol and 0 to 0.20 μmol while the activity of biohybrid systems under irradiation was almost the same (2.43 and 2.32 μmol for 6-hour and 13-hour irradiation separately).

Figure 3.17, summarizes the optimized hydrogen production performance of LP41/HydA BL21 biohybrid systems. There was 1.61 μmol hydrogen produced from the biohybrid system under irradiation while there was 0.59 μmol from the dark control, which shows 2.7 times increase. For the *E. coli* alone group, 0.36 μmol hydrogen was generated both in dark and under irradiation, which might indicate that irradiation has no obvious influence on the performance of the HydA BL21 sample alone. For LP41 polymer alone, there was only 0.02 μmol hydrogen produced.

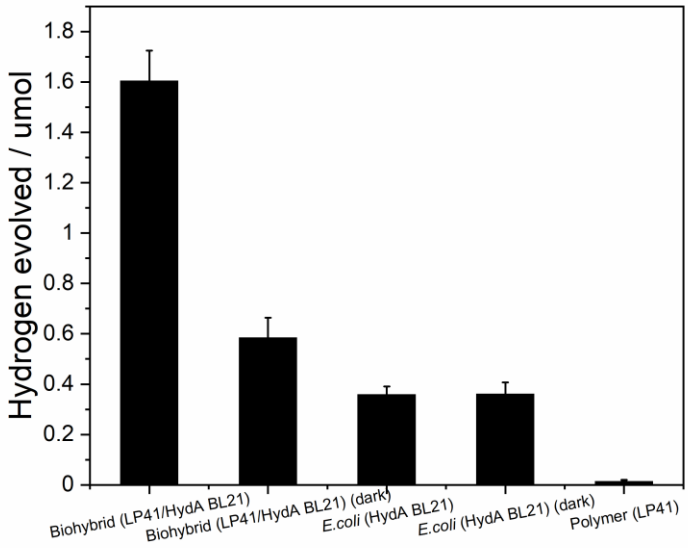

Figure 3.17 Hydrogen production performance of LP41/HydA BL21 biohybrid systems. The measurement was conducted after 2 hours in dark followed by 6 hours under irradiation with 1 mM ascorbic acid as sacrificial electron donor. Plots and error bars represent the averages and standard deviations of at least three assays for samples containing *E. coli*.

3.2 Assembly Strategy II

Although assembly strategy I was a relatively simple procedure, it involves all the chemicals used for hydrogenase induction/expression in the reaction mixture for photocatalytic hydrogen measurement. This complicates the biohybrid system and makes it challenging to clarify the synergy between materials and microorganisms and the underlying mechanisms. Assembly strategy II as described in **Figure 3.18**, by directly coupling the *E. coli* with expressed [FeFe] hydrogenase with polymer nanoparticles, gives rise to a much simpler biohybrid solution with only *E. coli*, polymer particle, and sacrificial electron donor involved.

The *E. coli* BL21 strain was grown and enable to express [FeFe] hydrogenases using a procedure based on previously reported work.[10] The cells were then harvested by pelleting, washing, and redispersion before they were used in the assembly process giving the polymer-bacteria hybrid systems.

Table 3.5 Components of PBS (Phosphate Buffered Saline) (1×, pH 7.4) per litre.

Component	Amount	Concentration
NaCl	8.0 g	0.137 M
KCl	0.2 g	0.0027 M
Na_2HPO_4	1.44 g	0.01 M
KH_2PO_4	0.245 g	0.0018 M

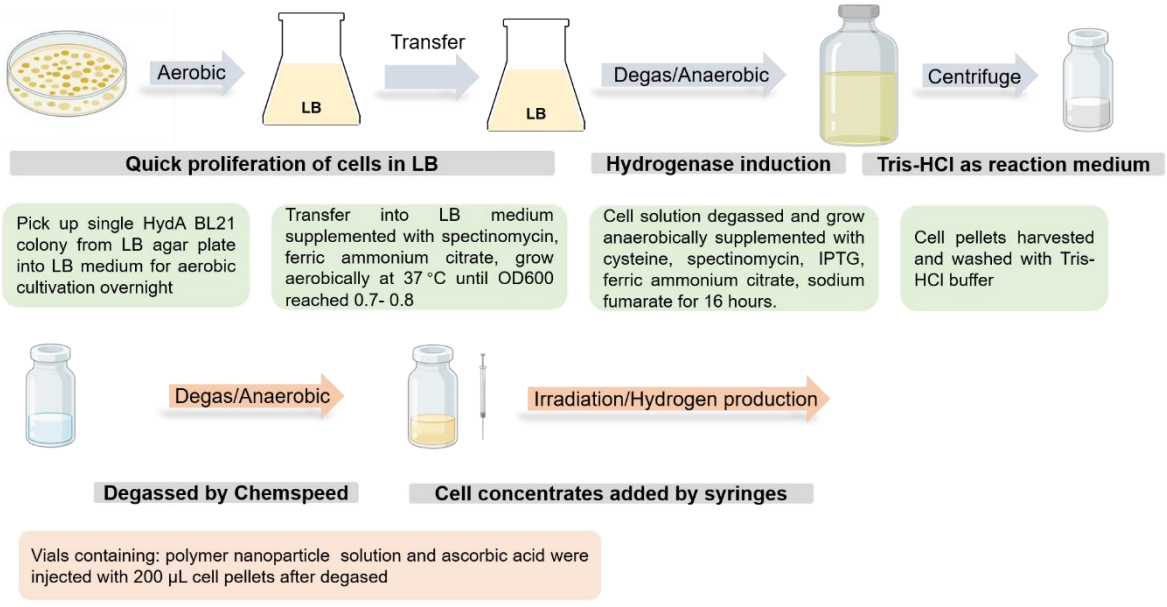

Figure 3.18 Assembly strategy II: hydrogenase induction, biohybrid assembly, and hydrogen production.

We found that the dispersion medium for the polymer nanoparticles and *E. coli* cells is a critical factor in the assembly process, along with the physio-chemical properties of the materials such

as polymer particle size, surface charge, and surface hydrophobicity/hydrophilicity. When high salt content media were used, such as phosphate-buffered saline agar and M9 Minimal agar (**Table 3.2** and **3.4**), the polymer nanoparticles aggregated and the attachment efficiency to *E. coli* cells was reduced significantly, as evident in confocal microscopy when LP41/*E. coli* biohybrid samples were excited at 488 nm. For instance, using M9 minimal agar, we observed aggregates of LP41 nanoparticles separated from the *E. coli* cells, and phosphate-buffered saline agar resulted in aggregates of the polymer nanoparticles with bacteria cells (**Figure 3.19**). Similar aggregation was also observed previously for related polymer photocatalysts in high salt-content media.[20] Thus, a low ionic strength medium, such as tris(hydroxymethyl)aminomethane hydrochloride (Tris-HCl), appears to be required for the generation of the hybrid systems.

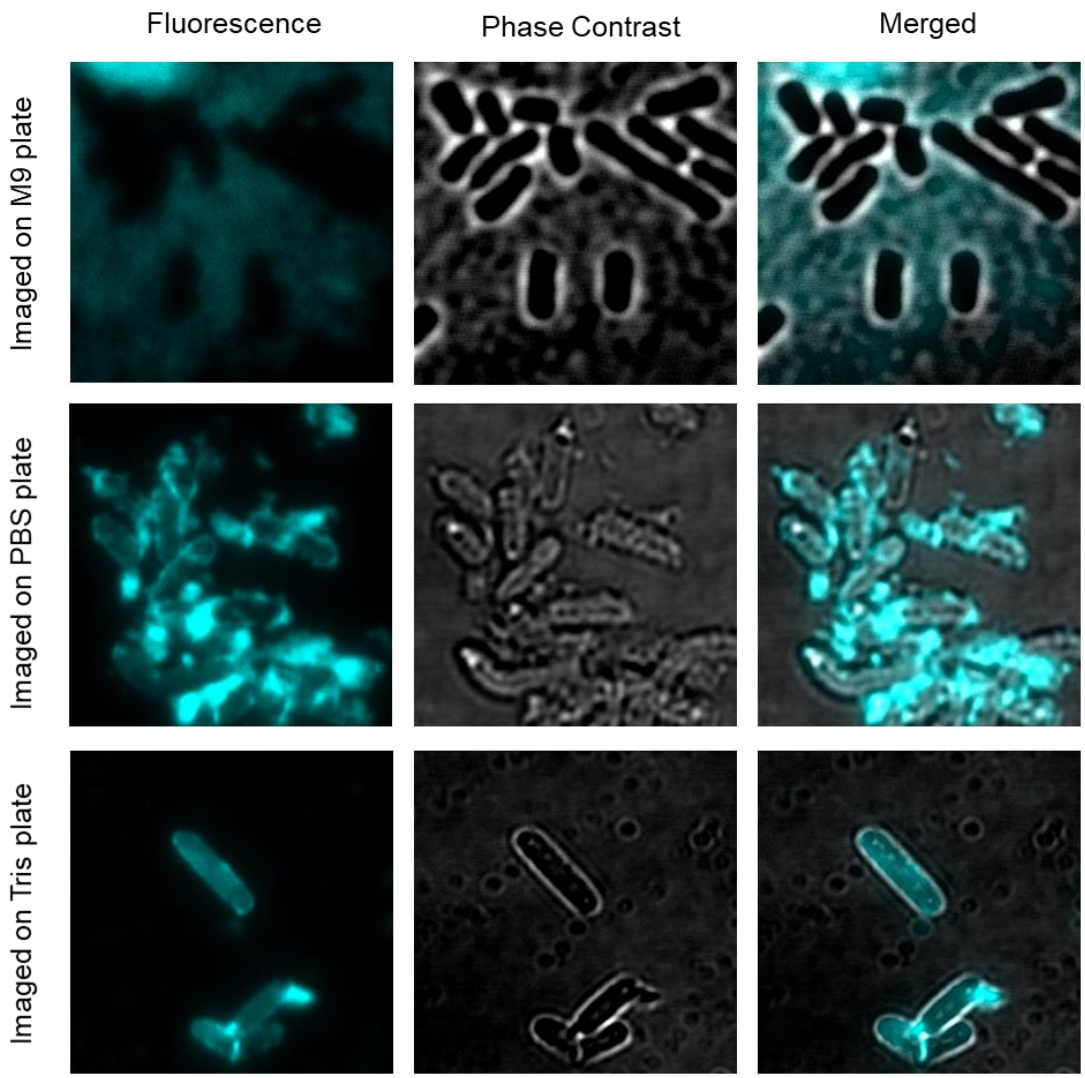

Figure 3.19 Confocal images of HydA *E. coli* (100 µL concentrates in 10 mM Tris-HCl) incubated with LP41 nanoparticles (1.0 mL, 5 mg L^{-1}) for 5 mins (λ_{exc} = 488 nm) imaged on 10 mM tris(hydroxymethyl)aminomethane hydrochloride (Tris-HCl)/agar, 1 ×phosphate-buffered saline (PBS)/agar, and 1 ×M9 minimal media (M9)/agar plates.

Based on these observations, we assembled the recombinant *E. coli* (HydA BL21) with the polymer nanoparticles in a 10 mM Tris-HCl (pH 7) buffer with 1 mM ascorbic acid after nitrogen purging to give the biohybrid systems. SEM and confocal images revealed that the polymer nanoparticles localized on the surface of the *E. coli* cells, while some free polymer nanoparticles were also present (**Figure 3.20**). Although quantifying the attachment of the polymer nanoparticles was difficult, it is evident that LP21 attaches less effectively to the surface of the *E. coli* cells (**Figure 3.21**).

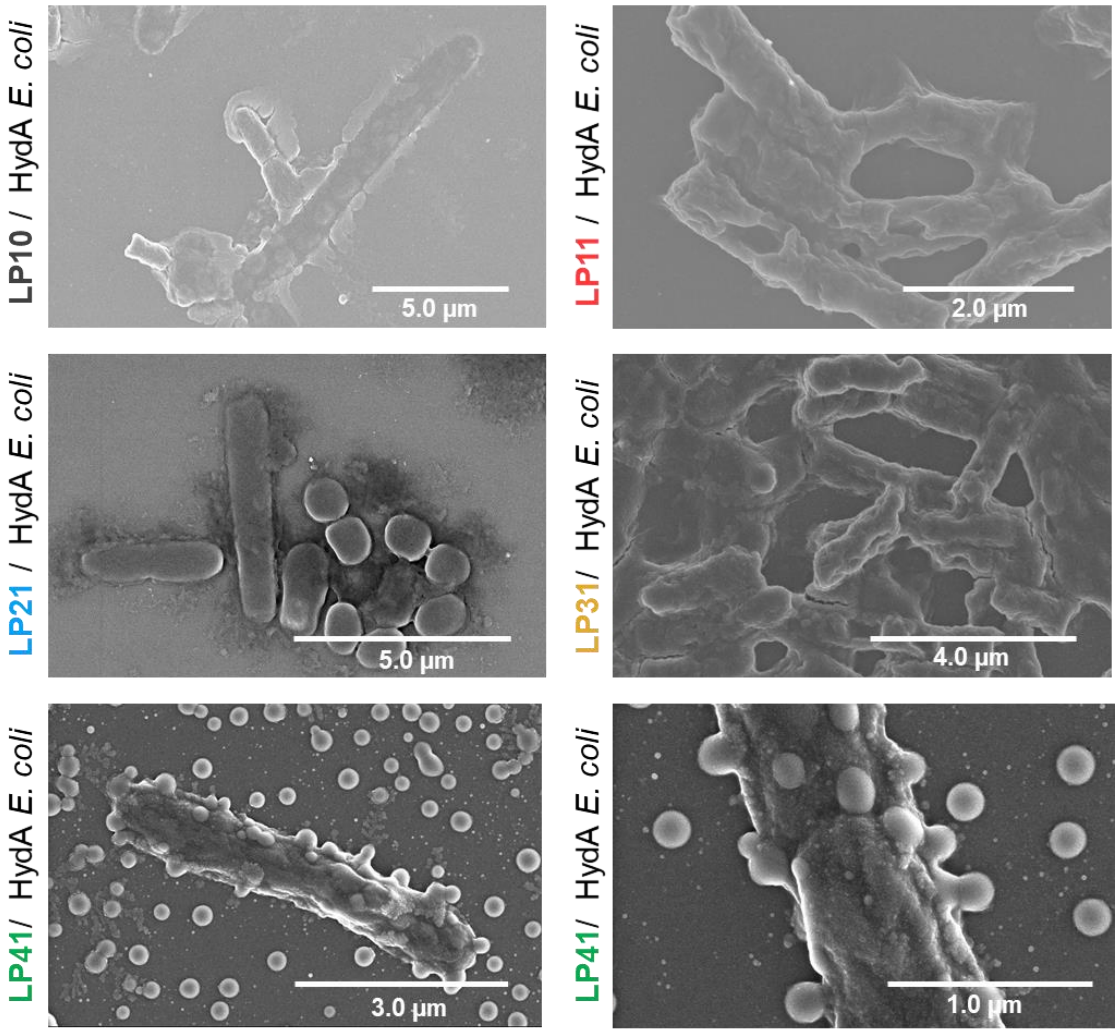

Figure 3.20 SEM images of HydA *E. coli* (200 µL concentrates in 10 mM Tris-HCl) incubated with LP10, LP11, LP21, LP31, and LP41 nanoparticles (2.0 mL, 10 mg L^{-1}).

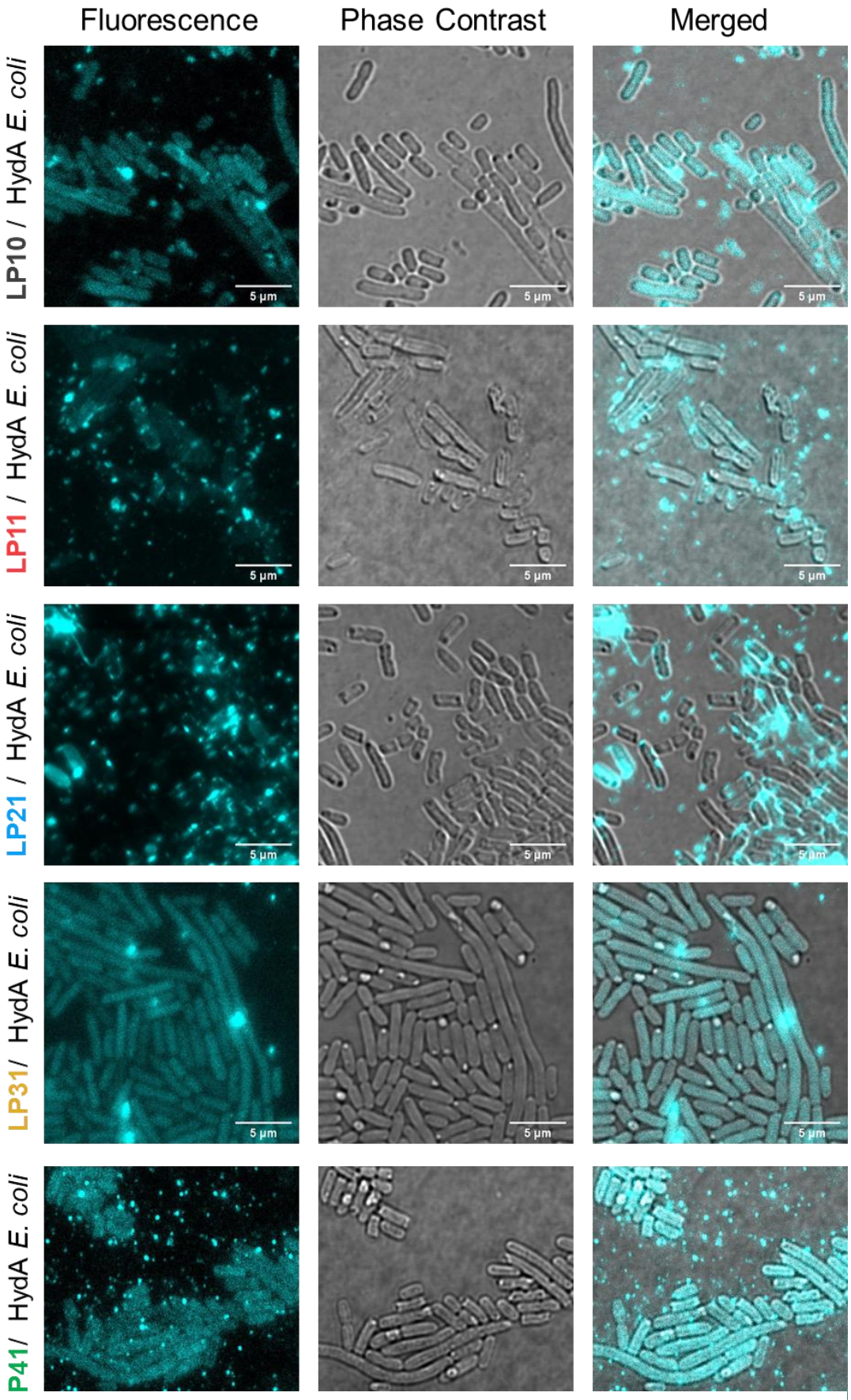

Figure 3.21 Confocal images of HydA *E. coli* (100 µL concentrates in 10 mM Tris-HCl) incubated with LP10, LP11, LP21, L31, and LP41 nanoparticles (1.0 mL, 5 mg L^{-1}) for 5 mins (λexc = 488 nm).

3.3 Photobiocatalytic Hydrogen Evolution Performance

3.3.1 Different Conjugated Polymers

The performance of the polymer-*E. coli* hybrid systems for photobiocatalytic hydrogen production was evaluated under AM1.5G solar simulator irradiation for three hours in Tris-HCl buffer, using ascorbic acid acting as the sacrificial hole-scavenger. The results showed that *E. coli* (HydA BL21) alone was found to be inactive and did not produce any detectable hydrogen, while the polymer nanoparticles alone produced only a small amount of hydrogen ranging from 4 nmol h^{-1} for LP41 to 13 nmol h^{-1} for LP21 (**Figure 3.22**). The limited activity of these polymers on their own can be attributed to the cocatalytic activity of residual palladium in the materials that originates from the Suzuki-Miyaura polycondensation reaction. When the polymer nanoparticles were coupled with *E. coli* cells, the amount of hydrogen produced significantly increased. The LP41 biohybrid system produced 148 nmol h^{-1}, which was 31 times more than the polymer nanoparticles alone. The LP10 and LP11 biohybrid systems also showed increased hydrogen evolution, producing 100 nmol h^{-1} and 89 nmol h^{-1}, respectively. By

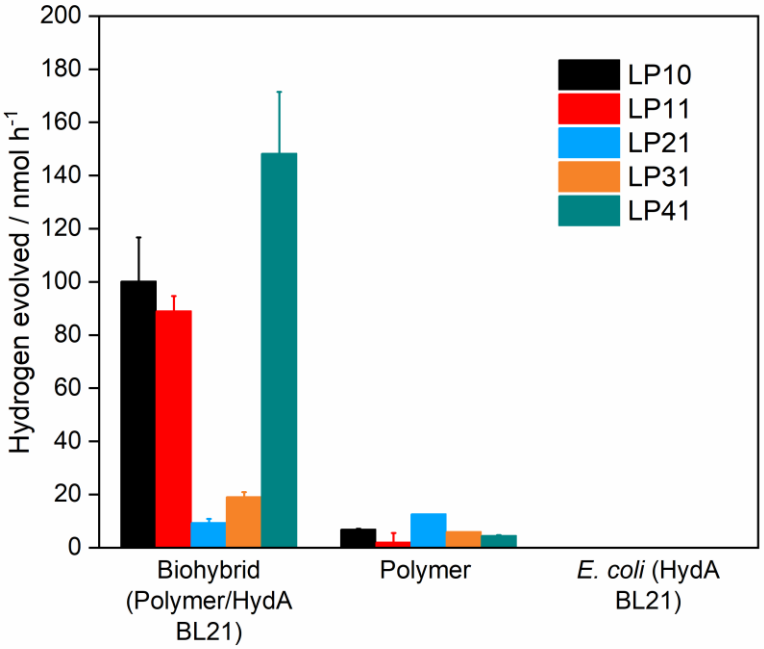

Figure 3.22 Hydrogen production performance of five biohybrid systems with different conjugated polymer nanoparticles (50 mg L^{-1}, LP10, LP11, LP21, LP31, and LP41) alongside polymer and *E. coli* control groups. All of the hydrogen production reactions were conducted in 10 mM tris(hydroxymethyl)aminomethane chloride buffer (pH 7, Tris-HCl) supplemented with 1 mM ascorbic acid as the hole sacrificial agent under irradiation of an AM 1.5G solar simulator for 3 h. Biohybrid reactions consist of 4.3 mL polymer nanoparticle solution, 200 µL *E. coli* concentrates, 0.5 mL 100 mM Tris-HCl, and 50 µL 0.1 M ascorbic acid.

contrast, the LP21 hybrid system showed a net reduction in the amount of hydrogen produced (2 nmol h^{-1}). The LP31 hybrid system showed only a small increase in hydrogen production (19 nmol h^{-1}).

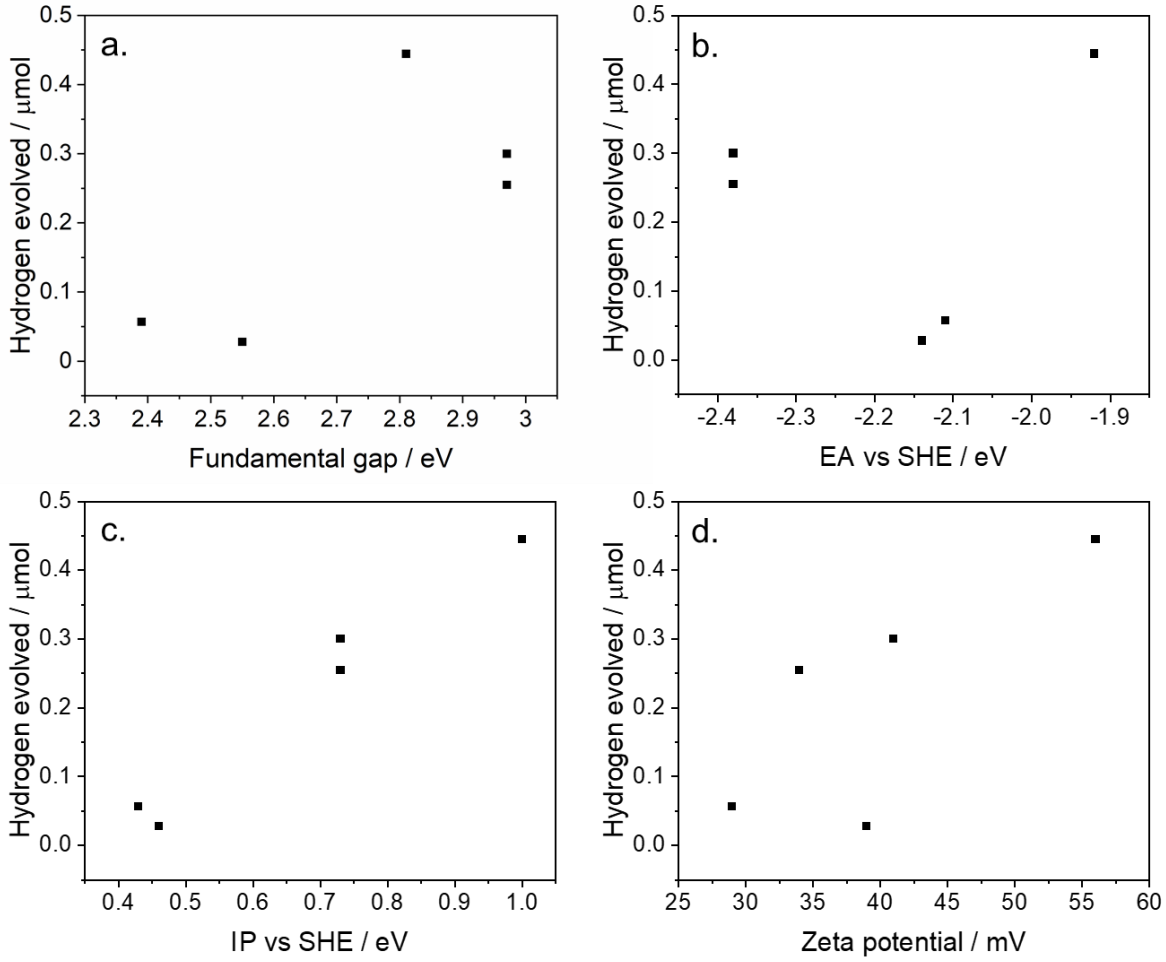

Figure 3.23 Correlation between the biohybrids' photobiocatalytic activity and the polymer fundamental gap **(a)** / EA value **(b)** / IP value **(c)**/zeta-potential **(d)**.

Consistent with our previous findings on conjugated polymer photocatalysts, there is little correlation between the observed hydrogen evolution rates and the polymers' predicted EA values, assuming that the potentials of the LP11-LP41 photocatalysts are similar to those of their LP1-4 counterparts. By contrast, there is a clear correlation with the predicted IP values (**Figure 3.23**). This is because the oxidation of the ascorbic acid electron donor is required for hydrogen evolution. All polymers are predicted to have a sufficiently negative EA, and hence a significant driving force for proton reduction (**Figure 3.24**), while the predicted IP of polymers LP2 and LP3 are barely positive enough to drive ascorbic acid oxidation. There is

also an apparent correlation with the polymer particles' zeta-potential, most likely because the zeta-potential of the polymer particles varies in a similar fashion to their IP values.

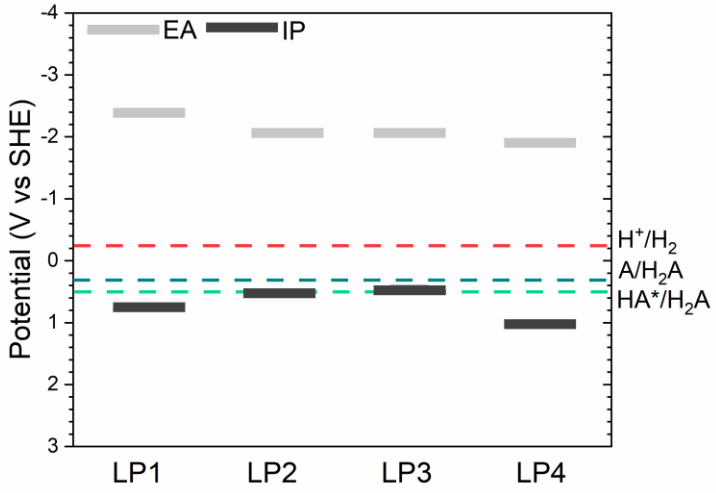

Figure 3.24 Predicted charge carrier potentials (IP, EA) of the polymers considered calculated through (TD-)DFT for oligomer models in water. Dashed colored lines indicate the potentials for different solution reactions: red, proton reduction; cyan and green, two-hole (A/H_2A) and one-hole ($HA\cdot/H_2A$) oxidation of ascorbic acid. All solution potentials shown are for pH 6.5, the experimentally measured pH of a 10 mM tris(hydroxymethyl)aminomethane chloride buffer (pH 7, Tris-HCl) supplemented with 1 mM ascorbic acid.

Table 3.6 Predicted potentials for the different solution half-reactions at pH 0 were taken from previous work, potentials at pH 6.5 were estimated based on equation: $E = E^0 - 0.05916 \times pH$, E^0: potential at pH 0. Ascorbic acid* and dehydroascorbic acid are the one-hole and two-hole oxidation products of ascorbic acid, respectively.

Solution half-reaction	Potential (V vs. SHE)	
	pH 0	pH 6.5
H+ (aq) + e- -> 1/2 H_2 (g)	0	-0.38
Ascorbic acid* (aq) + H^+ (aq) + e^- -> Ascorbic acid (aq)	0.80	0.42
Dehydroascorbic acid + 2 H^+ (aq) + 2e^- -> Ascorbic acid (aq)	0.40	0.015

The polymer mass normalized LP41/*E. coli* biohybrid system has a photobiocatalytic sacrificial hydrogen evolution rate of 3.442 mmol g^{-1} h^{-1}. Over a 36-hour period, this biohybrid system produced 3,334 nmol of hydrogen (**Figure 3.25**). Steady hydrogen production observed for 20 hours did not exhibit any significant rate change. By contrast, *E. coli* (HydA BL21) alone produced no measurable quantity of hydrogen, while the conjugated polymer LP41 produced only 452 nmol. Although there are very few estimates of the generation time of bacteria in biohybrid systems under photocatalytic conditions, *E. coli* can divide every 20 min in the laboratory under aerobic, nutrient-rich conditions.[21] This might indicate that the physical interactions between *E. coli* cells and polymer particles in the biohybrid suspension are

dynamic. Furthermore, despite differences in growth conditions, *E. coli* shares the same sigmoidal growth curve tendency starting with a lag phase followed by a logarithmic phase, a stationary phase, and a death phase.[22] It takes approximately 12-16 hours for *E. coli* to transfer from the logarithmic phase to stationary in optimal laboratory conditions (nutrient-rich media, 37 °C and agitation),[23] which might explain the appearance of plateaus after 20 hours in **Figure 3.25a**.

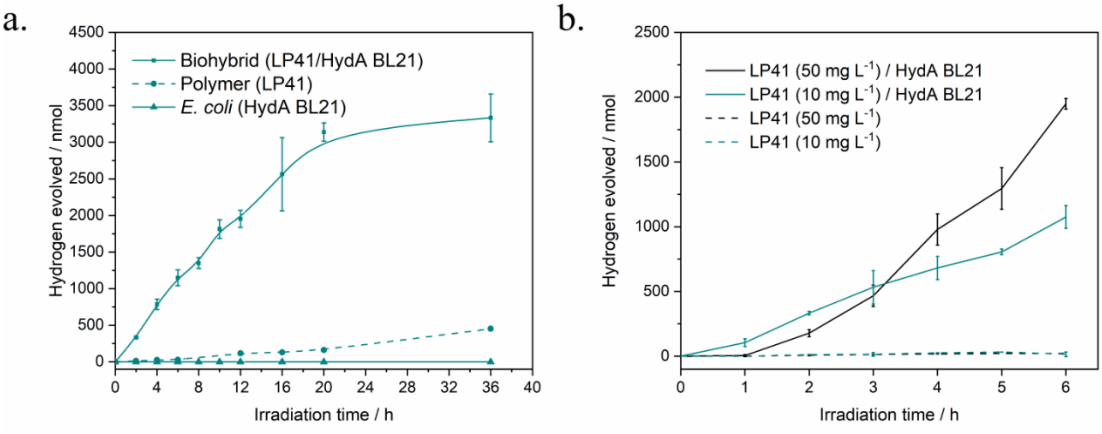

Figure 3.25 (a) The H_2 formation rate by the biohybrid (10 mg L^{-1} LP41/HydA BL21), the polymer (10 mg L^{-1} LP41), and *E. coli* (HydA BL21). (b) The H_2 formation rate by the biohybrid (LP41/HydA BL21) and the polymer (LP41) with 50 and 10 mg L^{-1} polymer concentration, respectively.

As expected, the biohybrid system did not produce hydrogen in the dark or under irradiation in the absence of ascorbic acid. Taken together, these results support the formation of a biohybrid system in which both components—the conjugated polymer and the genetically engineered *E. coli* cells—take part in a photocatalytic process.

3.3.2 Different Reaction Medium

Some conjugated polyelectrolytes have been shown previously to be bactericidal, both in the dark and under irradiation.[24] We therefore investigated whether the *E. coli* cells in the biohybrid remained viable in the presence of the charged polymer nanoparticles. When glucose was added as an energy and carbon source to the reaction medium, *E. coli* wild-type (WT) BL21(DE3) cells were able to produce hydrogen at a rate of 10 nmol h^{-1} through glucose fermentation without irradiation (**Figure 3.27**),[25] while it remained inactive in the dark without glucose (**Figure 3.28**). For comparison, the hydrogen evolution rate of the LP41/*E. coli* biohybrid system was approximately 200 nmol h^{-1} under irradiation in the presence of 100 mM Tris-HCl, 150 mM NaCl, 0.4 wt. % glucose, and 1 mM ascorbic acid.

The biohybrid system also remained active for glucose fermentation in the dark at a rate of 15 nmol $h^{-1}$with ascorbic acid or 10 nmol h^{-1} without ascorbic acid, similar to *E. coli* WT BL21(DE3) under the same conditions (around 10 nmol h^{-1} with or without ascorbic acid) (**Figure 3.27, 3.28**). Taken together, these results indicate that the lack of light energy and a carbon source in the reaction medium inhibits the fermentation pathways. The *E. coli* cells in the biohybrid system remained viable after assembly with the conjugated polymer and relatively stable under photocatalytic conditions, as evident from 36-hours irradiation experiments in **Figure 3.25a**.

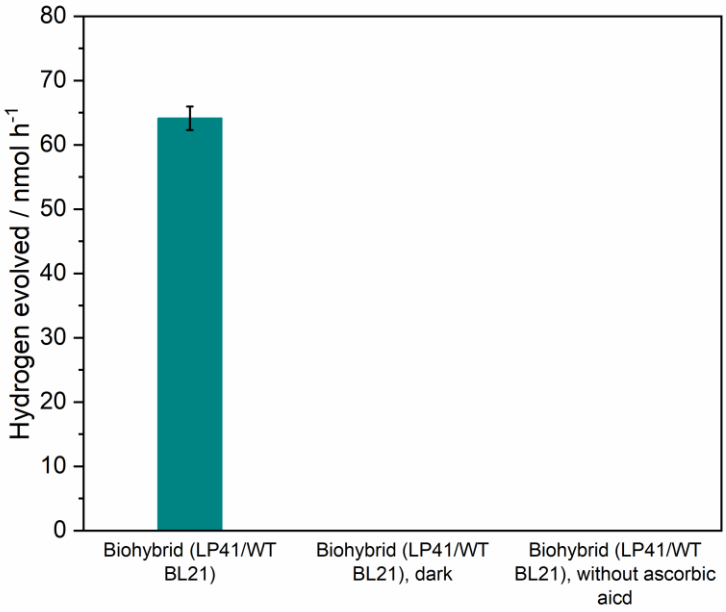

Figure 3.26 Hydrogen production performance of LP41 coupled with WT *E. coli* in 10 mM Tris-HCl with 1 mM ascorbic acid under irradiation with the comparison of the biohybrid system in dark and the one without ascorbic acid.

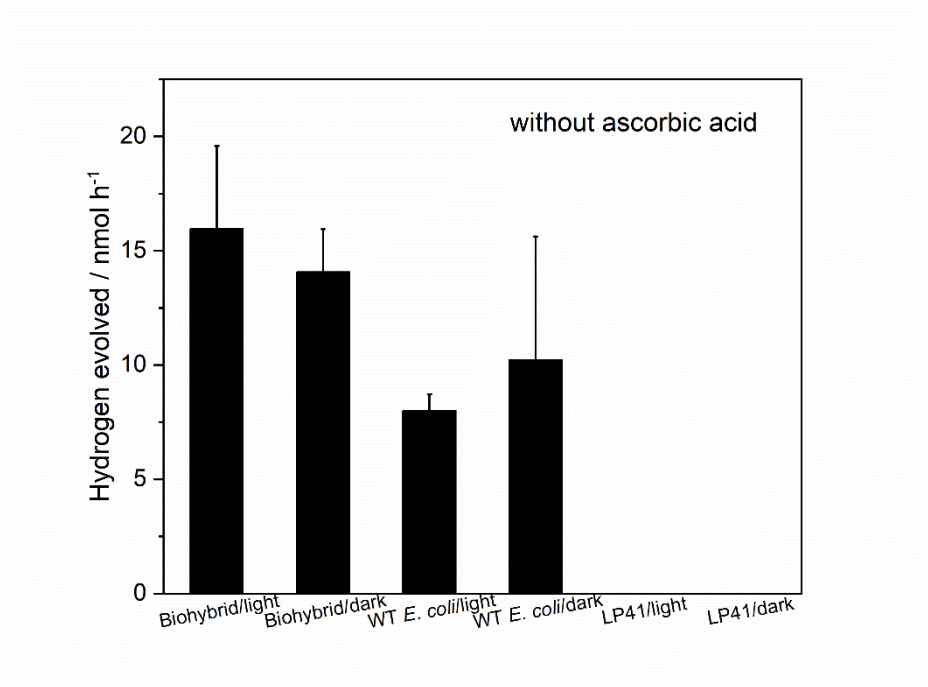

Figure 3.27 Hydrogen production performance of LP41 coupled with WT *E. coli* in 100 mM Tris-HCl/150 mM NaCl/0.4 wt. % glucose medium with and without irradiation.

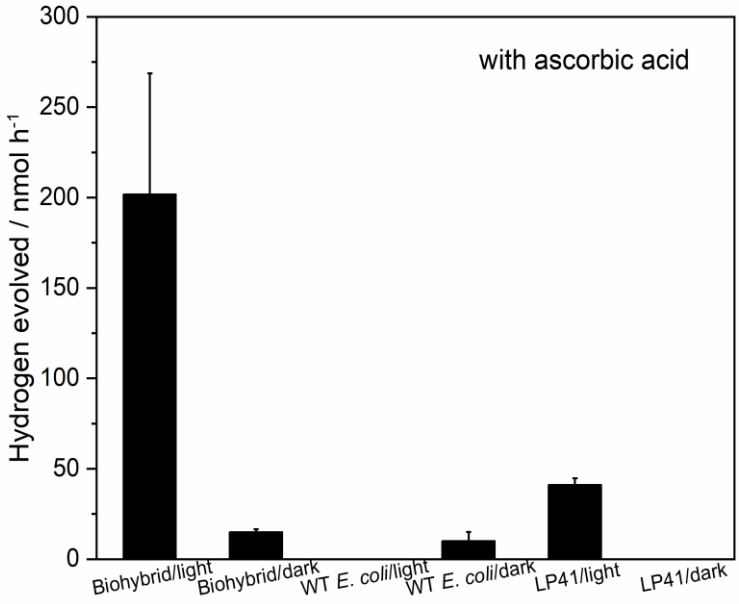

Figure 3.28 Hydrogen production performance of LP41 coupled with WT *E. coli* in 100 mM Tris-HCl/150 mM NaCl/0.4 wt. % glucose medium with 1 mM ascorbic acid as sacrificial electron donor with and without irradiation.

3.3.3 Variation in Sacrificial Electron Donor (SED)

Different concentrations (0.5, 1.0, and 2.0 mM) of ascorbic acid were used in the LP41 biohybrid system as shown in **Figure 3.29**. It was clear that no detectable hydrogen was produced when no ascorbic acid was added. The biohybrid had the highest rate of 118 nmol h^{-1} when 2 mM was used while the polymer alone also had a rate of 42 nmol h^{-1}. The biohybrid system produced a similar amount of hydrogen when 0.5 mM (49 nmol h^{-1}) and 1.0 mM (54 nmol h^{-1}) AA were added and no measurable hydrogen contributed from the polymer alone group.

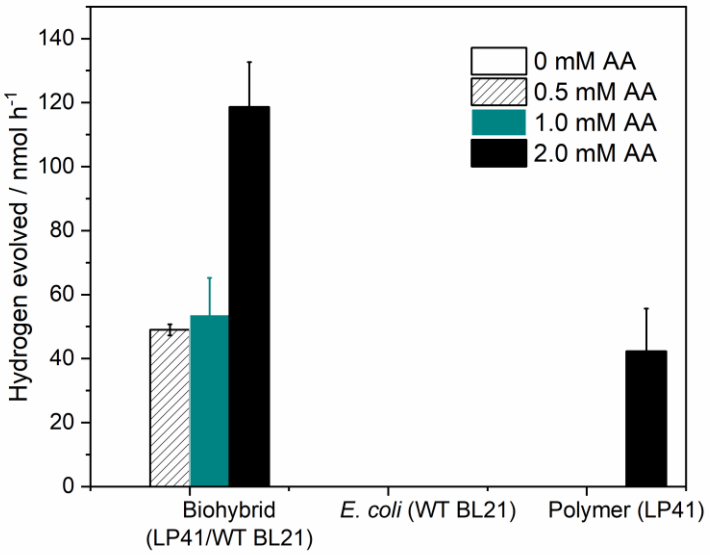

Figure 3.29 Influence of ascorbic acid (AA) concentration on hydrogen production performance.

3.3.4 Different *E. coli* strain

We also explored the role of the [FeFe]-hydrogenase in *E. coli* BL21(DE3) in the biohybrid system with the LP41 polymer. When HydA BL21 without [FeFe]-hydrogenase expression was used in the biohybrid, a reduced hydrogen evolution rate of 50 nmol h^{-1} was observed compared to the biohybrid with expressed [FeFe]-hydrogenase (181 nmol h^{-1}) (**Figure 3.30**). The hydrogen evolution rate was similar to the biohybrid system containing *E. coli* WT BL21(DE3) (64 nmol h^{-1}) that only expresses relatively less effective [NiFe]-hydrogenase. We therefore infer that the 3-time increase in hydrogen evolution activity can be attributed to the overexpressed [FeFe]-hydrogenases in the biohybrid system, excluding the possibility that other factors, such as aggregation of the conjugated polymers, might be responsible for the

increase in activity for hydrogen production and suggesting a photocatalytic process occurring between the conjugated polymer and *E. coli* cells.

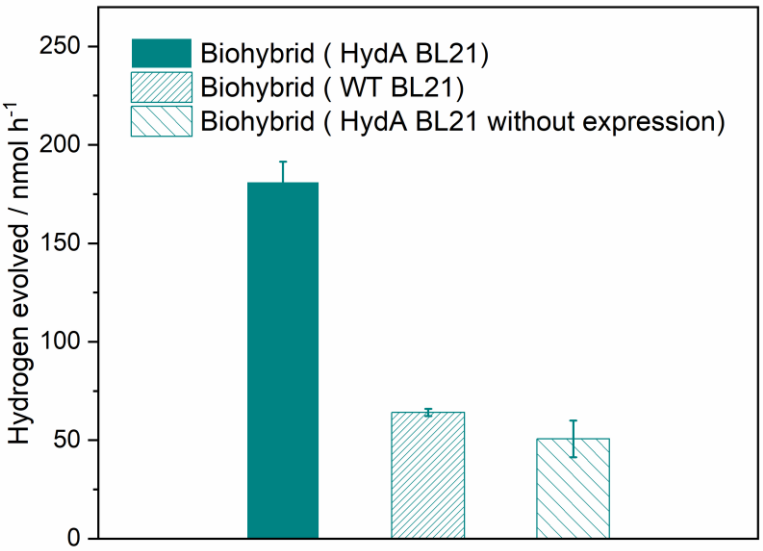

Figure 3.30 Hydrogen production performance of LP41 coupled with the wide type (WT) BL21 and HydA BL21 without [FeFe] hydrogenase expression was selected as control groups alongside LP41. Evolved hydrogen was normalized to same cell concentration (optical density, OD_{600} = 1.0) for different *E. coli* strains. All of the hydrogen production reactions were conducted in 10 mM tris(hydroxymethyl)aminomethane chloride buffer (pH 7, Tris-HCl) supplemented with 1 mM ascorbic acid as the hole sacrificial agent under irradiation of an AM 1.5G solar simulator for 3 h. Biohybrid reactions consist of 4.3 mL polymer nanoparticle solution, 200 µL *E. coli* concentrates, 0.5 mL 100 mM Tris-HCl, and 50 µL 0.1 M ascorbic acid. Plots and error bars represent the averages and standard deviations of at least two assays.

3.3.5 Dye-Sensitized Biohybrid Systems

Dye sensitization is a strategy often used in photocatalysts to improve their photocatalytic performance by enhancing the total absorption cross-section of the system.[26] However, not much work has been reported especially in the content of biohybrid photocatalytic systems. This is because catalytic performance is influenced by a host of factors, such as light absorption, thermodynamic driving force, exciton recombination, charge carrier mobility, physical surface properties, and so on. Beyond the basic question of whether a given material/dye is likely to absorb visible light, these factors are generally hard to predict. Also, the variables interact in complex ways.[27] The use of automation and robotics might greatly accelerate the testing of large numbers of dye/polymer combination. The potential of such approaches was shown for

abiotic photocatalyst discovery[27] and optimization.[28] These strategies could be expanded in biohybrid systems to include, for example, dye-sensitization strategies and the addition of mediator components that might enhance charge transfer processes. The work in this section is a preliminary study to explore the possibilities of assembling dye-sensitised biohybrid systems by using robotic workflow.

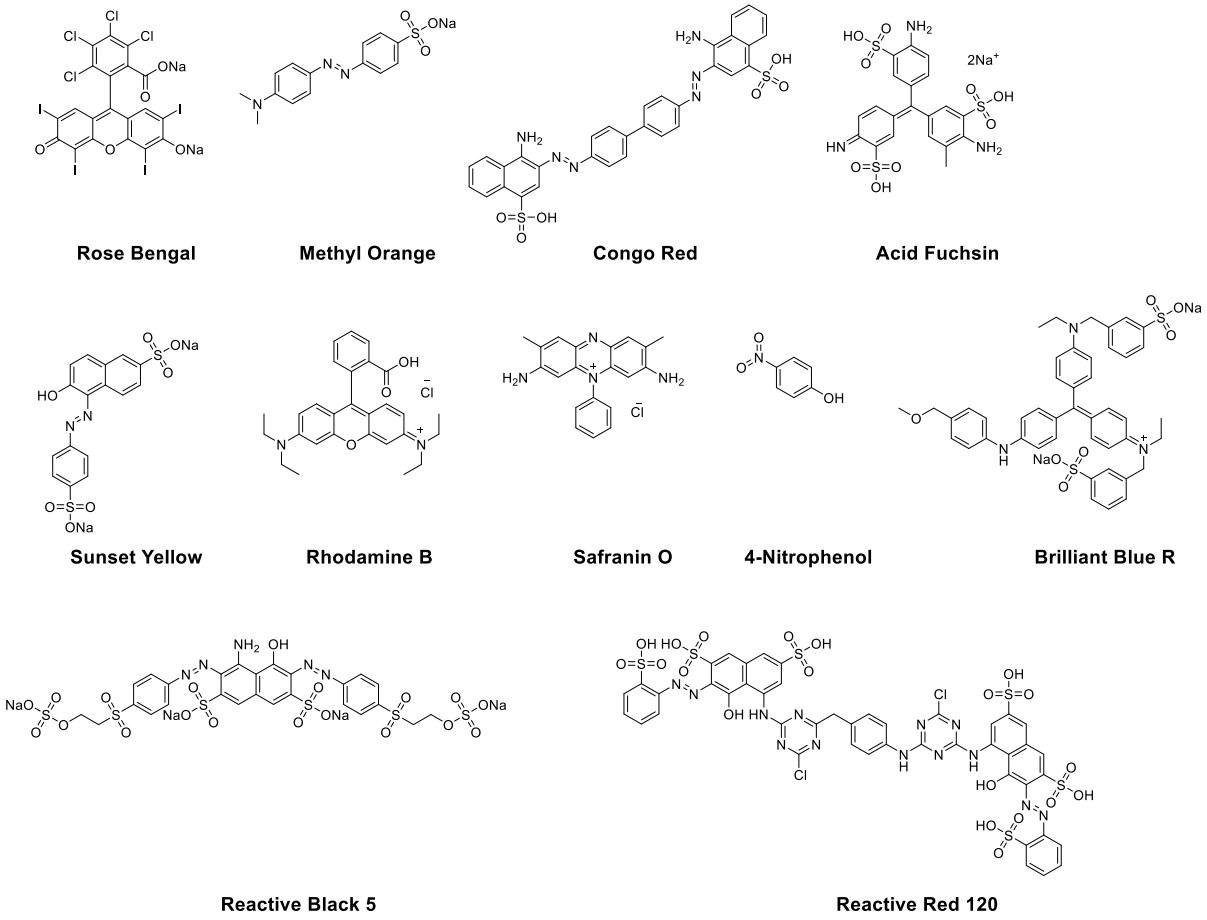

Figure 3.31 Chemical structures of dyes.

Furthermore, to increase the activity of the biohybrid system by matching the absorption better to the solar spectrum, different dyes, photocatalytic active organic molecules, and dye-polymer composites were assembled with WT *E. coli* cells as described. Eleven water-soluble dyes: Reactive Black 5, Safranin O, Reactive Red 120, Congo Red, Rose Bengal, Brilliant Blue R, Acid Fuchsin, Sunset Yellow FCF, Methyl Orange, Rhodamine B, and 4-Nitrophenol (**Figure 3.31**) were assembled with *E. coli* cells in 10 mM Tris-HCl (pH 7) with 1 mM ascorbic acid as a sacrificial electron donor to form dye/*E. coli* biohybrid systems and three final dye concentrations of 0.01, 0.02, and 0.1 mM were explored. In addition, four photocatalytic active organic molecules: 1,3,5-Tribenzoylbenzene, 9H-Thioxanthen-9-one, 4,4'-Biphenyldicarboxaldehyde, and azobenzene were coupled with *E. coli* cells as well. By

following the same nanoprecipitation method for polymer nanoparticles, four dye aqueous solutions with a final concentration of 25 mg L^{-1} were prepared. Furthermore, dye-polymer LP41 composites were also prepared and coupled with *E. coli* cells with dye concentrations of 6.25, 12.25, and 18.75 mg L^{-1}, respectively.

Table 3.7 Hydrogen production performance of water-soluble dye/*E. coli* biohybrid systems 10 mM tris(hydroxymethyl)aminomethane chloride buffer (pH 7, Tris-HCl) supplemented with 1 mM ascorbic acid as the hole sacrificial agent under irradiation of an AM 1.5G solar simulator for 3 h. Plots and error bars represent the averages and standard deviations of at least two assays.

Dye			Dye concentration / mM		
			0.5	0.1	0.02
D1	Reactive Black 5	H_2 / nmol h^{-1}	0[a]	0[a]	0[a]
D2	Safranin O	H_2 / nmol h^{-1}	0[a]	0[a]	0[a]
D3	Reactive Red 120	H_2 / nmol h^{-1}	0[a]	0[a]	5.4 ± 2.0
D4	Congo Red	H_2 / nmol h^{-1}	0[a]	0[a]	4.5 ± 3.6
D5	Rose Bengal	H_2 / nmol h^{-1}	0[a]	0[a]	0[a]
D6	Brilliant Blue R	H_2 / nmol h^{-1}	0[a]	43.5 ± 6.6	27.6 ± 19.7
D7	Acid Fuchsin	H_2 / nmol h^{-1}	0[a]	14.4 ± 10.2	69.7 ± 21.3
D8	Sunset Yellow FCF	H_2 / nmol h^{-1}	0[a]	0[a]	6.9 ± 0.1
D9	Methyl Orange	H_2 / nmol h^{-1}	0[a]	5.2 ± 7.4	22.6 ± 8.4
D10	Rhodamine B	H_2 / nmol h^{-1}	0[a]	0[a]	0[a]
D11	4-Nitrophenol	H_2 / nmol h^{-1}	0[a]	0[a]	0[a]

[a] No hydrogen detected.

Using water-soluble dyes (such as Reactive Black 5), no detectable hydrogen was produced when the dye concentration was 0.5 mM; although there was more hydrogen formation with reduced dye concentrations, LP41/*E. coli* biohybrid systems (109 nmol h^{-1}) still perform better than these dye/*E. coli* biohybrid systems as shown in **Table 3.7**.

Light-absorbing organic molecules are useful components in photocatalysts and could potentially be applied to fabricate with polymers to enhance the photocatalytic performances as dyes. Four photocatalytic active organic molecules which showed relatively high photocatalytic hydrogen performance (D12: 1,3,5-Tribenzoylbenzene, D13: 9H-Thioxanthen-9-one, D14: 4,4'-Biphenyldicarboxaldehyde, D15: Azobenzene)[29] were fabricated into polymer solution by the same nanoprecipitation method and coupled with WT *E. coli* cells.

As shown in **Figure 3.32**, there was little hydrogen produced from these dye/*E. coli* biohybrid systems with a dye concentration of 25 mg L^{-1}, but for dye-polymer composites/*E. coli* biohybrid systems, there is an improvement in hydrogen formation which might be due to multiple reasons, such as an expanded absorption spectrum.[29]

Based on all these comparative study findings, the role of polymer nanoparticles in this biohybrid system is more than just photosensitizer although a more systematic study is still needed to obtain a full understanding of the improved hydrogen production performance for this dye-sensitized biohybrid system.

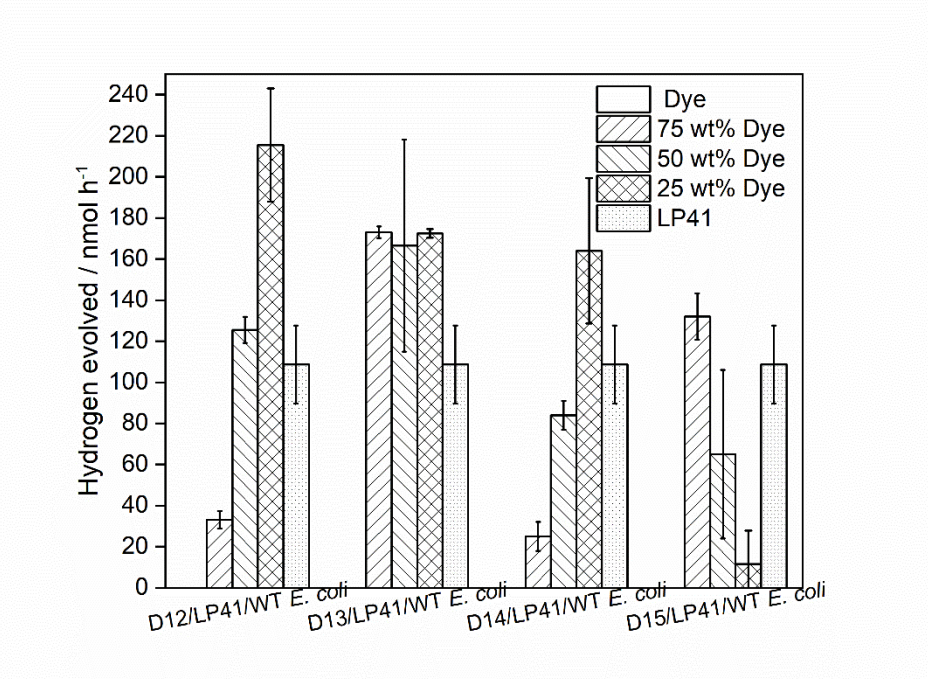

Figure 3.32 Hydrogen production performance of photocatalytic active organic molecules/WT *E. coli* biohybrid systems (D12: 1,3,5-Tribenzoylbenzene, D13: 9H-Thioxanthen-9-one, D14: 4,4'-Biphenyldicarboxaldehyde, D15: Azobenzene).

3.4 Summary

In this chapter, nanoparticles of a series of conjugated polymers with different backbone structures were assembled with engineered *E. coli* cells that express [FeFe]-hydrogenases, and the formed biohybrid systems were shown to be active for sacrificial hydrogen production from ascorbic acid solutions. The polymer/*E. coli* biohybrid systems were significantly more active than either the polymer nanoparticles or the *E. coli* cells in isolation under the same conditions. The biohybrid of LP41 (a co-polymer of fluorene and dibenzo[*b*,*d*]thiophene sulfone) and *E. coli* was the most active material studied, with an absolute hydrogen evolution rate of 148 nmol h^{-1}. Compared with the other polymers in this study, LP41 had a favourable driving force for hole scavenger oxidation, an appropriate particle size, and a positive surface charge that resulted in the formation of a biohybrid system with higher activity. The study also highlighted the crucial role of the hydrogenase type expressed in *E. coli*.

Overall, this study adds to our fundamental understanding of this new type of organic biohybrid system. While these systems are as yet far from practical, not least because of the use of a sacrificial hole scavenger, these results do suggest that organic semiconductors are equally viable for biohybrid photocatalyst manufacture and that they may offer certain advantages over inorganic materials, such as low toxicity, engineerable surface properties, and solution processability.

3.5 References

(1) Li, T.; Jiang, Q.; Huang, J.; Aitchison, C. M.; Huang, F.; Yang, M.; Dykes, G. F.; He, H.-L.; Wang, Q.; Sprick, R. S.; Cooper, A. I.; Liu, L.-N. Reprogramming Bacterial Protein Organelles as a Nanoreactor for Hydrogen Production. *Nat. Commun.* **2020**, *11* (1), 5448. https://doi.org/10.1038/s41467-020-19280-0.

(2) Adams, M. W.; Mortenson, L. E. The Physical and Catalytic Properties of Hydrogenase II of Clostridium Pasteurianum. A Comparison with Hydrogenase I. *J. Biol. Chem.* **1984**, *259* (11), 7045–7055. https://doi.org/https://doi.org/10.1016/S0021-9258(17)39835-6.

(3) Akhtar, M. K.; Jones, P. R. Deletion of IscR Stimulates Recombinant Clostridial Fe-Fe Hydrogenase Activity and H2-Accumulation in Escherichia Coli BL21(DE3). *Appl. Microbiol. Biotechnol.* **2008**, *78* (5), 853–862. https://doi.org/10.1007/s00253-008-1377-6.

(4) Kamp, C.; Silakov, A.; Winkler, M.; Reijerse, E. J.; Lubitz, W.; Happe, T. Isolation and First EPR Characterization of the [FeFe]-Hydrogenases from Green Algae. *Biochim. Biophys. Acta - Bioenerg.* **2008**, *1777* (5), 410–416. https://doi.org/https://doi.org/10.1016/j.bbabio.2008.02.002.

(5) Sybirna, K.; Antoine, T.; Lindberg, P.; Fourmond, V.; Rousset, M.; Méjean, V.; Bottin, H. Shewanella Oneidensis: A New and Efficient System for Expression and Maturation of Heterologous [Fe-Fe] Hydrogenase from Chlamydomonas Reinhardtii. *BMC Biotechnol.* **2008**, *8*, 73. https://doi.org/10.1186/1472-6750-8-73.

(6) Kuchenreuther, J. M.; Grady-Smith, C. S.; Bingham, A. S.; George, S. J.; Cramer, S. P.; Swartz, J. R. High-Yield Expression of Heterologous [FeFe] Hydrogenases in Escherichia Coli. *PLoS One* **2010**, *5* (11), 4–10. https://doi.org/10.1371/journal.pone.0015491.

(7) Winkler, M.; Esselborn, J.; Happe, T. Molecular Basis of [FeFe]-Hydrogenase Function An Insight into the Complex Interplay between Protein and Catalytic Cofactor. *Biochim. Biophys. Acta - Bioenerg.* **2013**, *1827* (8–9), 974–985. https://doi.org/10.1016/j.bbabio.2013.03.004.

(8) Yacoby, I.; Pochekailov, S.; Toporik, H.; Ghirardi, M. L.; King, P. W.; Zhang, S. Photosynthetic Electron Partitioning between [FeFe]-Hydrogenase and

Ferredoxin:NADP+-Oxidoreductase (FNR) Enzymes in Vitro. *Proc. Natl. Acad. Sci.* **2011**, *108* (23), 9396–9401. https://doi.org/10.1073/pnas.1103659108.

(9) King, P. W.; Posewitz, M. C.; Ghirardi, M. L.; Seibert, M. Functional Studies of [FeFe] Hydrogenase Maturation in an Escherichia Coli Biosynthetic System. *J. Bacteriol.* **2006**, *188* (6), 2163–2172. https://doi.org/10.1128/JB.188.6.2163-2172.2006.

(10) Li, T.; Jiang, Q.; Huang, J.; Aitchison, C. M.; Huang, F.; Yang, M.; Dykes, G. F.; He, H. L.; Wang, Q.; Sprick, R. S.; Cooper, A. I.; Liu, L. N. Reprogramming Bacterial Protein Organelles as a Nanoreactor for Hydrogen Production. *Nat. Commun.* **2020**, *11* (1), 1–10. https://doi.org/10.1038/s41467-020-19280-0.

(11) Nicolet, Y.; Piras, C.; Legrand, P.; Hatchikian, C. E.; Fontecilla-Camps, J. C. Desulfovibrio Desulfuricans Iron Hydrogenase: The Structure Shows Unusual Coordination to an Active Site Fe Binuclear Center. *Structure* **1999**, *7* (1), 13–23. https://doi.org/10.1016/s0969-2126(99)80005-7.

(12) Bertani, G. Lysogeny at Mid-Twentieth Century: P1, P2, and Other Experimental Systems. *J. Bacteriol.* **2004**, *186* (3), 595–600. https://doi.org/10.1128/JB.186.3.595-600.2004.

(13) Krasna, A. I. Proflavin Catalyzed Photoproduction of Hydrogen from Organic Compounds. *Photochem. Photobiol.* **1979**, *29* (2), 267–276.

(14) Adar, E.; Degani, Y.; Goren, Z.; Willner, I. Photosensitized Electron-Transfer Reactions in. Beta.-Cyclodextrin Aqueous Media: Effects on Dissociation of Ground-State Complexes, Charge Separation, and Hydrogen Evolution. *J. Am. Chem. Soc.* **1986**, *108* (16), 4696–4700.

(15) Balanda, P. B.; Ramey, M. B.; Reynolds, J. R. Water-Soluble and Blue Luminescent Cationic Polyelectrolytes Based on Poly(p-Phenylene). *Macromolecules* **1999**, *32* (12), 3970–3978. https://doi.org/10.1021/ma982017w.

(16) Dai, C.; Panahandeh-Fard, M.; Gong, X.; Xue, C.; Liu, B. Water-Dispersed Conjugated Polyelectrolyte for Visible-Light Hydrogen Production. *Sol. RRL* **2019**, *3* (3), 1–6. https://doi.org/10.1002/solr.201800255.

(17) Yoshida, A.; Nishimura, T.; Kawaguchi, H.; Inui, M.; Yukawa, H. Enhanced Hydrogen Production from Glucose Using Ldh- and Frd-Inactivated Escherichia Coli Strains. *Appl.*

Microbiol. Biotechnol. **2006**, *73* (1), 67–72. https://doi.org/10.1007/s00253-006-0456-9.

(18) Foster, J. W. Escherichia Coli Acid Resistance: Tales of an Amateur Acidophile. *Nat. Rev. Microbiol.* **2004**, *2* (11), 898–907.

(19) Pienaar, J. A.; Singh, A.; Barnard, T. G. Acid-Happy: Survival and Recovery of Enteropathogenic Escherichia Coli (EPEC) in Simulated Gastric Fluid. *Microb. Pathog.* **2019**, *128*, 396–404.

(20) Aitchison, C. M.; Sprick, R. S.; Cooper, A. I. Emulsion Polymerization Derived Organic Photocatalysts for Improved Light-Driven Hydrogen Evolution. *J. Mater. Chem. A* **2019**, *7* (6), 2490–2496. https://doi.org/10.1039/C8TA11383A.

(21) Gibson, B.; Wilson, D. J.; Feil, E.; Eyre-Walker, A. The Distribution of Bacterial Doubling Times in the Wild. *Proceedings. Biol. Sci.* **2018**, *285* (1880). https://doi.org/10.1098/rspb.2018.0789.

(22) Navarro Llorens, J. M.; Tormo, A.; Martínez-García, E. Stationary Phase in Gram-Negative Bacteria. *FEMS Microbiol. Rev.* **2010**, *34* (4), 476–495. https://doi.org/10.1111/j.1574-6976.2010.00213.x.

(23) Fujikawa, H.; Kai, A.; Morozumi, S. A New Logistic Model for Escherichia Coli Growth at Constant and Dynamic Temperatures. *Food Microbiol.* **2004**, *21* (5), 501–509. https://doi.org/https://doi.org/10.1016/j.fm.2004.01.007.

(24) Wang, Y.; Jett, S. D.; Crum, J.; Schanze, K. S.; Chi, E. Y.; Whitten, D. G. Understanding the Dark and Light-Enhanced Bactericidal Action of Cationic Conjugated Polyelectrolytes and Oligomers. *Langmuir* **2013**, *29* (2), 781–792. https://doi.org/10.1021/la3044889.

(25) Förster, A. H.; Gescher, J. Metabolic Engineering of Escherichia Coli for Production of Mixed-Acid Fermentation End Products. *Front. Bioeng. Biotechnol.* **2014**, *2* (MAY), 1–12. https://doi.org/10.3389/fbioe.2014.00016.

(26) Wang, X.; Chen, L.; Chong, S. Y.; Little, M. A.; Wu, Y.; Zhu, W.-H.; Clowes, R.; Yan, Y.; Zwijnenburg, M. A.; Sprick, R. S.; Cooper, A. I. Sulfone-Containing Covalent Organic Frameworks for Photocatalytic Hydrogen Evolution from Water. *Nat. Chem.* **2018**, *10* (12), 1180–1189. https://doi.org/10.1038/s41557-018-0141-5.

(27) Bai, Y.; Wilbraham, L.; Slater, B. J.; Zwijnenburg, M. A.; Sprick, R. S.; Cooper, A. I. Accelerated Discovery of Organic Polymer Photocatalysts for Hydrogen Evolution from Water through the Integration of Experiment and Theory. *J. Am. Chem. Soc.* **2019**, *141* (22), 9063–9071. https://doi.org/10.1021/jacs.9b03591.

(28) Burger, B.; Maffettone, P. M.; Gusev, V. V; Aitchison, C. M.; Bai, Y.; Wang, X.; Li, X.; Alston, B. M.; Li, B.; Clowes, R.; Rankin, N.; Harris, B.; Sprick, R. S.; Cooper, A. I. A Mobile Robotic Chemist. *Nature* **2020**, *583* (7815), 237–241. https://doi.org/10.1038/s41586-020-2442-2.

(29) Li, X.; Maffettone, P. M.; Che, Y.; Liu, T.; Chen, L.; Cooper, A. I. Combining Machine Learning and High-Throughput Experimentation to Discover Photocatalytically Active Organic Molecules. *Chem. Sci.* **2021**, *12* (32), 10742–10754. https://doi.org/10.1039/D1SC02150H.

Chapter 4 :

Mechanism Exploration of Biohybrid Systems

Chapter Contributions: The thesis author conducted time-correlated single photon counting (TCSPC) measurement and analysis. Transient absorption (TA) spectroscopy measurement was conducted with the help of Dr Adrian M. Gardner, and data analysis was performed by Dr Adrian M. Gardner and Prof. Alexander J. Cowan. The thesis author and Dr Nigel Gotts performed sample preparation for metabolomics analysis. Dr Adam Burke performed GC-MS experiments, and data analysis was conducted with the help of Dr Adam Burke.

4.1 Background

After the construction of the polymer/*E. coli* biohybrid system described in Chapters 2 and 3, the next step was to use and modulate the metabolic pathways of microorganisms to produce value-added chemicals. The multiple metabolic pathways of biological organisms ensure the selective generation of metabolic molecules from water, CO_2, and N_2. An additional energy source from the flow of electrons is required to perform the necessary redox chemistry, and much research has gone into providing needed electron flow through direct and indirect electrical pathways.

In TiO_2/*E. coli* hybrids that were developed for photocatalytic H_2 production, methyl viologen (MV^{2+}) was used as a redox mediator to shuttle electrons between microbes and inorganic photocatalysts;[1] Notably, H_2 formation was detected even in the absence of MV^{2+}, indicating that electrons may also be transferred directly from the conduction band of TiO_2 to the microorganism.[1] Additionally, biosynthetic materials, like CdS,[2,3] were reported to be constructed cell-material hybrid systems without the addition of electron transfer agents. Furthermore, a dual pathway was proposed through transient absorption spectroscopy studies: a non-hydrogenase-mediated pathway and a membrane-bound hydrogenase-mediated pathway.[4]

However, most research was focused on inorganic semiconductor/microorganism biohybrid systems, much less is known about organic semiconductor/microorganism biohybrid systems. Without a deeper understanding of the underlying electron transport mechanism, the development of hybrid photosynthesis will remain a trial-and-error exercise. Therefore, it is of great importance to reveal the fundamental EET process to optimize and advance different envisioned applications in hybrid photosynthesis.

In this chapter, spectroscopic techniques, such as time-correlated single-photon counting and transient absorption spectroscopy, alongside metabolic analysis, were applied to study more in the context of these systems to give insights into the possible charge transfer.

4.2 Spectroscopic Techniques

4.2.1 Fluorescence Intensity

To gain insight into the mechanism especially the nature of the interaction between the nanoparticles of LP41 and wide-type *E. coli* BL21 (DE3), fluorescence intensity was assessed as a function of the concentration of *E. coli* and ascorbic acid.

Three measurement groups, (1) LP41 polymer nanoparticle solution with different amounts of *E. coli* concentrates (0, 10, 25, 50, 75, and 100 μL), (2) LP41 / *E. coli* suspension with different ascorbic acid (AA) concentrations (0, 0.2, 0.5, 1.0, 1.5, and 2.0 mM), (3) LP41 polymer nanoparticle solution with different ascorbic acid concentrations (0, 0.2, 0.5, 1.0, 1.5, and 2.0 mM), were listed in **Table 4.1**. All the groups were in 10 mM Tris-HCl (pH 7) buffer.

Table 4.1 Measurement groups for fluorescence spectroscopy.

Group	Polymer	*E. coli* / μL	Ascorbic acid / mM
1	10 mg/L LP41	0	0
	10 mg/L LP41	10	0
	10 mg/L LP41	25	0
	10 mg/L LP41	50	0
	10 mg/L LP41	75	0
	10 mg/L LP41	100	0
2	10 mg/L LP41	50	0
	10 mg/L LP41	50	0.2
	10 mg/L LP41	50	0.5
	10 mg/L LP41	50	1.0
	10 mg/L LP41	50	1.5
	10 mg/L LP41	50	2.0
3	10 mg/L LP41	0	0
	10 mg/L LP41	0	0.2
	10 mg/L LP41	0	0.5
	10 mg/L LP41	0	1.0
	10 mg/L LP41	0	1.5
	10 mg/L LP41	0	2.0

Based on the absorption spectrum and emission spectrum of the LP41 nanoparticle solution in Chapter 2, the emission (λ_{exc} = 400 nm) and excitation (λ_{em} = 470 nm) spectra of these three groups were recorded in **Figure 4.1**. It was found that both *E. coli* and ascorbic acid could quench the fluorescence intensities of LP41 although in a different manner.

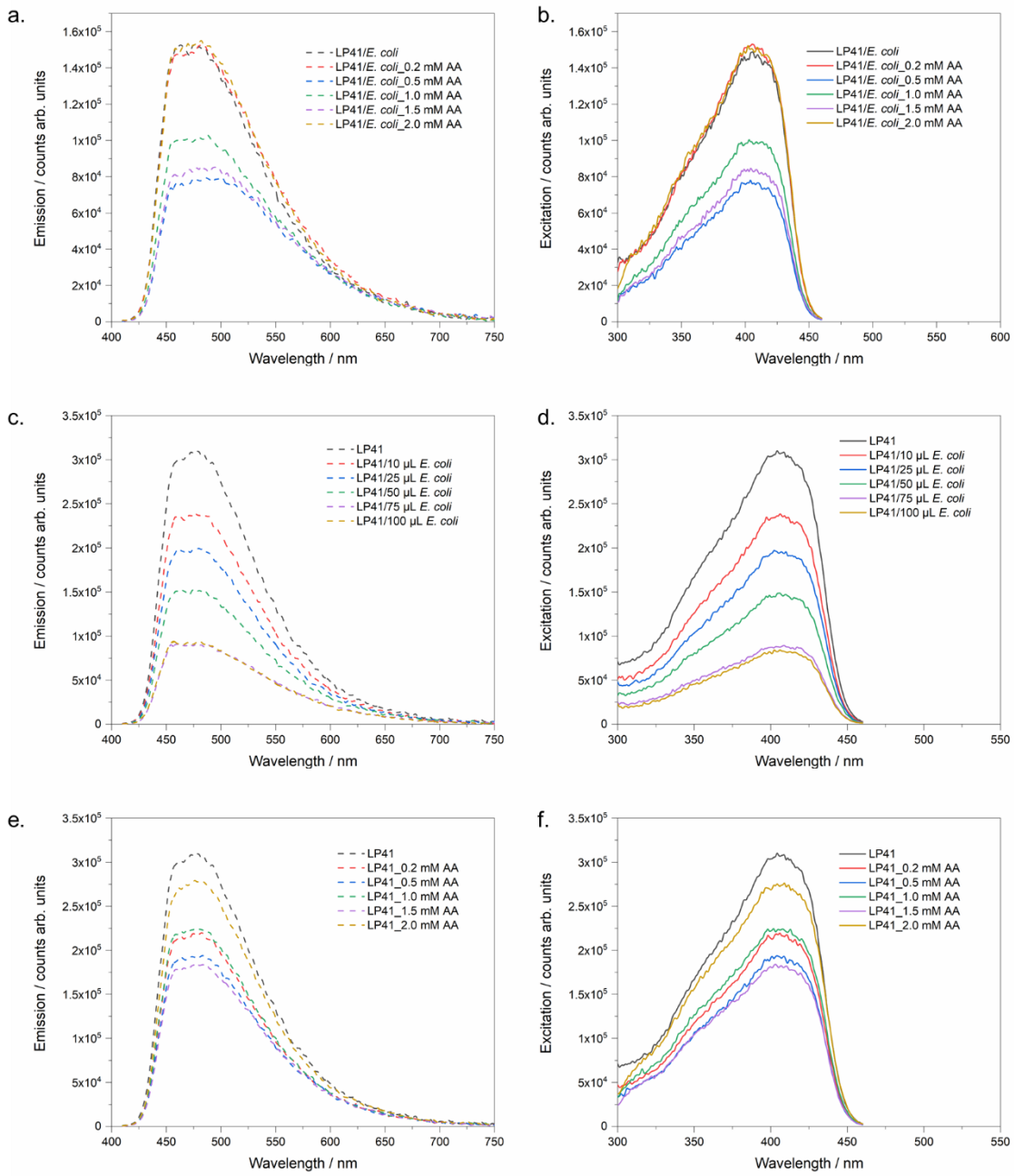

Figure 4.1 Emission (a) and excitation (b) spectrum of LP41/*E. coli* biohybrid systems with different ascorbic acid concentrations; Emission (c) and excitation (d) spectrum of LP41/*E. coli* biohybrid systems with different *E. coli* amount; Emission (e) and excitation (f) spectrum of LP41 sample with different ascorbic acid concentrations. Excitation wavelength is 400 nm, and emission wavelength was 470 nm for all measurements.

Fluorescence quenching refers to any process that decreases the fluorescence intensity of a sample,[5] and results in a dissipation of the fluorophore's electronic energy as heat.[5] A variety of molecular interactions can result in quenching, including excited-state reactions, molecular rearrangements, energy transfer, ground-state complex formation, and collisional quenching.[6] In addition, it is worthwhile to mention that apparent fluorescence quenching can also occur

due to the optical properties of the sample; for example, high turbidity can result in decreased fluorescence intensities.[5]

Stern-Volmer analysis was then conducted to study their fluorescence quenching mechanisms in **Table 4.2** and **Figure 4.2**. Stern-Volmer equation:[5]

$$\frac{I_0}{I} = 1 + \mathrm{k_q}\tau_0|Q| = 1 + K_\mathrm{D}|Q| \qquad \textit{Equation 4.1}$$

I_0: the fluorescence intensity in the absence of quencher

I: the fluorescence intensity in the presence of quencher

k_q: the biomolecular quenching constant

τ_0: the lifetime of the fluorophore in the absence of quencher

Q: the concentration of quencher

K_D: Stern-Volmer quenching constant, $K_D = k_q\tau_0$

The Stern-Volmer plots revealed *E. coli* to be a more effective quencher than ascorbic acid with greater I_0/I values for the same concentration ratio of $C_{quencher}/C_{quencher,0}$. However, the turbidity of samples increased when more *E.coli* was added which might also cause decreased fluorescence intensities.[5] When *E. coli* was applied as a quencher, there is a linear relationship between I_0/I and $C_{quencher}/C_{quencher,0}$,

$$y = 2.4956 * x + 0.9939, r = 0.96374 \qquad \textit{Equation 4.2}$$

It might suggest a classic dynamic quenching originating from diffusive encounters between *E. coli* and polymer particles during the lifetime of the photoexcited states.[7] However, no obvious linear relationship was observed for LP41/*E. coli* with AA and LP41 with AA (**Table 4.2**), which might indicate a different quenching mechanism compared with *E. coli* as a quencher.

Table 4.2 Stern-Volmer analysis of three sets of samples: LP41 with different amounts of *E. coli*, LP41/*E. coli* with different AA concentrations, and LP41 with different AA concentrations. I_0 / I: the inverse of normalized emission intensity at 470 nm; $C_{quencher}/C_{quencher,0:}$ the relative equivalence of quenchers.

Sample	I_0/I	$C_{quencher}/C_{quencher,0}$
LP41	1.000	0
LP41/10 µL *E. coli*	1.273	0.10
LP41/25 µL *E. coli*	1.529	0.25
LP41/50 µL *E. coli*	2.058	0.50
LP41/75 µL *E. coli*	3.365	0.75
LP41/100 µL *E. coli*	3.225	1.0
LP41/ 50 µL *E. coli*	1.000	0
LP41/50 µL *E. coli*_0.2 mM AA	1.007	0.10
LP41/50 µL *E. coli*_0.5 mM AA	1.922	0.25
LP41/50 µL *E. coli*_1.0 mM AA	1.451	0.50
LP41/50 µL *E. coli*_1.5 mM AA	1.753	0.75
LP41/50 µL *E. coli*_2.0 mM AA	0.947	1.0
LP41	1.000	0
LP41_0.2 mM AA	1.392	0.1
LP41_0.5 mM AA	1.580	0.25
LP41_1.0 mM AA	1.373	0.50
LP41_1.5 mM AA	1.678	0.75
LP41_2.0 mM AA	1.107	1.0

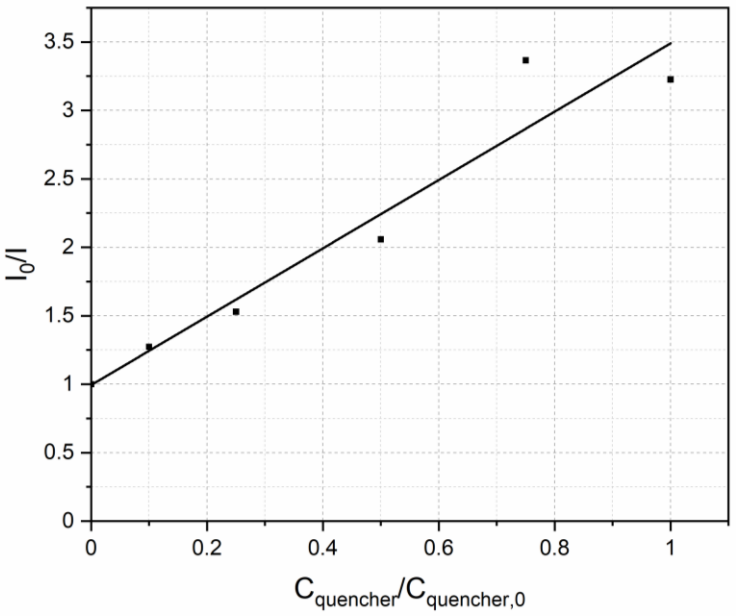

Figure 4.2 Linear relationship between I_0/I and $C_{quencher}/C_{quencher,0}$ of LP41/*E. coli* biohybrid systems with different amounts of *E. coli* concentrates. $C_{quencher}/C_{quencher,0}$: the relative equivalence of quenchers.

4.2.2 Time-Correlated Single Photon Counting

The observation of a linear Stern-Volmer plot is generally indicative of a single class of fluorophore,[8] but the plot alone does not prove that collisional quenching of fluorescence has occurred, static quenching (formation of a nonfluorescent ground-state complex between the fluorophore and quencher) could also result in linear Stern-Volmer plots. Their lifetime measurements can distinguish static and dynamic quenching.

The Stern-Volmer equation may also be obtained by considering the fraction of excited fluorophores relative to the total, which is given by the ratio of the decay rate in the absence of quencher (γ) to the total decay rate in the presence of quencher ($\gamma + k_q|Q|$):[5]

$$\frac{I}{I_0} = \frac{\gamma}{\gamma + k_q|Q|} = \frac{1}{1 + K_D|Q|} \qquad \textit{Equation 4.3}$$

And since collisional quenching is a rate process that depopulates the excited state, the lifetime in the absence (τ_0) and presence (τ) of quencher are given by:

$$\tau_0 = \gamma^{-1} \qquad \textit{Equation 4.4}$$

$$\tau = \left(\gamma + k_q|Q|\right)^{-1} \qquad \textit{Equation 4.5}$$

Therefore,

$$\frac{\tau_0}{\tau} = 1 + k_q|Q| \qquad \textit{Equation 4.6}$$

$$\frac{I_0}{I} = \frac{\tau_0}{\tau} \qquad \textit{Equation 4.7}$$

It illustrates an important characteristic of collisional quenching, that is an equivalent decrease in fluorescence intensity and lifetime. The decrease in lifetime occurs because quenching is an additional rate process that depopulates the excited state. The decrease in yield occurs because quenching depopulates the excited state without fluorescence emission. Static quenching does not decrease the lifetime because only the fluorescent molecules are observed, and the uncomplex fluorophore has the unquenched lifetime τ_0.

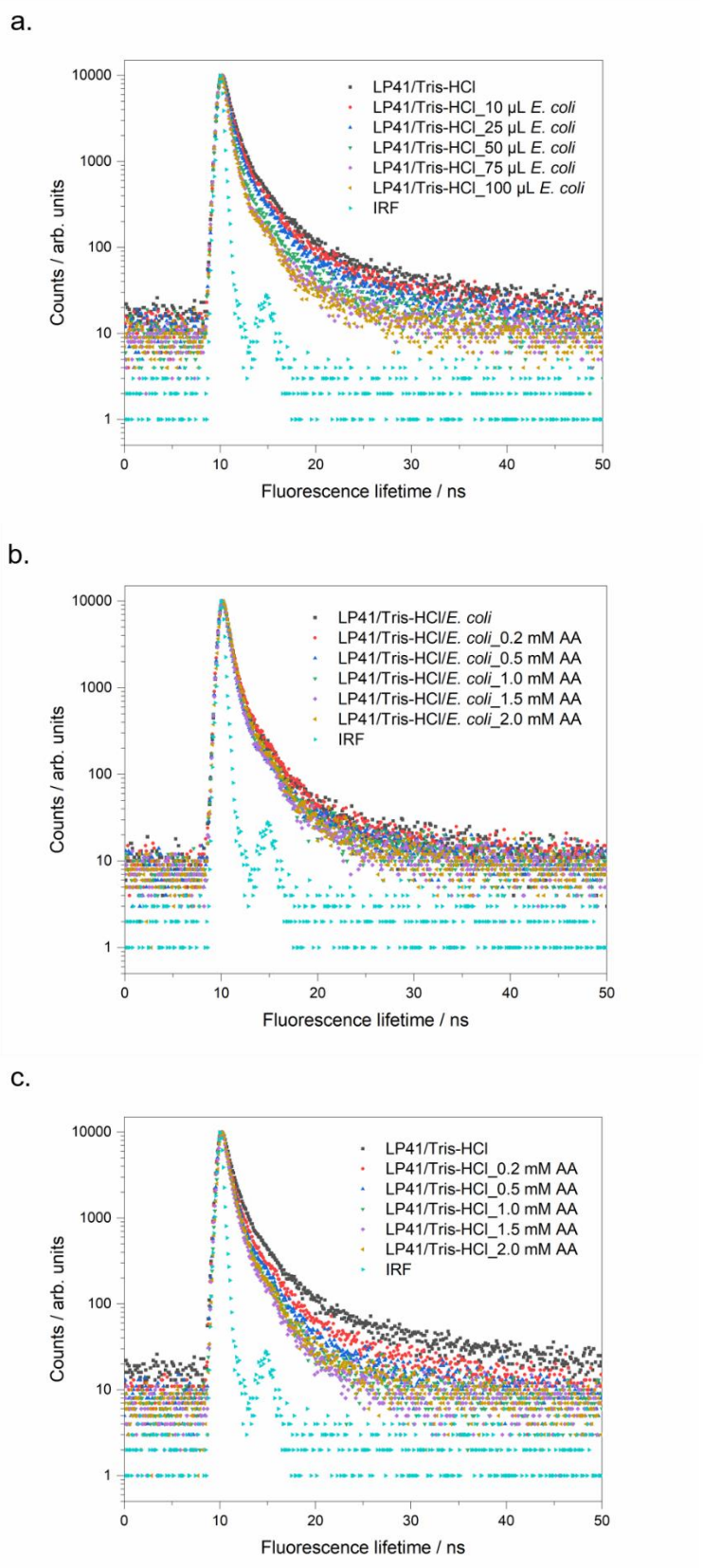

Figure 4.3 Decay curves of LP41/*E. coli* biohybrid systems with different *E. coli* amounts (a) and different ascorbic acid concentrations (b); and LP41 with different ascorbic acid concentrations with instrument response function (IRF).

Table 4.3 Estimated fluorescence lifetimes for biohybrid systems with different *E. coli* amounts and different ascorbic acid concentrations; and LP41 nanoparticle solution with different ascorbic acid concentrations.

	τ_1 / ns	SD_1[a] / ns	B_1 / %	τ_2 / ns	SD_2 / ns	B_2 / %	τ_3 / ns	SD_3 / ns	B_3 / %	χ^2	τ_{AVG}[b] / ns	SD[c] / ns
LP41	0.66	0.02	59.32	2.20	0.07	32.69	11.58	0.50	7.99	1.17	2.04	0.07
LP41/10 µL *E. coli*	0.56	0.02	57.73	1.85	0.06	34.05	10.04	0.36	8.23	1.24	1.78	0.06
LP41/25 µL *E. coli*	0.50	0.02	61.10	1.85	0.05	32.30	10.49	0.46	6.60	1.18	1.60	0.06
LP41/50 µL *E. coli*	0.45	0.01	69.09	1.66	0.06	25.73	9.11	0.48	5.18	1.14	1.21	0.05
LP41/75 µL *E. coli*	0.49	0.01	80.62	1.50	0.09	15.99	7.54	0.48	3.39	1.26	0.89	0.04
LP41/100 µL *E. coli*	0.40	0.01	74.51	1.46	0.06	21.92	8.42	0.53	3.58	1.30	0.92	0.04
LP41/*E. coli*	0.45	0.01	69.09	1.66	0.06	25.73	9.11	0.48	5.18	1.14	1.21	0.05
LP41/*E. coli*_0.2 mM AA	0.47	0.01	69.28	1.72	0.06	26.36	9.06	0.54	4.35	1.21	1.18	0.05
LP41/*E. coli*_0.5 mM AA	0.33	0.01	67.45	1.18	0.04	27.75	6.68	0.32	4.80	1.26	0.87	0.03
LP41/*E. coli*_1.0 mM AA	0.42	0.01	73.38	1.46	0.06	23.41	7.72	0.55	3.21	1.21	0.90	0.04
LP41/*E. coli*_1.5 mM AA	0.44	0.01	77.73	1.29	0.09	18.80	5.34	0.39	3.46	1.36	0.77	0.04
LP41/*E. coli*_2.0 mM AA	0.49	0.02	73.40	1.46	0.08	23.29	6.37	0.47	3.31	1.22	0.91	0.05
LP41	0.66	0.02	59.32	2.20	0.07	32.69	11.58	0.50	7.99	1.17	2.04	0.07
LP41_0.2 mM AA	0.69	0.01	76.55	2.39	0.10	19.63	11.45	0.75	3.83	1.24	1.44	0.06
LP41_0.5 mM AA	0.48	0.01	64.31	1.64	0.05	31.19	8.08	0.42	4.67	1.58	1.20	0.04
LP41_1.0 mM AA	0.34	0.02	53.05	1.17	0.04	41.18	4.73	0.25	5.77	1.26	0.94	0.04
LP41_1.5 mM AA	0.33	0.02	56.43	1.07	0.04	37.86	4.26	0.22	5.71	1.22	0.84	0.04
LP41_2.0 mM AA	0.38	0.02	54.33	1.16	0.04	40.57	5.47	0.25	5.09	1.29	0.96	0.04

a. SD: Standard deviation for τ. b. Fluorescence lifetimes for all samples obtained from fitting time-correlated single photon counting decays to a sum of three exponentials, which yield τ_1, τ_2, and τ_3 according to $\sum_{i=1}^{n}\left(A + B_i exp\left(^{-t}/_{\tau_i}\right)\right)$. τ_{AVG} is the weighted average lifetime calculated as $\sum_{i=1}^{n} B_i\tau_i$. c. SD for τ_{AVG} is calculated as $\sum_{i=1}^{n} B_i SD_i$.

TCSPC was then applied to obtain the fluorescence lifetimes. The estimated weighted average fluorescence lifetime of the nanoparticle of LP41 polymer in 10 mM Tris-HCl was reduced from 2.04 ns to 0.92 ns when 100 µL WT *E. coli* in 10 mM Tris-HCl was added (**Table 4.3**, **Figure 4.3**). The addition of 2 mM ascorbic acid to the LP41/*E. coli* biohybrids with 50 µL WT *E. coli* reduced the fluorescence lifetime from 1.21 ns to 0.91 ns. Likewise, the fluorescence lifetime of the conjugated polymer LP41 alone was reduced from 2.04 ns to 0.96 ns when 2 mM ascorbic acid was added. In addition, there was no equivalent decrease in fluorescence intensities and lifetimes (**Table 4.3**) which might indicate that the decreased fluorescence intensities were not caused by collisional quenching (alone).

In terms of the quenching mechanism, there are at least three mechanisms: (1) intersystem crossing or the heavy atom effect; (2) electron exchange or Dexter interactions; (3) photoinduced electron transfer.

Quenching through intersystem crossing (ISC) (**Figure 4.4**) is thought to cause the excited singlet state to become an excited triplet state, and since the triplet states are usually long-lived and also quenched by oxygen, and they are likely to be quenched to the ground state by the quencher or return to the ground state by non-radiative decay.[9]

$$F* + Q \xrightarrow{k_{ISC}} F_T^* \xrightarrow{Q} heat$$
$$\xrightarrow{k_{nr}} heat$$

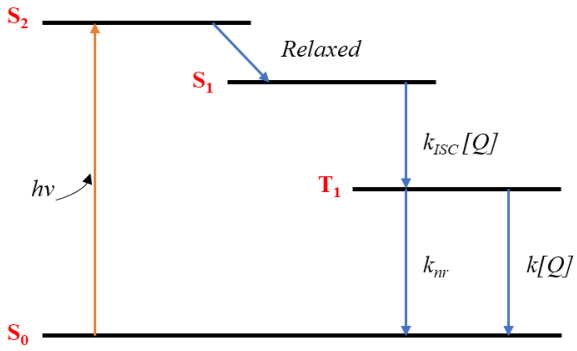

Figure 4.4 Quenching by intersystem crossing.

Electron exchange or Dexter interactions (**Figure 4.5**) normally involves three steps: (1) the excited donor (D_E) has an electron in the lowest-unoccupied molecular orbital (LUMO) which is transferred to the acceptor; (2) the acceptor (A_E) transfers an electron from its highest-occupied molecular orbital (HOMO) back to the donor; (3) the acceptor is left in an excited state.[10]

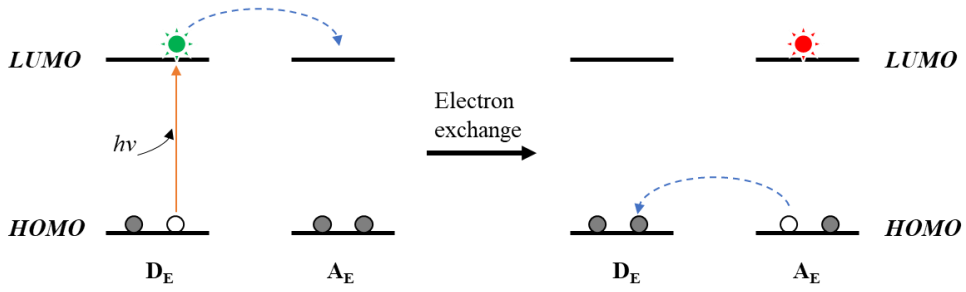

Figure 4.5 Schematic for stepwise electron exchange.

The third mechanism is photoinduced electron transfer (PET) (**Figure 4.6**), in which a complex is formed between the electron donor (D_P) and the electron acceptor (A_P), yielding $D_P^+A_P^-$. This complex can return to the ground state without the emission of a photon and the extra electron on the acceptor is returned to the electron donor.[11]

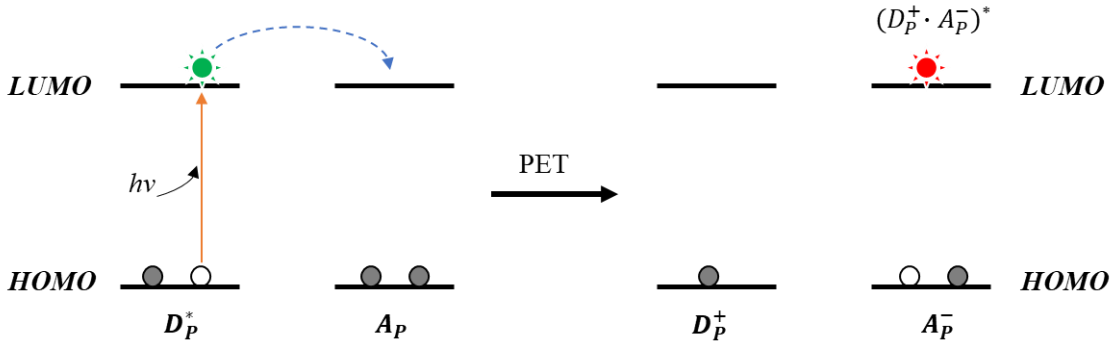

Figure 4.6 Photoinduced electron transfer.

However, it is often difficult to know the mechanism of quenching as they are not mutually exclusive, and quenching may occur by a combination of these mechanisms. Moreover, only through TCSPC results, it is difficult to identify the specific quenching mechanism for this polymer/*E. coli* biohybrid system as these mechanisms are not mutually exclusive, and many reports indicate that quenching occurs by a combination of different mechanisms. More techniques are needed to explore for further details.

4.2.3 Transient Absorption Spectroscopy

To gain further insight into the LP41/*E. coli* biohybrid system, we performed transient absorption (TA) spectroscopy on the LP41 polymer and the LP41/*E. coli* biohybrid system (**Figure 4.7, 4.8**). After excitation at 400 nm, the LP41 spectrum at 1 ps was dominated by a broad photoinduced absorption centred at 750 nm and a negative band at 500 nm, which is in

good agreement with the emission spectrum of the sample (Figure 4.8) and was assigned to stimulated emission. The decay of the broad band at 750 nm correlated with a decrease in stimulated emission and the growth of a band at 575 nm. We assigned the photoinduced absorption at 750 nm to a singlet excitonic species based on agreement with structurally related species[12] and the correlation to the recovery of the stimulated emission band. The band at 575 nm was assigned to a charge transfer state at early times (~1 ps) and electron polarons following hole scavenging, as for other similar polymers.[12] Charge transfer states and polaron states such as polaron pairs and electron polarons are likely to have similar transient UV/visible spectra, making it hard to discriminate them. The 575 nm band appeared to first form within the instrument response function (~1 ps) and continued to grow within the first 100 ps, consistent with reported ultrafast kinetics of similar polymers.[12] At longer time scales of 100 ps to 3 ns, the remaining population of the initially formed excitonic state (750 nm centre) decayed, in line with the TCSPC data that showed a lifetime of ~2 ns.

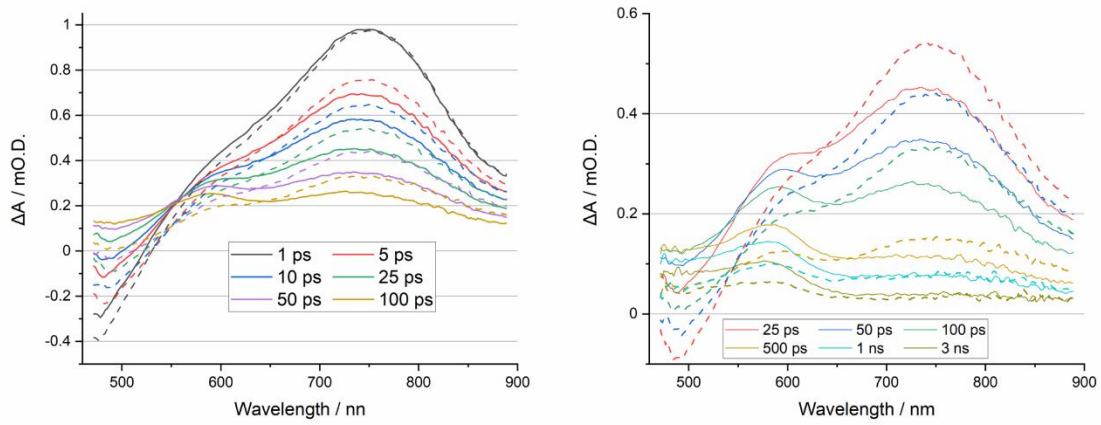

Figure 4.7 TA spectra normalized at the global maximum (ΔA) for 10 mg/L LP41 polymer nanoparticle in Tris-HCl aqueous solution (solid line) and 10 mg/L LP41 polymer nanoparticle in Tris-HCl aqueous solution with 1 mM ascorbic acid (dashed line) at key pump-probe delays as indicated.

The addition of ascorbic acid (dashed lines in **Figure 4.8**) resulted in no change of the nature of the photogenerated species on the picosecond timescale, with both the photoinduced absorptions at 750 and 575 nm, assigned to the initially formed singlet exciton and charge transfer/polaron state. However, the relative ratios of the 750 nm and 575 nm bands change in intensity in the presence of the ascorbic acid < 1 ns, with the yield of the 750 nm band being greater. The presence of ascorbic acid may not only introduce an electron donor but also modify the solvent/reaction environment with the potential for direct interactions between the ascorbic acid and LP41 that might give rise to changes in emission yields and lifetimes. TA spectra

showed that on the picosecond-timescale, ascorbic acid did not change the rate/yield of the charge transfer state/polaron pair species at 575 nm, but the photocatalysis data clearly showed that ascorbic acid is required for activity. We, therefore, conclude that ascorbic acid may play a role in quenching the charge transfer state to prevent recombination on the nanoscale and slower timescales and that electron transfer from LP41 occurs on the timescales that are slower than studied here.

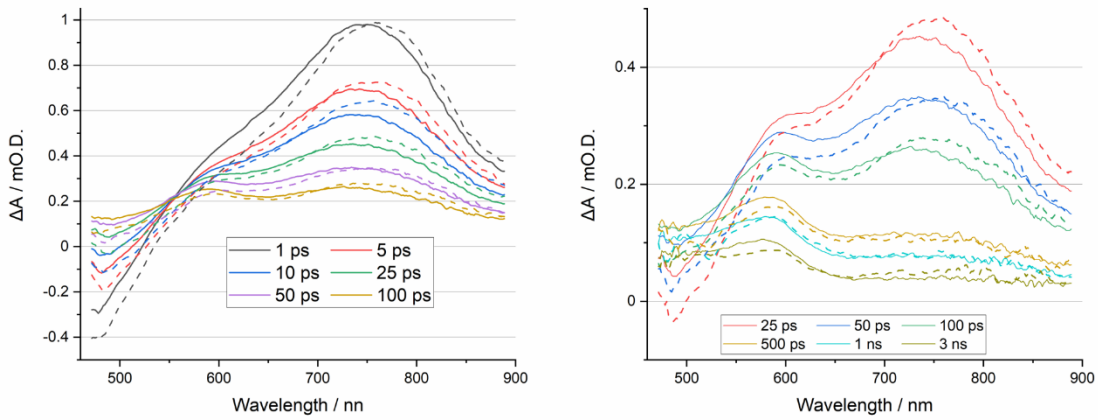

Figure 4.8 TA spectra normalized at the global maximum (ΔA) for 10 mg/L LP41 polymer nanoparticle in Tris-HCl aqueous solution (solid line) and 10 mg/L LP41 polymer nanoparticle/25 µL *E. coli* in Tris-HCl aqueous solution (dashed line) at key pump-probe delays as indicated.

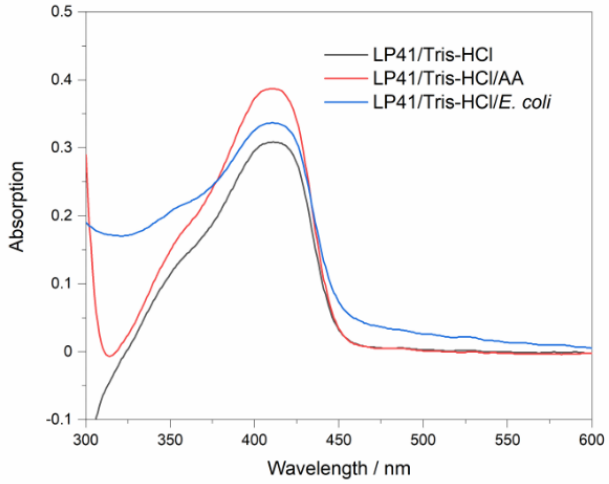

Figure 4.9 UV-vis spectra of samples conducted for TA measurements, 10 mg/L LP41 polymer nanoparticle in Tris-HCl aqueous solution (with/without ascorbic acid, with/without 25 µL *E. coli*).

TA spectra were recorded for LP41/*E. coli* samples supported the conclusion that electron transfer to *E. coli* BL21(DE3) was slow. These showed that the photoinduced absorption at 575

nm is retained to 3 ns (the longest timescale that can be studied here) in the presence of *E. coli* BL21(DE3).

4.3 Metabolomics Analysis

Spectroscopic techniques discussed above were applied to explore the extracellular electron transfer involved in the biohybrid system. It would also be interesting to find out the intracellular electron transfer pathways, or how the photogenerated electrons contribute to the increased hydrogen production performance of the biohybrid system. This can be clarified through metabolomics analysis to some extent. Furthermore, it would also be worthwhile to know other interesting (both extracellular and intracellular) metabolites other than hydrogen, which might help to explain the stability of the biohybrid systems and open new avenues for this field.

4.3.1 Cell Loading Amount Determination

Metabolic analysis is typically normalised based on cell mass, and there are several methods for measuring cell mass, including the gravimeter method, which uses ordinary balances to weigh a sample (dry weight/mL) after water has been removed.[13] An indirect method for calculating cell mass is turbidimetry. Cell cultures are turbid, and they absorb some of the light and let the rest of it pass through. When, a beam of light is allowed to pass through a suspension of bacteria, the bacteria particles coming in the path of light cause scattering and absorption of light depending on the cell density as per Beer-Lambert's law.[14]

$$A = log_{10}\frac{I_0}{I} = \varepsilon * c * d \qquad \textbf{\textit{Equation 4.8}}$$

The Lambert-Beer-Law, also known as Beer's Law, empirically relates the absorption of light to the properties of the sample. This law states that there is a logarithmic relationship between the transmission of light through a specific sample (A, absorbance, with I = intensity of outgoing light and I_o = intensity of incoming light), the molar extinction coefficient for a specific compound (ε), the concentration of the absorbing species in the material (c) and the distance the light travels (d).

The reduction in the amount of light transmitted light, therefore, depends on the cell density or cell mass in the culture suspension. It is measured as % transmittance or optical density (O.D.). The most common method for estimating the number of cells in a liquid suspension is the use of optical density measurements (OD) at a wavelength of 600 nm (OD_{600}).[15] For turbid samples such as cell cultures, the major contributor for the absorbance measured is light scattering and

not the result of molecular absorption following the Beer-Lambert Law. A calibration curve can be constructed by comparing measured OD_{600} to expected OD_{600} over a range of different concentrations. Expected OD_{600} is determined by counting cell number using an alternative technique (for example microscope slide method) and converting to OD_{600} using the rule of thumb that 1 OD_{600} = 5 * 10^8 cells/mL for *E. coli*.

Table 4.4 Measured OD_{600} values for all the sample groups. Three replicates were conducted for samples containing *E. coli*.

Polymer	***E. coli*/µL**	**Ascorbic acid [c]/µL**	**OD_{600}[d]**	**OD_{600}[d]**	**OD_{600}[d]**
/	50	50	0.2594	0.2546	0.2845
/	100	50	0.4895	0.5195	0.5125
/	150	50	0.8176	0.7734	0.7745
/	200	50	1.0351	0.9857	0.9701
5 mg/L	50	50	0.2702	0.2787	0.2775
5 mg/L	100	50	0.5094	0.5287	0.5246
5 mg/L	150	50	0.7657	0.7626	0.7691
5 mg/L	200	50	1.0416	1.0052	0.9677
10 mg/L	50	50	0.2893	0.3164	0.2966
10 mg/L	100	50	0.5410	0.5666	0.5287
10 mg/L	150	50	0.7862	0.8238	0.7628
10 mg/L	200	50	1.0886	1.0325	0.9683
25 mg/L	50	50	0.3418	0.3571	0.3474
25 mg/L	100	50	0.5912	0.6438	0.6224
25 mg/L	150	50	0.8211	0.9070	0.8088
25 mg/L	200	50	1.2247	1.0969	1.0497
50 mg/L	50	50	0.4712	0.5064	0.4612
50 mg/L	100	50	0.7005	0.7299	0.6793
50 mg/L	150	50	0.8914	1.0286	0.9231
50 mg/L	200	50	1.2096	1.2211	1.1640
5 mg/L	/	50	/	0.0106	0.0251
10 mg/L	/	50	/	0.0422	0.0471
25 mg/L	/	50	/	0.1270	0.1042
50 mg/L	/	50	/	0.2601	0.2312
/	/	50	/	0.0003	0.0026
/	/	50	/	-0.0093	-0.0016
/	/	50	/	-0.0113	0.0011
/	/	50	/	0.0012	-0.0038

a: 10 mM Tris-HCl solution; b: 100 mM Tris-HCl solution; c: 0.1 M ascorbic acid; d: three biological replicates for samples with *E. coli* involved conducted in different weeks; e: 10 mM Tris-HCl/1 mM AA as blank for the OD_{600} measurements; f: water as blank for the OD_{600} measurements.

To determine the actual amount of *E. coli* cells in polymer/*E. coli* biohybrid samples, we first explored the influence of polymer presence in biohybrid samples on OD_{600} values. For *E. coli* alone, there is a linear relationship between cell amounts and OD_{600} values:

$y = 0.00495 * x + 0.0212$, r = 0.99852 ***Equation 4.9***

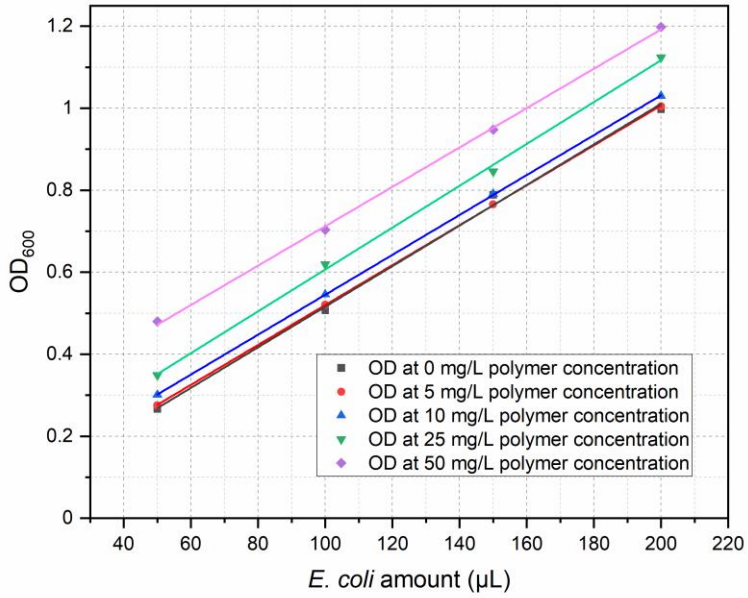

Figure 4.10 Linear relationship between *E. coli* amounts and OD_{600} values with 0, 5, 10, 25, and 50 mg/L LP41 polymer concentrations in LP41/*E. coli* biohybrid samples. Each point represents the mean value of three replicates. Statistics analysis was conducted for three replicates and it shows that there is no significant difference at the 0.05 level.

For LP41/*E. coli* biohybrid samples with different polymer concentrations (5, 10, 25, 50 mg/L) as described in **Table 4.4**, good linearity was also observed between *E. coli* amounts and total OD_{600} values of the biohybrid samples as plotted in **Figure 4.10**. Equations are shown below

5 mg/L polymer concentration:

$y = 0.00487 * x + 0.03345, r = 0.99998$ ***Equation 4.10***

10 mg/L polymer concentration:

$y = 0.00487 * x + 0.0585, r = 0.99998$ ***Equation 4.11***

25 mg/L polymer concentration:

$$y = 0.0051 * x + 0.0964, r = 0.99928$$ ***Equation 4.12***

50 mg/L polymer concentration:

$$y = 0.0048 * x + 0.2321, r = 0.99967$$ ***Equation 4.13***

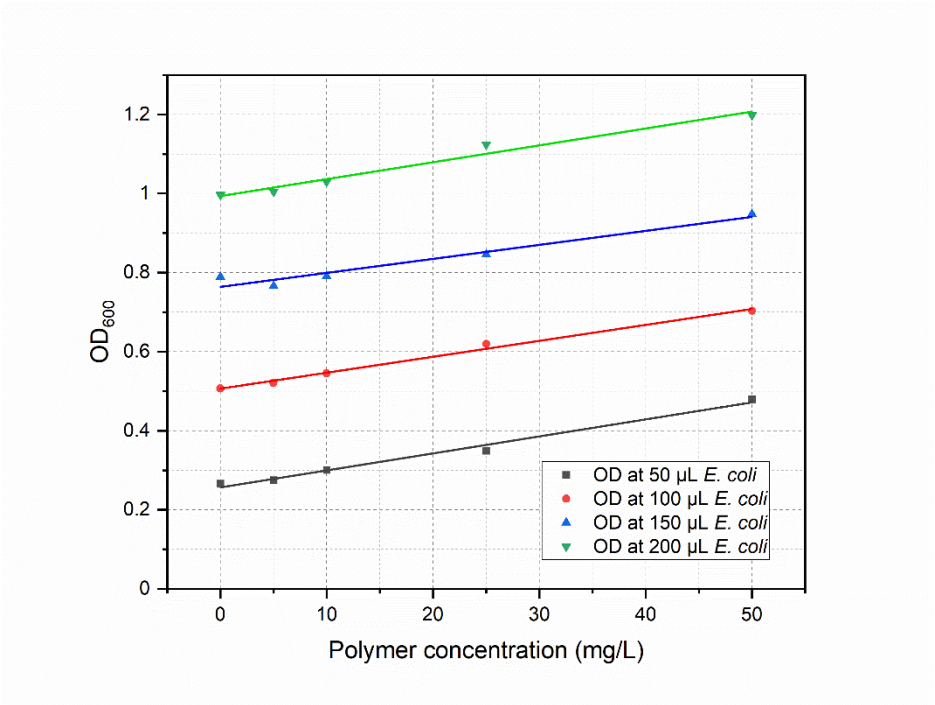

Figure 4.11 Linear relationship between polymer concentrations and OD_{600} values with 50, 100, 150, and 200 µL *E. coli* separately in LP41/*E. coli* biohybrid samples. Each point represents the mean value of three replicates. Statistics analysis was conducted for three replicates and it shows that there is no significant difference at the 0.05 level.

It was found that the linearity between *E. coli* amounts and OD_{600} values for different fixed polymer concentrations are not the same, which might be attributed to the difference in turbidity for polymer solutions with different polymer concentrations.

We, therefore, further studied the relationship between polymer concentrations and OD_{600} values in polymer/*E. coli* biohybrid systems as plotted in **Figure 4.11**. It was observed that there is better linearity for biohybrid systems with fixed *E. coli* amounts of 50 and 100 µL compared with biohybrid systems with 150 and 200 µL fixed amounts

50 µL *E. coli*:

$$y = 0.0043 * x + 0.2566, r = 0.99344$$ ***Equation 4.14***

100 µL *E. coli*:

$$y = 0.00403 * x + 0.50655, r = 0.99627 \quad \textbf{Equation 4.15}$$

150 µL *E. coli*:

$$y = 0.00354 * x + 0.76397, r = 0.97597 \quad \textbf{Equation 4.16}$$

200 µL *E. coli*:

$$y = 0.00427 * x + 0.99378, r = 0.98714 \quad \textbf{Equation 4.17}$$

As 10 mg/L LP41 polymer/100 µL *E. coli* was used for the biohybrid system assembly and metabolic analysis, the actual *E. coli* amounts in the biohybrid samples are supposed to be obtained by subtracting the OD_{600} value of 100 µL *E. coli* sample from the total OD_{600} value of the 10 mg/L polymer/100 µL *E. coli* biohybrid sample.

4.3.2 Sample Preparation

Sample preparation procedures were conducted based on *'Laboratory Guide for Metabolomics Experiment'*, SOP 6 'Quenching and extraction of microbial cells in media for metabolomic analysis' written by Professor Roy Goodacre's group.

4.3.2.1 Quenching Procedure

Cold (-48 °C) 60% methanol was added into experimental samples to quench internal cellular processes but not leech metabolites into the cell medium. After centrifugation, supernatant and pellet samples were obtained and ready for subsequent extraction or storage at -80 °C until extraction can be performed (**Figure 4.12**). There is also including an OD_{600} determination for

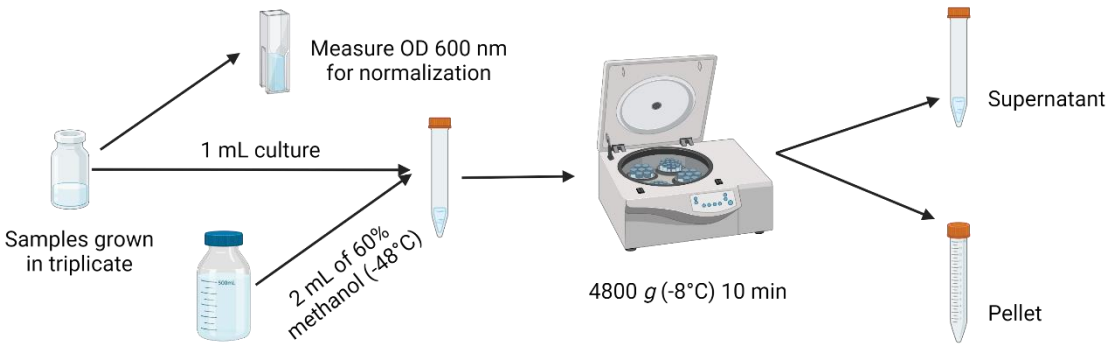

Figure 4.12 Initial quenching and pelletization process.

all experimental samples with replicates ($n \geq 3$) in order to normalize for biomass differences between experimental samples.

4.3.2.2 Removal of Polymer Nanoparticles

The supernatant samples still contain the polymers after the initial quenching step (sample 0-1, 0-2, and 0-3) and after the following centrifugation (sample 1-1, 1-2, 1-3) as shown in **Figure 4.13**. Therefore, the polymer nanoparticles need to be removed from the supernatant solutions before being injected into columns.

Pore size relates to the membrane filter's ability to filter out particles of a certain size. For example, a 0.20-µm membrane will filter out particles with a diameter of 0.2 microns or larger from a filtration stream. With ultrafiltration (membrane with pore size within 0.01-0.1 µm), filter pore size is irrelevant because the pores are so small.[16] These filters are rated according to their nominal molecular weight limit (NMWL) or their molecular weight cut-off (MWCO).[17] Centrifugal filters with 3000 and 30,000 NMWL were used for the LP41 polymer nanoparticle removal procedure. **Figure 4.14**, shows that the emission intensity of samples 1-4, 1-5, and 1-6 (filtered by 3000 NMWL) and samples 1-7 and 1-8 (filtered by 30,000 NMWL) decreased

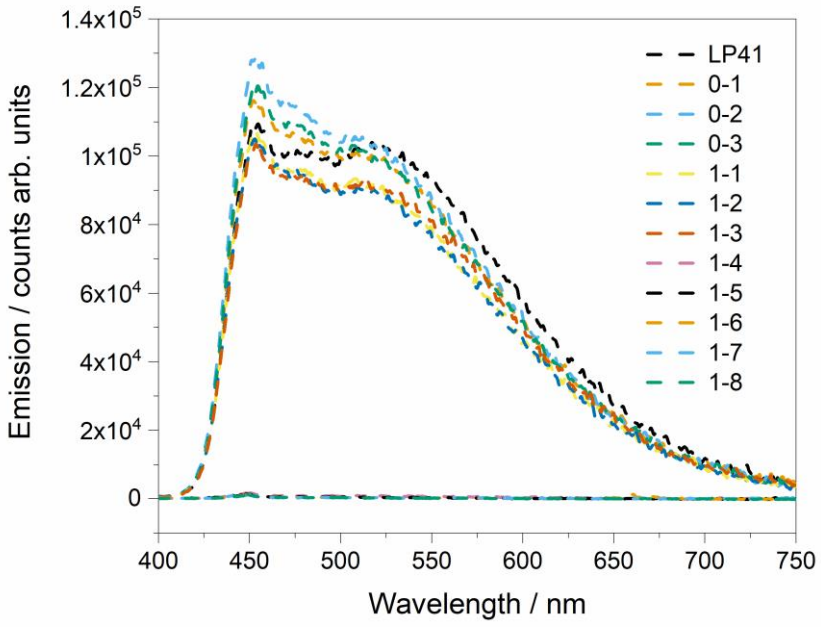

Figure 4.13 Emission spectrum of untreated LP41 polymer nanoparticle solution, supernatant solutions after initial quenching step (sample 0-1, 0-2, and 0-3) and following centrifugation (sample 1-1, 1-2, and 1-3), supernatant solutions after filtration by using 3000 NMWL (sample 1-4, 1-5, and 1-6) and 30,000 NMWL (sample 1-7 and 1-8).

dramatically compared with untreated samples. It might indicate that fewer nanoparticles are presented in the sample solution. For the difference between these two filters, 3000 NMWL is too small as there was still 1.5 mL sample solution left in the concentrator while for 30, 000 one there is around 50 µL solution left which is attributed to the dead space of the concentrator.

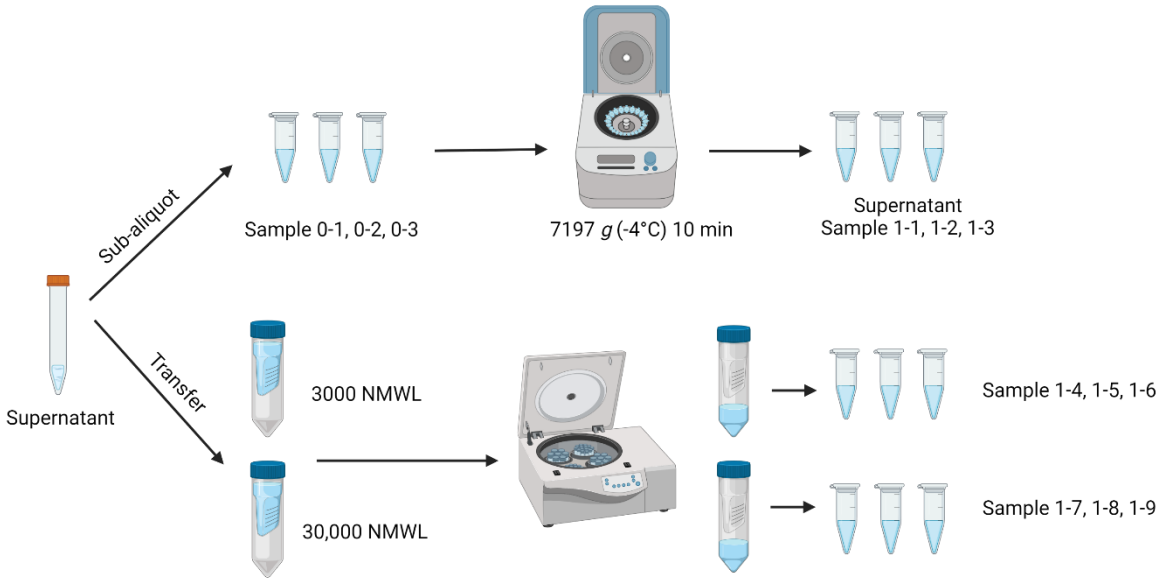

Figure 4.14 Removal of polymer nanoparticles from supernatant samples.

4.3.2.3 Extraction Procedure

Extraction procedures were conducted by the following diagram (**Figure 4.15**) for supernatant and pellet samples separately combined with polymer removal procedures by using centrifugal filters.

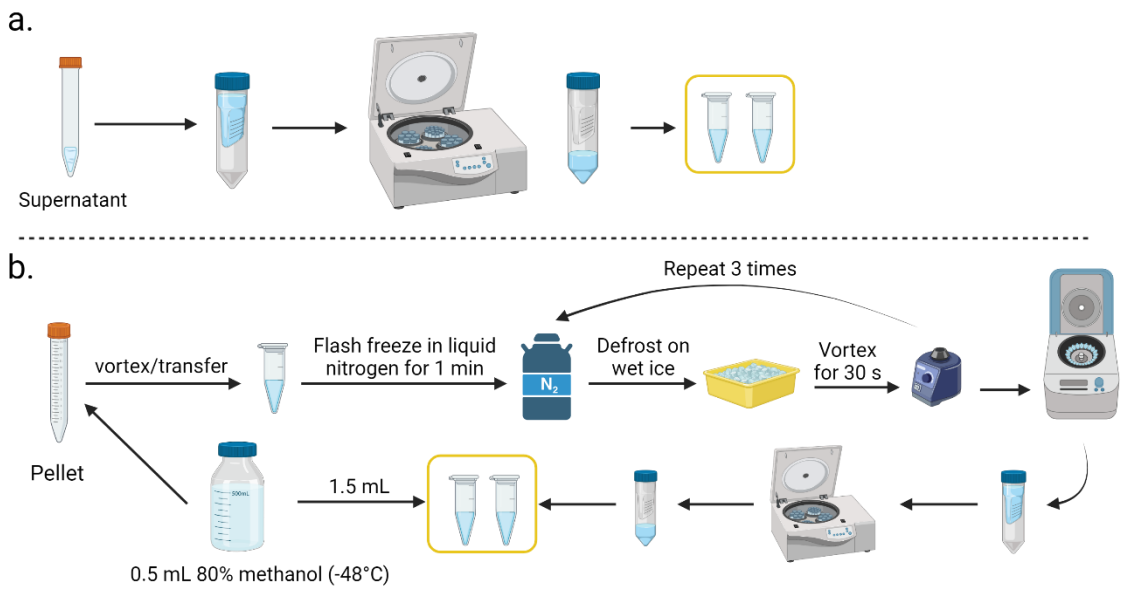

Figure 4.15 Extraction process of supernatant and pellet samples.

4.4 Summary

Spectroscopic techniques (time-correlated single photon counting, transient absorption (TA) spectroscopy) were first applied to explore the charge transfer mechanism of the LP41 polymer nanoparticle /*E. coli* biohybrid systems.

Fluorescence lifetime and TA studies suggest slow charge transfer between the conjugated polymer and the bacterial cells under irradiation.

In addition, metabolites analysis was also used to explore the electron transfer mechanism, especially the intracellular part. An experimental workflow based on the reported SOP was developed for biohybrid sample preparation for GC-MS analysis, including quenching and extraction steps, polymer removal, and cell mass determination. Future work will be focused on GC-MS data analysis and biological interpretation.

4.5 References

(1) Honda, Y.; Hagiwara, H.; Ida, S.; Ishihara, T. Application to Photocatalytic H2Production of a Whole-Cell Reaction by Recombinant Escherichia Coli Cells Expressing [FeFe]-Hydrogenase and Maturases Genes. *Angew. Chemie - Int. Ed.* **2016**, *55* (28), 8045–8048. https://doi.org/10.1002/anie.201600177.

(2) Sakimoto, K. K.; Wong, A. B.; Yang, P. Self-Photosensitization of Nonphotosynthetic Bacteria for Solar-to-Chemical Production. *Science (80-.).* **2016**, *351* (6268), 74–77. https://doi.org/10.1126/science.aad3317.

(3) Wang, B.; Zeng, C.; Chu, K. H.; Wu, D.; Yip, H. Y.; Ye, L.; Wong, P. K. Enhanced Biological Hydrogen Production from Escherichia Coli with Surface Precipitated Cadmium Sulfide Nanoparticles. *Adv. Energy Mater.* **2017**, *7* (20), 1–10. https://doi.org/10.1002/aenm.201700611.

(4) Kornienko, N.; Sakimoto, K. K.; Herlihy, D. M.; Nguyen, S. C.; Alivisatos, A. P.; Harris, C. B.; Schwartzberg, A.; Yang, P. Spectroscopic Elucidation of Energy Transfer in Hybrid Inorganic-Biological Organisms for Solar-to-Chemical Production. *Proc. Natl. Acad. Sci. U. S. A.* **2016**, *113* (42), 11750–11755. https://doi.org/10.1073/pnas.1610554113.

(5) Lakowicz, J. R.; Lakowicz, J. R. Quenching of Fluorescence. *Princ. Fluoresc. Spectrosc.* **1983**, 257–301.

(6) Zhuang, X.; Ha, T.; Kim, H. D.; Centner, T.; Labeit, S.; Chu, S. Fluorescence Quenching: A Tool for Single-Molecule Protein-Folding Study. *Proc. Natl. Acad. Sci.* **2000**, *97* (26), 14241–14244. https://doi.org/10.1073/pnas.97.26.14241.

(7) Guan, X.; Erşan, S.; Hu, X.; Atallah, T. L.; Xie, Y.; Lu, S.; Cao, B.; Sun, J.; Wu, K.; Huang, Y.; Duan, X.; Caram, J. R.; Yu, Y.; Park, J. O.; Liu, C. Maximizing Light-Driven CO2 and N2 Fixation Efficiency in Quantum Dot–Bacteria Hybrids. *Nat. Catal.* **2022**, *5* (November). https://doi.org/10.1038/s41929-022-00867-3.

(8) Lakowicz, J. R. *Principles of Fluorescence Spectroscopy*; Springer, 2006.

(9) Kawaoka, K.; Khan, A. U.; Kearns, D. R. Role of Singlet Excited States of Molecular Oxygen in the Quenching of Organic Triplet States. *J. Chem. Phys.* **1967**, *46* (5), 1842–1853.

(10) Dexter, D. L. A Theory of Sensitized Luminescence in Solids. *J. Chem. Phys.* **1953**, *21* (5), 836–850.

(11) Nad, S.; Pal, H. Electron Transfer from Aromatic Amines to Excited Coumarin Dyes: Fluorescence Quenching and Picosecond Transient Absorption Studies. *J. Phys. Chem. A* **2000**, *104* (3), 673–680.

(12) Hillman, S. A. J.; Sprick, R. S.; Pearce, D.; Woods, D. J.; Sit, W.-Y.; Shi, X.; Cooper, A. I.; Durrant, J. R.; Nelson, J. Why Do Sulfone-Containing Polymer Photocatalysts Work So Well for Sacrificial Hydrogen Evolution from Water? *J. Am. Chem. Soc.* **2022**, *144* (42), 19382–19395. https://doi.org/10.1021/jacs.2c07103.

(13) Davies, H. G.; Deeley, E. M. An Integrator for Measuring the "Dry Mass" of Cells and Isolated Components. *Exp. Cell Res.* **1956**, *11* (1), 169–185. https://doi.org/https://doi.org/10.1016/0014-4827(56)90201-4.

(14) Beer. Bestimmung Der Absorption Des Rothen Lichts in Farbigen Flüssigkeiten. *Ann. Phys.* **1852**, *162* (5), 78–88. https://doi.org/https://doi.org/10.1002/andp.18521620505.

(15) Myers, J. A.; Curtis, B. S.; Curtis, W. R. Improving Accuracy of Cell and Chromophore Concentration Measurements Using Optical Density. *BMC Biophys.* **2013**, *6* (1), 1–16.

(16) Schäfer, A. I.; Mauch, R.; Waite, T. D.; Fane, A. G. Charge Effects in the Fractionation of Natural Organics Using Ultrafiltration. *Environ. Sci. Technol.* **2002**, *36* (12), 2572–2580. https://doi.org/10.1021/es0016708.

(17) Erickson, H. P. Size and Shape of Protein Molecules at the Nanometer Level Determined by Sedimentation, Gel Filtration, and Electron Microscopy. *Biol. Proced. Online* **2009**, *11* (1), 32. https://doi.org/10.1007/s12575-009-9008-x.

Chapter 5 :

Summary and Future Work

5.1 Summary

In this work, a series of co-polymers of bis(8-bromo-*n*-octyl)-fluorene with phenylene (LP1), thiophene (LP2), 2,2'-bithiophene (LP3), and dibenzo[*b*,*d*]thiophene sulfone (LP4) were synthesized in Chapter 2. The polymers were then modified through polymer-analogous reactions on the alkyl-bromo functional groups giving trimethylammonium substituted polymers (LP11, LP21, LP31, and LP41). The photocatalytic hydrogen evolution rate of nanoparticles of these 4 polymers was evaluated in ascorbic acid and TEA system, respectively.

The nanoparticles of these conjugated polymers with different backbone structures were assembled with engineered *E. coli* cells that express [FeFe]-hydrogenases, and the formed biohybrid systems were shown to be active for sacrificial hydrogen production from ascorbic acid solutions in Chapter 3. The polymer/*E. coli* biohybrid systems were significantly more active than either the polymer nanoparticles or the *E. coli* cells in isolation under the same conditions. The biohybrid of LP41 (a co-polymer of fluorene and dibenzo[b,d]thiophene sulfone) and *E. coli* was the most active material studied, with an absolute hydrogen evolution rate of 148 nmol h-1. Compared with the other polymers in this study, LP41 had a favourable driving force for hole scavenger oxidation, an appropriate particle size, and a positive surface charge that resulted in the formation of a biohybrid system with higher activity. The study also highlighted the crucial role of the hydrogenase type expressed in *E. coli*.

PL lifetime and TA studies suggest, although do not prove, charge transfer between the conjugated polymer and the bacterial cells under irradiation.

Overall, this study adds to our fundamental understanding of this new type of organic biohybrid system. While these systems are far from practical, not least because of the use of a sacrificial hole scavenger, the results do suggest that organic semiconductors are equally viable for biohybrid photocatalyst manufacture and that they may offer certain advantages over inorganic materials, such as low toxicity, engineerable surface properties, and solution processability.

5.2 Future Work

Organic semiconductor/microorganism biohybrid systems are less explored compared with inorganic materials-based biohybrid systems. There are various aspects worthwhile to study further towards practical application in the future.

Firstly, from the materials side, compared with linear polymers, CMPs and COFs with porous structures and high surface areas show greater potential in this respect. Microorganism immobilization has yet to be demonstrated using CMPs and COF. However, enzyme immobilization has been reported with COFs, which also raises another important property of the surfaces— the pore size. The reported chemically stable hollow spherical COF possesses mesoporous (2–50 nm) shells that provide adequate space for enzyme immobilisation.[1] Apart from specific design and synthesis routes of CMPs and COFs, it was also shown that simple inorganic salts could alter the formation of micropores to macro-micro pores in CMPs,[2] which might facilitate the microorganism immobilization in biohybrid applications. As such, porous organic materials such as CMPs and COFs with high porosity and macropores/mesopores offer another opportunity for the assembly of biohybrids through the immobilization of microorganisms.

Secondly, it is also interesting to find out other attachment strategies other than non-covalent binding through electrostatic interactions. The irreversible adhesion to surfaces by forming covalent bonds is another promising alternative. Metal-organic frameworks (MOFs) were reported to uniformly wrap *Morella thermoacetica* bacteria for cytoprotection in artificial photosynthesis. The MOF-bacteria interface involves direct bonding between phosphate units on the cell surface and zirconium clusters on the MOF monolayer.[3] Recently, a "saccharide bridge" has been applied to promote the accumulation of conjugated polymer nanoparticles around *Pseudomonas aeruginosa*[4] and *E. coli*.[5] Adhesive bacteria such as *E. coli* can express type 1 pili where lectin domain FimH is the contributing adhesive site,[6] and mannoside have been shown to bind adhesion FimH on *E. coli*.[7] Phenylboronic acid (PBA) group in conjugated polymers can interact with the mannotriose or lactulose on the bacterial surface through the high affinity between diols and PBA,[8] and mannotriose, as mannose derivative, can occupy adhesion sites of adhesive *E. coli*,[9] both of which promote the specific attachment of conjugated polymers on the bacteria together. This strategy has been applied in the antiadhesive treatment of bacteria and sterilization applications, and we believe that it could also provide insights into the assembly of material-bacteria hybrids in the semi-artificial photosynthesis field. Taking

fluorene-phenyl-based polymers as an example, compared with polymers FP1 and FP2 which mainly rely on nonspecific interactions, polymer FP3 with PBA groups could improve the attachment to bacterial cells through both nonspecific and specific interactions; the latter may also facilitate electron transfer between materials and microorganisms. Furthermore, instead of using PBA to interact with mannotriose that can occupy the adhesive sites on bacteria, mannose-substituted conjugated polymers,[10] such as FP4, could also be candidates in organic material-based biohybrids. Furthermore, instead of particles of semiconductors, microorganisms can also be attached to polymer films and/or electrodes which brings about various configurations of biohybrid systems.

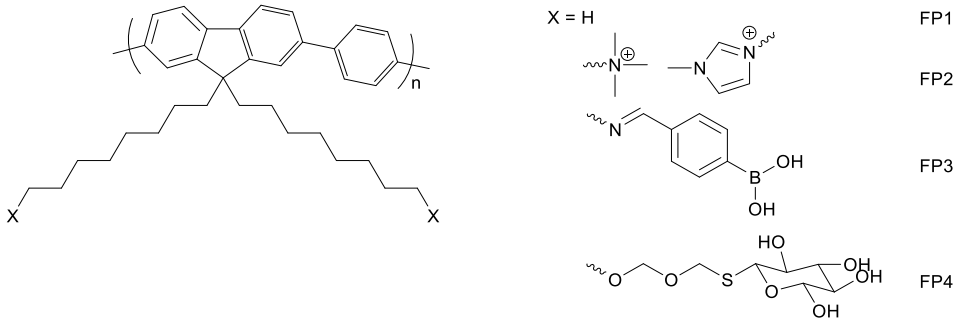

Figure 5.1 Structures of polymers.

Thirdly, other than *E. coli* mainly used in this project, many other microorganisms can be assembled with organic materials for different reactions, for example, nitrogen fixation and CO_2 reduction, which is challenging with fully artificial systems.

Lastly, stability is the other important indicator in evaluating the biohybrid systems, which is mainly limited by the activity of the microorganisms involved. Using a flow system equipped with automation to separate materials from biohybrid suspension and replace them with fresh cell culture at regular intervals might provide opportunities to address this challenge. Additionally, more effort should be made to gain an understanding of the underlying fundamental processes in these biohybrid systems. In particular, electron transport chains and intracellular electron transport should be studied in more detail, and spectroscopic techniques, such as transient absorption spectroscopy coupled with metabolic analysis, should allow further insight. For some redox-active materials, cyclic voltammetry[11] has also been reported to explore the interactions between biological and artificial components.

5.3 References

(1) Kandambeth, S.; Venkatesh, V.; Shinde, D. B.; Kumari, S.; Halder, A.; Verma, S.; Banerjee, R. Self-Templated Chemically Stable Hollow Spherical Covalent Organic Framework. *Nat. Commun.* **2015**, *6* (1), 6786. https://doi.org/10.1038/ncomms7786.

(2) Chen, J.; Yan, W.; Townsend, E. J.; Feng, J.; Pan, L.; Del Angel Hernandez, V.; Faul, C. F. J. Tunable Surface Area, Porosity, and Function in Conjugated Microporous Polymers. *Angew. Chemie - Int. Ed.* **2019**, *58* (34), 11715–11719. https://doi.org/10.1002/anie.201905488.

(3) Ji, Z.; Zhang, H.; Liu, H.; Yaghi, O. M.; Yang, P. Cytoprotective Metal-Organic Frameworks for Anaerobic Bacteria. *Proc. Natl. Acad. Sci. U. S. A.* **2018**, *115* (42), 10582–10587. https://doi.org/10.1073/pnas.1808829115.

(4) Liu, L.; Wang, X.; Zhu, S.; Yao, C.; Ban, D.; Liu, R.; Li, L.; Wang, S. Controllable Targeted Accumulation of Fluorescent Conjugated Polymers on Bacteria Mediated by a Saccharide Bridge. *Chem. Mater.* **2020**, *32* (1), 438–447. https://doi.org/10.1021/acs.chemmater.9b04034.

(5) Liu, L.; Wang, X.; Ban, D.; Zhu, S.; Li, L. Controllable Accumulation of Conjugated Polymer Nanoparticles on the Surface of Adhesive Bacteria. *Colloids Surfaces A Physicochem. Eng. Asp.* **2020**, *591* (January), 124569. https://doi.org/10.1016/j.colsurfa.2020.124569.

(6) Barras, A.; Martin, F. A.; Bande, O.; Baumann, J.-S.; Ghigo, J.-M.; Boukherroub, R.; Beloin, C.; Siriwardena, A.; Szunerits, S. Glycan-Functionalized Diamond Nanoparticles as Potent E. Coli Anti-Adhesives. *Nanoscale* **2013**, *5* (6), 2307–2316. https://doi.org/10.1039/C3NR33826F.

(7) Spaulding, C. N.; Klein, R. D.; Ruer, S.; Kau, A. L.; Schreiber, H. L.; Cusumano, Z. T.; Dodson, K. W.; Pinkner, J. S.; Fremont, D. H.; Janetka, J. W.; Remaut, H.; Gordon, J. I.; Hultgren, S. J. Selective Depletion of Uropathogenic E. Coli from the Gut by a FimH Antagonist. *Nature* **2017**, *546* (7659), 528–532. https://doi.org/10.1038/nature22972.

(8) Ma, R.; Shi, L. Phenylboronic Acid-Based Glucose-Responsive Polymeric Nanoparticles: Synthesis and Applications in Drug Delivery. *Polym. Chem.* **2014**, *5* (5), 1503–1518. https://doi.org/10.1039/C3PY01202F.

(9) Yan, X.; Sivignon, A.; Yamakawa, N.; Crepet, A.; Travelet, C.; Borsali, R.; Dumych, T.; Li, Z.; Bilyy, R.; Deniaud, D.; Fleury, E.; Barnich, N.; Darfeuille-Michaud, A.; Gouin, S. G.; Bouckaert, J.; Bernard, J. Glycopolymers as Antiadhesives of E. Coli Strains Inducing Inflammatory Bowel Diseases. *Biomacromolecules* **2015**, *16* (6), 1827–1836. https://doi.org/10.1021/acs.biomac.5b00413.

(10) Xue, C.; Velayudham, S.; Johnson, S.; Saha, R. Highly Water-Soluble, Fluorescent, Conjugated Fluorene-Based Glycopolymers with Poly(Ethylene Glycol)-Tethered Spacers for Sensitive Detection of Escherichia Coli. *Chem. Eur. J.* **2009**, 2289–2295. https://doi.org/10.1002/chem.200801875.

(11) Gai, P.; Yu, W.; Zhao, H.; Qi, R.; Li, F.; Liu, L.; Lv, F.; Wang, S. Solar-Powered Organic Semiconductor–Bacteria Biohybrids for CO 2 Reduction into Acetic Acid. *Angew. Chemie Int. Ed.* **2020**, *59* (18), 7224–7229. https://doi.org/10.1002/anie.202001047.

Chapter 6 :

Materials and Methods

Section 6.1 links to all materials and methods in Chapter 2, Section 6.2 links to Chapter 3, and Section 6.3 links to Chapter 4.

6.1 Experimental Methods

6.1.1 Monomer Synthesis

2,7-Dibromo-9,9-bis(8-bromo-n-octyl)-fluorene

The compound was synthesized following a previously reported procedure.[1] NaOH (30 mL, aqueous solution 50 wt. %) was added to a solution of 2,7-dibromo-9*H*-fluorene (5.0 g, 15 mmol), 1,8-dibromo-*n*-octane (8.5 mL, 46 mmol), and tetrabutylammonium bromide (TBAB, 0.5 g, 1.5 mmol) in toluene (60 mL). The mixture was then heated to 60 °C for 12 h. After cooling to room temperature, phases were separated, and the aqueous phase was extracted with chloroform. The organic solution was washed with deionized water, the organic phase was then dried by magnesium sulfate, filtered, and concentrated in vacuo to give residues which were then purified by silica gel column chromatography, ethyl acetate/hexane = 1:50 by volume ratio, to obtain colourless solid (6.3 g, 59%). ^{1}H NMR (400 MHz, $CDCl_3$, δ): 7.52 (d, 2H, ^{3}J = 8 Hz, Ar-H), 7.46 (dd, 2H, ^{4}J = 2 Hz, ^{3}J = 8 Hz, Ar-H), 7.43 (d, 2H, ^{4}J = 2 Hz, Ar-H), 3.35 (t, 4H, ^{3}J = 8 Hz; -CH_2Br), 1.91 (m, 4H; -CH_2-), 1.77 (m, 4H; -CH_2-), 1.31 (m, 4H; -CH_2-), 1.14-1.05 (br, 12H; -CH_2-), 0.57 (br, 4H; -CH_2-).

6.1.2 Polymerization

Reagents and solvents were purchased from Manchester Organics, Sigma-Aldrich, Fluorochem, Ark Pharm, Apollo, Combi-Blocks, TCI Europe, Carbosynth and used as received without further purification.

6.1.2.1 General procedure for the synthesis of polymers via Suzuki-Miyaura-type polycondensation

A flask was charged with the monomers, toluene, Starks' catalyst, and an aqueous solution of Na_2CO_3. The mixture was degassed by bubbling with N_2 for 30 minutes, before [$Pd(PPh_3)_4$] was added, and heated. The mixtures were evaporated to dryness and washed with water. The crude polymer was then further purified by Soxhlet extraction with methanol, acetone, and ethyl acetate. The high molecular weight fraction of the polymer was recovered by Soxhlet extraction with chloroform. The chloroform was removed and the polymer redissolved in a minimal amount of chloroform, precipitated into large access of methanol, filtered off, and dried under reduced pressure.

LP1: 1,4-Benzenediboronic acid bis(pinacol) ester (264 mg, 0.80 mmol), 2,7-dibromo-9,9-bis(8-bromo-*n*-octyl)-fluorene (567 mg, 0.80 mmol), toluene (30 mL), Na_2CO_3 (10 mL, 2 M), Starks' catalyst (1 drops), and [Pd (PPh_3)$_4$] (18.6 mg) were used in this reaction. After 2 days at 110 °C the reaction was worked up as described above giving the product as a yellow solid in 55% yield (0.457 g). Anal. Calcd for **LP1** $(C_{35}H_{44}Br_2)_n$: C, 67.31; H, 7.10; Br, 25.59%. Found: C, 67.62; H, 6.72; Pd, 0.17%. ^{1}H NMR (400 MHz, $CDCl_3$, δ): 7.82 (m, 6H, Ar-H), 7.66-7.49 (m, 4H, Ar-H), 3.32 (t, 4H, ^{3}J = 6Hz, -CH_2Br), 2.09 (br, 4H, -CH_2-), 1.75 (m, 4H, -CH_2-), 1.31-1.12 (m, 16H, -CH_2-), 0.78 (br, 4H, -CH_2-).

LP2: 2,5-Thiophenediboronic acid bis(pinacol) ester (268.8 mg, 0.80 mmol), 2,7-dibromo-9,9-bis(8-bromo-*n*-octyl)-fluorene (567 mg, 0.80 mmol), toluene (30 mL), Na_2CO_3 (10.0 mL, 2 M), Starks' catalyst (1 drop), and [Pd (PPh_3)$_4$] (18.6 mg) were used in this reaction. After 2 days at 110 °C the reaction was worked up as described above giving the product as an orange solid in 21% yield (0.175 g). Anal. Calcd for **LP2** $(C_{33}H_{42}Br_2S)_n$: C, 62.86; H, 6.71; Br, 25.34; S, 5.08%. Found: C, 69.45; H, 6.79; S, 3.80, Pd, 0.40%. ^{1}H NMR (400 MHz, $CDCl_3$, δ): 7.72-7.56 (m, 6H, Ar-H), 7.48-7.40 (m, 2H, Ar-H), 3.32 (m, 4H, -CH_2Br), 2.01 (br, 4H, -CH_2-), 1.75 (m, 4H, -CH_2-), 1.28-1.09 (m, 16H, -CH_2-), 0.65 (br, 4H, -CH_2-).

LP3: 2,2′-Bithiophene-5,5′-diboronic acid bis(pinacol) ester (334.5 mg, 0.80 mmol), 2,7-dibromo-9,9-bis(8-bromo-*n*-octyl)-fluorene (567 mg, 0.80 mmol), toluene (30 mL), Na_2CO_3 (10.0 mL, 2 M), Starks' catalyst (1 drops), and [Pd (PPh_3)$_4$] (18.6 mg) were used in this reaction. After 2 days at 110 °C the reaction was worked up as described above giving the product as a coral solid in 44% yield (0.397 g). Anal. Calcd for **LP3** $(C_{37}H_{44}Br_2S_2)_n$: C, 62.36; H, 6.22; Br, 22.42; S, 9.00%. Found: C, 64.89; H, 6.10; S, 8.13, Pd, 0.0093%. ^{1}H NMR (400 MHz, $CDCl_3$, δ): 7.70-7.46 (m, 6H, Ar-H), 7.34-7.20 (m, 4H, Ar-H), 3.31 (m, 4H, -CH_2Br), 2.01 (br, 4H, -CH_2-), 1.74 (m, 4H, -CH_2-), 1.28-1.09 (m, 16H, -CH_2-), 0.69 (br, 4H, -CH_2-).

LP4: 3,7-Bis(4,4,5,5-tetramethyl-1,3,2-dioxaborolan-2-yl)dibenzo[*b,d*]thiophene sulfone (374.5 mg, 0.80 mmol), 2,7-dibromo-9,9-bis(8-bromo-*n*-octyl)-fluorene (567 mg, 0.80 mmol), toluene (30 mL), Na_2CO_3 (10.0 mL, 2 M), Starks' catalyst (1 drops), and [Pd(PPh_3)$_4$] (18.6 mg) were used in this reaction. After 2 days at 110 °C the reaction was worked up as described above giving the product as a light-yellow solid in 36% yield (0.122 g). Anal. Calcd for **LP4** $(C_{41}H_{46}Br_2O_2S)_n$: C, 64.57; H, 6.08; Br, 20.95; O, 4.20; S, 4.20%. Found: C, 65.98; H, 5.74; S, 3.16, Pd, 0.027%. ^{1}H NMR (400 MHz, $CDCl_3$, δ): 8.19 (2H, s), 8.05-7.95 (m, 6H, Ar-H), 7.74-

7.60 (m, 4H, Ar-H), 3.33 (t, 4H, ^3J = 8 Hz, -CH_2Br), 2.13 (br, 4H, -CH_2-), 1.76 (m, 4H, -CH_2-), 1.35-1.05 (m, 16H, -CH_2-), 0.71 (br, 4H, -CH_2-).

LP5_χ: 2,7-dibromo-9,9-bis(8-bromooctyl)-fluorene (m mmol), 2,7-dibromo-9,9-bis(8-octyl)-fluorene (n mmol), 9,9-dioctyl-9H-fluorene-2,7-diboronic acid bis(pinacol) ester ((m+n) mmol), toluene (25 mL), Na_2CO_3 (10.0 mL, 2 M), Starks' catalyst (1 drops), and [$Pd(PPh_3)_4$] (18.6 mg) were used in this reaction. After 2 days at 110 °C the reaction was worked up as described above giving the product as a yellow solid in yield of 23% for LP5_0.10, 36% for LP5_0.25, and 20.6% for LP5_0.50.

Anal. Calcd for **LP5_0.10** ($C_{58}H_{82}Br_{0.4}$)$_n$: C, 86.59; H, 10.49; Br, 2.91%. Found: C, 86.59; H, 10.49; Pd, 0.085%. ^{1}H NMR (400 MHz, $CDCl_3$, δ): 7.95-7.50 (m, 60H, Ar-H), 3.32 (t, 3H, ^3J = 6Hz, -CH_2Br), 2.12 (br, 36H, -CH_2-), 1.75 (m, 4H, -CH_2-), 1.14 (m, 200H, -CH_2-), 0.78 (m, 90H, -CH_2CH_3).

Anal. Calcd for **LP5_0.25** ($C_{58}H_{81}Br_1$)$_n$: C, 82.75; H, 9.97; Br, 7.28%. Found: C, 82.75; H, 9.97; Pd, 0.040 %. ^{1}H NMR (400 MHz, $CDCl_3$, δ): 7.95-7.50 (m, 24H, Ar-H), 3.32 (m, 4H, -CH_2Br), 2.12 (br, 13H, -CH_2-), 1.75 (br, 3H, -CH_2-), 1.36-0.90 (m, 80H, -CH_2-), 0.81 (m, 30H, -CH_2CH_3).

Anal. Calcd for **LP5_0.50** ($C_{58}H_{80}Br_2$)$_n$: C, 74.34; H, 8.61; Br, 17.05%. Found: C, 73.34; H, 8.61; Pd, 0.150%. ^{1}H NMR (400 MHz, $CDCl_3$, δ): 7.95-7.58 (m, 12H, Ar-H), 3.32 (t, 4H, ^3J = 6Hz, -CH_2Br), 2.37-1.70 (m, 12H, -CH_2-), 1.39-1.10 (m, 40H, -CH_2-), 0.82 (m, 12H, -CH_2CH_3).

6.1.2.2 General procedure for the synthesis of trimethylamine substituted polymers

General procedure for the synthesis of trimethylamine substituted polymers.[2] 100 mg LP1, LP2, LP3, LP4, and LP5 were dissolved in $CHCl_3$ (20 mL), and then a solution of trimethylamine in ethanol (30 wt. %, 10 mL) was added. The reaction mixture was stirred for 48 hours at room temperature. The solvent was evaporated, and the product was dried under a vacuum.

LP11: Obtained as a yellow solid in 78% yield (78 mg). Anal. Calcd for **LP11** ($C_{41}H_{62}N_2$)$_n$: C, 84.47; H, 10.72; N, 4.81%. Found: C, 63.76; H, 7.74; N, 2.88; Pd, 0.16%. ^{1}H NMR (400 MHz, DMSO, δ): 8.2`0-7.40 (m, 10H, Ar-H), 3.36 (s, 4H, -CH_2-), 3.22 (br, 4H, -CH_2-), 3.01 (m, 18H, -CH_3), 1.55 (s, 4H, -CH_2-), 1.31-0.85 (m, 16H, -CH_2-), 0.65 (br, 4H, -CH_2-).

LP21: Obtained as an orange solid in 45% yield (45 mg). Anal. Calcd for **LP21** ($C_{39}H_{60}N_2S$)$_n$: C, 79.53; H, 10.27; N, 4.76; S, 5.44%. Found: C, 62.85; H, 7.73; N, 2.95; S, 3.37; Pd 0.43%.

^{1}H NMR (400 MHz, DMSO, δ): 8.12-7.10 (m, 8H, Ar-H), 3.25-2.90 (m, 26H, -CH_2-, -CH_3), 1.53 (s, 4H, -CH_2), 1.21-0.85 (m, 24H, -CH_2-).

LP31: Obtained as a coral solid in 58% yield (58 mg). Anal. Calcd for **LP31** $(C_{43}H_{62}N_2S_2)_n$: C, 76.96; H, 9.31; N, 4.17; S, 9.55%. Found: C, 62.43; H, 7.34; N, 2.81; S, 6.91; Pd, 0.0093%. ^{1}H NMR (400 MHz, DMSO, δ): 8.15-7.10 (m, 10H, Ar-H), 3.36 (s, 4H, -CH_2-), 3.17 (br, 4H, -CH_2-), 2.99 (m, 22H, -CH_2-, -CH_3), 1.54 (s, 4H, -CH_2-), 1.38-0.37 (m, 20H, -CH_2-).

LP41: Obtained as a light-yellow solid, 71% yield (71 mg). Anal. Calcd for **LP41** $(C_{47}H_{64}N_2O_2S)_n$: C, 78.29; H, 8.95; N, 3.88; O, 4.44; S, 4.45%. Found: C, 60.67; H, 6.66; N, 2.64; S, 3.43%; Pd, 0.021%. ^{1}H NMR (400 MHz, DMSO, δ): 8.65-7.80 (m, 12H, Ar-H), 3.35 (s, 8H, -CH_2-), 3.16 - 2.98 (m, 18H, -CH_3), 1.53 (s, 4H, -CH_2-), 1.38-0.35 (m, 20H, -CH_2-).

LP51: Obtained as a light-yellow solid in yield of 36% for LP51_0.10, 38% for LP51_0.25, and 24% for LP51_0.50.

Anal. Calcd for **LP51_0.10** $(C_{59}H_{84}N_{0.8})_n$: C, 88.54; H, 10.90; N, 0.55%. Found: C, 88.54; H, 10.90; N, 0.55; Pd, 0.097%. ^{1}H NMR (400 MHz, $CDCl_3$, δ): 7.95-7.50 (m, 60H, Ar-H), 3.32 (m, 13H, -CH_3), 2.13 (br, 40H, -CH_2-), 1.14 (m, 200H, -CH_2-), 0.81 (m, 90H, -CH_2CH_3).

Anal. Calcd for **LP51_0.25** $(C_{62}H_{87}N_2)_n$: C, 87.60; H, 11.01; N, 1.38%. Found: C, 86.96; H, 10.50; N, 2.53; Pd, 0.060%. ^{1}H NMR (400 MHz, $CDCl_3$, δ): 7.95-7.50 (m, 24H, Ar-H), 3.49-3.30 (m, 18H, -CH_3), 2.12 (br, 16H, -CH_2-), 1.14 (br, 80H, -CH_2-), 0.90-0.69 (m, 30H, -CH_2CH_3).

Anal. Calcd for **LP51_0.50** $(C_{64}H_{98}N_2)_n$: C, 85.84; H, 11.03; N, 3.13%. Found: C, 85.84; H, 11.03; N, 3.13; Pd, 0.209 %. ^{1}H NMR (400 MHz, $CDCl_3$, δ): 7.90-7.57 (m, 12H, Ar-H), 3.30 (m, 18H, -CH_3), 2.12 (br, 12H, -CH_2-), 1.41-1.09 (m, 40H, -CH_2-), 0.79 (m, 10H, -CH_2CH_3).

6.1.3 Nanoparticle Fabrication

Conjugated polymers were self-assembled into polymer (nano)particles in water through reprecipitation methods.[3,4] To achieve this, the conjugated polymers (10 mg) were dissolved by stirring in THF (12.5 mL). 3 mL of the polymer/THF solution was added quickly to 12 mL of deionized water while sonicating the mixture under 30 ℃ for around 10 seconds. The THF was removed by partial evaporation at 65 ℃ for 5 hours.

6.1.4 Characterization Methods

^{1}H NMR spectra were recorded using a Bruker Avance 400 NMR spectrometer. CHN Analysis was performed on a Thermo EA1112 Flash CHNS-O Analyzer using standard microanalytical procedures. Single detection gel permeation chromatography (GPC) was calibrated against polystyrene standards (Agilent EasiCal PS-2 standards), and performed using an Agilent 1260 Infinity II GPC/SEC system (Agilent, UK), two PLgel 5 μm MIXED-D columns and a PL gel 5 μm guard column, with samples detected by refractive index (RI). Powder X-ray diffraction (PXRD) measurements were performed on a PANalytical X'Pert PRO MPD, with a Cu X-ray source, used in high throughput transmission mode with Kα focusing mirror and PIXCEL 1D detector. Thermogravimetric analysis was performed on an EXSTAR6000 by heating samples at 10 °C min^{-1} under nitrogen in open platinum pans from 25 to 600 °C. UV-Visible absorption spectra of polymer nanoparticle dispersions, polymer solutions in chloroform, and thin film were recorded on a Shimadzu UV-2550 UV-Vis spectrometer. Photoluminescence spectra of the polymer nanoparticle solution and thin film were measured with a Shimadzu RF-5301PC fluorescence spectrometer at room temperature. Dynamic light scattering and zeta-potential measurements were performed on a Malvern Zetasizer Nano Particle Sizer at 25 °C. Inductively coupled plasma optical emission spectrometry analysis was performed on an ICP-OES Agilent 5110 after a microwave digest of the materials in nitric acid (67-69%, trace metal analysis grade) to determine the palladium content. Photoelectron spectroscopy in air (PESA) measurements were recorded using a Riken Keiki PESA spectrometer (Model AC-2). Samples for PESA were prepared on ITO glass substrates. SEM measurements were performed on Hitachi S4800 cold field emission scanning electron microscope (FE-SEM) and imaging was conducted at a working voltage of 3.0 kV and a working distance of 8 mm using a combination of upper and lower secondary electron detectors.

6.1.5 Photocatalysis Experiments

High throughput hydrogen evolution experiments: The Agilent Technologies vials (crimp top, headspace, clear with graduation marks and write-on spot, flat bottom, 10 mL, 23 × 46 mm) were charged with approximately 4.5 mL of polymer nanoparticle solution. Degassed scavenger solutions were loaded in the robot and water from an ELGA water purification system was degassed with nitrogen and connected to the setup. The system was closed and flushed with nitrogen from the house supply for 6 hours. The automatic setup dispenses the requisite amount of liquids and seals the vials with Agilent Technologies caps (crimp,

headspace, with septum, 20 mm, silver aluminium cap with safety feature, moulded PTFE/butyl septum). The total volume of the reaction mixture was 5.0 ± 0.1 mL in each vial. The vials were illuminated with an Oriel Solar Simulator 94123A with an output of 1.00 sun on a Stuart Scientific Gyro rocker SRT9 for 130 minutes (classification IEC 60904-9 2007 spectral match A, uniformity classification A, temporal stability A, 1600 W Xenon light source, 25 × 25 cm output beam, Air mass 1.5G filter, 350-1000 nm). After photocatalysis, the amount of evolved hydrogen was measured on an Agilent Technologies GC 7890B connected to an Agilent Technologies headspace sampler 7697A.

6.1.6 Computational Methods

The IP and EA values of LP2 and LP3 were calculated using a previously developed approach[5,6] based on ΔDFT calculations on the neutral, cationic and anionic versions of oligomer models of the polymers. These calculations used the B3LYP[7,8,9,10] density functional, the DZP[11] basis-set and the COSMO[12] implicit solvation model to describe the dielectric environment of the polymer (particles). All DFT calculations were performed using the Turbomole[13,14] 7.5 code and all calculations were performed on 8 phenyl equivalent long oligomeric models. Starting structures for the latter were obtained using a CREST/gfn2-xTB[15,16] conformer search.

6.2 Experimental Methods

6.2.1 Polymer Synthesis

Synthesis of LP10: General procedure for the synthesis of imidazolium substituted polymers.[1] 0.1g LP1 (see Chapter 2 for details) was dissolved in N_2 purged toluene (40 mL), and 1-methylimidazole (2 g, 24 mmol) were added dropwise. After the reaction was stirred at 40 °C for 12 hours. Then MeOH (100 mL) was added to dissolve precipitated polymer and the reaction was stirred at 40 °C for 5 days. After the solution was concentrated in vacuo, the residue was poured into 100 mL ethyl acetate and precipitates were filtered, washed with acetone several times, and dried in a vacuum oven overnight at room temperature to obtain imidazolium substituted yellow solid LP10 in 74% yield (74 mg). Anal. Calcd for **LP10** $(C_{43}H_{50}N_4)_n$: C, 82.12; H, 8.97; N, 8.91%. Found: C, 64.61; H, 7.09; N, 2.88; Pd, 0.16%. ^{1}H NMR (400 MHz, DMSO, δ): 8.10-7.60 (m, 16H, Ar-H), 4.06 (br, 4H, -CH_2-), 3.81 (br, 4H, -CH_2-), 1.65 (s, 4H, -CH_2-), 1.31-0.50 (m, 20H, -CH_2-).

Synthesis of LP6: 1,4-Benzenediboronic acid bis(pinacol) ester (264 mg, 0.80 mmol), 2,7-dibromo-9,9-bis(8-bromooctyl)-fluorene (283 mg, 0.40 mmol), 2,7-dibromo-9,9-bis(8-octyl)-fluorene (M1', 219 mg, 0.40 mmol), toluene (10 mL), Na_2CO_3 (6.0 mL, 2 M), Starks' catalyst (1 drops), and [$Pd(PPh_3)_4$] (18.6 mg) were used in this reaction. After 2 days at 110 °C the reaction was worked up as described above giving the product as a yellow solid in 65% yield (0.498 g). Anal. Calcd for LP6 $(C_{70}H_{88}Br_2)_n$: C, 77.19; H, 8.14; Br, 14.67%. Found: C, 78.59; H, 8.12; Pd, 0.32%. ^{1}H NMR (400 MHz, $CDCl_3$, δ): 7.90-7.60 (m, 20H, Ar-H), 3.32 (t, 4H, ^{3}J = 6Hz, -CH_2Br), 2.09 (s, 6H, -CH_2-), 1.75 (m, 4H, -CH_2-), 1.12 (m, 42H, -CH_2-), 0.78 (m, 10H, -CH_2CH_3).

Synthesis of LP61: FP8BrFP8 were dissolved in $CHCl_3$ (20 mL), and then a solution of trimethylamine in ethanol (30 wt %, 10 mL) was added. The reaction mixture was stirred for 48 h at room temperature. The solvent was evaporated, and the product was dried under vacuum. Anal. Calcd for **LP61** $(C_{76}H_{106}N_2)_n$: C, 87.13; H, 10.20; N, 2.67%. Found: C, 73.80; H, 8.33; N, 2.03; Pd, 0.20%. ^{1}H NMR (400 MHz, DMSO, δ): 7.85-7.59 (m, 20H, Ar-H), 3.16 (br, 4H, -CH_2-), 3.30 (m, 18H, -CH_3), 2.15 (s, 4H, -CH_2-), 1.51-1.07 (m, 48H, -CH_2-), 0.74 (m, 10H, -CH_2CH_3).

6.2.2 Generation of Constructs

The *hydA* (GenBank accession code AAL23572.1) and *fd* (GenBank accession code XP_001692808.1) genes from *Chlamydomonas reinhardtii* were codon-optimized for heterologous expression in *E. coli*. The Fd protein was fused to the N-terminus of HydA with a 15 amino acid linker composed of GGGGSGGGGSGGGGS. The *hydGX* and *hydEF* genes from *Shewanella oneidensis* (GenBank accession code AE014299.2: 4070148- 4074530), which encode the maturases HydE, HydF and HydG were synthesized. The *fd-hydA* gene was ligated to pCDFDueT-1 linearized by EcoRI and AscI, together with the *hydGX* and *hydEF* gene fragments, to generate the *hyd* vector.

6.2.3 Western Blotting

Briefly, 30 μg of total protein was loaded into each well. Western Blotting was performed using primary mouse monoclonal anti-His (Invitrogen, dilution 1:3000), and horseradish peroxidase-conjugated goat anti-mouse IgG secondary antibody (Agrisera, dilution 1:10,000). Signals were visualized using a chemiluminescence kit (Bio-Rad). Immunoblot images were collected by ImageQuant LAS 4000 software version 1.2.1.119. Immunoblot protein quantification was performed using ImageJ software (version 1.52 h).

6.2.4 Characterization Methods

6.2.4.1 Scanning electron microscope (SEM) characterization of E. coli incubated with polymer nanoparticles

E. coli was harvested by centrifuging at 7197 rcf (relative centrifugal force) for 5 min and washed with 10 mM Tris-HCl buffer 3 times. After the supernatant was discarded, the cell pellet was resuspended in 10 mM Tris-HCl. Then 200 μL cell suspension was incubated with 2.0 mL 10 mg L^{-1} polymer nanoparticle solution for 10 mins at room temperature. To prepare specimen for SEM characterization, 10 μL of the mixture was pipetted on top of silica disc which was mounted on a metal stub by silver-containing glue. Then the dried specimen was coated with chromium for 15 seconds by Quorum Q150T ES.

SEM measurements were performed on Hitachi S4800 cold field emission scanning electron microscope (FE-SEM) and imaging was conducted at a working voltage of 3.0 kV and a working distance of 8 mm using a combination of upper and lower secondary electron detectors.

6.2.4.2 Confocal fluorescence microscope characterization of E. coli incubated with polymer nanoparticles

E. coli was harvested by centrifuging at 7197 rcf for 5 min and washed with 10 mM Tris-HCl buffer 3 times. After the supernatant was discarded, the cell pellet was resuspended in 10 mM Tris-HCl. Then 100 µL cell suspension was incubated with 1.0 mL 5 mg L^{-1} polymer nanoparticle solution for 10 mins at room temperature. To immobilize the cells for imaging 10 µL of the mixture was pipetted on top of Tris-HCl/agar and a dried drop was cut out and placed against cover-slip. Live-cell confocal fluorescence imaging was performed on a LSM 780 microscope (Zeiss) and 63× oil-immersion objective (numerical aperture: 1.46) and excitation at 488 nm were used in imaging. Images were processed with FIJI image processing package.

6.2.5 Photobiocatalytic Hydrogen Production Measurement

For the photocatalytic hydrogen production measurements, suspension of recombinant *E. coli* cells was prepared as follows: Cells were harvested from 20 mL cell solution by centrifugation (10 min, 4,000 rcf) after 16 hours of induction. After the supernatant was carefully removed by syringes, the cell pellet was then resuspended in 1.0 mL 10 mM Tris-HCl (pH 7) buffer after washing with 10 mL 10 mM Tris-HCl buffer three times.

For high throughput solar simulator measurements, 4.3 mL 50 mg L-1 polymer nanoparticle solution, 0.5 mL 100 mM Tris-HCl (pH 7) buffer, and 50 µL 0.1 M ascorbic acid were added into headspace vials (Agilent, 10 mL, width 22.75 × height 46 mm) and purged with nitrogen in a Sweigher Chemspeed Technologies for 6 hours. After 200 µL collected cell suspension was injected into vials, all sample vials were irradiated under the solar simulator (AM1.5G, Class AAA, IEC/JIS/ASTM, 1440 W xenon, 12 × 12 in., MODEL: 94123A) agitated on a rocker/roller device. Gaseous products were analyzed on a Shimadzu GC-2010 equipped with Shimadzu HS-20 injecting a sample from the headspace sampler via a transfer line (temperature 150 °C) onto a Rt-Msieve 5 Å column with He as the carrier gas at a flow rate of 30 mL min-1. Hydrogen was detected with a barrier discharge ionization detector referencing against standard gases with known concentrations of hydrogen.

6.3 Experimental Methods

6.3.1 Transient Absorption (TA) Measurements

The apparatus employed to obtain transient absorption, TA, and spectra of the CTFs of interest has been recently reported.[17] Briefly, ~1 W from a Ytterbium laser system (PHAROS Short-Pulse 10 W, PH1-SP-10W, Light Conversion) with an output wavelength of 1028 nm, a repetition rate of 10 kHz, and pulse duration of ~170 fs is used to drive an Optical Parametric Amplifier, OPA (ORPHEUS, Light Conversion) in tandem with a second harmonic generation module (LYRA, Light Conversion) in order to generate radiation centered at 400 nm with a bandwidth (FWHM) of 3 nm. This 400 nm output was used as the pump source for subsequent TA measurements, which employed a commercial TA spectrometer (HARPIA, Light Conversion). The probe light was a visible white light supercontinuum generated by focusing < 0.1 W of 1028 nm radiation onto a sapphire window. The pump and probe beams were focused on 1 mm and 600 μm spots in the sample. The pump laser beam was chopped, resulting in an effective pumping repetition rate of 5 kHz. The power of the chopped beam incident on the sample was 200 μW. The samples were suspensions of LP41 polymer nanoparticle (~10 mg L^{-1} LP41 polymer concentration) in 10 mM Tris-HCl buffer with/without 25 μL *E. coli* concentrates supplemented with/without 1 mM ascorbic acid, held within a quartz cuvette with a 10 mm path length. To maintain a stable suspension and to prevent sample degradation, the sample was continually stirred. The probe light was spectrally dispersed by a spectrograph (Kymera 193i, Andor), employing a grating of 150 lines/mm, blazed at 800 nm, and detected using an NMOS detector (S3901, Hamamatsu). Data were analysed using Carpetview software (Light Conversion); all data were normalised to the global maximum ΔA to account for changes in UV/Vis absorption spectra between different samples.

6.3.2 Polymer/*E. coli* Biohybrid Sample Preparation For GC-MS Measurement

6.3.2.1 Proposed polymer nanoparticle removal procedure

Stage 1: Initial quenching and pelletisation

1) Add 2 mL of sample to a 15 mL falcon tube.
2) Add 4 mL of cold (-48 °C) LCMS grade 60% aqueous methanol solution to the falcon tube.
3) Invert the falcon tube 10 times to mix content.
4) Centrifuge samples at 4,800 g for 10min at -4 °C to pellet cellular mass and protein precipitate.

5) Decant supernatant to a labelled 15 mL falcon tube.
6) Re-centrifuge original sample at 4,800 g for 10 min at -4 °C to further pellet.
7) Decant residual supernatant to its labelled 15 mL falcon tube.
8) Store the two falcon tubes – one with supernatant the other with the pellet – in a -80 °C freezer.
9) Check the fluorescence of supernatant sample 0 (0-1, 0-2, 0-3)

Stage 2: Polymer nanoparticle removal from the supernatant sample

1) Centrifuge 6.0 mL supernatant samples (0-4, 0-5, 0-6) at 7,197 g for 10 min at -4 °C to pellet polymer particles.
2) Decant supernatant to a 15 mL falcon tube.
3) Transfer 2 mL solution to a 2 mL Eppendorf tube (labelled sample 1; 1-1, 1-2, 1-3) for fluorescence check.
4) Transfer 3 mL solution to an Amicon Ultra-4 centrifugal filter units (3,000 NMWL)
5) Centrifuge samples at 7,197 g for 10 min at -4 °C, labelled sample 1-4, 1-5, 1-6 for fluorescence check
6) Transfer 3 mL solution to a VIVASPIN 6 centrifugal filter units (30,000 NMWL)
7) Centrifuge samples at 7,197g for 10 min at -4 °C, labelled sample 1-7, 1-8, 1-9 for fluorescence check.

6.3.2.2 Proposed Sample Preparation Procedure for GCMS Analysis

Stage 1: Initial quenching and pelletisation

1) Add 1 mL of sample to a 5 mL falcon tube.
2) Add 2 mL of cold (-48 ° C) LCMS grade 60% aqueous methanol solution to the falcon tube.
3) Invert the falcon tube 10 times to mix content.
4) Centrifuge samples at 4800 g for 10 min at -8 ° C to pellet cellular mass and protein precipitate.
5) Decant supernatant to a labelled 5 mL falcon tube.
6) Re-centrifuge the original sample at 4800 g for 10 min at -8 ° C to further pellet.
7) Decant residual supernatant to its labelled 5 mL falcon tube.
8) Store the two falcon tubes, one with supernatant the other with the pellet in a -80 ° C freezer.

Stage 2: Extra-cellular medium

1) Retrieve the supernatant tube from the -80 °C freezer.
2) Decant content into an Ultra-4 centrifugal filter unit.

3) Centrifuge content for 10 min at low temperature (< 4 °C) – to separate the supernatant containing disrupted cell biomass (post filter section of the tube) from the concentrated polymer nanoparticle (pre-filter section of the tube).
4) Transfer 1mL of supernatant from the centrifuge tube to each of two 2 mL Eppendorf tubes, then add 100 µL of internal standard to each tube.
5) Dry down all the samples then store in a -80 °C freezer.

Stage 3: Intra-cellular content

1) Retrieve the pellet tube from the -80 °C freezer.
2) Add 500 µL of cold (-48 °C) LCMS grade 80% aqueous methanol.
3) Suspend the pellet in the solution via vortex (to encourage separation of nanoparticle and biomass).
4) Transfer the dissolved pellet in to a chilled 2 mL Eppendorf tube.
5) Repeat steps 2-4 so that the final volume in the 2 mL Eppendorf tube is 1mL.
6) Snap freeze
    a. Snap freeze the 2 mL Eppendorf tube in liquid nitrogen for 1 min, then allow the solution to "thaw" on wet ice.
    b. Vortex the tube for 30s and repeat the snap freeze process two more times.
    c. Centrifuge the solution at -9 °C, 17.0 G for 5 min.
7) Transfer supernatant to an Ultra-4 centrifugal filter unit.
8) To the original (now empty) 2 mL Eppendorf tube:
    a. Add 1500 µL of cold (-48 °C) LCMS grade 80% aqueous methanol.
    b. Vortex, centrifuge, and transfer.
9) Centrifuge the Ultra-4 tube (containing ~2.5 mL of suspended pellet and extract solution) for 10 min at low temperature (< 4 °C) – to separate the supernatant containing disrupted cell biomass (post filter section of the tube) from the concentrated polymer nanoparticle (pre-filter section of the tube).
10) Transfer 1 mL of supernatant from the centrifuge tube to each of two 2 mL Eppendorf tubes, then add 100 µL of internal standard to each tube.
11) Dry down all the samples then store in a -80 °C freezer.

6.3.2.3 GC-MS Instrument Method

Table 6.1 GCMS instrument method

	Instrument Method
Instrument	Agilent 8890 Gas Chromatograph and 7250 Q-ToF Mass Spectrometer
Autosampler	CTC PAL3
Injection	1µL 100:1 split mode
Column	Agilent DB-5ms, 30m, 0.25mm, 10µm
GC-Program	Inlet: 280°C; Carrier gas: He 1mL/min; Column gradient: 70°C-4 min hold, 20°C/min to 300°C-4 min hold; Transfer line: 300°C
MS-Program	Solvent delay: 3.5 min; Source: 250°C; EI: 70 eV; m/z: 20-600; Scan rate: 20 Hz
Software	PAL Sequence Assistant, MassHunter Acquisition, MassHunter Qualitative Analysis v10.0
Running Order	Randomised
Running Time	20 min/sample

6.4 References

(1) Kim, K.; Suh, M.; Choi, J.; Lee, D.; Kim, Y.; Cheong, S. H.; Kim, D.; Jeon, D. Y. Conjugated Polyelectrolyte Hybridized ZnO Nanoparticles as a Cathode Interfacial Layer for Efficient Polymer Light-Emitting Diodes. *Adv. Funct. Mater.* **2015**, *25* (48), 7450–7456. https://doi.org/10.1002/adfm.201502360.

(2) Liu, B.; Gaylord, B. S.; Wang, S.; Bazan, G. C. Effect of Chromophore-Charge Distance on the Energy Transfer Properties of Water-Soluble Conjugated Oligomers. *J. Am. Chem. Soc.* **2003**, *125* (22), 6705–6714. https://doi.org/10.1021/ja028961w.

(3) Kurokawa, N.; Yoshikawa, H.; Hirota, N.; Hyodo, K.; Masuhara, H. Size-Dependent Spectroscopic Properties and Thermochromic Behavior in Poly(Substituted Thiophene) Nanoparticles. *ChemPhysChem* **2004**, *5* (10), 1609–1615. https://doi.org/10.1002/cphc.200400117.

(4) Kurokawa, N.; Yoshikawa, H.; Hirota, N.; Hyodo, K.; Masuhara, H.; Szymanski, C.; Wu, C.; Hooper, J.; Salazar, M. A.; Perdomo, A.; Dukes, A.; McNeill, J. Single Molecule Nanoparticles of the Conjugated Polymer MEH-PPV, Preparation and Characterization by near-Field Scanning Optical Microscopy. *J. Phys. Chem. B* **2005**, *109* (18), 8543–8546. https://doi.org/10.1021/jp051062k.

(5) Guiglion, P.; Butchosa, C.; Zwijnenburg, M. A. Polymeric Watersplitting Photocatalysts; a Computational Perspective on the Water Oxidation Conundrum. *J. Mater. Chem. A* **2014**, *2* (30), 11996–12004. https://doi.org/10.1039/C4TA02044H.

(6) Guiglion, P.; Monti, A.; Zwijnenburg, M. A. Validating a Density Functional Theory Approach for Predicting the Redox Potentials Associated with Charge Carriers and Excitons in Polymeric Photocatalysts. *J. Phys. Chem. C* **2017**, *121* (3), 1498–1506. https://doi.org/10.1021/acs.jpcc.6b11133.

(7) Becke, A. D. Density-functional Thermochemistry. III. The Role of Exact Exchange. *J. Chem. Phys.* **1993**, *98* (7), 5648–5652. https://doi.org/10.1063/1.464913.

(8) Lee, C.; Yang, W.; Parr, R. G. Development of the Colle-Salvetti Correlation-Energy Formula into a Functional of the Electron Density. *Phys. Rev. B. Condens. Matter* **1988**, *37* (2), 785–789. https://doi.org/10.1103/physrevb.37.785.

(9) Vosko, S. H.; Wilk, L.; Nusair, M. Accurate Spin-Dependent Electron Liquid

Correlation Energies for Local Spin Density Calculations: A Critical Analysis. *Can. J. Phys.* **1980**, *58* (8), 1200–1211. https://doi.org/10.1139/p80-159.

(10) Stephens, P. J.; Devlin, F. J.; Chabalowski, C. F.; Frisch, M. J. Ab Initio Calculation of Vibrational Absorption and Circular Dichroism Spectra Using Density Functional Force Fields. *J. Phys. Chem.* **1994**, *98* (45), 11623–11627. https://doi.org/10.1021/j100096a001.

(11) Schäfer, A.; Horn, H.; Ahlrichs, R. Fully Optimized Contracted Gaussian Basis Sets for Atoms Li to Kr. *J. Chem. Phys.* **1992**, *97* (4), 2571–2577. https://doi.org/10.1063/1.463096.

(12) Klamt, A.; Schüürmann, G. COSMO: A New Approach to Dielectric Screening in Solvents with Explicit Expressions for the Screening Energy and Its Gradient. *J. Chem. Soc. Perkin Trans. 2* **1993**, No. 5, 799–805. https://doi.org/10.1039/P29930000799.

(13) Ahlrichs, R.; Bär, M.; Häser, M.; Horn, H.; Kölmel, C. Electronic Structure Calculations on Workstation Computers: The Program System Turbomole. *Chem. Phys. Lett.* **1989**, *162* (3), 165–169. https://doi.org/https://doi.org/10.1016/0009-2614(89)85118-8.

(14) Furche, F.; Ahlrichs, R.; Hättig, C.; Klopper, W.; Sierka, M.; Weigend, F. Turbomole. *WIREs Comput. Mol. Sci.* **2014**, *4* (2), 91–100. https://doi.org/https://doi.org/10.1002/wcms.1162.

(15) Pracht, P.; Bohle, F.; Grimme, S. Automated Exploration of the Low-Energy Chemical Space with Fast Quantum Chemical Methods. *Phys. Chem. Chem. Phys.* **2020**, *22* (14), 7169–7192. https://doi.org/10.1039/C9CP06869D.

(16) Bannwarth, C.; Ehlert, S.; Grimme, S. GFN2-XTB—An Accurate and Broadly Parametrized Self-Consistent Tight-Binding Quantum Chemical Method with Multipole Electrostatics and Density-Dependent Dispersion Contributions. *J. Chem. Theory Comput.* **2019**, *15* (3), 1652–1671. https://doi.org/10.1021/acs.jctc.8b01176.

(17) Fu, Z.; Wang, X.; Gardner, A. M.; Wang, X.; Chong, S. Y.; Neri, G.; Cowan, A. J.; Liu, L.; Li, X.; Vogel, A.; Clowes, R.; Bilton, M.; Chen, L.; Sprick, R. S.; Cooper, A. I. A Stable Covalent Organic Framework for Photocatalytic Carbon Dioxide Reduction. *Chem. Sci.* **2020**, *11* (2), 543–550. https://doi.org/10.1039/C9SC03800K.

6.5 Appendix

6.5.1 NMR spectra

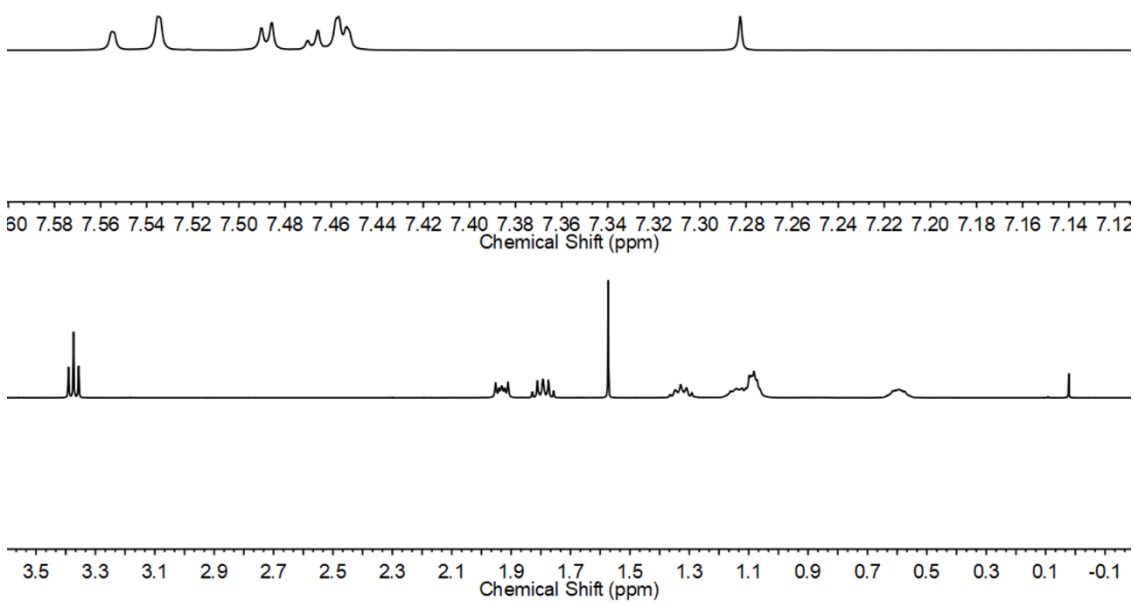

Figure 6.1 NMR spectra of 2,7-Dibromo-9,9-bis(8-bromo-n-octyl)-fluorene in $CDCl_3$.

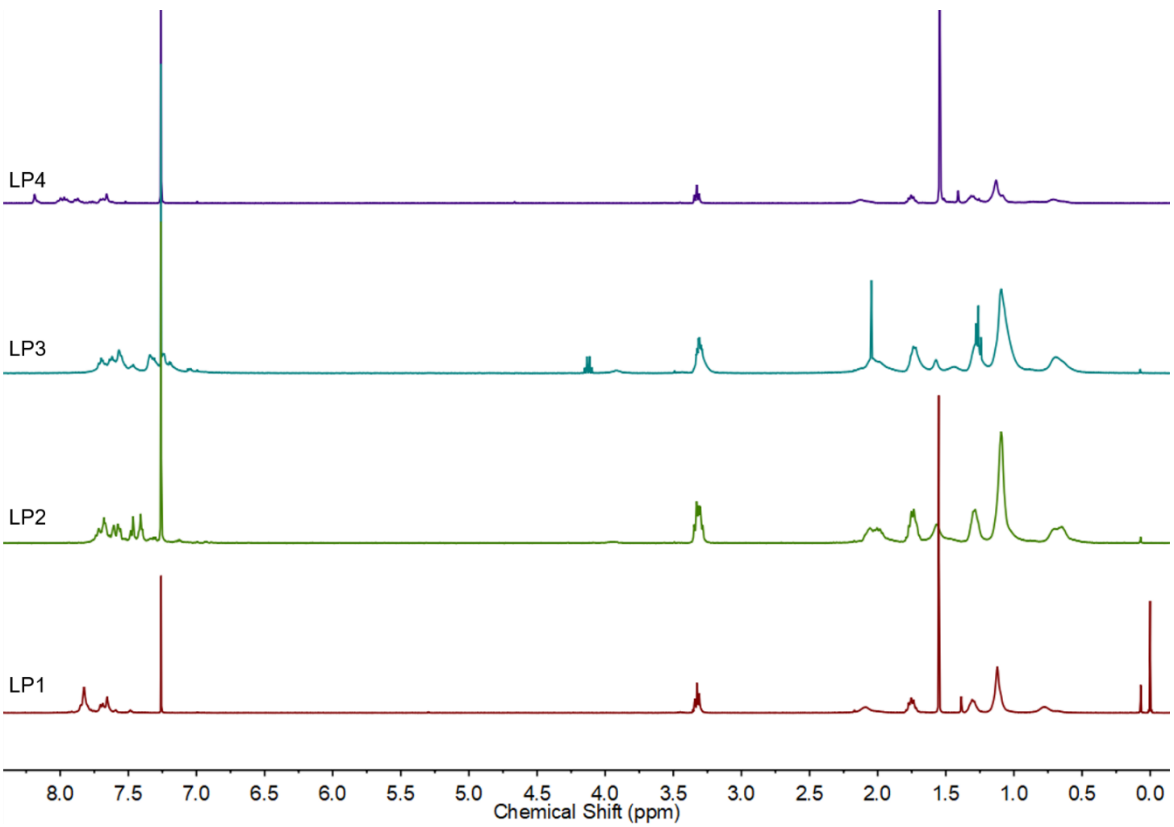

Figure 6.2 NMR spectra of polymer LP1, LP2, LP3, and LP4 in $CDCl_3$.

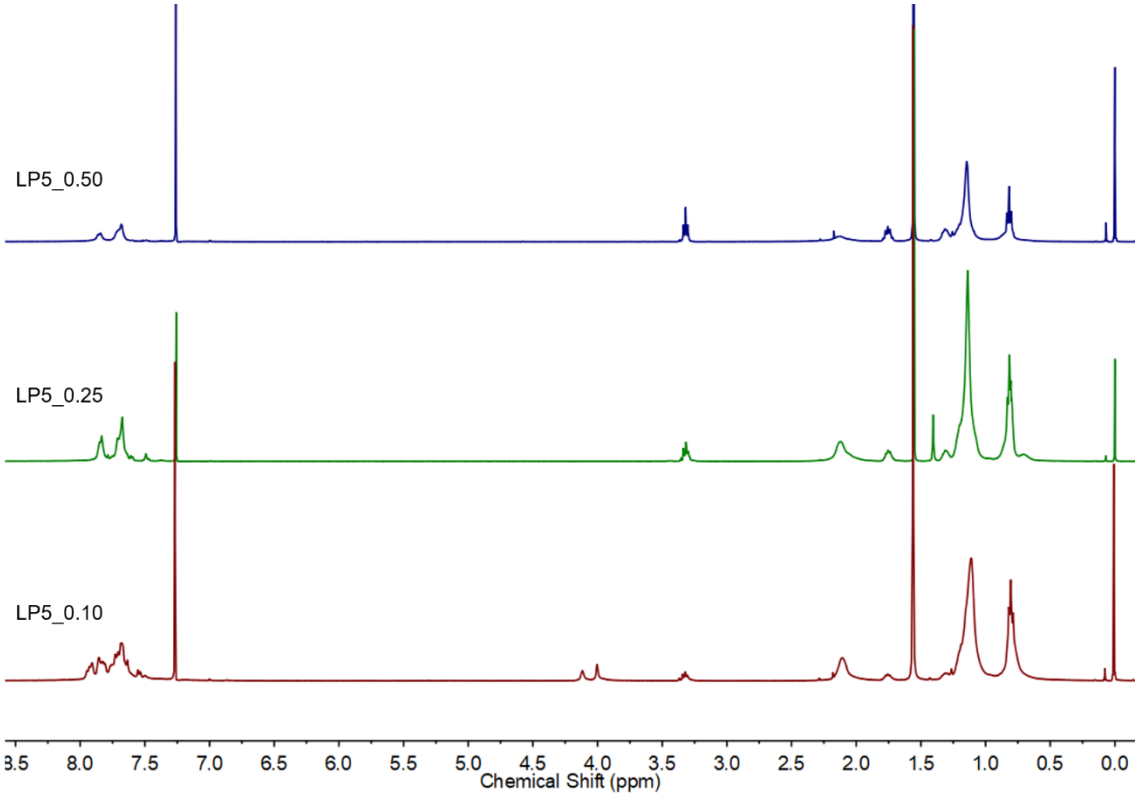

Figure 6.3 NMR spectra of polymer LP5_0.50, 0.25, .010 in $CDCl_3$.

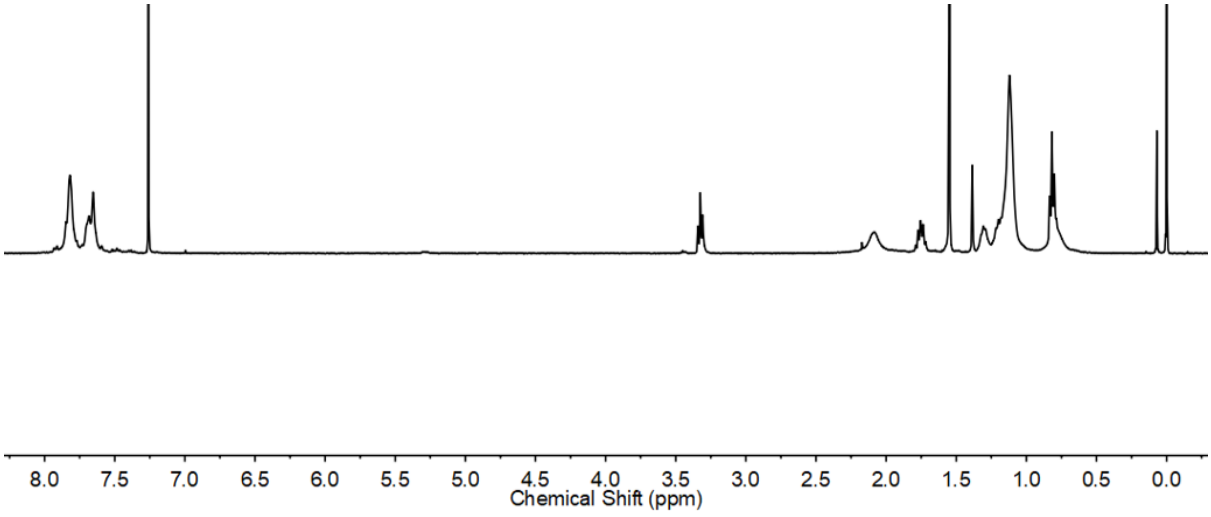

Figure 6.4 NMR spectrum of polymer LP6 in $CDCl_3$.

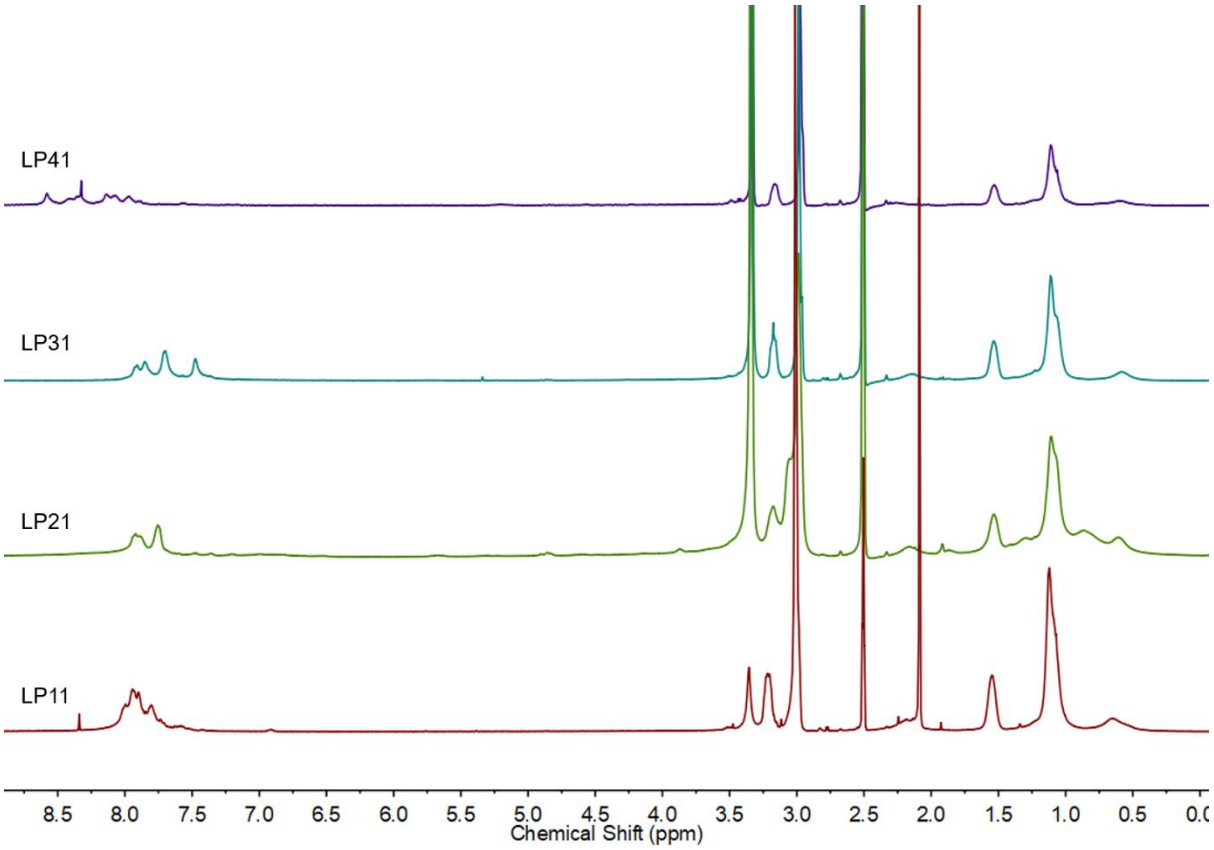

Figure 6.5 NMR spectra of polymer LP11, LP21, LP31, and LP41 in DMSO.

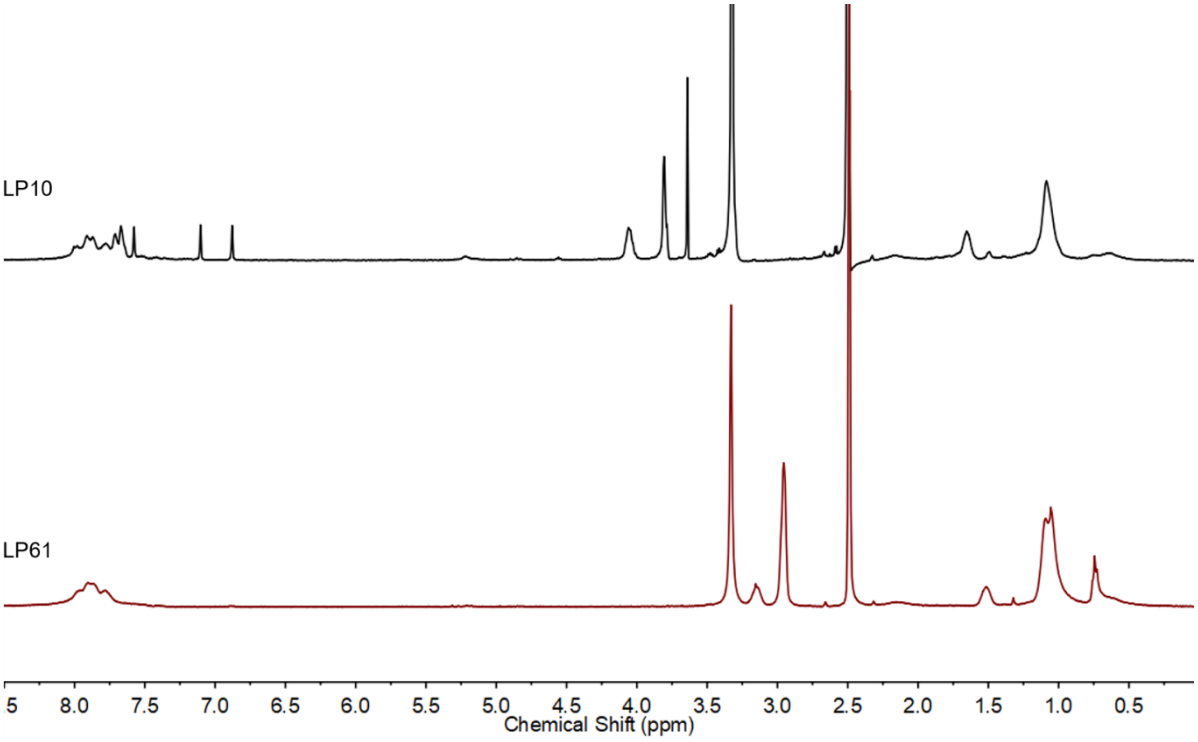

Figure 6.6 NMR spectra of polymer LP10 and LP61 in DMSO.

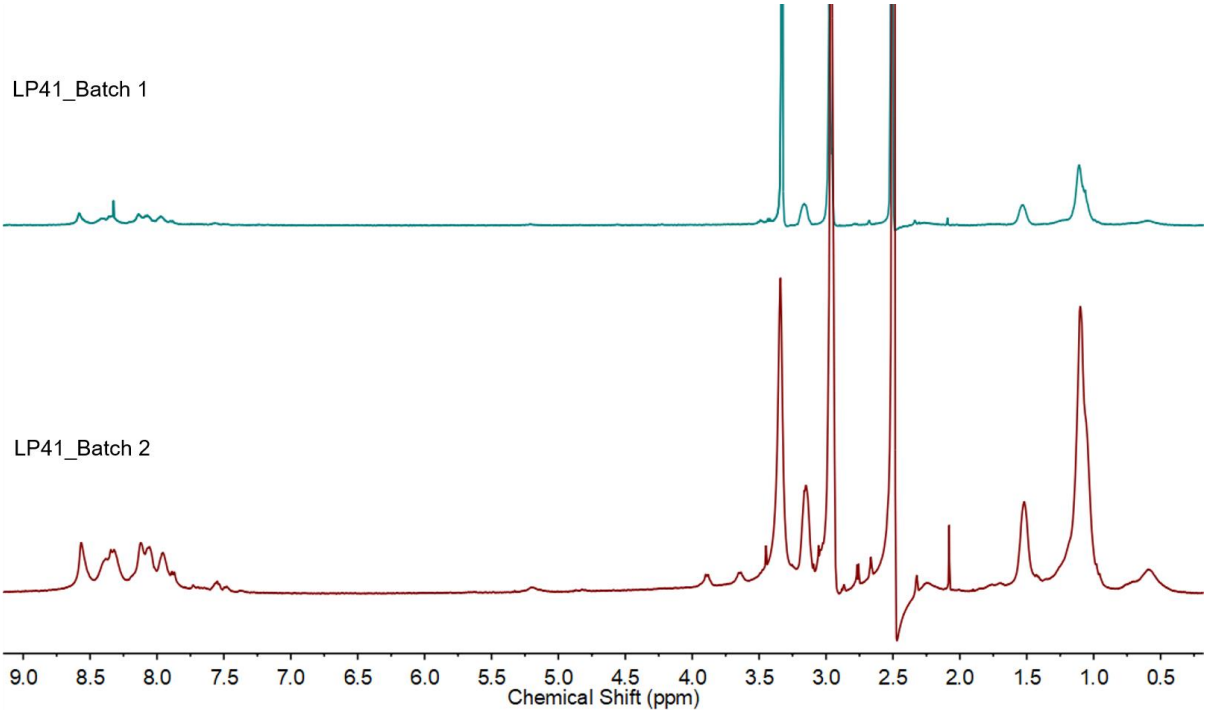

Figure 6.7 NMR spectra of LP41 in DMSO from two batches.